

INFLUENCE OF THE FLANGE ON THE ULTIMATE SHEAR
CAPACITY OF REINFORCED CONCRETE T-BEAMS

by

Youssef M. H. Hammad
(B.Sc., D.B.C.I.E.)

March 1978

A Thesis presented to the University of
Sheffield for the Degree of Doctor of
Philosophy

IMAGING SERVICES NORTH

Boston Spa, Wetherby
West Yorkshire, LS23 7BQ
www.bl.uk

CONTAINS
PULLOUTS

BEST COPY AVAILABLE.

VARIABLE PRINT QUALITY

To my Mother

C O N T E N T S

<u>CHAPTER</u>		<u>PAGE NO</u>
	<u>LIST OF FIGURES</u>	v
	<u>LIST OF TABLES</u>	x
	<u>NOTATIONS</u>	xi
	<u>ACKNOWLEDGEMENT</u>	xiv
	<u>SUMMARY</u>	xv
1	<u>INTRODUCTION</u>	
	1.1 Preamble	1
	1.2 Purpose and Scope	3
	1.3 Layout of Thesis	4
2	<u>PREVIOUS RESEARCH ON T-BEAMS</u>	
	2.1 Introduction	6
	2.2 Previous Experimental and Analytical Work on Reinforced Concrete T-beams	7
	2.2.1 Tests by Ferguson and Thompson	7
	2.2.2 Tests by Al-Alusi	8
	2.2.3 Tests by Neville and Lord	9
	2.2.4 Study by Taub and Neville	10
	2.2.5 Tests by Guralnick	11
	2.2.6 Tests by Ramakrishnan	12
	2.2.7 Tests by Loenhardt	15
	2.2.8 Analysis by Placas and Regan	16
	2.2.9 Tests by Khan	18
	2.2.10 Study by Tang	18
	2.2.11 Tests by Swamy, Andriopoulos and Adepegba	19
	2.2.12 Tests by Yunus	19
	2.2.13 Tests by Swamy, Bandyopad- hyay and Erikitoila	20
	2.2.14 Theory by Swamy and Quereshi	21
	2.3 Critical Study	23
	2.3.1 Introduction	23
	2.3.2 Analytical data	23
	2.3.3 Discussion	24
	2.3.4 Conclusions	28
	2.4 Concluding Remarks	29
3	<u>FINITE ELEMENT APPROACH</u>	
	3.1 General	30
	3.2 Three Dimensional Finite Element	35

3.2.1	Introduction	35
3.2.2	Hexahedron Isoparametric elements	36
3.2.2.1	Shape Functions	36
3.2.2.2	Isoparametric Concept	38
3.2.2.3	Element Stresses and Strains	40
3.2.2.4	Evaluation of Element Matrices	42
3.2.2.5	Element Stiffness	44
3.2.2.6	Numerical Integration	46
3.2.3	Bar Elements	48
3.2.3.1	Introduction	48
3.2.3.2	Element Properties	49
3.2.4	Assembly and Solution	52
3.3	Non-linear Incremental Analysis	53
3.3.1	Introduction	53
3.3.2	Method of Variable stiffness	54
3.3.3	Incremental Procedure	56
3.4	Non-linearity and Isoparametric elements	59
4	<u>REINFORCED CONCRETE BEHAVIOUR AND ITS FAILURE LAWS</u>	
4.1	Introduction	61
4.2	Behaviour of Concrete under Load	61
4.2.1	Internal behaviour	61
4.2.2	Uniaxial stress behaviour	64
4.2.3	Compressive and tensile strength	64
4.3	Failure Laws	65
4.3.1	Introduction	65
4.3.2	Failure Laws in Tension zones	69
4.3.3	Failure Laws in tension-compression zones	70
4.3.3.1	Mahmood and Hannant Failure Criteria	71
4.3.3.2	Cedolin, Crutzen and Poli Failure Criteria	73
4.4	Crack Simulation	75
4.4.1	Introduction	75
4.4.2	Crack initiation	76
4.4.3	Interlocking on initiated cracks	81

	4.4.4	Constitutive Relationships	82
	4.5	Steel Behaviour	86
5		<u>COMPUTER PROGRAM</u>	
	5.1	Introduction	88
	5.2	Structure of the Program	88
	5.3	Output of the Program	94
	5.4	Concluding Remarks	94
6		<u>EXPERIMENTAL PROGRAMME</u>	
	6.1	Introduction	96
	6.2	Properties of Materials	97
	6.2.1	Concrete Mix Design	97
	6.2.1.1	Introduction	97
	6.2.1.2	Materials	98
	6.2.1.2.1	Aggregates	98
	6.2.1.2.2	Cement	98
	6.2.1.2.3	P F A	100
	6.2.1.3	Mix Design Procedure	100
	6.2.1.4	Mixing and Casting	103
	6.2.1.5	Tests & Size of Test Specimens	103
	6.2.1.6	Discussion of Results	106
	6.2.1.7	Conclusions	109
	6.2.2	Tensile Reinforcement	109
	6.3	Design of Beams	110
	6.4	Description of Test Series	111
	6.5	Instrumentation	114
	6.6	Manufacturing of Beams	115
	6.7	Testing Apparatus	117
	6.8	Testing Procedure	118
	6.9	Investigation for the location of the preformed crack	119
	6.9.1	Introduction	119
	6.9.2	Details of Tests	119
	6.9.3	Discussion of Results	120
	6.9.3.1	Load-deflection Relations	120
	6.9.3.2	Concrete strains in the shear span	121
	6.9.3.3	Steel strains	122
	6.9.3.4	Cracking and Modes of Failure	122
	6.9.3.5	Strength characteristics	123
	6.9.4	Location of the Preformed crack for the next Tests	124

7	<u>COMPARISON OF COMPUTER ANALYSIS RESULTS WITH EXPERIMENTAL DATA</u>	
7.1	Introduction	126
7.2	Comparison	127
7.2.1	Method of Analysis	127
7.2.2	Beams with different preformed crack positions	128
7.2.3	Beams with different flange width and thickness	133
7.2.3.1	Group 1	133
7.2.3.2	Group 2	136
7.2.3.3	Group 3	139
7.3	Conclusions	142
8	<u>EFFECTIVE WIDTH AND SHEAR RESISTANCE OF THE FLANGE</u>	
8.1	Introduction	144
8.2	Effective width of the flange	145
8.2.1	Shear stresses in the flange	145
8.2.2	Definition of the 'Effective width'	147
8.2.3	Factors influencing the 'Effective width'	148
8.2.4	Prediction of the 'Effective width'	150
8.3	Shear Resistance of the flange	152
8.3.1	Introduction	152
8.3.2	Prediction of shear resistance of the flange	154
8.3.3	Shear strength of the flange with respect to results of full beam tests	159
8.4	Conclusions	169
9	<u>CONCLUSIONS, LIMITATIONS AND SUGGESTIONS FOR FUTURE WORK</u>	
9.1	Conclusions	171
9.2	Limitations and suggestions for future work	174
	<u>REFERENCES</u>	178
	<u>APPENDIX A</u>	185

LIST OF FIGURES

<u>Figure No</u>		<u>Page No</u>
<u>Chapter 2</u>		
2.1 a to b	Cracking and ultimate stress vs a/d ratio	8
2.2	Typical load-deflection curves for T-beams, failing in shear	13
2.3	Equilibrium conditions at an inclined plane	17
2.4	Actual and modified longitudinal stress distribution across flange width according to elastic theory	23
2.5	Effective distance 'x' of flange vs flange width/rib width ratio	25
2.6	Effective distance 'x' of flange vs flange width/rib width ratio	27
2.7	Effective distance 'x' of flange vs longitudinal reinforcement	27
2.8	Effective distance 'x' of flange vs longitudinal reinforcement	27
2.9	Effective distance 'x' of flange vs longitudinal reinforcement	27
2.10	Effective distance 'x' of flange vs shear reinforcement	27
2.11	Effective distance 'x' of flange vs shear reinforcement	27
2.12	Effective distance 'x' of flange vs shear span/effective depth ratio	27
<u>Chapter 3</u>		
3.1	Isometric view of triangular element with linear displacement model plotted in the third direction	30
3.2.	Incremental and iterative procedures	34
3.3	Shape functions for quadratic ele- ments of serendipity family	36

<u>Figure No</u>		<u>Page No</u>
3.4	Normalised co-ordinates for a rectangle	37
3.5	20-node hexahedron	37
3.6	Typical bar element in curvilinear directions within a hexahedron element	49
3.7	Incremental-iteration procedure	56
3.8	Flow chart for incremental procedure	57
 <u>Chapter 4</u> 		
4.1	The stages of cracking in concrete	62
4.2	Stress-strain relationship of concrete under uniaxial tension	62
4.3	Element numbers	69
4.4	Failure surface for plain concrete subjected to short-term multiaxial stresses	70
4.5	Failure surface for tensile stress states	70
4.6	Load-deflection curve - beam TBX V	71
4.7	Failure equations under tension-compression-compression-stresses	71
4.8	Comparison of experimental results and proposed equations for tensile stresses	74
4.9	Tensile stress-strain relationship and fracture of concrete	77
4.10	Idealisation of macroscopic fracture patterns in tension-compression zones	78
4.11 a to b	Load-deflection curves - beams TBX V and TBX VI	81
4.12	Load-deflection curve - beam TBX V	81
4.13	Typical stress-strain curve for cold-worked steel	86

Chapter 5

- 5.1 Flow diagram for the main operations in the computer program 88

Chapter 6

- 6.1 Influence of water/fine material ratio on cube and flexure strength 108
- 6.2 Influence of fine material/aggregate ratio on cube and flexure strength 108
- 6.3 Cube and flexure strength vs age 108
- 6.4 Strain profile for reinforced concrete beams 110
- 6.5 Longitudinal and cross sections of beams 113
- 6.6 Details of instrumentation 114
- 6.7 Details of crack formers 116
- 6.8 Schematic layout of test rig 117
- 6.9 Locations of preformed cracks for beams of series I 120
- 6.10 Shear force-deflection curves 120
- 6.11 Concrete strains across the flange width 121
- a to c
- 6.12 Shear force vs steel strains at midspan 122
- 6.13 Location of failure planes 124
- 6.14 Suggested location and inclination of preformed crack 124

Chapter 7

- 7.1 Part of the flange to be analysed by Finite Element Method 127
- 7.2 Finite element mesh for beams of series I & II 127
- a to c
- 7.3 Midspan load-deflection curves 129

<u>Figure No</u>		<u>Page No</u>
7.4 a to d	Crack patterns resulting from analysis	130
7.5 a to d	Modes of failure	130
7.6 a to c	Load-deflection curves	133
7.7 a to c	Crack patterns resulting from analysis	134
7.8 a to c	Modes of failure	134
7.9 a to c	Shear stress distributions before failure	135
7.10 a to c	Load-deflection curves	137
7.11 a to c	Crack patterns resulting from analysis	137
7.12 a to c	Modes of failure	137
7.13 a to c	Shear stress distributions before failure	138
7.14 a to c	Load-deflection curves	139
7.15 a to c	Crack patterns resulting from analysis	139
7.16 a to c	Modes of failure	139
7.17 a to c	Shear stress distributions before failure	141
 <u>Chapter 8</u> 		
8.1	Schematic shear stress distribution in the flange of a T-beam	145
8.2	Integration points and stress components	147
8.3	Shear stress distribution at the middle surface for different flanges	147

<u>Figure No</u>		<u>Page No</u>
8.4	Effective width at ultimate load	150
8.5	Effective width at ultimate load	150
8.6	Effective width at ultimate load	150
8.7	Effective width at ultimate load	150
8.8	Shear stress distribution in the compression zone of rectangular beam at ultimate load	154

LIST OF TABLES
=====

<u>TABLE NO</u>		<u>PAGE NO</u>
	<u>Chapter 2</u>	
2.1	Distance 'x' of the Flange (Placas Equation)	26
	<u>Chapter 3</u>	
3.1	Graus-Legendre Quadrature Constants	47
	<u>Chapter 4</u>	
4.1	Principal Stresses in the Flange at Ultimate Load	66
4.2	Principal Stresses in the Flange at Ultimate Load	67
4.3	Principal Stresses in the Flange at Ultimate Load	68
4.4	Crack Patterns	80
	<u>Chapter 6</u>	
6.1	Sieve Analysis of Available Aggregate	99
6.2	Specification of Fly-Ash	101
6.3	Replacement Factors for PFA	104
6.4	Proportions of the Mixes and Weight of Materials by Cubic Metre	105
6.5	Slump and VB for the Mixes	107
6.6	Compressive and Flexural Strength	108
	<u>Chapter 7</u>	
7.1	Shear forces carried by the Flange	136
7.2	Shear forces carried by the Flange	138
7.3	Shear forces carried by the Flange	141
	<u>Chapter 8</u>	
8.1	Evaluated 'Effective width'	149
8.2	'Effective width' of the Flange	153
8.3	Shear strength of the Flange	156
8.4	Al-Alusi Tests	160
8.5	Placas Tests	162
8.6	Erikitoala Tests	164
8.7	Ferguson Tests	166
8.8	Ramakrishnan Tests	168

NOTATIONS

A_s	Cross sectional area of main tensile reinforcement
A_{sb}	Amount of steel required for balanced section
A_{sl}	Cross sectional area of links
a	Shear span
B	Flange width
b_o	Web width
$2b_e$	'Effective width' of flange
C	Longitudinal force in the compression zone
$C_i, C_j,$ C_l, K_q	Coefficients of integration rules
d	Effective depth of beam
d_n	Depth of neutral axis from top fibre
E, E_c	Elastic modulus of concrete
E_s	Modulus of elasticity for steel
F	Shear transfer factor
f_c	Average compressive stress in the compression zone at shear failure
f_{cu}	Cube compressive stress of concrete
f'_c, σ_{cy}	Cylinder compressive strength of concrete
f_t	Principal tensile stress of concrete
f'_t	Tensile strength of concrete
f_y	Yield strength of steel
G	Shear modulus for concrete
h	Over-all depth of beam

I_1, I_2, I_3	Stress invariants
m	Total number of integration points
n	Total number of finite elements
P	Total external load
q	Integration point
r'	$2A_{s1}/(b_o S)$, S = spacing between links
T	Tensile reinforcement
t	Thickness of the compression flange
U	Strain energy for elastic body
U_e	Internal strain energy for the element
u, v, w	Components of displacements in x, y, z directions
V	Shear force
V_c	Shear resistance of concrete in the compression zone at the critical section
V_{cr}	Shear force producing shear cracking
V_l	Shear force carried by a link
V_u	Shear force causing shear failure
v	Nominal shear stress
v'_c	Limiting stress in pure shear
v_{cr}	Cracking shear stress
v_u	Ultimate shear stress
x, y, z	Cartesian co-ordinates
ρ	$A_s/(b_o d)$
ρ_b	$A_{sb}/(b_o d)$
π	Total potential energy
ν	Poisson's ratio
ξ, η, ζ	Normalised co-ordinates

$\sigma_1, \sigma_2, \sigma_3$	Principal stresses
$\sigma_x, \sigma_y, \sigma_z$	Component of normal stresses in x, y and z directions
$\tau_{xy}, \tau_{yz},$ τ_{zx}	Component of shear stresses
ϵ_s	Steel strains
$\epsilon_x, \epsilon_y, \epsilon_z$	Components of normal strains in x, y, and z directions
$\gamma_{xy}, \gamma_{yz},$ γ_{zx}	Components of shear strains
[A]	Normalised modal matrix
[B]	Strain matrix
[D], [D]*	Elasticity matrix
[K], [K _o]	Over-all stiffness matrix
[K _e]	Element stiffness matrix
[K _s]	Bar element stiffness matrix
[N]	Shape functions matrix
{ F _e }	Fictitious forces vector
{ R }, { ΔR }	Total and incremental load vectors
{ δ }, { δ _o }, { δ _e }	Nodal displacement vectors
{ Δδ }	Incremental displacement vector
{ σ }, { Δσ }	Total and incremental stress vectors
{ ε }, { Δε }	Total and incremental strain vectors

A C K N O W L E D G E M E N T S

The author wishes to thank Mr R Jones and Dr R N Swamy for their continuous interest, assistance and guidance throughout the period of this project.

He would also thank Professors D Bond and T H Hanna for their help and encouragement.

Acknowledgements are due to the Technical and Secretarial staff of the Department of Civil and Structural Engineering for their assistance during the progress of this work.

The help and advice of the staff at the Computer Centre, Sheffield University are most appreciated.

Thanks are also extended to the friends and colleagues for their advice and assistance and Mrs C Roscoe for typing the thesis.

Finally, the author wishes to acknowledge his gratitude to his mother and members of the family for their help.

S U M M A R Y

Despite the considerable amount of research on shear transfer mechanism, a clear understanding of the shear carried by the uncracked compression zone concrete of T-beams at ultimate load and the shear stress distribution has not yet been achieved. This thesis presents theoretical and experimental studies of the shear carried by the compression zone in T-beams.

In the theoretical study, a 3-dimensional finite element stress analysis was applied. Maximum stress and octahedral failure criteria were used to predict cracking of concrete in tension and tension-compression zones respectively. Non-linearity of concrete due to cracking was tackled through a 'variable stiffness' technique in conjunction with an incremental procedure. Twenty node hexahedron isoparametric elements and bar elements were used to model the concrete and reinforcement respectively. A computer program was written to include these aspects.

The theoretical study was supplemented by two series of tests on full scale laboratory beams with preformed shear cracks. The main parameters investigated were the location of the preformed crack and the variation in the flange width and thickness.

Load-deflection curves, failure load and crack patterns obtained from the theoretical analysis were compared with the experimental results. Shear stress distribution in the flange was found to be concentrated over the webs, reducing

significantly towards the outer edges. Equations for evaluating an 'effective width' were developed using non-linear regression analysis. An expression was also developed for predicting the shear resistance of the compression zone using the effective width and an average value of the shear stress. From these equations, the contribution of the flange in resisting shear forces at ultimate load was found to be between 50% and 70% of the total shear strength of T-beams.

shear cracks in the web area of the shear span. The internal shear transfer mechanism existing before failure is not fully known. In the case of out web reinforcement, it has been suggested that formation of shear cracks that extend along the length resisted by a combination of shear stresses in the concrete of the uncracked portion and (1) interlock of aggregate on the opposite faces of the crack, and (2) lever effect of main longitudinal reinforcement.

Despite the vast amount of research work carried out on shear in the past, this work was directed to investigate certain parameters affecting the shear strength of beams. For attempts have been made to assess the contribution of each shear component in carrying its share of the total shear force. This is probably due to the difficulty in separating each component in special tests. However, the experimental investigations that have been carried out on rectangular beams to assess the relative magnitude of shear stress components, have shown that about 60% of the total shear

INTRODUCTION

1.1 Preamble

In order to develop ultimate strength theories for design purposes, a good knowledge of structural behaviour is necessary. One of the sudden and dangerous failures of reinforced concrete beams is the so-called shear failure. This failure is characterised by the formation of inclined shear cracks in the web area of the shear span of the beams. The internal shear transfer mechanism existing in the beam before failure is not fully known. In the case of beams without web reinforcement, it has been suggested that, after the formation of shear cracks the external shear forces are resisted by a combination of three components: (1) Shear stresses in the concrete of the uncracked compression zone, (2) Interlock of aggregate on the opposite faces of the shear crack, and (3) Dowel effect of main longitudinal reinforcement.

Despite the vast amount of research work carried out on shear in the past, this work was directed to investigate certain parameters affecting the shear strength of beams. Few attempts have been made to assess the contribution of each shear component in carrying its share of the total shear force. This is probably due to the difficulty in separating each component in special tests. However, the experimental investigations that have been carried out on rectangular beams to assess the relative magnitude of these shear components, have shown that about 40% of the total shear

can be carried by the compression zone, between 15-25% by dowel forces and between 33%-50% by aggregate interlock.

Most of the available data has been obtained from test beams having rectangular cross sections, although, in practice the majority of beams are built as T-beams. It is expected that T-beams behave differently than rectangular beams. This is probably due to (1) The aggregate interlock being less important in T-beams than rectangular beams, due to the proportionately smaller width of cracked concrete, (2) The greater contribution of the flange in resisting shear forces because of the stronger compression zone.

So far, only limited experimental and theoretical research work has been done on T-beams. An analysis of the existing information shows that the present prediction equations for the shear strength of the beams are not satisfactory.

A rigorous investigation of the contribution of the flange in resisting shear forces and the distribution of shear stresses within the flange has not yet been made either theoretically or experimentally. This is why the current code of practice gives nothing about the contribution of the flange in resisting shear forces and in fact considers the flanged section as rectangular with the width being that of the rib. With the development of ultimate design theories for shear in reinforced concrete structures, the need for knowing the contribution of the flange in resisting shearing forces becomes necessary and it should lead to more economical design of T-beams.

1.2 Purpose and Scope

It is generally believed that a large part of the shear force resisted by a reinforced concrete T-beam is carried by the compression zone in the flange.

Shear and compressive stress distributions across the width of the flange are not uniform and therefore direct determination of the shear carried by the concrete of the compression zone is difficult. In bending problems an 'effective width' concept is used in conjunction with an assumed uniform stress distribution. This enables the flexural strength to be assessed without complicated calculations.

The purpose of the present project is to investigate the contribution of the flange in carrying shear forces and possibly arriving at an 'effective width' of flange for use in the assessment of shear strength.

Theoretical and experimental investigations have been carried out as follows:

- (1) **Theoretical study:** The aim of the theoretical study is to compute the shear stress distribution in the concrete of the compression zone in the presence of flexural compression stresses. The shear force resisted by the compression zone at ultimate load can then be determined. To achieve this for a flanged beam a 3-dimensional stress analysis using non-linear finite element approach has been applied. Material failure laws have been incorporated in the finite element model to predict the behaviour of the

beams up to the ultimate stage. The deformations, failure load, crack patterns and stress distributions of the beams have been predicted. The project involves the preparation of a computer program which has sufficient flexibility to enable the introduction of other material properties laws and for it to be used for further research work.

(2) Experimental study: The experimental part of the study was to verify the theoretical work and to investigate the effects of some of the major parameters on the shear carried by the compression zone. Full size T-beams were cast and tested. To assess the shear strength of the flange the beams were provided with preformed cracks in the web area of the shear spans. Two series of beams were tested:

(1) Series I included a beam without cracks and four beams with different locations of preformed crack. This series was carried out to investigate the position of the preformed crack and its effects on the strength and behaviour of the beams.

(2) Series II included beams with different flange widths and flange thicknesses to investigate the effects of these parameters on the shearing force carried by the compression zone.

1.3 Layout of Thesis

Chapter 2 reviews the research work on shear strength of T-beams. A critical study is presented in this chapter for the current prediction equations for the strength of T-beams.

Chapters 3, 4 and 5 deal with the Finite Element approach. In Chapter 3, the formulation of the isoparametric elements and the incremental non-linear method are described; in Chapter 4, the material behaviour and the development of failure laws are discussed and in Chapter 5, the organisation and structure of the computer program is explained.

The experimental programme is discussed in Chapter 6. The mix design and trial tests to determine the best location for the preformed crack are discussed and details of the beams, instrumentation and method of testing are also given.

Chapter 7, describes the application of the Finite Element Method which has been developed to the analysis of T-beams and then a comparison between the experimental and analytical data is presented.

The information obtained from the theoretical analysis is used to develop equations to evaluate the 'effective width' and the shear strength of the flange in Chapter 8. In this chapter a comparison between the shear strength of the flange and the total shear strength of beams is also made using experimental data of other authors.

Conclusions are made from time to time at the end of each chapter, but in Chapter 9, the main conclusions derived from the project are presented. The limitations of the work presented and suggestions for future work are also made.

PREVIOUS RESEARCH ON T-BEAMS

2.1 Introduction

In the last few decades research work on the shear strength of reinforced concrete beams has been largely directed towards an empirical examination of the influence of the following parameters on shear resistance: longitudinal steel percentage, shear span, beam slenderness and web reinforcement. Recently research work has concentrated on the contribution of the various components in resisting shear forces. This has led to a better understanding of the mechanism of shear failure, although this is still far from being completely settled.

The BS Code of Practice (CP 110, 1972) (1) and the recent design recommendations (2), (3) make no distinction between rectangular and flanged beams. Their design rules were derived from the available experimental information, mainly on rectangular beams. However, experimental investigations show that T-beams behave differently from rectangular beams, and the ultimate shear strength of T-beams is found to be generally higher than that for comparable rectangular beams. Therefore the current recommended design methods under-estimate the shear strength of T-beams.

A review of shear theories and methods of analysis of the shear strength of reinforced concrete beams can be found in references (2) and (3). These methods were concerned mainly with rectangular beams, due to there being experimental data on this type more than on any other.

This chapter is divided into two parts:

- (1) A review of the various methods, experimental and analytical, used to assess the behaviour and shear resistance of T-beams.
- (2) A critical study of the existing analytical methods used to predict the shear strength of T-beams.

2.2 Previous Experimental and Analytical Work on Reinforced Concrete T-beams

Despite the increased amount of research work on T-beams during recent years, only limited experimental information is still available for the shear resistance of T-beams. Those of Braune and Myers (4) had concrete of very low cube strength (12-15 N/mm²) and are possibly irrelevant in terms of structural concrete strength used nowadays. These tests are therefore not discussed any further.

2.2.1 Tests by Ferguson and Thompson (5)

They tested 24 beams without web reinforcement. These tests had cylinder compressive strength and web area as variables. The cylinder strength varied between 17.5 and 45.4 N/mm². The beams were tested under two point loads with shear span/depth ratio (a/d) ranging between 3.4 and 6.22. They concluded that the diagonal tensile strength increases very slowly as the compressive strength increases. An empirical formula was suggested to calculate the ultimate diagonal tensile strength as

$$v_u = 145 + .02 f'_c \quad (\text{in imperial units}) \quad (2.1)$$

where v_u = the ultimate shear stress is calculated from the standard relationship:

$$v = V/(b_o jd) \quad (\text{in imperial units}) \quad (2.2)$$

and f'_c = the cylinder compressive strength.

Equation (2.1) neglects the contribution to strength of many parameters such as flange width, flange thickness, shear span and longitudinal reinforcement.

Moreover the calculation of the ultimate shear stress using equation (2.2) is not applicable in the case of flanged beams.

2.2.2 Tests by Al-Alusi (6)

Al-Alusi conducted tests on 25 simple span T-beams to investigate the effect of shear span/depth ratio and variation of longitudinal reinforcement on cracking strength, mode of failure and ultimate strength. He also studied the effect of mesh reinforcement in the flange and of compression reinforcement.

Al-Alusi drew the following conclusions from his tests:

- (1) When the shear span/depth ratio was between 4.0 and 8.0, the ratios v_{cr}/f'_c and v_u/f'_c were constant as shown in Fig 2.1. These curves were expressed by the following equations:

$$v_{cr}/f'_c = 0.046 \quad (\text{in imperial units}) \quad (2.3)$$

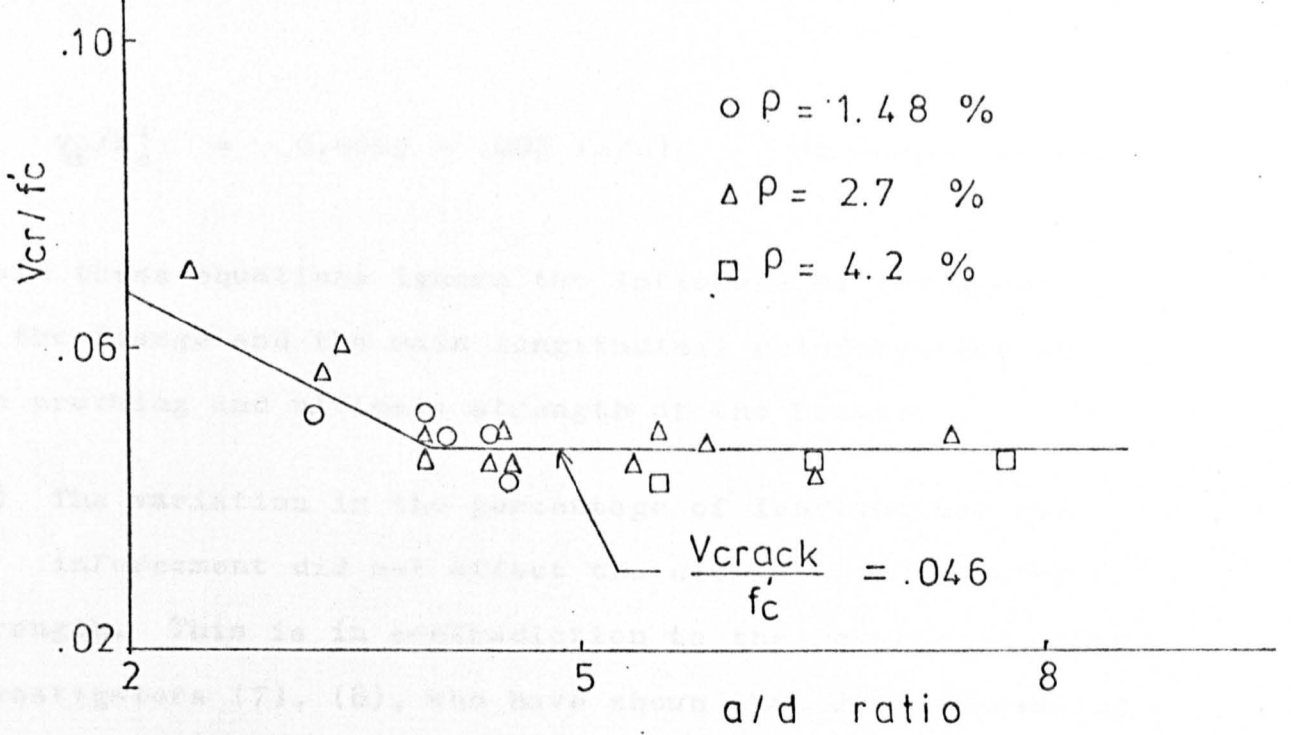


FIG. 2.1.a. CRACKING STRESS vs. a/d RATIO

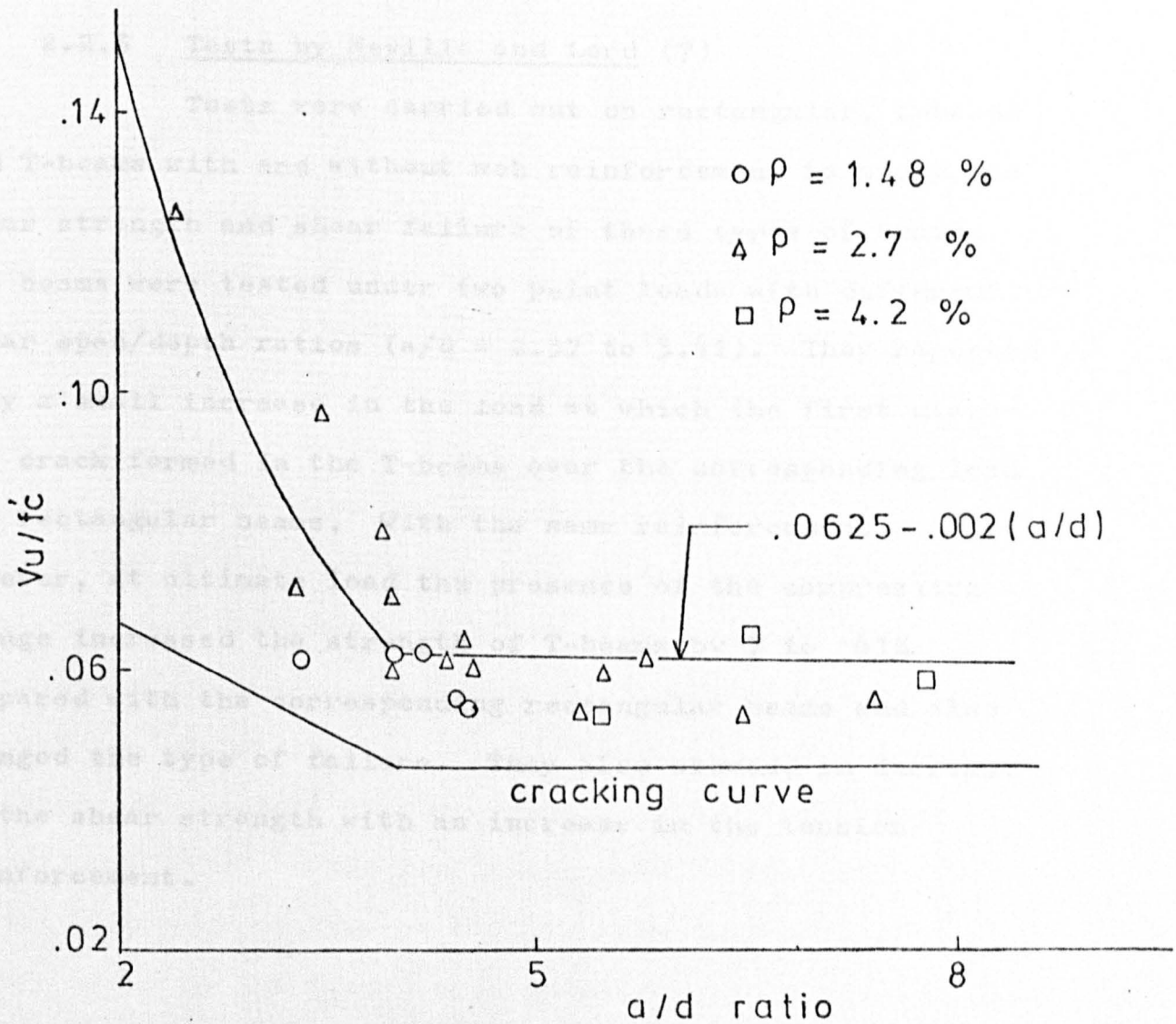


FIG. 2.1.b. ULTIMATE STRESS vs. a/d RATIO
(After Al - Alusi, 6)

$$v_u / f'_c = 0.0625 - .002 (a/d) \quad (\text{in imperial units}) \quad (2.4)$$

Again these equations ignore the influence of the geometry of the flange and the main longitudinal reinforcement on the cracking and ultimate strength of the beams.

(2) The variation in the percentage of longitudinal reinforcement did not affect the ultimate or cracking strength. This is in contradiction to the results of other investigators (7), (8), who have shown that with increasing amounts of longitudinal tensile steel, the ultimate shear strengths of beams also increase.

2.2.3 Tests by Neville and Lord (7)

Tests were carried out on rectangular, L-beams and T-beams with and without web reinforcement to study the shear strength and shear failure of these types of beams. The beams were tested under two point loads with different shear span/depth ratios ($a/d = 2.37$ to 3.41). They reported only a small increase in the load at which the first diagonal crack formed in the T-beams over the corresponding load for rectangular beams, with the same reinforcement. However, at ultimate load the presence of the compression flange increased the strength of T-beams by 7 to 61% compared with the corresponding rectangular beams and also changed the type of failure. They also showed, an increase in the shear strength with an increase in the tension reinforcement.

2.2.4 Study by Taub and Neville (8)

The influence of various factors on the behaviour and shear strength of rectangular, L- and T-beams was described by Taub and Neville in a comparative study. They criticised the present methods of design for taking the shear strength of T- or L-beams as equal to the shear strength of rectangular beams having the same web width as T-beams. They also did not agree with the Code of Practice in calculating the shear stress in concrete by the standard formula

$$v = V/(b_o jd) \quad (\text{in imperial units})$$

as this is not based on the correct factors influencing the shear strength of beams.

Their conclusions were similar to those found by Al-Alusi for the relationship between the ultimate shear capacity and shear span/depth ratio. Further, they reported that the a/d ratio has a considerable influence on the mode of failure in rectangular beams. With small a/d ratios, diagonal tension cracks are propagated from the point of application of load to the support in an almost straight line and shear compression failure usually takes place. With larger a/d ratios, one diagonal tension crack forms and extends along the main tension steel causing failure by splitting of concrete in this area. Adequate anchorage at the support will prevent the latter mode of failure. The actual behaviour of T-beams differs from that of rectangular beams, since as the flange area increases, this provides a

stronger compression zone. Thus failure occurs generally in shear-tension and not shear compression even for small a/d ratios.

Taub and Neville conducted tests on pairs of rectangular and T-beams and observed that the ultimate shear strength of T-beams was between 13% and 61% higher than the ultimate shear strength of the corresponding rectangular beams with the same longitudinal reinforcement. Similar results were observed for the shear cracking strength. This supported their views on the behaviour and shear strength of T-beams.

They also showed that a considerable increase in the shear capacity of a beam occurred when the amount of main tension steel was increased for a/d ratios between 3 and 5. They found that for a/d ratios less than 2 the effect of increasing the main steel was negligible.

2.2.5 Tests by Guralnick (9)

Guralnick tested 42 T-beams to examine flexural and shear failures when using high strength steel for longitudinal reinforcement. The beams had identical cross-section, the flange width was 584mm and flange thickness was 102mm, web width was 188mm, and total depth was 387mm. The a/d ratios ranged between 2.95 and 6.10. All beams were with web reinforcement except seven beams which were with plain web. Twenty-four beams failed in diagonal tension and 2 failed in shear compression.

Guralnick concluded that:

(1) The use of high strength steel for beam reinforcement in connection with current code provisions for shear and diagonal tension results in adequate safety with regard to shear failure.

(2) The uncracked compression concrete and web reinforcement, each contribute to the total shear resistance of the beams. The relative contributions to the total shear resistance are influenced by a number of factors, such as beam section properties, loading pattern and physical properties of the concrete.

(3) Stirrups in the immediate vicinity of concentrated loads or reactions carry a much smaller proportion of the total external shear than elsewhere, due to the presence at such locations of vertical compression stresses which reduce the diagonal tension cracking. Later Swamy and Quereshi (10) found that the first stirrups should be placed at $0.75x$ effective depth from the support, and in point loaded beams, the nearest stirrup should be within a $0.75x$ effective depth from the load point.

2.2.6 Tests by Ramakrishnan (11)

Ramakrishnan tested 110 beams under one or two point loads. He studied the mode of failure and ultimate shearing strength of beams without web reinforcement and the effect of the addition of web reinforcement in the form of vertical or inclined stirrups. Major and secondary factors influencing the shear strength of beams were involved in the investigation, such as: effect of concrete

properties, shear span-effective depth ratio, percentage of longitudinal reinforcement, transverse flange reinforcement, geometrical properties of the cross-section of the beams and effect of magnitude of deflection on the shearing strength.

From deformation measurements he noticed abrupt changes in the deflections and strains after the formation of the major diagonal crack. A typical load-deflection curve he obtained for T-beams is shown in Figure 2.2. The compression strains at the top fibre of the beams in the shear span diminished with increasing load and eventually became tensile. The linearity of strain distribution through the depth was also disturbed in the shear span with concentrations of strains above the diagonal crack. The measurements also showed that for T-beams, the ultimate maximum concrete compression strains never reached the crushing strains of concrete which meant that no shear-compression failure was encountered for T-beams.

Ramakrishnan observed that the actual ultimate strength was not affected by the increase in the width of the flange from 152mm to 254mm (web width was 76mm). But the increase of the flange width from 76 mm to 152 mm increased the ultimate loads. This led him to suggest that there is a limit to the width of the flange beyond which it is not effective in increasing the ultimate shearing resistance of the beams, and this depends on the extent to which the redistribution of internal stresses is possible. Tests showed that beams with thicker flanges had higher shearing resistance. He referred that

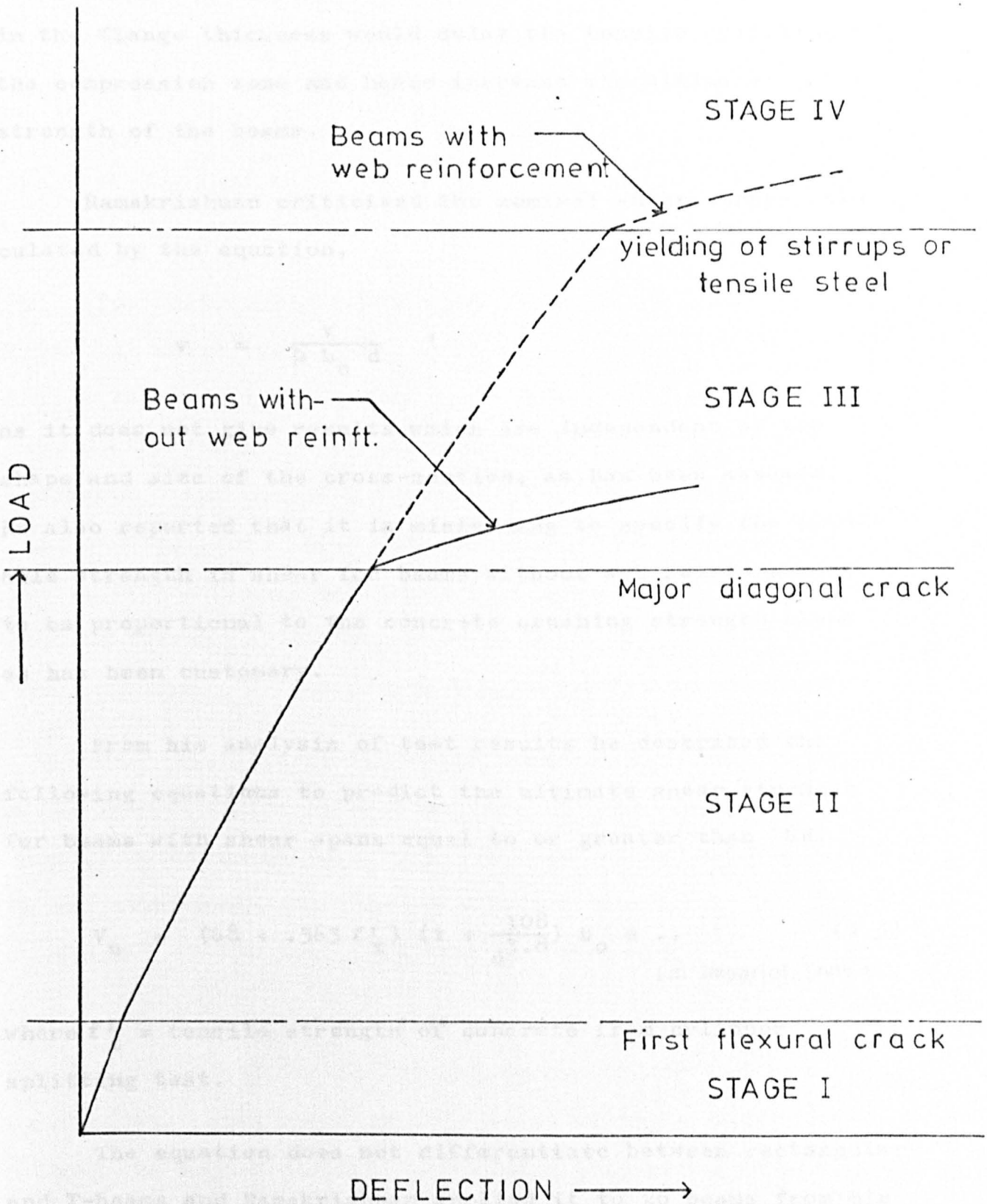


FIG.2.2. TYPICAL LOAD - DEFLECTION CURVES FOR T-BEAMS FAILING IN SHEAR (Schematic - After Ramakrishnan ,11)

to the tensile mode of failure in the flange, as the increase in the flange thickness would delay the tensile splitting of the compression zone and hence increase the ultimate strength of the beams.

Ramakrishnan criticised the nominal shear stress calculated by the equation,

$$v = \frac{V}{\frac{7}{8} b_o d} ,$$

as it does not give results which are independent of the shape and size of the cross-section, as has been assumed. He also reported that it is misleading to specify the allowable strength in shear for beams without web reinforcement to be proportional to the concrete crushing strength alone as has been customary.

From his analysis of test results he described the following equations to predict the ultimate shear strength for beams with shear spans equal to or greater than $6d$.

$$V_u = (68 + .363 f'_t) \left(1 + \frac{108}{d^{3.8}}\right) b_o d \dots \quad (2.5)$$

(in imperial units)

where f'_t = tensile strength of concrete from cylinder splitting test.

The equation does not differentiate between rectangular and T-beams and Ramakrishnan applied it to 26 beams from his tests which included both types.

2.2.7 Tests by Leonhardt (12)

Shear tests were carried out at Stuttgart from 1961 to 1963 to examine the mechanism of shear failure and the parameters influencing the ultimate shear load. The shear strength at the cracked stage was analysed by the classical Mörch truss analogy method.

The tests showed that stirrups began to carry load after the shear cracks had entered the compression zone at a high level of loading near the ultimate stage, and the stresses in the stirrups was increased by decreasing the web thickness. The measured tensile forces in the stirrups remained far below those calculated by the truss analogy even for thin webs. This confirmed that part of the shear force must be carried by the shear stresses in the compression zone and dowel effect of the longitudinal reinforcement.

The test results indicated that the inclination of shear cracks varies between 30° and 45° and depends mainly on the stiffness ratio b_o/B and to some extent on the amount of web reinforcement. The inclination increased with decreasing b_o/B and increasing web reinforcement.

Leonhardt concluded that in normal T-beams where B/b_o was between 3 and 6, the web reinforcement carries less than half of the total shear force even at ultimate load conditions. He suggested that the trusses considered to simulate the actual mechanism of internal shear forces must have compression chords at different inclinations and diagonal web struts with angles less than 45° . However, this method of representing the shear failure mechanism has been found

to be inaccurate (2), (3). This is mainly due to the fact that the compression members are much stiffer than the thin tensile members.

2.2.8 Analyses by Placas and Regan (13), (14)

Placas and Regan used a semi-empirical approach in predicting equations for shear cracking and ultimate shear strength of beams. For shear cracking they suggested:

$$\frac{V_{cr}}{b_o d} = 8 \left[f'_c \frac{100 A_s}{b_o d} \right] \leq 12 (f'_c)^{1/3} \dots \quad (2.6)$$

(in imperial units)

where V_{cr} = shear force producing shear cracking

f'_c = cylinder compressive strength of concrete

A_s = cross-sectional area of main tensile reinforcement

This equation is based upon the assumption that failure occurs when the principal tensile stress reaches some limiting value. This limiting value was taken according to the failure criteria developed by Cowan and verified by Reeves (15)

where

$$f_t = 1.02 (f'_c)^{2/3} \dots \quad (\text{in imperial units}) \quad (2.7)$$

and f_t = principal tensile stress of concrete.

Reeves carried out tests on thin-walled plain concrete hollow cylinders to investigate the properties of concrete under direct and shear stresses. For his limited number of tests, he showed that failure in this case agreed more closely

with the principal stress criterion proposed by equation (2.7).

Strictly speaking, equation (2.6) was developed for cracking in rectangular beams. When it is used for T-beams there is a safety margin of between 15% to 20% due to the uncertainty of dowel action and aggregate interlock. In addition the limiting tensile value proposed by equation (2.7) is far below the tensile strength of concrete, (1.8 N/mm^2 for $f_{cu} = 35 \text{ N/mm}^2$).

At ultimate load, failure in T-beams may result from a shearing action in the compression zone. Placas and Regan considered the vertical equilibrium of forces acting along an inclined shear crack as shown in Fig 2.3. Then assuming that the longitudinal stresses at the level of the underside of the flange near the load are low, so that an almost pure shear condition exists there prior to failure. The principal tensile stresses can be approximated to the nominal shear stresses $(\frac{V_c}{t (b_o + x)})$. Failure occurs in a tensile manner when this shear stress reaches the tensile strength of concrete which is taken as $25(f'_c)^{1/3}$. The area of flange $t (b_o + x)$ involved in resisting the shear forces was determined from experimental tests as $t (b_o + 6")$. The equation for T-beams failing in shear is:

$$V_c = 25 (f'_c)^{1/3} \cdot t (b_o + 6") \dots \text{ (in imperial units) (2.8)}$$

and for T-beam with web reinforcement:

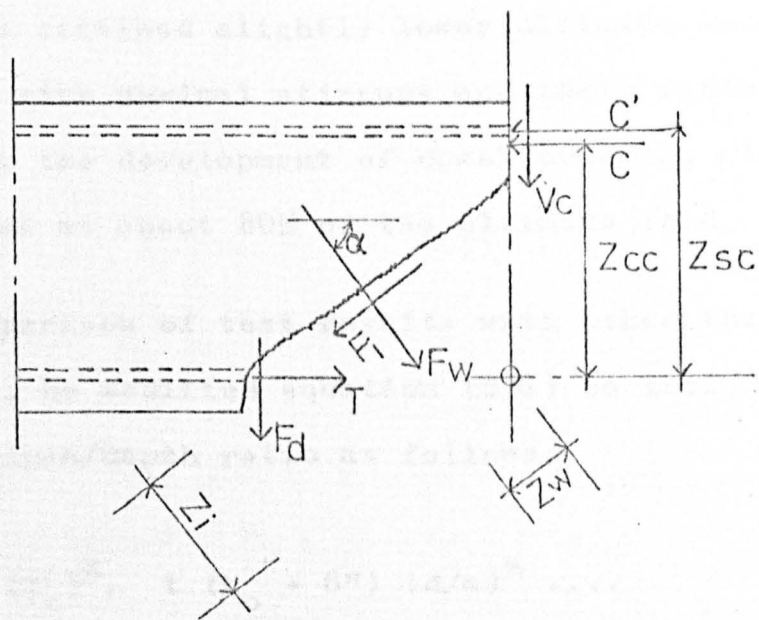


FIG. 2.3. EQUILIBRIUM CONDITIONS AT AN INCLINED PLANE - After Placas and Regan,

$$V_u = 2 (d' - t) b_o r f_{yw} + 25 (f'_c)^{1/3} \cdot t (b_o + 6")$$

(in imperial units)(2.9)

A discussion on this equation is presented in Section 2.3.

2.2.9 Tests by Khan (16)

Khan conducted tests on 24 T-beams to investigate the shear strength of T-beams using bent up bars as shear reinforcement. He concluded that bent up bars are a reliable and efficient form of shear reinforcement. Nevertheless, the beams attained slightly lower ultimate shear loads than beams with nominal stirrups and their failure was expediated by the development of dowel cracking along the longitudinal steel at about 80% of the ultimate load.

On his comparison of test results with other theories and design codes, he modified equation (2.8) to include the effect of shear span/depth ratio as follows:

$$V_c = 36 (f'_c)^{1/3} \cdot t (b_o + 6") (d/a)^{1/4} \dots \quad (2.10)$$

(in imperial units)

2.2.10 Study by Tang (17)

Tang carried out an investigation on the shear strength of large concrete box girders and suggested that the effective width of flange to be used in shear calculation should be related to the flange thickness t as follows:

$(b_o + 2t)$, because in large concrete box girders the flanges may be thicker than those used in normal buildings.

2.2.11 Tests by Swamy, Andriopoulos and Adepegba (18)

Tests were carried out to examine arching action as applied to the mechanism of beams failing in shear. They showed that the tensile force in the longitudinal steel was far from uniform along the length of the bars, but this is essential for arch action to take place.

2.2.12 Tests by Yunus (19)

Thirty-eight T-beams were tested under two symmetrical concentrated loads. The parameters studied were the amount of web reinforcement, the shear span/depth ratio and the amount of longitudinal reinforcement.

The test results indicated the following:

- (1) There was an increase in the cracking load and the ultimate shear strength of beams with reducing a/d ratios. The ultimate shear strength for beams with $a/d = 3.5$ was 63% of that with $a/d = 2.0$.
- (2) The web reinforcement crossed by the diagonal crack became effective in resisting shear forces and yielded before failure of the beam took place.
- (3) The ultimate shear strength of the beams increased with increasing the percentage of longitudinal reinforcement particularly with small a/d ratios. The ultimate shear strength for beams with $\rho = 2.96\%$ was 76% of that with $\rho = 5.28\%$.
- (4) The failure of the beams with small a/d ratios was by crushing of the web, while for those

with larger a/d ratios, the failure was by tensile splitting in the compression zone.

2.2.13 Tests by Swamy, Bandyopadhyay and Erikkitola (20)

They reported tests on T-beams to investigate the effect of flange width, longitudinal steel ratio and web reinforcement.

The results confirmed that the ultimate strength in shear of T-beams is much higher than that of rectangular beams of the same web width, effective depth, ρ/ρ_b (ρ_b = amount of steel required for balanced section), concrete strength and web reinforcement. For beams with $\rho/\rho_b = 0.75$ and flange width/web width ratios from 2 to 7, the ^{increase of} ultimate shear strength ranged from 28% to 113% of that of the rectangular beams for beams without web reinforcement, while for beams with web reinforcement the increases ranged from 45% to 150%.

The shear cracking loads depended primarily upon the concrete strength, while the failure loads depended on the dimensions of the cross section, the amounts of the longitudinal and web reinforcement, the strength of the concrete and the shear span.

The results showed that the shear strength increases as the amount of web reinforcement increases. However, the rate of increase in shear strength decreased as the amount of web steel was increased and heavy stirrups did not guarantee the removal of the risk of shear failure. This agrees with the findings of Taub and Neville (8) on rectangular beams.

The results suggest that the flange needs to be stiff enough, either through adequate thickness or suitable deployment of steel, to prevent horizontal splitting along the web flange junction. This is related to the horizontal shearing stress along the root of the flange and the instability of the flange outstands.

2.2.14 Theory by Swamy and Quereshi (21)

Mohr's failure theory was used to represent the biaxial state of shearing and compressive stresses in the compression zone of T-beams with long shear spans.

A failure envelope for Mohr's circle was developed to take into account the shear compression intersections as follows:

$$\frac{v}{v'_c} = \frac{1 + \phi\sqrt{\phi}}{2\phi} \sqrt{1 - \frac{(f'_c/f''_c - \frac{1-\phi}{2})^2}{(\frac{1+\phi}{2})^2}} \quad (2.11)$$

(in imperial units)

where

$$\phi = \frac{f'_t}{f''_c} , \quad f'_t = 6 \sqrt{f'_c} , \quad f''_c = .85 f'_c ,$$

and

$$v'_c = \frac{f'_c \cdot f'_t}{f''_c + f'_t}$$

A relation for interaction coefficient was found as:

$$K_i = \frac{v/v'_c}{f'_c/f''_c} = \frac{f''_c}{v'_c} \left(\frac{1 - 0.5 K_s}{1.05 a/d} \right) \quad (2.12)$$

The depth of the compression zone at shear failure was related to that of flexural failure by:

$$K_s = (1.25 - A_s/A_{sb}) K_f \geq 0.5 K_f \neq t \dots \quad (2.13)$$

where $K_s d$ = depth of compression zone at shear failure

$K_f d$ = depth of compression zone at flexural failure

The ultimate shear strength of the compression zone is:

$$V_c = v \cdot B \cdot K_s d \quad (\text{in imperial units}) \quad (2.14)$$

A Uniform stress distribution was assumed for bending and shear stresses in the flange. It was also assumed that the shear force at failure was resisted by the compression zone and dowel action only. According to the observations by Taylor (22) and other investigators the dowel forces represent between 12% and 20% of the total shear force; it was therefore assumed that the dowel action carries only 10% of the total shear as a conservative value.

Mohr's failure theory does not account for the effect of the intermediate principal stress, whereas its importance for concrete has been shown by many authors (23), (24).

Quereshi's theory does not evaluate the shear stress distribution across the flange width but instead uses a simplified rectangular stress block, which contradicts the idea of concentrating the shear stresses in the area of flange around the web.

2.3 Critical Study

2.3.1 Introduction

In the approaches used in the design of flanged beams in flexure, the phenomenon of shear lag has been recognised and therefore elastic calculations are made on simplified stress systems (25), such as shown in Fig 2.4. This introduces the idea of using an 'effective width' of the flange for the flexural calculations. The same 'effective width' cannot be used for the design of reinforced concrete beams in shear, mainly because it was obtained from consideration of longitudinal stresses in the compression zone alone and neglects the vertical shear stresses. However, the concept of using an 'effective width' for shear calculations seems a convenient approach, and therefore will be considered later in Chapter 8. Experimental evidence shows that the vertical shear stresses resisted by the concrete in the compression zone play an important role on the shear failure mechanism and the ultimate shear strength of reinforced concrete T-beams. The actual shear stress distribution in a flanged beam is not yet known due to the difficulties involved in trying to measure it experimentally. This is why many researchers adopt a more empirical approach to estimate the shear strength of T-beams.

In the following section, the equations developed by Placas and Regan for the ultimate strength of T-beams are analysed with the test results available.

2.3.2 Analytical Data

The analysis was carried out using the existing experimental data from references (6), (9), (13) and (20). For the purpose of this analysis, Placas' and Regan's

Equation (2.9) was modified by replacing D_c by $D_c + 2a$ and b by b_w to give

$$V_u = 2(a' + t) \rho_w f_y + \dots$$

The first part of equation (2.15) represents the shear capacity of the web reinforcement, and the second part represents the concrete resistance in the compression zone. For beams without web reinforcement only the second part of equation (2.15) was applied for the ultimate shear capacity.

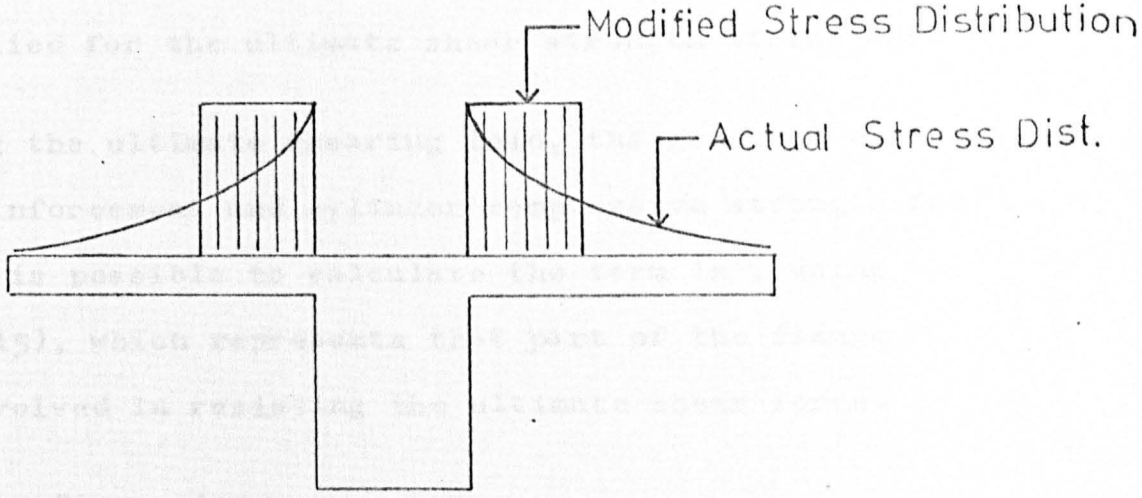


FIG. 2.4. ACTUAL AND MODIFIED LONGITUDINAL STRESS DISTRIBUTION ACROSS FLANGE WIDTH ACCORDING TO ELASTIC THEORY

3.3.3. Discussion
 The stress distribution across the flange width was calculated using equation (2.15) for the range of tests reported in Table 2.1. The results obtained are plotted against the flange width to depth ratio (b/d), percentage reinforcement and shear span/depth ratios (a/d). This is to study the factors influencing the effective width and to compare the value taken by Placas and Regan as $(b_w = 0.85)$ with the calculated values from the equation.

Table 2.1 shows the scatter in the distances 'a' as the flange width, thickness and longitudinal reinforcement change. In Swamy's tests the distances 'a' ranged between

equation (2.9) was modified by replacing $(b_o + 6")$ by a new effective width $(b_o + x)$. Thus:

$$V_u = 2(d' - t) b_o r f_{yw} + 25 (f'_c)^{1/3} \cdot t (b_o + x) \dots \quad (2.15)$$

The first part of equation (2.15) represents the shear resistance of the web reinforcement, and the second part for the concrete resistance in the compression zone. For beams without web reinforcement only the second part of the equation was applied for the ultimate shear strength of the beam.

Knowing the ultimate shearing load, the geometry of the beam, web reinforcement and cylinder compressive strength for concrete, it is possible to calculate the term 'x', using equation (2.15), which represents that part of the flange outstands involved in resisting the ultimate shear force.

2.3.3. Discussion

The values of the distance 'x' calculated using equation (2.15) for the range of tests available, were tabulated and plotted against the flange width/web width ratio $(\frac{B}{b_o})$, percentages of longitudinal reinforcement, web reinforcement and shear span/depth ratios (a/d). This is to study the factors influencing the 'effective width' and to compare the value taken by Placas and Regan as $(b_o + 6")$ with the calculated values from the equation.

Table 2.1 shows the scatter in the distance 'x' as the flange width, thickness and longitudinal reinforcement change. In Swamy's tests the distance 'x' ranged between

125 mm and 400 mm for beams without web reinforcement, and between 100 mm and 375 mm for beams with web reinforcement. In Al-Alusi's tests the distance 'x' was smaller and even less than the value taken by Placas and Regan which was 152 mm. This may be due to the thin flange used in the tests (31 mm). Guralnick tests gave a range between 125 mm and 425 mm for the distance 'x' which is similar to that of Swamy's despite the difference in geometry and longitudinal reinforcement between the tests. In Placas tests the distance 'x' increased from 125 mm to 325 mm, which is more than twice the value 152 mm taken in the equation (2.9).

Fig 2.5 shows the relationship between the flange width/rib width ratio and the distance 'x' for beams with different values of web reinforcement and longitudinal main steel. These data indicate a rapid increase in the effective distance 'x' as B/b_o increases from 2 to 3, then a smaller increase as B/b_o increases from 3 to 7, and finally a nearly constant value for 'x' as B/b_o increases from 7 to 10. It is clear that the constant value of 'x' = 6" taken by Placas and Regan is a lower bound value.

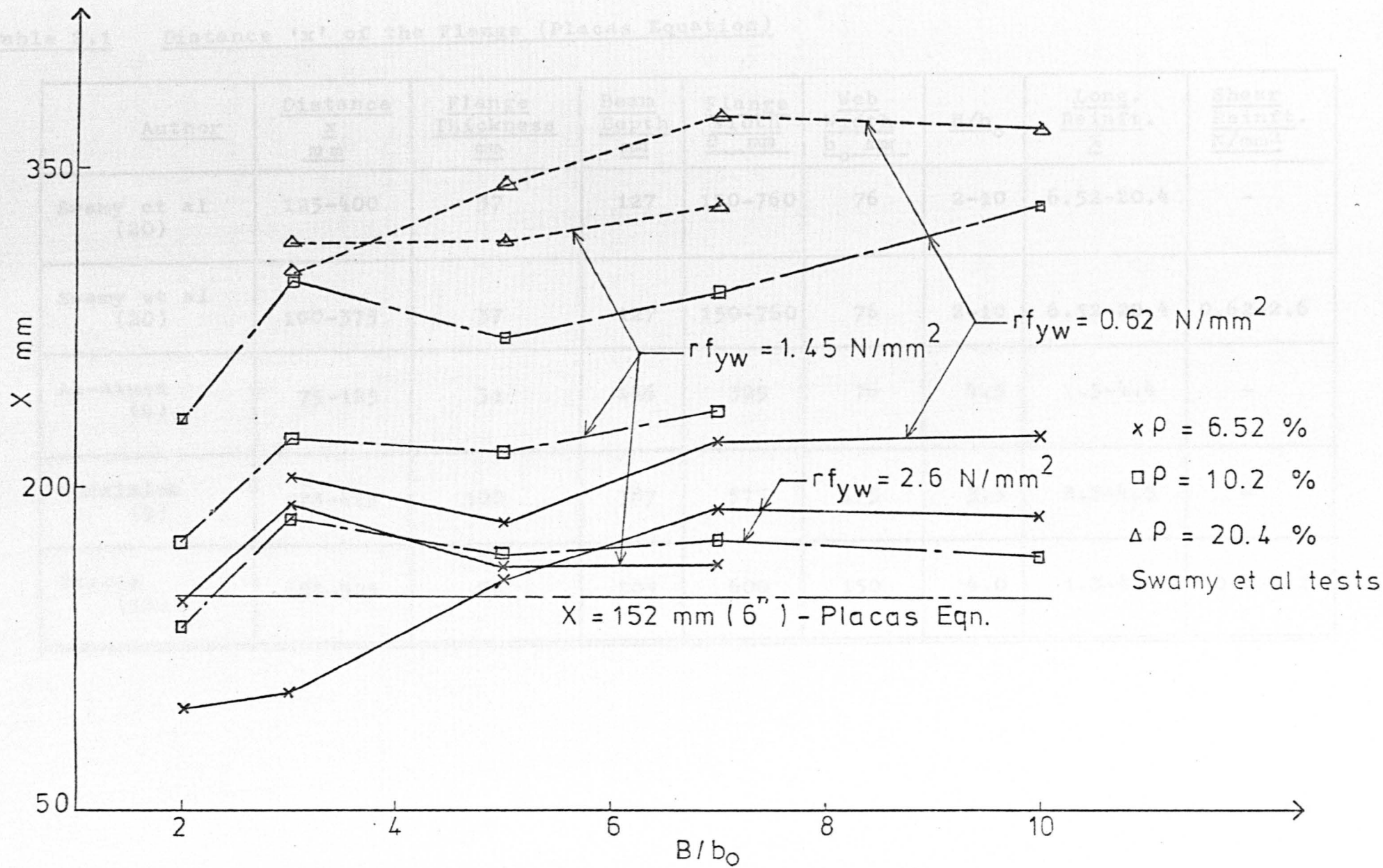


FIG. 2.5. EFFECTIVE DISTANCE "X" OF FLANGE vs. FLANGE WIDTH/RIB WIDTH RATIO (Placas Eqn.)

Table 2.1 Distance 'x' of the Flange (Placas Equation)

<u>Author</u>	<u>Distance</u> <u>x</u> <u>mm</u>	<u>Flange</u> <u>Thickness</u> <u>mm</u>	<u>Beam</u> <u>Depth</u> <u>mm</u>	<u>Flange</u> <u>Width</u> <u>B mm</u>	<u>Web</u> <u>Width</u> <u>b_o mm</u>	<u>B/b_o</u>	<u>Long.</u> <u>Reinft.</u> <u>%</u>	<u>Shear</u> <u>Reinft.</u> <u>N/mm²</u>
Swamy et al (20)	125-400	37	127	150-760	76	2-10	6.52-20.4	-
Swamy et al (20)	100-375	37	127	150-760	76	2-10	6.52-20.4	0.62-2.6
Al-Alusi (6)	75-125	31	146	325	76	4.3	1.5-4.4	-
Guralnick (9)	125-425	100	387	575	175	3.3	2.3-4.3	-
Placas (13)	125-325	76	305	600	150	4.0	1.3-4.2	0.4-2.2

For beams without web reinforcement Fig 2.6 shows that 'x' increases as B/b_o increases from 2 to 5, then a very little change in 'x' as B/b_o increases from 5 to 10. Again the distance 'x' = 6" is a lower bound value and clearly underestimates the contribution of the flange.

Figures 2.7-2.9 show the relationships between the distance 'x' and percentage of main longitudinal reinforcement. They indicate that, for beams with web reinforcement, the distance 'x' increases with increase in the main reinforcement and that the rate of increase is nearly constant. For beams without web reinforcement, there was a small increase in 'x' as the longitudinal steel percentage increased from 6.52% to 10.2% and a sharp increase in 'x' as the percentage increased from 10.2% to 20.4%. This is probably due to the greater effects of dowel action in those beams with high percentages of main reinforcement. The Placas equation does not allow for the effect of dowel action, but assumes that all the shear force is resisted by the compression zone in the flange. However, in reality, dowel action, shear stresses in the compression zone and aggregate interlock all contribute to the shear strength.

Figures 2.10 and 2.11 show the relationships between the distance 'x' and the percentage of shear reinforcement. Figure 2.10 indicates a decrease in the distance 'x' with increasing the shear reinforcement but Fig 2.11 indicates nearly no effect on the distance 'x' with increasing web reinforcement.

Figure 2.12 shows the relationship between the distance

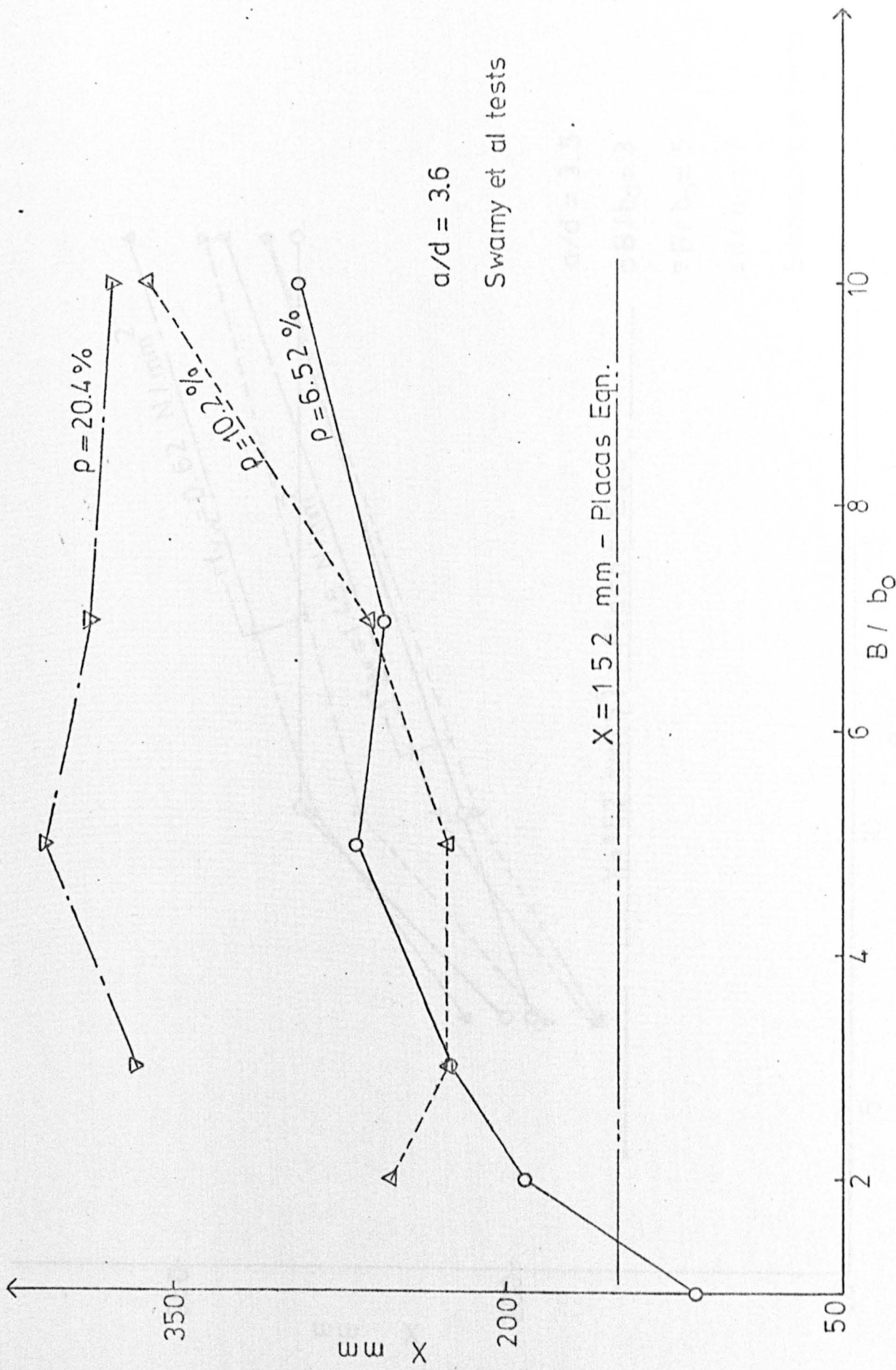


FIG. 2.6. EFFECTIVE DISTANCE "X" OF FLANGE vs. FLANGE WIDTH / RIB WIDTH RATIO (Placas Eqn.)

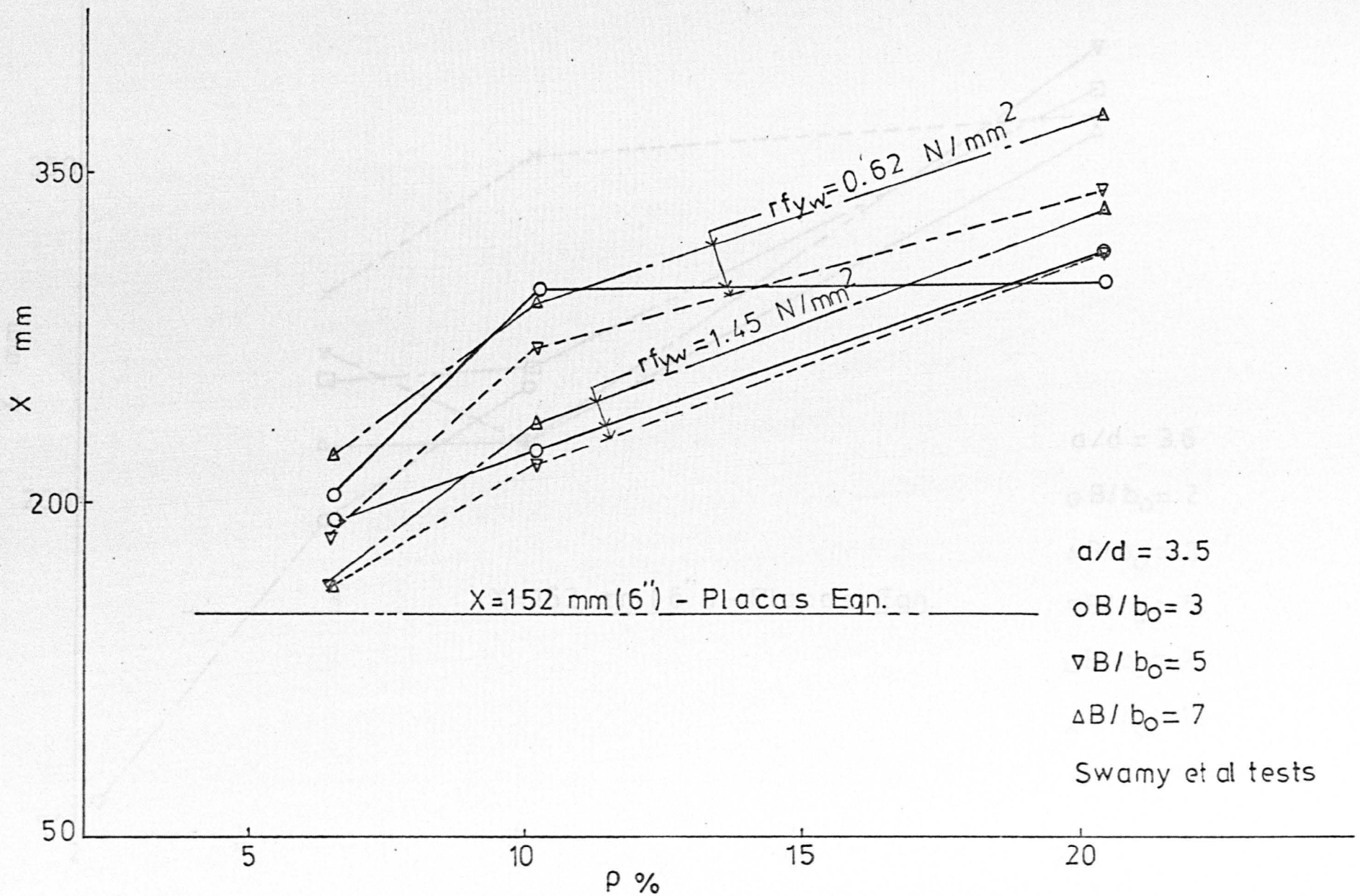


FIG. 2.7. EFFECTIVE DISTANCE "X" OF FLANGE vs. LONGITUDINAL REINFORCEMENT (Placas Eqn.)

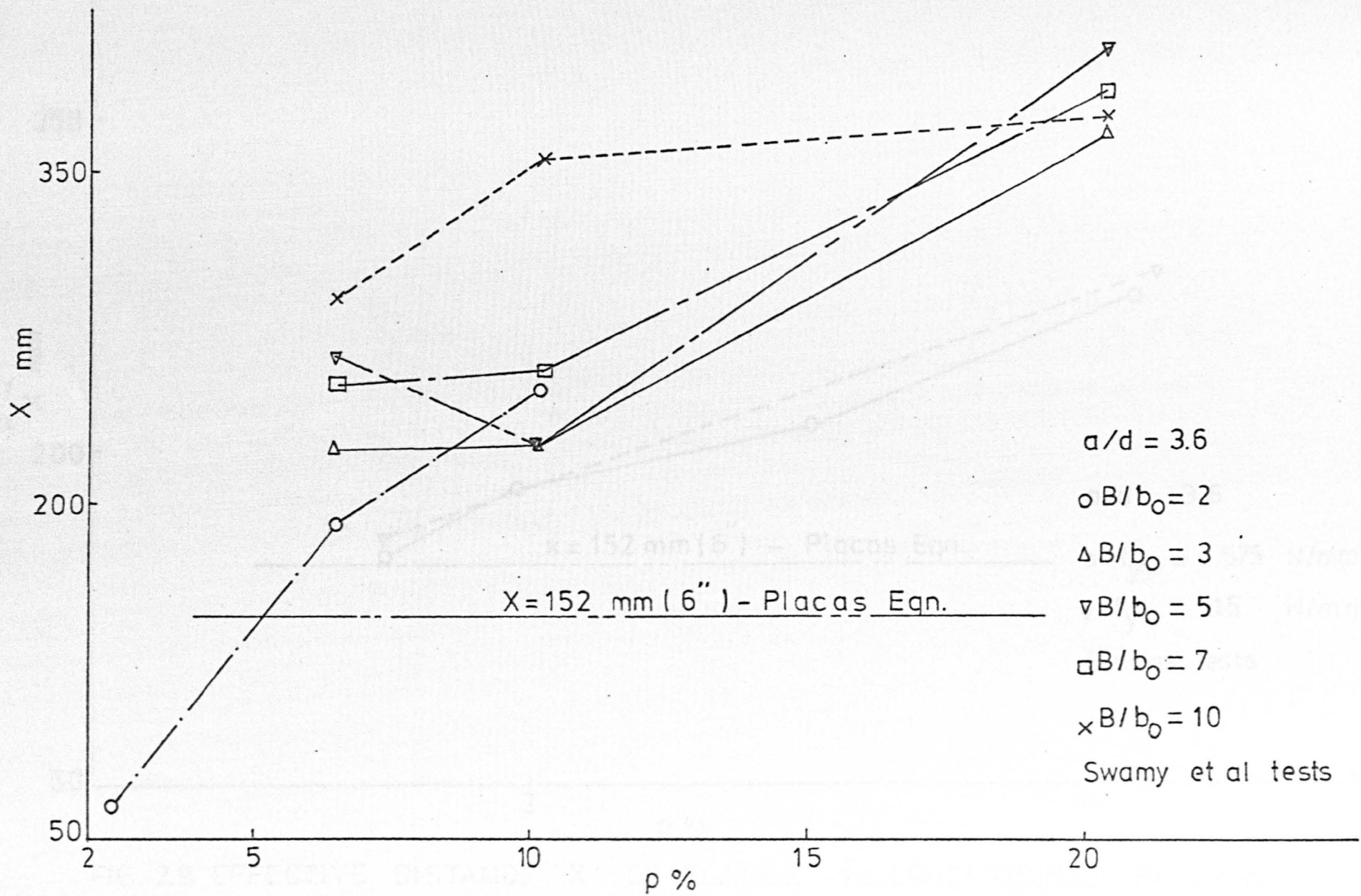


FIG. 2.8. EFFECTIVE DISTANCE "X" OF FLANGE vs. LONGITUDINAL REINFORCEMENT (Placas Eqn.)

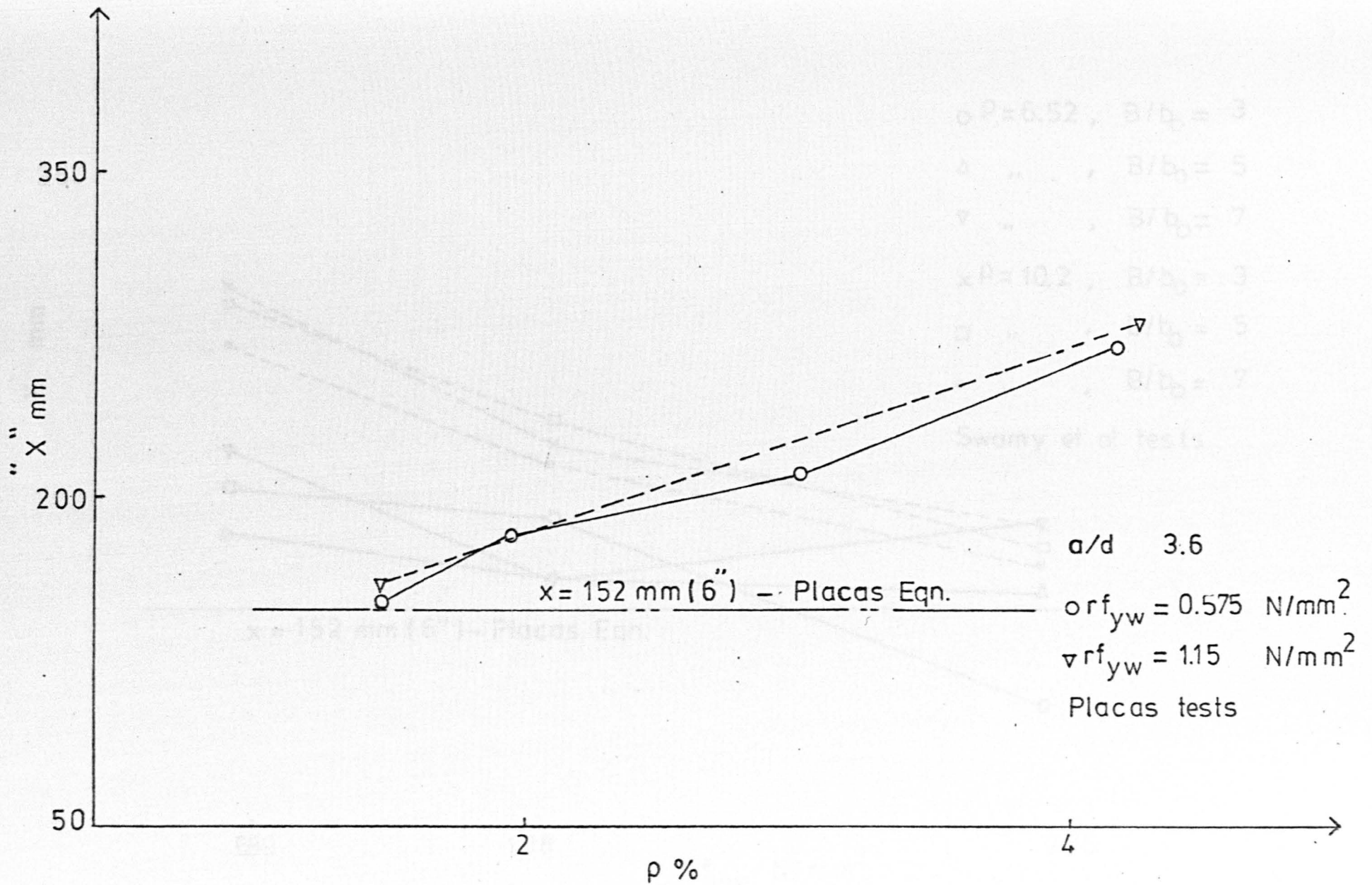


FIG. 2.9. EFFECTIVE DISTANCE "X" OF FLANGE vs. LONGITUDINAL REINFORCEMENT (Placas Eqn.)

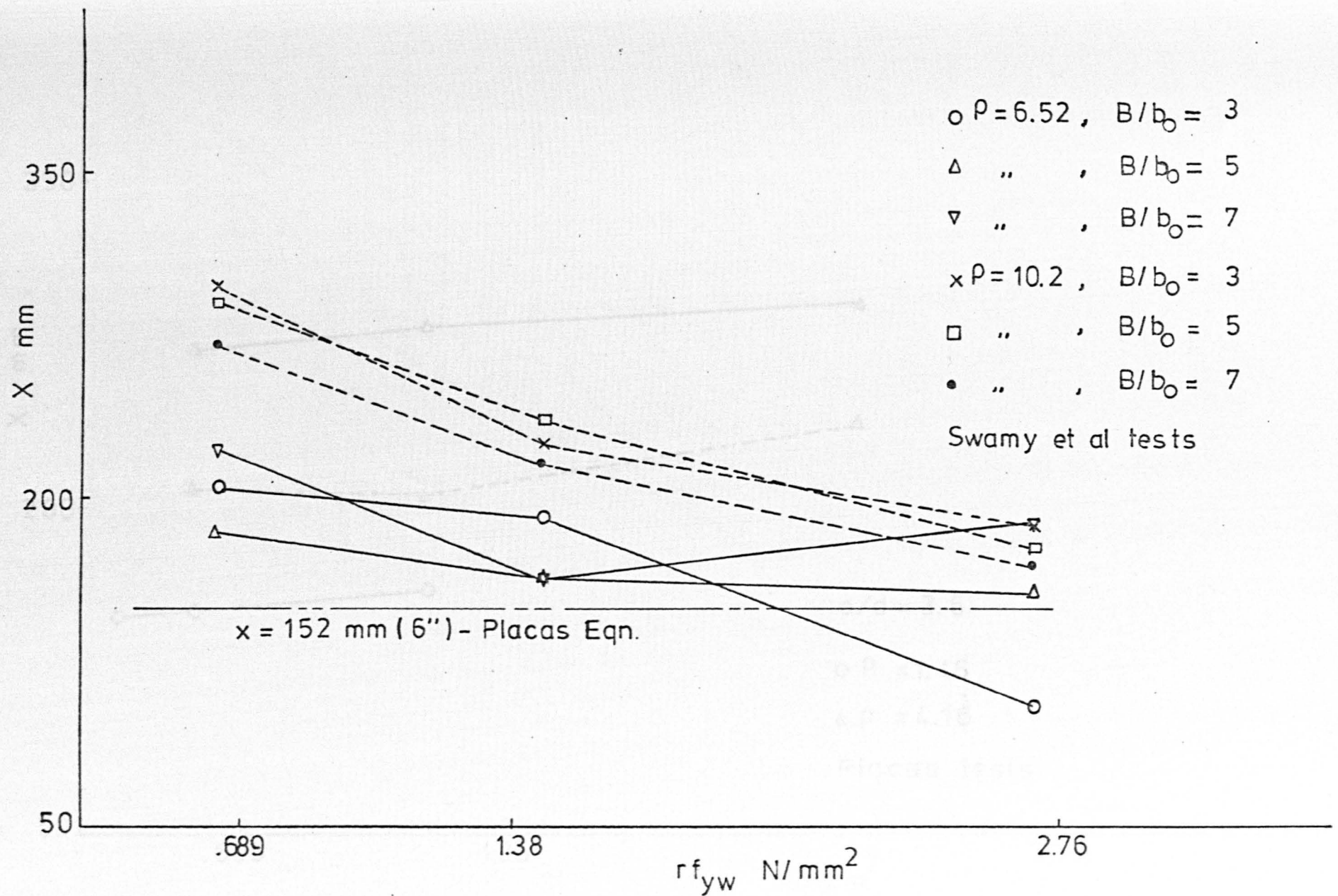


FIG. 2.10. EFFECTIVE DISTANCE "X" OF FLANGE vs. SHEAR REINFORCEMENT (Placas Eqn.)

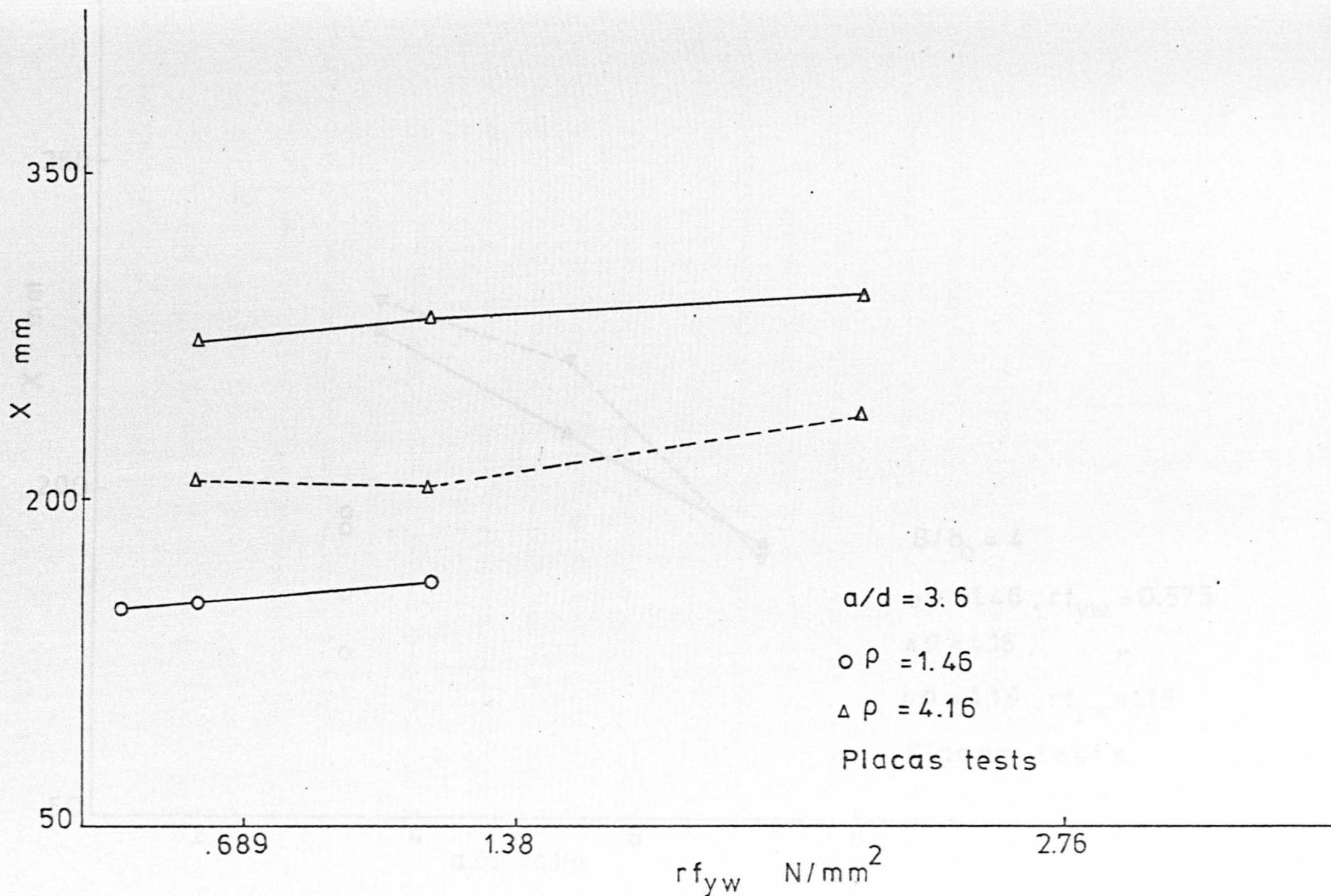


FIG.2.11. EFFECTIVE DISTANCE "X" OF FLANGE vs. SHEAR REINFORCEMENT
(Placas Eqn.)

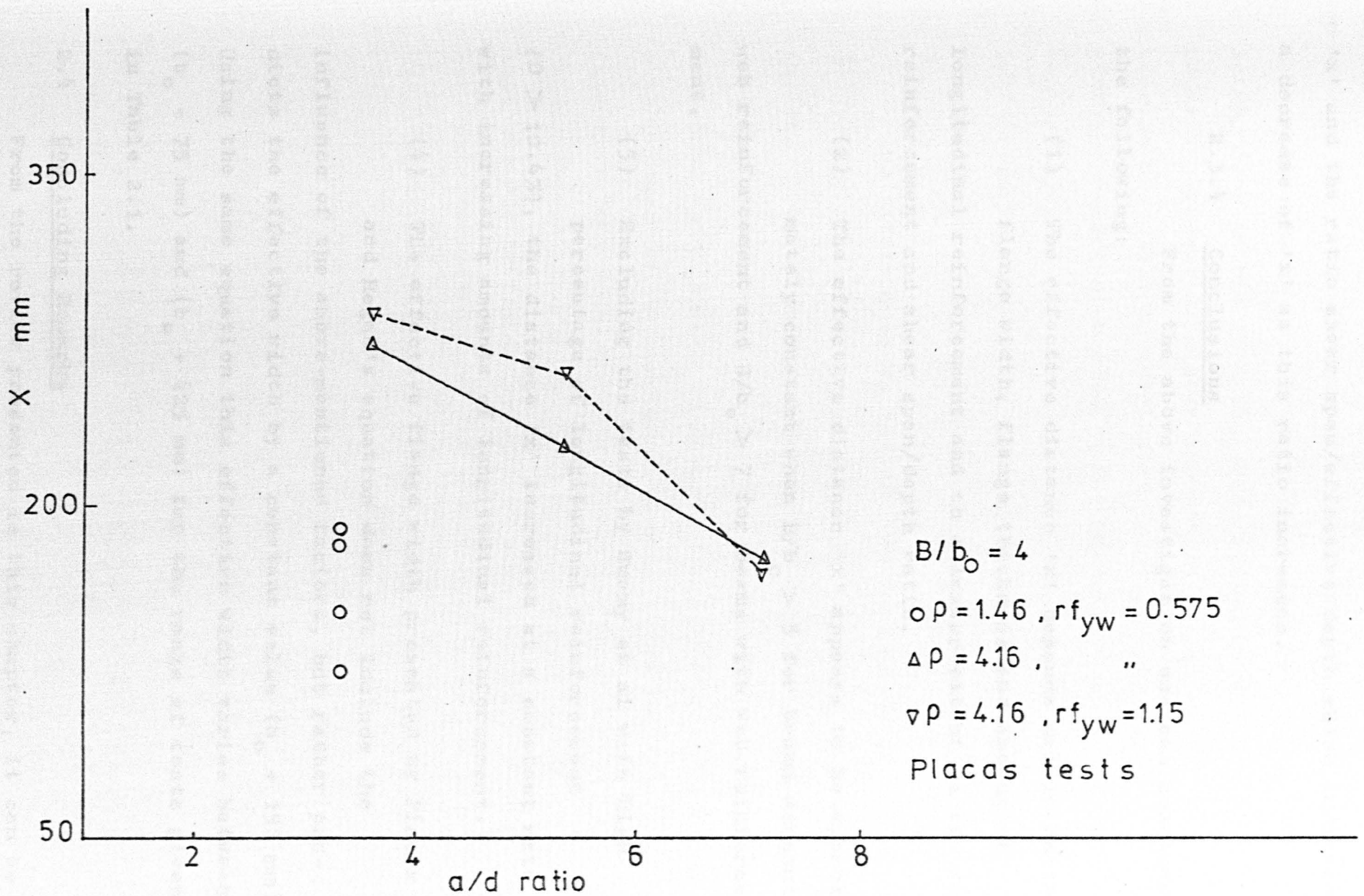


FIG. 2.12. EFFECTIVE DISTANCE "X" OF FLANGE vs. SHEAR SPAN/EFFECTIVE DEPTH RATIO - (Placas Eqn.)

'x' and the ratio shear span/effective depth which indicates a decrease of 'x' as this ratio increases.

2.3.4 Conclusions

From the above investigation one can conclude the following:

(1) The effective distance 'x' depends mainly on the flange width, flange thickness and amount of longitudinal reinforcement and to a lesser extent on the web reinforcement and shear span/depth ratio.

(2) The effective distance 'x' appears to be approximately constant when $B/b_o > 5$ for beams without web reinforcement and $B/b_o > 7$ for beams with web reinforcement.

(3) Excluding the tests by Swamy et al with high percentage of longitudinal reinforcement ($\rho > 10.4\%$), the distance 'x' increased at a constant rate with increasing amounts of longitudinal reinforcement.

(4) The effective flange width presented by Placas and Regan's equation does not include the influence of the above-mentioned factors, but rather predicts the effective width by a constant value ($b_o + 152$ mm). Using the same equation this effective width varies between ($b_o + 75$ mm) and ($b_o + 425$ mm) for the range of tests given in Table 2.1.

2.4 Concluding Remarks

From the review presented in this chapter, it can be

seen that the contribution of the flange of T-beams in resisting shear forces has not been assessed. Experimental information proved that the shear strength of reinforced concrete T-beams is higher than that of comparable rectangular beams. This is attributed to the inclusion of a stronger compression zone in the flange. The relative contribution of the flange to the total shear resistance is influenced by a number of factors such as flange geometry and amount of main longitudinal reinforcement.

The discrepancy in the analytical methods reviewed is due to the fact that the internal mechanism of the shear failure is not completely understood. Moreover, it is difficult to separate analytically the components involved in resisting shear forces in beams. The previous analytical methods ignored the contribution of the dowel action and aggregate interlock on the ultimate strength of the beam and considered all the shear force to be carried by the flange. This results in the deficiency of these methods in representing the true strength of the compression zone and consequently the strength of the beams.

CHAPTER 3

FINITE ELEMENT APPROACH

3.1 General

The Finite Element Method (FEM) is widely accepted now for the analysis of structural members. For linear analysis, this method is well established and available in standard texts (26), (27).

The basis of the method is to represent the structure by a finite number of subregions (called elements). These elements are interconnected at joints, called nodal points, existing on their boundaries. The variation of displacements over each element is approximated by unknown functions (called displacement functions or displacement models), in such a way that continuity of the function (or its derivative) is preserved across element boundaries. The unknown magnitudes of the displacement functions are the displacements at the nodal points, Fig 3.1 Hence, the final solution will yield the approximate displacements at the nodal points. The degree of approximation which can be achieved will very much depend on the element shape and on the form of the displacement functions (26). Polynomials are used to express the displacement model due to its ease in mathematical manipulation.

The total potential energy of the structure is represented by the sum of the internal energy stored as a result of the deformations and the potential energy of the external loads. When the total potential energy is minimum then the structure is in a state of equilibrium.

Defining the total potential energy Π of the element by $\Pi = U - W$, where U is the strain energy of the element and W is the work done by the external load P , then

$$\Pi = \int V_e - P \delta$$

The minimum of Π can be obtained by differentiation of Π with respect to the displacements and equating the result to zero:

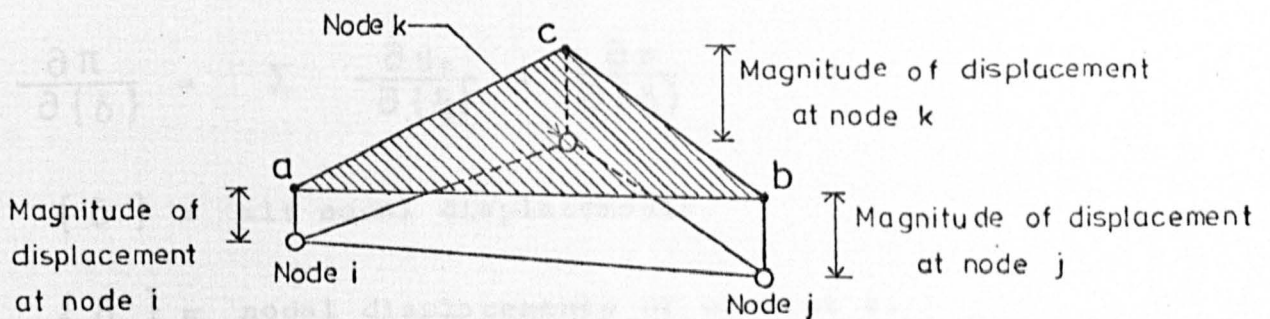


FIG. 3.1. ISOMETRIC VIEW OF TRIANGULAR ELEMENT WITH LINEAR DISPLACEMENT MODEL PLOTTED IN THE THIRD DIRECTION - (After Desai & Abel , 27)

Defining the total potential energy by π , the internal strain energy of the element by U_e and the potential energy of the external load by P , then

$$\pi = \sum U_e + P \quad (3.1)$$

The minimum of π can be obtained by differentiating it with respect to the displacements and equating the result to zero:

$$\frac{\partial \pi}{\partial \{\delta\}} = \sum \frac{\partial U_e}{\partial \{\delta_e\}} + \frac{\partial P}{\partial \{\delta\}} = 0 \quad (3.2)$$

where $\{\delta\} =$ all nodal displacements

$\{\delta_e\} =$ nodal displacements of element e .

Equation (3.2) can be written in the form

$$[K] \{\delta\} - \{R\} = 0 \quad (3.3)$$

Where $[K]$ is the overall stiffness matrix of the structure and $\{R\}$ is the imposed loading system.

A typical element contribution can be given by:

$$\frac{\partial U_e}{\partial \{\delta_e\}} = [K_e] \{\delta_e\} + \{F_e\} \quad (3.4)$$

where $[K_e] =$ the element stiffness matrix

$\{F_e\} =$ fictitious forces acting on the element nodes

Equation (3.3) is the equilibrium equation or load displacement relation for the loaded structure.

The rules used in the assembly of equation (3.2) are the same as the assembly of equilibrium equations for structural elements. The equilibrium equations for the structure are then obtained by combining the equations for the individual elements. These equations are modified for the given boundary constraints and then solved to obtain the unknown displacements.

When the finite element analysis was first introduced, simple element shapes, with minimum number of degrees of freedom, were exclusively used. The simplest two-dimensional element was the 3-node triangle. Its equivalent in three dimensions was the tetrahedron element with four nodal corners. However, during the evolution of the method, it has become apparent that for a given total number of degrees of freedom in a structure, accuracy is increased for larger elements with a greater number of degrees of freedom. Furthermore, with reducing the number of elements, the cost of data preparation and equation solution would reduce drastically. To use a small number of elements to represent a complex geometrical outline of a real problem introduces a difficulty in the larger elements. This difficulty has been overcome by allowing the elements to have curved sides. This step has been achieved by distorting the simple element forms into others of more arbitrary shape as shown in Fig 3.5. This led to the introduction of various isoparametric element families (28), (29). These elements have been used with

much success for elasticity problems in two and three dimensional cases.

To date the majority of finite element applications to structural systems has been limited to two dimensional elements, such as plane stress systems, plates and shells. However, the method is equally applicable for the solution of practical cases in three dimensions. In some practical problems, two dimensional approximations give an adequate and economic finite element model. But, all practical cases of the structural systems are in reality three dimensional problems.

In many applications of FEM in structural mechanics, it is convenient to use linear formulations of problems to obtain engineering solutions. The solution in this case is unique and both the relationships of stress-strain and strain-displacements are explicitly linear. However, many practical problems do not preserve such linearity and definitely require non-linear analysis if realistic results are to be obtained. Examples of such problems are the load-deflection behaviour of structures, plasticity problems in soil and rock mechanics, crack formation and propagation in reinforced concrete, etc.

In the last decade, most research work has been directed towards the application of FEM to non-linear problems. In general the non-linearity in structural engineering is due to:

- (1) Large geometric deformations; in this case the strain-displacement relations are non-linear and it is out of the

scope of this study.

(2) Non-linear material properties.

The non-linear behaviour of concrete is caused by either tensile cracking or by internal microcracking in compression. Assuming small strains, ie linear strain - displacement relationship, thus the non-linearity in concrete can be achieved through the formulation of appropriate constitutive laws. Small step, incremental approaches are used in which the non-linear solution is achieved by readjusting the material constants in the linear problem so that at the final stage the constitutive law is satisfied. So, the non-linear technique is based on the linear elastic formulation of the FEM.

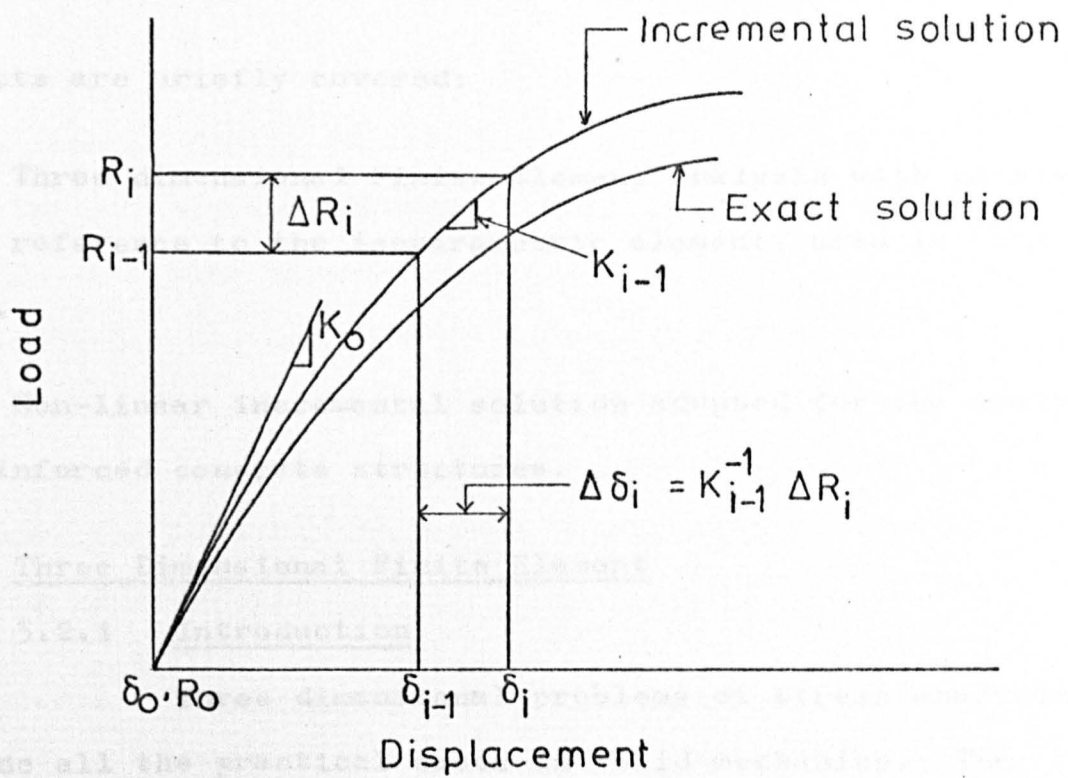
Two procedures are widely used in the non-linear analysis:

(1) Incremental procedures in which the non-linear problem is approximated as a series of linear problems, Fig 3.2.1. Equilibrium is only approximately followed.

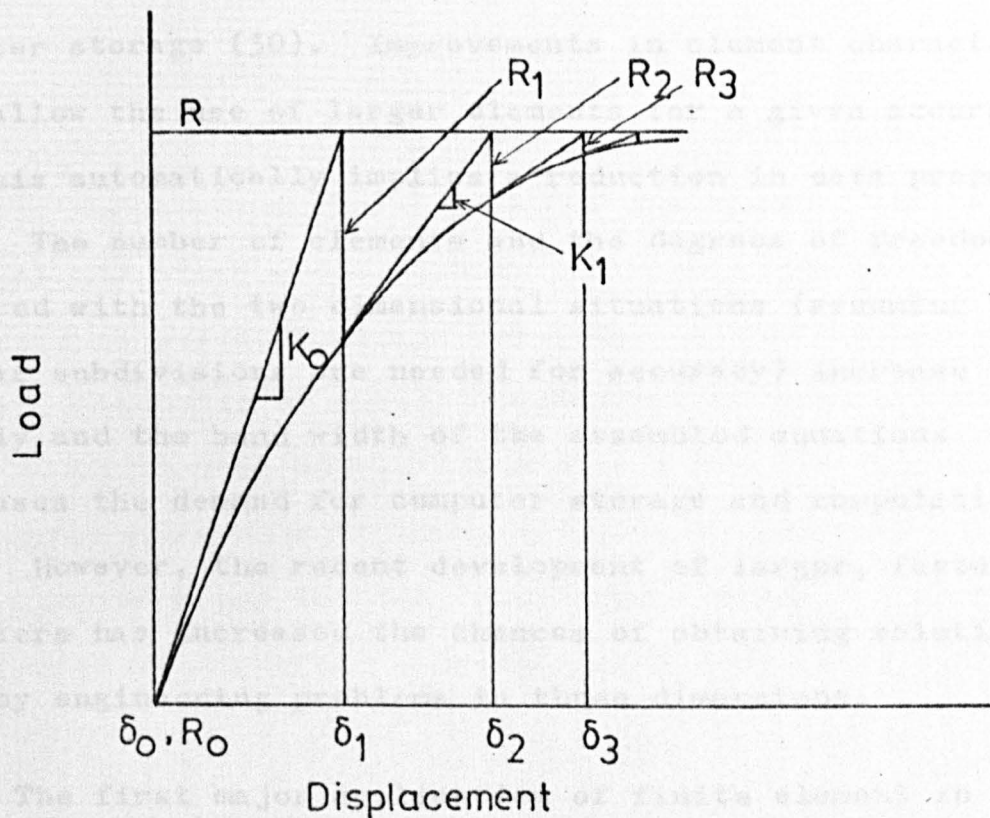
(2) Iterative procedures in which successive corrections to the same elastic problem are performed until equilibrium is approached, Fig 3.2.2.

For higher accuracy, a mixed procedure, ie a combination of incremental and iterative schemes is used.

The basic formulation of the displacement Finite Element model and the non-linear procedures are explained in many texts such as (26) and (27). In this chapter two



(1) Basic incremental procedure



(2) Iterative or Newton procedure

FIG. 3.2. INCREMENTAL AND ITERATIVE PROCEDURES

(After Desai & Abel , 27)

subjects are briefly covered:

- (1) Three dimensional Finite Element Analysis with particular reference to the isoparametric elements used in this study.
- (2) Non-linear incremental solution adopted for the analysis of reinforced concrete structures.

3.2 Three Dimensional Finite Element

3.2.1 Introduction

Three dimensional problems of stress analysis include all the practical cases in solid mechanics. The practical implementation of three dimensional stress analysis by finite elements encounters two main difficulties. These are the cost of data preparation and the excessive demand on computer storage (30). Improvements in element characteristics allow the use of larger elements for a given accuracy and this automatically implies a reduction in data preparation. The number of elements and the degrees of freedom as compared with the two dimensional situations (assuming that similar subdivisions are needed for accuracy) increase rapidly and the band width of the assembled equations increases the demand for computer storage and computation time. However, the recent development of larger, faster computers has increased the chances of obtaining solutions to many engineering problems in three dimensions.

The first major application of finite element in three dimensional stress analysis was by Argyris (31), (32), using a constant strain tetrahedron and the refined ten nodes

tetrahedron. The development of the isoparametric hexahedron element family by Zienkiewicz (26) and his colleagues (28), (29), (33), introduced a significant advance in three dimensional finite element analysis. The efficiency of these elements has been proved in elastic solid analysis and recently in non-linear and plasticity problems (34). In reinforced concrete applications, Suidan and Schnobrich (35) used the 20-node hexahedron to evaluate cracking and crushing of concrete.

3.2.2 Hexahedron Isoparametric Elements

The basic formulation of the isoparametric elements can be found in references (26) and (29), but the formulation of the 20-node hexahedron used in this study is discussed briefly in the following sections.

3.2.2.1 Shape Functions

A shape function is a function which has unit value at one nodal point of the element and zero value at all other nodal points. The shape functions are expressed in polynomials and the order of the polynomial (linear, quadratic or cubic) defines the unknown displacements along element edges. Quadratic shape functions for a rectangular element are shown in Fig 3.3. The shape functions are the basis for the displacement model. A shape function is required for each degree of freedom at every nodal point.

Shape functions are expressed conveniently in terms of the normalised local-co-ordinate system. This is a local system which permits the specification of a point within the

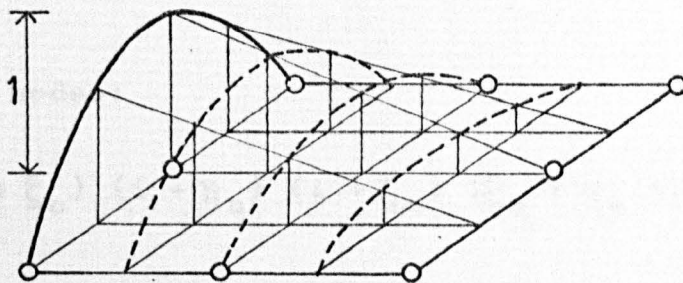
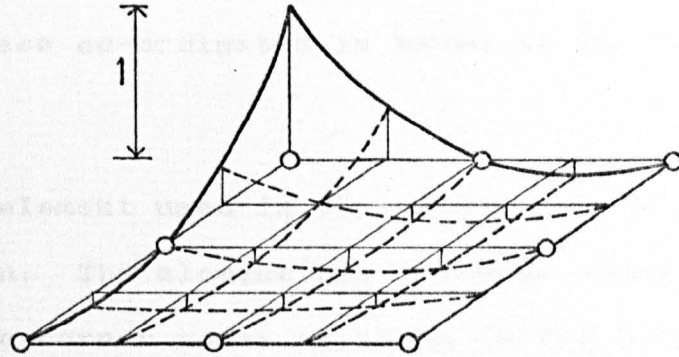
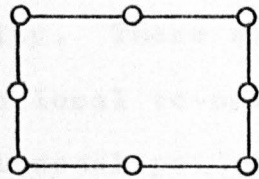


FIG. 3.3. SHAPE FUNCTIONS FOR QUADRATIC ELEMENTS OF SERENDIPITY FAMILY

(After Zienkiewicz , 26)

element by a set of dimensionless numbers whose magnitudes never exceed unity. These systems are usually arranged so that some of the local co-ordinates have unit magnitude at primary external nodal points as shown in Fig 3.4. Such normalised co-ordinates, also, with its limits ± 1 facilitate the integration required to obtain the element stiffness. The element in these co-ordinates is known as the 'parent element'.

The parent element used in this study is the parabolic 20 node hexahedron. The element has one node along each edge in addition to the corner nodes as shown in Fig 3.5. In the normalised co-ordinates, the element is a cubic, Fig 3.5.a. The normalised co-ordinates ξ , η , ζ are used with values ± 1 on cube sides.

Defining $\xi_0 = \xi\xi_i$, $\eta_0 = \eta\eta_i$, $\zeta_0 = \zeta\zeta_i$, then the shape functions $[N_i]$, as given by (26), (29) and (36), are:

for corner nodes:

$$N_i = \frac{1}{8} (1 + \xi_0) (1 + \eta_0) (1 + \zeta_0) (\xi_0 + \eta_0 + \zeta_0 - 2) \quad (3.5)$$

for midside nodes:

$$\xi_i = 0, \quad \eta_i = \pm 1, \quad \zeta_i = \pm 1$$

$$N_i = \frac{1}{4} (1 - \xi^2) (1 + \eta_0) (1 + \zeta_0) \quad (3.6)$$

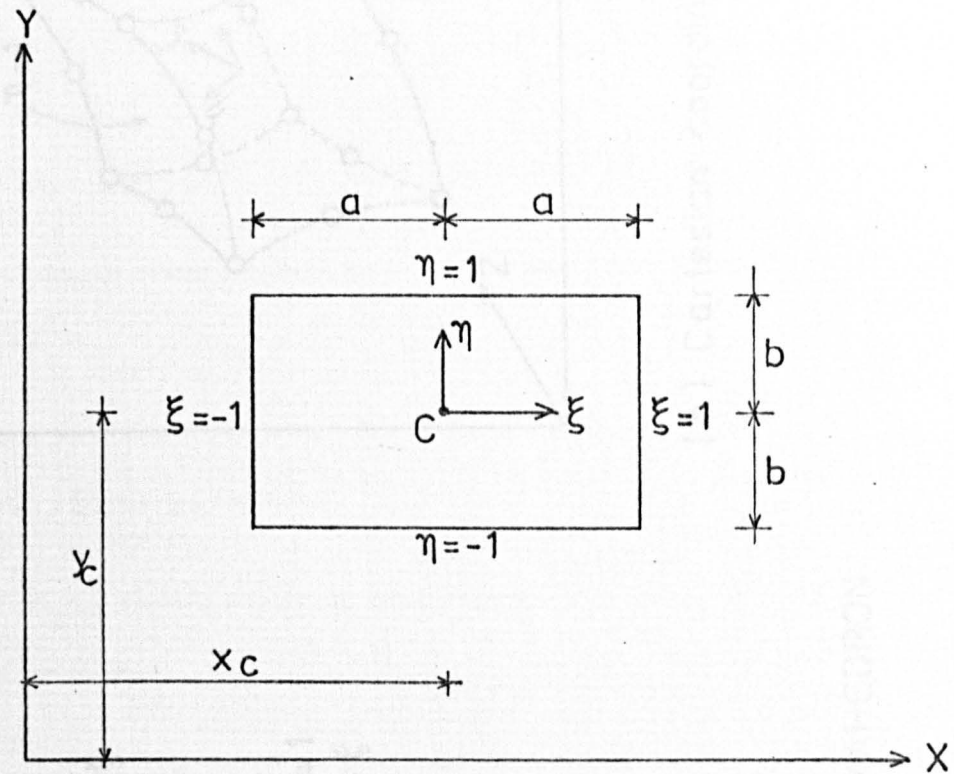
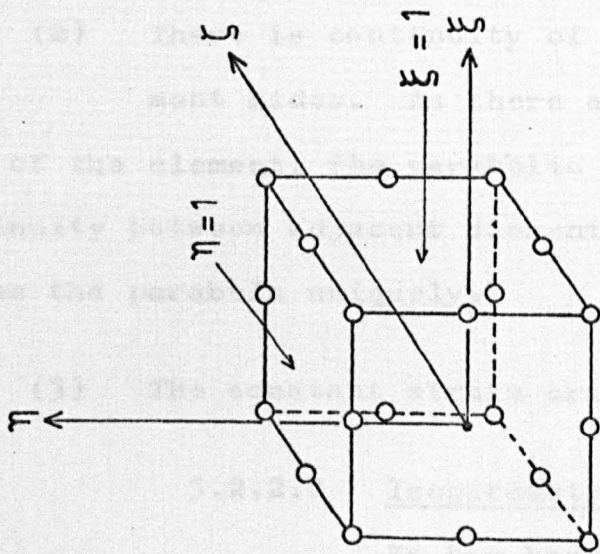
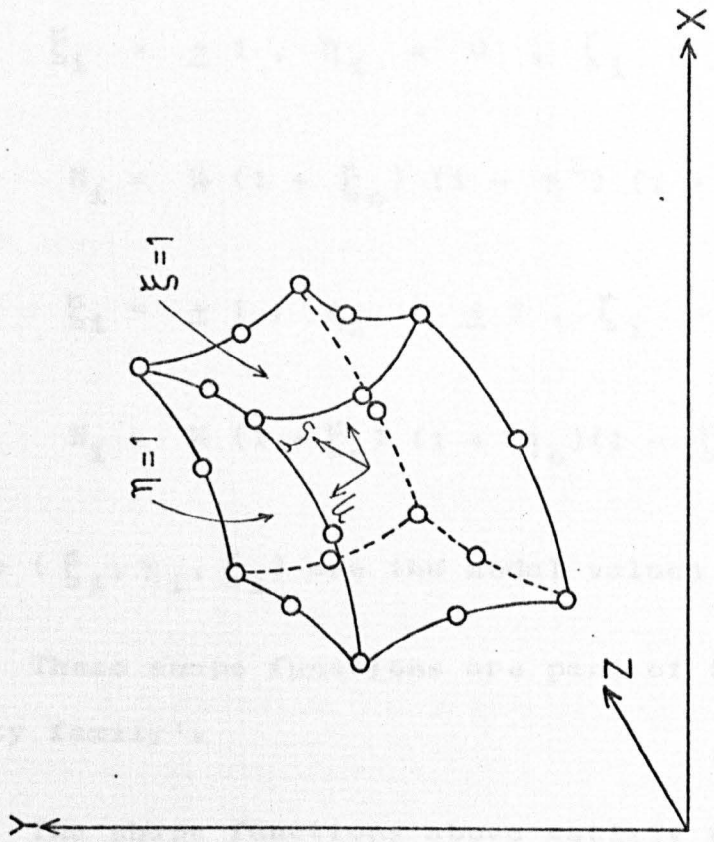


FIG. 3. 4. NORMALIZED COORDINATES FOR A RECTANGLE



(a) Local coordinates



(b) Cartesian coordinates

FIG. 3.5. 20 - NODE HEXAHEDRON

$$\xi_i = \pm 1, \eta_i = 0, \zeta_i = \pm 1$$

$$N_i = \frac{1}{4} (1 + \xi_0) (1 - \eta^2) (1 + \zeta_0) \quad (3.7)$$

$$\xi_i = \pm 1, \eta_i = \pm 1, \zeta_i = 0$$

$$N_i = \frac{1}{4} (1 + \xi_0) (1 + \eta_0) (1 - \zeta^2) \quad (3.8)$$

where (ξ_i, η_i, ζ_i) are the nodal values of (ξ, η, ζ) .

These shape functions are part of the so-called 'serendipity family'.

The shape functions above satisfy the general properties of shape functions such as:

- (1) $N_i = 1$ at node i and equal to zero at all other nodes.
- (2) There is continuity of displacements along element sides. As there are three nodes along each edge of the element, the parabolic variation will ensure continuity between adjacent elements as the three points define the parabola uniquely.
- (3) The constant strain criterion.

3.2.2.2 Isoparametric Concept

It has been mentioned earlier that the isoparametric elements can be distorted into arbitrary shapes to suit the complex boundaries existing in real problems, particularly when the behaviour of the structure

depends on a small number of such elements. The parent element defined in the last section can be distorted to a more general form. Thus the element is mapped into distorted form in the manner shown in Fig 3.5.b, in which all positions of the nodes are arbitrary (26). The topology of the cube is retained and each edge of the cube is a quadratic curve in space, defined by the positions of the three nodes associated with the edge, (36). A new local co-ordinate system is defined for the element with the same constants $+1$ on the element faces as in the undistorted element. Thus ξ, η, ζ co-ordinates are distorted to a curvilinear set when plotted in Cartesian space.

The mapping from the local co-ordinates to the curvilinear co-ordinates in the Cartesian system must be unique and a one-to-one correspondence between points in the two systems must be established. Such co-ordinate relationships are provided by the isoparametric concept where the same shape functions used to define the variation in the unknown displacements are used to establish the co-ordinate transformations.

ie

$$\begin{Bmatrix} x \\ y \\ z \end{Bmatrix} = \sum_{i=1}^n [N_i] \begin{Bmatrix} x_i \\ y_i \\ z_i \end{Bmatrix} \quad (3.9)$$

where x_i, y_i, z_i are nodal co-ordinates in the Cartesian system and $N_i = N_i(\xi, \eta, \zeta)$ which are the shape functions given in terms of the local co-ordinates.

It has been demonstrated (26), (29), that the compatibility of displacement has been satisfied on element interfaces and any two adjacent distorted elements will be contiguous.

3.2.2.3 Element Stresses and Strains

Expressions for stresses and strains are required to substitute into the potential energy function (equation (3.1)): Moreover, the stresses and strains are important quantities for design purposes. Six components of stress or strain are relevant in three dimensional analysis.

Since when using isoparametric elements, the variation in displacements is expressed using the same shape functions as used to describe the geometry. Then by analogy with equation (3.9), the displacements can be given by:

$$\begin{Bmatrix} u \\ v \\ w \end{Bmatrix} = \sum_{i=1}^n [N_i] \begin{Bmatrix} u_i \\ v_i \\ w_i \end{Bmatrix} \quad (3.10)$$

where u_i , v_i and w_i are the nodal displacements and

$$N_i = N_i (\xi, \eta, \zeta).$$

Differentiating equation (3.10) and following the standard notation of Timoshenko's elasticity text, the strain displacement relationship can be defined as:

$$\begin{Bmatrix} \epsilon_x \\ \epsilon_y \\ \epsilon_z \\ \gamma_{xy} \\ \gamma_{yz} \\ \gamma_{zx} \end{Bmatrix} = \begin{Bmatrix} \frac{\partial u}{\partial x} \\ \frac{\partial v}{\partial y} \\ \frac{\partial w}{\partial z} \\ \frac{\partial u}{\partial y} + \frac{\partial v}{\partial x} \\ \frac{\partial v}{\partial z} + \frac{\partial w}{\partial y} \\ \frac{\partial w}{\partial x} + \frac{\partial u}{\partial z} \end{Bmatrix} = \begin{Bmatrix} \frac{\partial N_i}{\partial x} & 0 & 0 \\ 0 & \frac{\partial N_i}{\partial y} & 0 \\ 0 & 0 & \frac{\partial N_i}{\partial z} \\ \frac{\partial N_i}{\partial y} & \frac{\partial N_i}{\partial x} & 0 \\ 0 & \frac{\partial N_i}{\partial z} & \frac{\partial N_i}{\partial y} \\ \frac{\partial N_i}{\partial x} & 0 & \frac{\partial N_i}{\partial z} \end{Bmatrix} \begin{Bmatrix} u_i \\ v_i \\ w_i \end{Bmatrix} \quad (3.11)$$

This can be written in the form,

$$\{ \epsilon \} = [B] \{ \delta_e \} \quad (3.12)$$

where $\{ \epsilon \}$ = the strain components at an arbitrary point in the element,

$[B]$ is the strain matrix and
 $\{ \delta_e \}$ element nodal displacements

The stress-strain relationships in three-dimensional conditions are defined as

$$\{ \sigma \} = \begin{Bmatrix} \sigma_x \\ \sigma_y \\ \sigma_z \\ \tau_{xy} \\ \tau_{yz} \\ \tau_{zx} \end{Bmatrix} = \begin{Bmatrix} D_{11} & D_{12} & \dots & \dots & \dots & D_{16} \\ D_{21} & D_{22} & \dots & \dots & \dots & D_{26} \\ \cdot & \cdot & \cdot & \cdot & \cdot & \cdot \\ \cdot & \cdot & \cdot & \cdot & \cdot & \cdot \\ D_{61} & D_{62} & \dots & \dots & \dots & D_{66} \end{Bmatrix} \begin{Bmatrix} \epsilon_x \\ \epsilon_y \\ \epsilon_z \\ \gamma_{xy} \\ \gamma_{yz} \\ \gamma_{zx} \end{Bmatrix} \quad (3.13)$$

or

$$\{\sigma\} = [D]\{\epsilon\} \quad (3.14)$$

where σ_x , σ_y , σ_z are components of normal stresses in x, y, z directions.

τ_{xy} , τ_{yz} , τ_{zx} are components of shear stresses

[D] is known as the elasticity matrix.

Equation (3.13) constitutes the generalised Hook's law in the 3-dimensional case, where each of the six stress components is expressed as a linear function of the six components of strains. Thus equation (3.13) represents the constitutive law for a linear, elastic, anisotropic and homogeneous material. The matrix [D] is symmetric and contains elastic constants. This matrix in terms of the usual elastic constants E (elastic modulus) and ν (Poisson's ratio) can be written as:

$$[D] = \frac{E}{(1+\nu)(1-2\nu)} \begin{bmatrix} 1-\nu & \nu & \nu & 0 & 0 & 0 \\ \nu & 1-\nu & \nu & 0 & 0 & 0 \\ \nu & \nu & 1-\nu & 0 & 0 & 0 \\ 0 & 0 & 0 & \frac{1-2\nu}{2} & 0 & 0 \\ 0 & 0 & 0 & 0 & \frac{1-2\nu}{2} & 0 \\ 0 & 0 & 0 & 0 & 0 & \frac{1-2\nu}{2} \end{bmatrix} \quad (3.15)$$

3.2.2.4 Evaluation of Element Matrices

In section 3.2.2.1, the displacements model given by the shape functions was expressed in local

curvilinear co-ordinates. In order to evaluate the element properties such as the [B] matrix, stiffness matrix, etc, transformations are necessary. The [B] matrix of equation (3.12) is expressed in Cartesian derivatives and must be expressed in terms of local derivatives.

The chain rules of partial differentiation are applied as follows:

$$\begin{Bmatrix} \frac{\partial N_i}{\partial \xi} \\ \frac{\partial N_i}{\partial \eta} \\ \frac{\partial N_i}{\partial \zeta} \end{Bmatrix} = \begin{bmatrix} \frac{\partial x}{\partial \xi} & \frac{\partial y}{\partial \xi} & \frac{\partial z}{\partial \xi} \\ \frac{\partial x}{\partial \eta} & \frac{\partial y}{\partial \eta} & \frac{\partial z}{\partial \eta} \\ \frac{\partial x}{\partial \zeta} & \frac{\partial y}{\partial \zeta} & \frac{\partial z}{\partial \zeta} \end{bmatrix} \begin{Bmatrix} \frac{\partial N_i}{\partial x} \\ \frac{\partial N_i}{\partial y} \\ \frac{\partial N_i}{\partial z} \end{Bmatrix} = [J] \begin{Bmatrix} \frac{\partial N_i}{\partial x} \\ \frac{\partial N_i}{\partial y} \\ \frac{\partial N_i}{\partial z} \end{Bmatrix} \quad (3.16)$$

where [J] is known as the Jacobian matrix. As x, y, z are given in terms of ξ, η, ζ by equation (3.9), [J] can be found explicitly in terms of the local co-ordinates and can be expressed as:

$$[J] = \begin{bmatrix} \frac{\partial N_1}{\partial \xi} & \frac{\partial N_2}{\partial \xi} & \dots\dots\dots \\ \frac{\partial N_1}{\partial \eta} & \frac{\partial N_2}{\partial \eta} & \dots\dots\dots \\ \frac{\partial N_1}{\partial \zeta} & \frac{\partial N_2}{\partial \zeta} & \dots\dots\dots \end{bmatrix} \begin{bmatrix} x_1 & y_1 & z_1 \\ x_2 & y_2 & z_2 \\ \cdot & \cdot & \cdot \\ \cdot & \cdot & \cdot \end{bmatrix} \quad (3.17)$$

The Cartesian derivatives can be found by inverting equation (3.16) as follows:

$$\begin{Bmatrix} \frac{\partial N_i}{\partial x} \\ \frac{\partial N_i}{\partial y} \\ \frac{\partial N_i}{\partial z} \end{Bmatrix} = [J]^{-1} \begin{Bmatrix} \frac{\partial N_i}{\partial \xi} \\ \frac{\partial N_i}{\partial \eta} \\ \frac{\partial N_i}{\partial \zeta} \end{Bmatrix} \quad (3.18)$$

where $[J]^{-1}$ is the inverse of $[J]$.

3.2.2.5 Element Stiffness

For displacement methods of analysis, the principle of minimum potential energy has been used as discussed in Section 3.1. These principles are applied to the structure as a whole, ie to the assemblage of elements. In the finite element method the displacement models are assumed separately for each element of the structure, thus an integral can be used to operate on the sum of the various element displacements. But, because the integral of the summation is the same as the sum of individual integrals, the minimum principles can be applied to the elements separately. Thus, in the principle of minimum potential energy, to obtain the strain energy U , for a linear elastic body, an integral has to be performed as follows:

$$\begin{aligned} U &= \frac{1}{2} \iiint_V \{ \epsilon \}^T \{ \sigma \} dV = \frac{1}{2} \iiint_V \sum_{e=1}^n \{ \epsilon_e \}^T \{ \sigma_e \} dV \\ &= \frac{1}{2} \sum_{e=1}^n \iiint_{V_e} \{ \epsilon_e \}^T \{ \sigma_e \} dV_e \end{aligned} \quad (3.19)$$

where e denotes an element, and n is the total number of elements in the structure.

Substituting equations (3.12) and (3.14) in equation (3.19), the following expression can be obtained:

$$U_e = \frac{1}{2} \{ \delta_e \}^T \iiint_{v_e} [B]^T [D] [B] dv_e \quad (3.20)$$

where v_e is the element volume.

The stiffness matrix $[K_e]$ for the element is defined by the quantity under the integral

$$\text{ie } [K_e] = \iiint_{v_e} [B]^T [D] [B] dv_e \quad (3.21)$$

As the strain matrix is expressed in natural co-ordinates, it is necessary to carry out the above integration in these co-ordinates too. A transformation has to be made in which the determinant of $[J]$ is involved as follows:

$$dv_e = dx dy dz = \det [J] d\xi d\eta d\zeta \quad (3.22)$$

As the elemental volume is expressed in the normalised co-ordinates ξ , η and ζ which have the limits of ± 1 , the evaluation of the element stiffness can be reduced to that of finding the following integral:

$$[K_e] = \int_{-1}^1 \int_{-1}^1 \int_{-1}^1 [B]^T [D] [B] \det [J] d\xi d\eta d\zeta \quad (3.23)$$

As it can be seen, the integration is obtained in normalised co-ordinates which are based on the right cube and not on the complicated distorted shape.

3.2.2.6 Numerical Integration

While the limits of the integration in equation (3.23) are simple, the explicit formulation of it is difficult from the mathematical point of view and numerical integration becomes the only choice. This makes the evaluation of such element properties expressed in curvilinear co-ordinates direct, and in non-linear analysis it is easy to integrate over elements containing elastic and inelastic zones.

To carry out this type of analysis, the argument of the integral in equation (3.23) must be evaluated at a specific set of values of ξ , η , ζ within the element. These values have to be determined according to integration rules and their locations are called sampling or integration points. Making a weighted summation of these values, the integral can be evaluated. In the 3-dimensional case the integral I of equation (3.23) can be written as:

$$\begin{aligned}
 I &= \int_{-1}^1 \int_{-1}^1 \int_{-1}^1 f(\xi, \eta, \zeta) d\xi d\eta d\zeta \\
 &= \sum_{i=1}^m \sum_{j=1}^m \sum_{l=1}^m C_i C_j C_l f(a_i, a_j, a_l) \\
 &= \sum_{q=1}^{m^3} k_q f(a_i, a_j, a_l) \tag{3.24}
 \end{aligned}$$

where q is the integration point at $\xi = a_i$, $\eta = a_j$ and $\zeta = a_l$, $k_q = C_i \cdot C_j \cdot C_l$ which are the weighted co-efficients of the integral and m is the number of sampling points.

Irons (37) has proved that Gauss-Legendre quadrature

rules are the most efficient for the isoparametric elements. Moreover, Gauss integration points are suitable for direct stress calculations.

So the element stiffness of equation (3.23) can be evaluated numerically using Gauss quadrature as:

$$[K_e] = \sum_{q=1}^{m^3} K_q [B]^T [D][B] \det [J]_q \quad (3.25)$$

Table 3.1 shows the symmetrical positions of Gauss points a_j and the corresponding weighting coefficients C_j for the 2 and 3 point integration rules as given by Ref (38).

Table 3.1
Gauss-Legendre Quadrature Constants

$\pm a_j$			C_j		
m = 2					
0.57735	02691	89626	1.00000	00000	00000
m = 3					
0.77459	66692	41483	0.55555	55555	555556
0.00000	00000	00000	0.88888	88888	88889

Irons (39) also developed simpler integration formulae to minimise computational effort and has shown them to be as exact as the Gaussian type rules.

It is clear that the computational time depends on the number of integration points sampled in any element, or in

other words depends on the order of the integration rule (for example $2 \times 2 \times 2$ integration rule means performing the integration over 8 sampling points while $3 \times 3 \times 3$ means 27 points to be sampled in the integral). The type of integration rules required for exact integration of the stiffness matrix depends on the order of the stiffness equations (40) (2 and 3 point integration rules are required for linear and parabolic elements respectively). However, as element size decreases it would be expected that lower order rules would be adequate. For the parabolic element it is found that the 2-point rule is the minimum required to satisfy the constant strain convergence criterion.

Recently (41), reduced integration technique (which uses the minimum rules) has been used successfully in linear analysis and showed benefit related to computation time. It was also reported that the minimum integration rules produce more flexible elements with regards to the stiffnesses and that the sampling points of the lower order rules are the best points for stress calculations.

3.2.3. Bar Elements

3.2.3.1. Introduction

To retain the efficiency that a relatively small number of isoparametric elements are required to represent a structure, the reinforcing bars have to be idealised in a simple and accurate manner. As cracking and other non-linear effects are permitted in the concrete it is desirable to treat the reinforcement separately. Thus bar elements, simulating steel reinforcements, were allowed

to lie within the isoparametric elements (30), (40) and (42), as shown in Fig 3.6. The bar elements are restricted to lie along lines of constant ξ , η , ζ of the main elements. The variation of displacements along the bar will be affected by the displacements of the main element.

3.2.3.2. Element Properties

The shape functions and the element matrices for the bar element are derived following Ergatoudis (29).

Consider the element lying along a direction of constant η , ζ as shown in Fig 3.6. Shape functions for a 2-node element are defined by:

$$N_1 = \frac{1 - \xi}{2}, \quad N_2 = \frac{1 + \xi}{2} \quad (3.26)$$

The interpolation formula for displacements is given by:

$$\begin{Bmatrix} u \\ v \\ w \end{Bmatrix} = \sum_{i=1}^{n=2} [N_i] \begin{Bmatrix} u_i \\ v_i \\ w_i \end{Bmatrix} \quad (3.27)$$

This element represents linear variation of displacements and constant strain along the bar.

For a 3-node element the shape functions are:

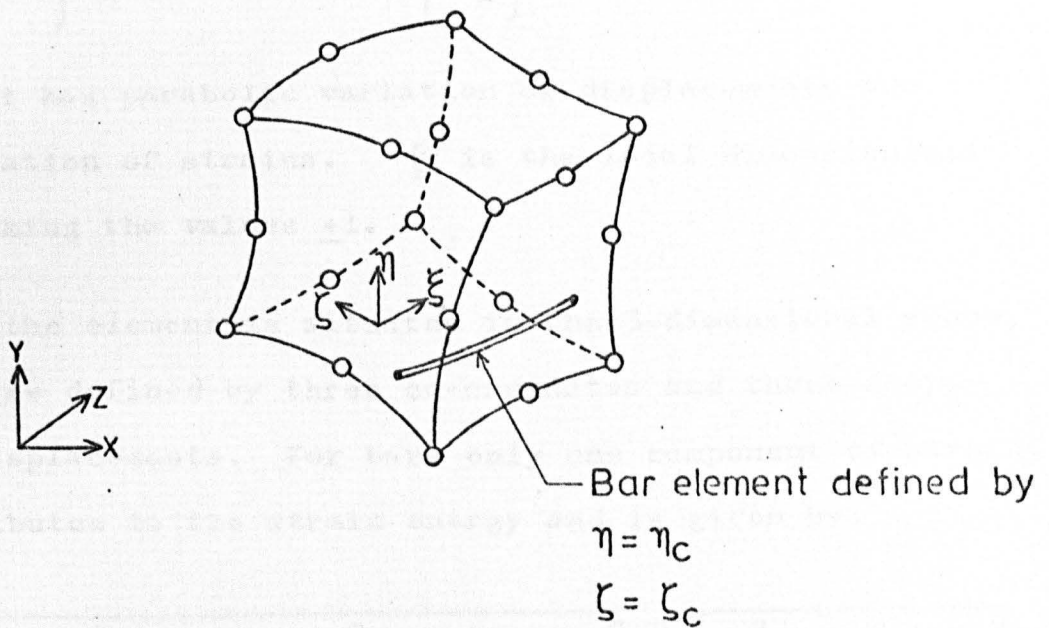


FIG. 3.6. TYPICAL BAR ELEMENT IN CURVILINEAR DIRECTIONS WITHIN A HEXAHEDRON ELEMENT

$$\begin{aligned}
 N_1 &= \frac{\xi(\xi - 1)}{2}, \quad N_2 = 1 - \xi^2 \\
 N_3 &= \frac{\xi(\xi + 1)}{2}
 \end{aligned} \tag{3.28}$$

and the interpolation functions in this case are

$$\begin{Bmatrix} u \\ v \\ w \end{Bmatrix} = \sum_{i=1}^{n=3} [N_i] \begin{Bmatrix} u_i \\ v_i \\ w_i \end{Bmatrix} \tag{3.29}$$

This element has parabolic variation of displacements and linear variation of strains. ξ is the local dimensionless variable taking the values +1.

When the element is situated in the 3-dimensional space, the nodes are defined by three co-ordinates and three components of displacements. For bars only one component of strain, ϵ_s , contributes to the strain energy and is given by:

$$\epsilon_s = \frac{\sqrt{(dx + du)^2 + (dy + dv)^2 + (dz + dw)^2} - \sqrt{dx^2 + dy^2 + dz^2}}{\sqrt{dx^2 + dy^2 + dz^2}} \tag{3.30}$$

where dx, dy, dz are the element co-ordinates and du, dv, dw are the incremental displacements.

Expanding equation (3.30) and neglecting second order terms, then:

$$\epsilon_s = \sqrt{1 + \frac{2dx \, du + 2dy \, dv + 2dz \, dw}{dx^2 + dy^2 + dz^2}} - 1 \tag{3.31}$$

And this can be written in the following form after a binomial expansion:

$$\epsilon_s = \frac{dx \, du + dy \, dv + dz \, dw}{dx^2 + dy^2 + dz^2} \quad (3.32)$$

Dividing the top and bottom by $d\xi^2$ gives

$$\epsilon_s = a \left[\frac{\partial x}{\partial \xi} \quad \frac{\partial y}{\partial \xi} \quad \frac{\partial z}{\partial \xi} \right] \begin{Bmatrix} \frac{\partial u}{\partial \xi} \\ \frac{\partial v}{\partial \xi} \\ \frac{\partial w}{\partial \xi} \end{Bmatrix} \quad (3.33)$$

where:

$$a = \frac{1}{\left(\frac{\partial x}{\partial \xi}\right)^2 + \left(\frac{\partial y}{\partial \xi}\right)^2 + \left(\frac{\partial z}{\partial \xi}\right)^2}$$

and

$$\frac{\partial x}{\partial \xi} = \sum \frac{\partial N_i}{\partial \xi} x_i \text{ etc}$$

Thus the strains can be obtained in terms of the Cartesian deflections $[\delta]$.

$$\epsilon_s = [B][\delta] \quad (3.34)$$

$$\text{where } [B] = a \left\{ [b] \frac{\partial N_1}{\partial \xi}, [b] \frac{\partial N_2}{\partial \xi}, \dots \right\}$$

$$\text{and } [b] = \left[\frac{\partial x}{\partial \xi} \quad \frac{\partial y}{\partial \xi} \quad \frac{\partial z}{\partial \xi} \right]$$

The stiffness is given by

$$[K_s] = \int_{-1}^1 [B]^T E_s [B] (\text{area}) \frac{ds}{d\xi} d\xi \quad (3.35)$$

where

$$\frac{ds}{d\xi} = \sqrt{\left(\frac{\partial x}{\partial \xi}\right)^2 + \left(\frac{\partial y}{\partial \xi}\right)^2 + \left(\frac{\partial z}{\partial \xi}\right)^2}$$

E_s = Young's modulus of the bar

area = Cross sectional area of the bar

3.2.4 Assembly and Solution

The individual stiffness matrices from the concrete and steel elements are suitably assembled using the geometry of the structure to form the global stiffness matrix $[K]$. Any external loads are also assembled in a load vector $\{R\}$. This leads to:

$$[K] \{ \delta \} = \{ R \} \quad (3.36)$$

which represents the assembly of the final equilibrium equations of the structure together with the prescribed boundary conditions.

The solution of the simultaneous equations (3.36) gives the unknown displacements $\{ \delta \}$ as:

$$\{ \delta \} = [K]^{-1} \{ R \} \quad (3.37)$$

This solution can be accomplished in many ways. The direct Gaussian elimination procedure is adopted for this analysis (see Chapter 5).

After the evaluation of the displacements, strains and stresses at the integration points can be easily calculated

by direct substitution in equations (3.12) and (3.14) respectively.

3.3 Non-linear Incremental Analysis

3.3.1 Introduction

It has been explained in Section 3.1 that non-linearity in concrete is due to changes in the material properties caused by tensile cracking or internal micro-cracking in compression. Thus the non-linearity in this case is achieved by the use of a suitable constitutive law for the material which is expressed by the elasticity matrix $[D]$.

The non-linear solution can be approximated by solving a series of linear problems. At the end of each stage, the equilibrium, compatibility and constitutive relations of the material must be satisfied. Compatibility requirements were met in the finite element formulation, so the non-linear solution has to preserve the equilibrium conditions and satisfy the constitutive relationships of the material.

Several methods have been suggested for the material non-linearity and the problem is still under intensive research. The method of 'unbalanced' forces has been used by Nayak (34) and Phillips (40), (42) to restore equilibrium at every load stage. An alternative is the 'variable elasticity' method proposed by Zienkiewicz (26).

In any of these methods the basic linear elastic equations given by equation (3.36),

$$\text{ie, } [K] \{ \delta \} - \{ R \} = 0$$

have to be solved. The non-linearity occurs in the stiffness

matrix $[K]$, which is a function of the material constitutive law given by equation (3.14).

For this study, the variable stiffness method is used in conjunction with the non-linear solution and this procedure is explained in the next section.

3.3.2 Method of Variable Stiffness

The 'variable elasticity' technique is based on the adjustment of the elasticity matrix $[D]$ according to the stress or strain level reached.

The constitutive law for the material behaviour can be expressed in the form:

$$f(\{\sigma\}, \{\epsilon\}) = 0 \quad (3.38)$$

If this constitutive law is written in the form of equation (3.14), but with the elasticity matrix being a function of the stress level reached, such as:

$$[D] = [D](\{\epsilon\}) = [D(\{\delta\})] \quad (3.39)$$

then the variable stiffness method can be applied (26).

As the final stiffness matrix is a function of the elasticity matrix, thus for equilibrium:

$$\psi(\{\delta\}) = [K(\{\delta\})]\{\delta\} - \{R\} = 0 \quad (3.40)$$

Equilibrium can be achieved by using simple iterative

procedures. For example, evaluating $[K(\{\delta_0\})] = [K_0]$ at displacement $\{\delta_0\} = 0$, then solve for $\{\delta_1\}$

$$\{\delta_1\} = [K_0]^{-1} \{R\} \quad (3.41)$$

Then the problem is resolved for the same load with the new elastic constants as:

$$\{\delta_n\} = [K]_{n-1}^{-1} \{R\} \quad (3.42)$$

The process is repeated until no further displacement changes occur. This indicates that the solution is accomplished and equilibrium is satisfied.

If the solution in equation (3.39) is used for small increments of stress and strains, then the solution has to be adopted for small load increments starting from previously arrived levels of stress and strain.

At the incremental level a number of cycles of analysis are to be performed for each load increment. In the first cycle, the load increment $\{\Delta R_i\}$ is applied and the temporary displacement increment $\{\Delta \delta_i^*\}$ is computed from

$$\{\Delta \delta_i^*\} = [K_{i-1}]^{-1} \{\Delta R_i\} \quad (3.43)$$

where $[K_{i-1}]^{-1}$ is the inverse of the stiffness matrix calculated at the end of the previous load increment using modified elasticity matrix. The displacement $\{\delta_i^*\}$ at this stage is computed:

$$\left\{ \delta_i^* \right\} = \left\{ \delta_{i-1} \right\} + \left\{ \Delta \delta_i^* \right\} \quad (3.44)$$

where $\left\{ \delta_{i-1} \right\}$ is the displacements at the end of the previous increment.

The stiffness matrix corresponding to $\left\{ \delta_i^* \right\}$ is evaluated and utilised to compute an approximation to another displacement increment $\left\{ \delta_{i+1}^* \right\}$ for the same load increment $\left\{ \Delta R_i \right\}$. The process is repeated until the difference in displacements of the last two cycles is sufficiently small. For each cycle the stiffness matrix $[K]$ is recalculated and a new solution of equations is obtained.

3.3.3 Incremental Procedure

The basis of the incremental procedure is the subdivision of the total load into many small partial loads or increments. One load increment is applied at a time on the structure and load-deformation behaviour can be obtained at the corresponding loading stage. Increments of displacements are obtained after the application of each load increment. The displacement increments are accumulated to give the total displacements at any stage of loading.

The 'variable elasticity' method explained in the last section is used with the incremental procedure. This means that the load is applied incrementally, but for each load increment successive iterations or cycles are performed until no further changes in displacements take place as shown in Fig 3.7. This indicates that the structure is approaching equilibrium and the next increment can be applied. In other words, for concrete structures where the deformations

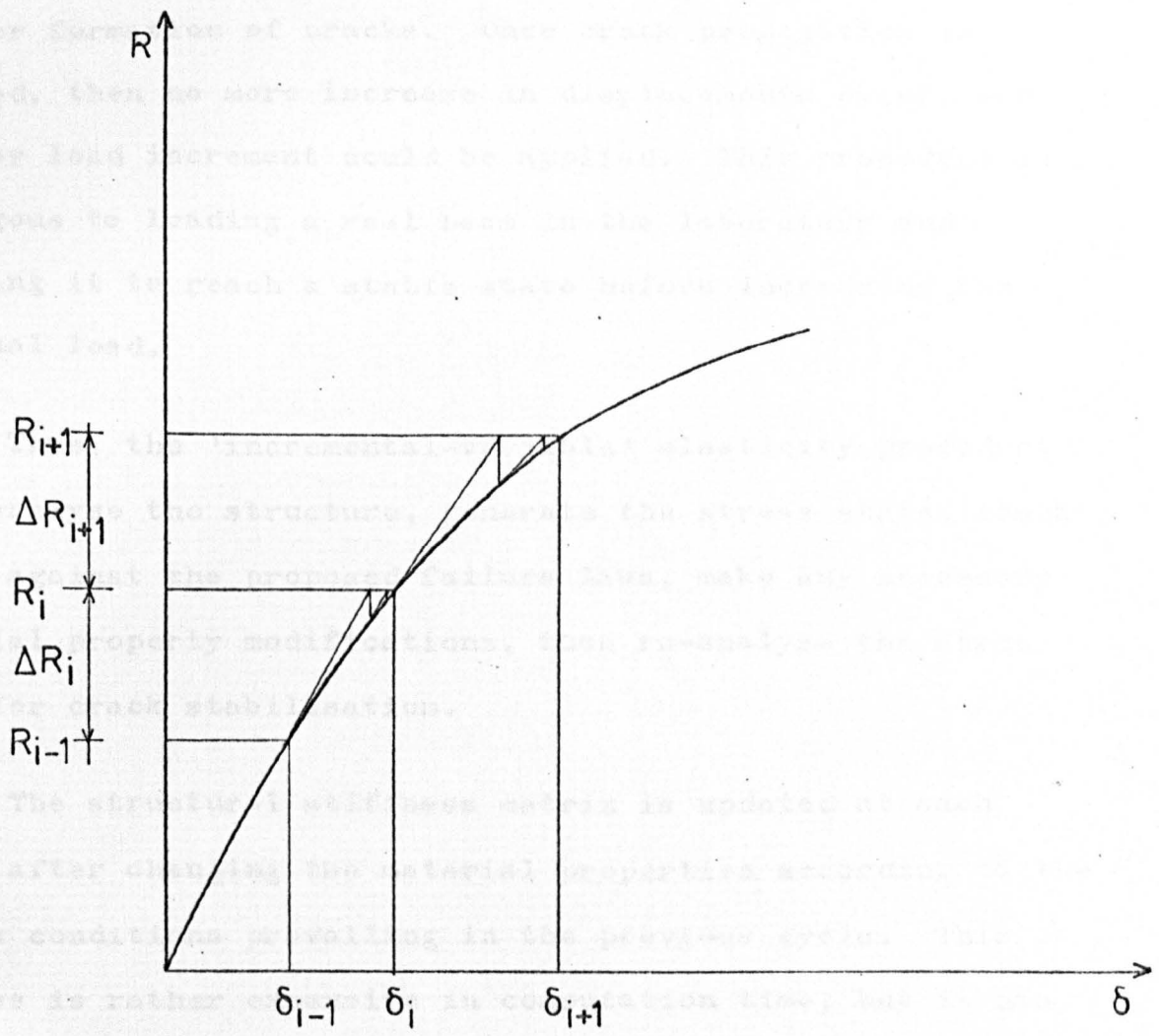


FIG. 3.7. INCREMENTAL - ITERATION PROCEDURE

(After Desai & Abel , 27)

are influenced by the cracking state reached, the structure is re-analysed under the same incremental load for any further formation of cracks. Once crack propagation is stopped, then no more increase in displacements occur, and another load increment could be applied. This procedure is analogous to loading a real beam in the laboratory and allowing it to reach a stable state before increasing the external load.

Thus, the 'incremental-variable' elasticity procedure must analyse the structure, generate the stress state, check these against the proposed failure laws, make any necessary material property modifications, then re-analyse the structure for crack stabilisation.

The structural stiffness matrix is updated at each cycle after changing the material properties according to the stress conditions prevailing in the previous cycle. This process is rather expensive in computation time, but it has the advantage of decreasing the number of cycles in each increment considerably, particularly in the early stages of loading where 2 cycles were found to be enough.

A flow chart for the incremental procedure is shown in Fig 3.8. The process contains two main cyclic loops. The outer loop is performed for each load increment. The inner loop repeats the displacement solutions for the same load increment until no more cracks are formed and the increase in displacements has stopped. This loop is terminated in step 7 if the limit on displacement specified by the input

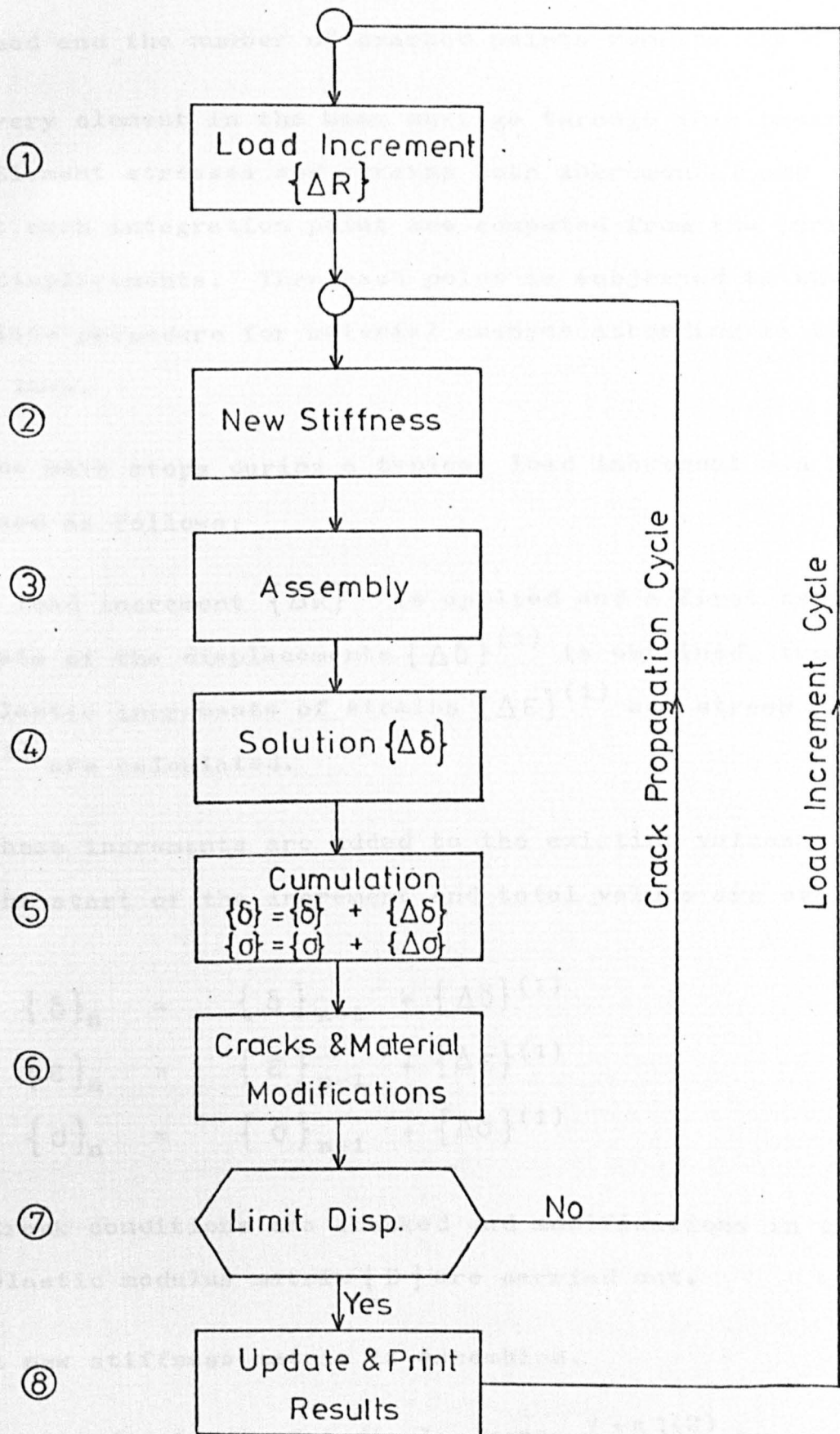


FIG. 3.8. FLOW CHART FOR INCREMENTAL PROCEDURE

is reached and the number of cracked points remains the same.

Every element in the beam must go through this procedure. Element stresses and strains both incremental and total at each integration point are computed from the incremental displacements. Then each point is subjected to the appropriate procedure for material changes according to the failure laws.

The main steps during a typical load increment can be summarised as follows:

- (1) A load increment $\{\Delta R\}$ is applied and a first estimate of the displacements $\{\Delta\delta\}^{(1)}$ is obtained, from which elastic increments of strains $\{\Delta\varepsilon\}^{(1)}$ and stress $\{\Delta\sigma\}^{(1)}$ are calculated.
- (2) These increments are added to the existing values at the start of the increment and total values are evaluated.

$$\begin{aligned}\{\delta\}_n &= \{\delta\}_{n-1} + \{\Delta\delta\}^{(1)} \\ \{\varepsilon\}_n &= \{\varepsilon\}_{n-1} + \{\Delta\varepsilon\}^{(1)} \\ \{\sigma\}_n &= \{\sigma\}_{n-1} + \{\Delta\sigma\}^{(1)}\end{aligned}$$

- (3) Crack conditions are checked and modifications in the elastic modulus matrix $[D]$ are carried out.
- (4) A new stiffness matrix is assembled.
- (5) A second estimate for displacements $\{\Delta\delta\}^{(2)}$ is obtained and $\{\Delta\varepsilon\}^{(2)} + \{\Delta\sigma\}^{(2)}$ are calculated.

(6) Then

$$\{ \delta \}_n = \{ \delta \}_{n-1} + \{ \Delta \delta \}^{(2)}$$

$$\{ \varepsilon \}_n = \{ \varepsilon \}_{n-1} + \{ \Delta \varepsilon \}^{(2)}$$

$$\{ \sigma \}_n = \{ \sigma \}_{n-1} + \{ \Delta \sigma \}^{(2)}$$

and the conditions in step (3) are satisfied.

(7) The difference between the last two displacements, DF, is calculated

$$DF = \{ \Delta \delta \}^{(2)} - \{ \Delta \delta \}^{(1)}$$

(8) Steps (4) to (7) are repeated until DF is sufficiently small (ie less than a prescribed value), or a maximum number of cycles exceeded.

3.4 Non-linearity and Isoparametric Elements

It has been mentioned before that numerical integration was used in evaluating the stiffnesses of the isoparametric elements. The state of stress at each integration point within the element is examined individually and the appropriate material property changes are performed accordingly. The element stiffness matrix is then obtained by a suitable weighted summation of the individual integration points. This makes it possible to integrate over linear and non-linear regions inside one element. This means that the element can contain elastic and inelastic zones under the same level of load.

It has been reported (45) that the sampling points of

Gauss-quadrature rules are good positions for evaluating stresses, and this will give more accurate prediction of non-linear behaviour.

Finally, the use of the high order displacement functions, yields a better approximation to the displacements, and this results in a smooth spread of non-linear zones.

Investigation into the strength and behaviour of concrete under various stress states have been conducted. However, with an experimental characteristic are obtained to obtain stress-strain relations and failure loads. Some of the more extensive tension-compression stress states are inadequate. Furthermore, most tests have been limited to the range of biaxial or triaxial compression, and only a few have been carried out on combined tension and compression. This is the main obstacle to develop acceptable failure criteria under combination of tensile and compressive stresses.

This chapter describes the material behaviour and the recent developments in failure criteria under biaxial and compressive stresses.

The behaviour of concrete and steel have been treated individually, then they are combined by placing the bars in their proper locations in the concrete.

4.3 Behaviour of concrete under load

4.3.1 Internal behaviour

Due to the heterogeneous nature of concrete, its overall mechanical and physical properties depend on

REINFORCED CONCRETE BEHAVIOUR AND ITS
FAILURE LAWS

4.1 Introduction

The use of reinforced concrete in structural members requires a thorough understanding of its material behaviour under various stress combinations. Numerous experimental investigations into the strength and deformation of concrete under uniaxial stress states have been conducted in the past. However, data on deformational characteristics and strength to obtain stress-strain relations and failure laws for concrete under multiaxial tension-compression stress states are inadequate. Furthermore, most tests have been limited to the cases of biaxial or triaxial compression, and only a few have been carried out on combined tension and compression. This is the main obstacle to develop^{ing} acceptable failure criteria under combinations of tensile and compressive stresses.

This chapter describes the material behaviour and the recent developments in failure criteria under tensile and compressive stresses.

The behaviour of concrete and steel have been treated individually, then they are combined by placing the bars in their proper locations in the elements.

4.2 Behaviour of concrete under Load

4.2.1 Internal Behaviour

Due to the heterogeneous nature of concrete, its overall mechanical and physical properties depend upon

the volume fractions properties of the constituents and the mechanism of interaction between the constituents. Due to the compaction process, hydration and shrinkage of fresh concrete, minor microcracks exist in concrete even before loading. It is believed now that the formation of these irrecoverable microcracks affect the fracture and the shape of the stress-strain curve near ultimate load. Newman and Newman (24) discussed clearly the theoretical and experimental investigation of this subject. The phenomena of microcracking and the internal behaviour under load until the final breakdown of the material are illustrated in Fig 4.1 and are described in the following stages according to ref (24):

(1) As the load is applied, localised cracks are initiated at isolated points of largest tensile strain concentration. Their formation relieves the strain concentration and equilibrium is rapidly restored, the accompanying energy changes and irrecoverable deformations are small. Thus these cracks are completely stable and do not propagate at this load stage. Up to 30-40% of the ultimate strength can be reached in this stage and the stress-strain curve slightly deviates from linearity.

(2) With increasing load, these initial stable cracks begin to propagate and multiply in a slow stable manner. Crack initiation of stage I continues and overlaps with crack propagation of stage II (Gaussian distribution is assumed to represent the distributions of crack initiation and propagation in Fig 4.1.a), and there is a transition

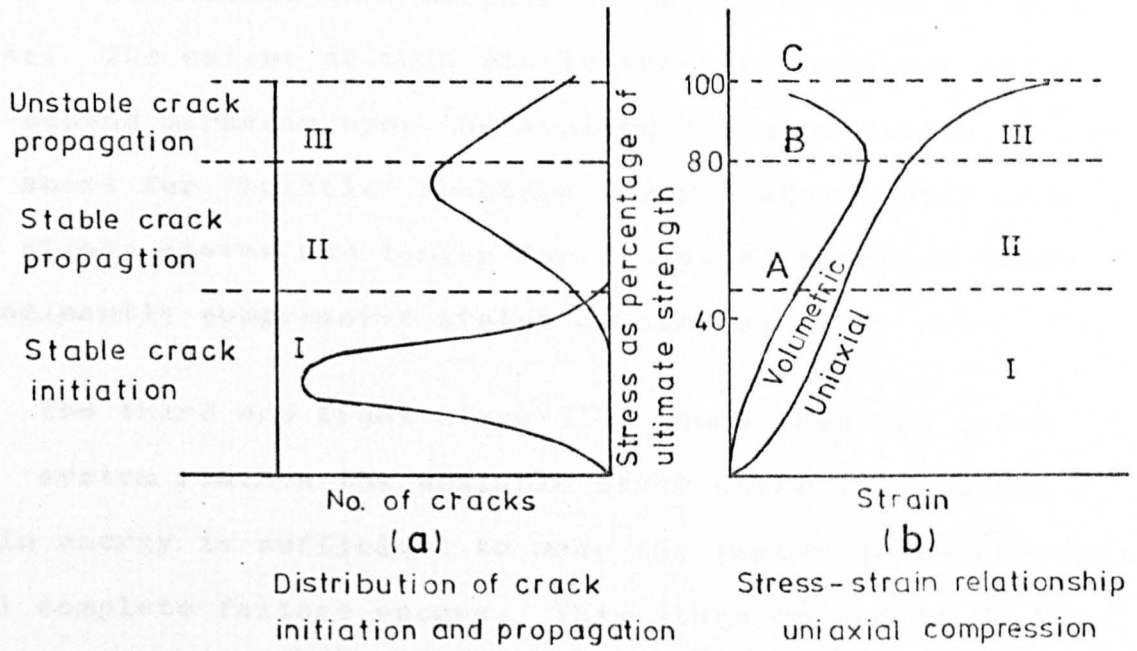


FIG. 4.1. THE STAGES OF CRACKING IN CONCRETE
(After Newman, 24)

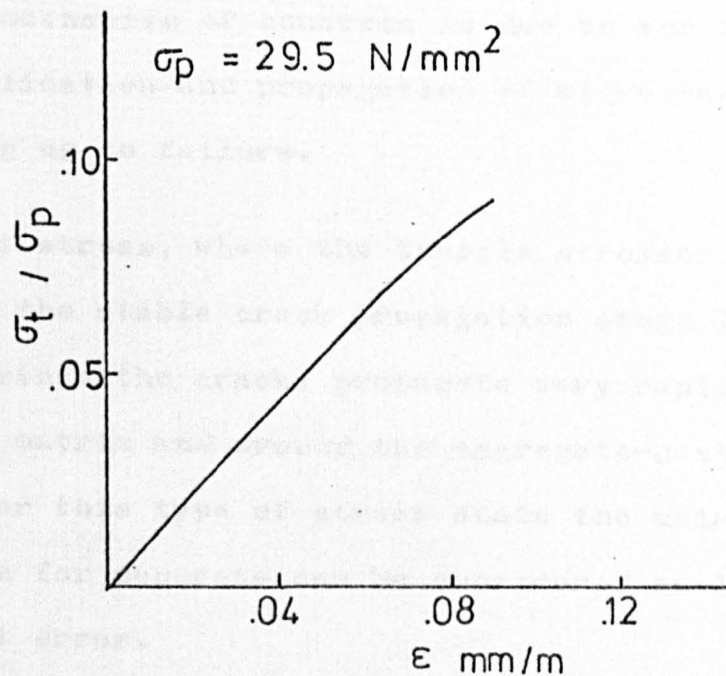


FIG. 4.2. STRESS - STRAIN RELATIONSHIP OF CONCRETE
UNDER UNIAXIAL TENSION - (After KUPFER, 48)

phase from the first to the second which does not occur at any single stress. During this second stage, if the stress level is maintained at a certain value, crack propagation ceases. The extent of this stable crack propagation stage will depend markedly upon the applied state of stress, being very short for 'brittle' fracture under predominantly tensile stress states and longer for 'plastic' fracture under predominantly compressive states of stress.

(3) The third and final Stage III occurs when the crack system reaches the unstable stage where the release of strain energy is sufficient to make the cracks self-propagating until complete failure occurs. This stage occurs at 70-90% of the ultimate stress and has been described as the 'critical stress or load' and is signified by a reversal in the volume change behaviour.

From this interpretation it can be seen that:

(a) The failure mechanism of concrete is due to the initiation, multiplication and propagation of microcracks from before loading up to failure.

(b) For states of stress, where the tensile stresses are predominant, the stable crack propagation stage II is of short duration since the cracks propagate very rapidly through the mortar matrix and around the aggregate-paste interface. Thus for this type of stress state the uniaxial stress-strain curve for concrete can be considered as linear without significant error.

4.2.2 Uniaxial Stress Behaviour

Figure 4.1.b shows the stress-strain curves for a typical concrete subjected to short-term monotonic loading up to failure in uniaxial compression. Many investigators suggest that up to 30-40% of the ultimate strength, the first part of the curves is reasonably straight with a slope equal to the tangent modulus of elasticity at zero load. The end of the straight part, 'A' is called the 'proportional limit'. The pre-existing cracks and those initiated through the first stage increase and multiply after the limit, until they reach a stage where a breakdown of the internal structure occurs. The deformation increases rapidly with the applied stress at this stage until it levels out at peak C which is called the ultimate stress. After the ultimate load the stress-strain curve may exhibit a descending portion if a sufficiently stiff machine is used in testing.

Many investigators (44) & (45) have given standard mathematical curves or complex formulæ from curve fitting to experimental data.

The uniaxial stress-strain curve in tension, Fig 4.2, is almost linear (46), (47) & (48). This can be seen from the short duration of stable crack propagation stage as explained in the previous section.

4.2.3 Compressive and Tensile Strength

The uniaxial compressive strength is generally used as a measure of the concrete quality. It is expressed

as cube strength or cylinder strength and can be obtained by testing cubes or cylinders with standard testing machines. The cylinder strength f'_c is approximately 0.8 x the cube strength $f'_{c u}$. For normal and good quality concrete f'_c ranges between 25 N/mm² to 50 N/mm². For this study the cube strength is taken to be around 35 N/mm².

Compared to the compressive strength, the tensile strength of concrete is small and ranges between .08 and .12 f'_c . Its value can be measured by direct tension tests, flexural strength tests or splitting tests. Different values may be obtained from these tests. The value of the flexural strength taken in this study is $7.5 \sqrt{f'_c}$ according to ACI-318, 1971.

4.3 Failure Laws in Tension and Tension-Compression Zones

4.3.1 Introduction

The failure laws are expressed in terms of principal stresses. Thus, in the finite element analysis, the concrete principal stresses σ_1 , σ_2 and σ_3 are computed from the six components of stresses obtained at each integration point of each element in the structure. The method of calculating the principal stresses from the stress components in x, y, & z co-ordinates is given in Appendix A.

The principal stresses in the compression zone of three T-beams obtained from the theoretical analysis at ultimate load are shown in Tables 4.1, 4.2 and 4.3. The beams named as TBX IV, TBX V and TBX VI. These beams have flange thickness of 70 mm and flange width of 350, 700 and 1050 mm

TABLE 4.1

Principal Stresses in the Flange-Beam TBX IV

(N/mm²) - Compression Positive

Element No	Principal Stress No	Sampling Points							
		1	2	3	4	5	6	7	8
1	1	-.335	-1.664	-.006	-.276	-.487	-.052	-.17	.058
	2	-.049	-.792	.495	.419	.067	.896	.043	.437
	3	.873	1.569	7.311	7.753	2.642	3.173	6.514	6.409
2	1	-1.763	-1.966	-.637	-.69	-.52	.069	-.029	.265
	2	1.416	-.452	.542	.342	.975	1.375	.485	1.483
	3	1.264	1.846	8.59	7.27	3.132	3.162	6.148	5.686
3	1	-.094	-.059	.078	-.176	-.022	-1.78	-.225	-.899
	2	.239	.271	.158	.004	.708	-.068	.112	-.242
	3	3.967	4.198	5.925	5.884	4.961	4.455	6.38	5.974
4	1	-.203	-.618	-.545	-1.156	-.222	.006	-.017	-.739
	2	.151	-.614	-.204	-.454	.759	1.627	1.019	.367
	3	4.085	4.111	6.123	5.864	4.465	4.492	6.74	7.333
5	1	-1.029	.034	-.178	-.15	.124	-.896	-.084	-.395
	2	.247	1.992	.178	.385	.211	-.191	.427	.049
	3	4.628	5.855	7.004	7.529	4.457	5.201	7.776	8.14
6	1	-1.783	-1.826	-.302	-.886	-1.996	-.633	-1.417	-.668
	2	-.56	-.431	.505	-.047	.219	2.7	-.144	4.14
	3	3.944	4.3	6.875	7.528	5.292	7.504	8.299	11.534

TABLE 4.2: Principal Stresses in the Flange-Beam TBX V (N/mm²) - Compression Positive

Element No	Principal Stress No	Sampling Points							
		1	2	3	4	5	6	7	8
1	1	-.052	-.575	-.138	-.235	-.121	-.67	.005	-.183
	2	-.053	.021	.026	-.119	-.053	.087	.163	.071
	3	1.054	1.17	5.235	5.672	1.283	2.041	5.955	6.183
2	1	-.905	-3.613	-.624	-.207	-1.237	-2.395	.112	-.426
	2	.086	-.791	.401	.931	.075	.183	.314	.293
	3	1.348	1.004	6.459	7.954	1.893	2.903	6.151	5.884
3	1	-3.197	-2.97	-.662	-1.234	-.917	-.78	.122	.476
	2	-2.294	-2.343	1.098	1.176	.525	1.784	.271	1.61
	3	-.576	-.61	8.236	8.767	2.627	1.904	6.095	5.484
4	1	-.163	-.752	.016	-.251	-.245	-.512	-.658	.482
	2	.124	-.143	.184	.244	.283	.867	-.10	1.16
	3	1.896	2.166	6.096	6.05	2.097	2.194	6.731	6.859
5	1	-.863	-1.282	-.238	-.298	-.336	-.926	-.251	-.943
	2	-.026	.542	.141	.522	-.021	-.375	.559	.099
	3	2.911	3.957	5.845	5.228	2.924	4.564	6.367	5.177
6	1	.031	-.687	-.825	-.187	.233	.112	-1.84	-1.071
	2	1.021	.507	.406	-.599	-.364	1.207	.906	1.533
	3	3.459	4.089	4.474	3.889	4.254	3.795	4.834	5.999
7	1	-.351	-.819	.139	-1.336	-.341	-.184	-.544	-.219
	2	.118	-.061	.526	-.542	.01	.744	-.092	.669
	3	1.466	2.636	8.38	6.436	1.474	2.357	8.988	8.195
8	1	-.986	-.649	-.315	-.399	-.502	-.978	-.212	-1.488
	2	-.465	.829	.033	.55	.219	-.303	.289	-.581
	3	2.753	5.198	7.074	7.774	2.528	2.53	8.392	9.555
9	1	-.446	-2.898	-.815	-3.149	-2.415	-.412	-1.037	-.946
	2	-.334	-.544	.161	-.384	.239	2.963	-.075	4.485
	3	4.988	3.872	6.007	6.121	2.39	7.814	10.026	12.815

- 67 -

TABLE 4.3 Principal Stresses in the Flange at Ultimate Load (N/mm^2)- Beam TBX VI
 Compression Positive

Element No	Principal Stress No	Sampling Points							
		1	2	3	4	5	6	7	8
1	1	-.058	-.379	-.289	-.649	-.064	-.952	-.134	-.341
	2	.072	-.015	-.052	-.018	.007	-.021	.044	.056
	3	.216	.559	4.023	4.475	.174	.712	4.773	5.361
2	1	-1.343	-3.754	-1.266	-.135	-1.758	-2.574	-.337	-.426
	2	.177	-.767	.266	.625	-.086	-.306	.156	.527
	3	1.121	.895	5.21	7.585	1.169	2.214	5.385	5.321
3	1	-3.367	-3.579	-.881	-1.18	-2.086	-1.429	.178	.65
	2	-2.269	-2.715	1.168	1.064	-.051	.804	.97	2.274
	3	-.274	-.894	6.84	7.271	1.136	1.74	5.752	4.151
4	1	-.224	-1.026	-.029	-.259	-.283	-.746	-.002	.021
	2	-.14	.043	.099	.116	-.066	.282	.196	.736
	3	.016	.744	5.347	5.495	.17	.558	5.932	5.985
5	1	-1.432	-2.093	-.289	-.116	-1.096	-1.777	-.136	-.597
	2	.087	.34	.168	.547	-.128	-.736	.306	.003
	3	1.157	2.905	5.441	4.648	.972	3.435	5.952	5.168
6	1	-.06	-.643	-1.128	-1.651	-.762	.166	-.888	1.643
	2	.142	.252	.26	.244	.918	1.378	.84	1.193
	3	3.155	2.6	3.668	3.033	4.294	5.641	4.558	4.474
7	1	.671	-.665	-.318	-.292	-.565	-.848	.208	.41
	2	-.157	-.156	-.095	.054	-.042	.339	.183	.74
	3	.027	.585	6.388	6.398	.559	.678	6.597	7.871
8	1	-.899	-1.475	-.329	-.548	-.862	-1.723	-.398	-1.1
	2	-.174	1.085	.138	.802	-.434	.089	.318	-.352
	3	.73	3.005	6.563	6.901	.54	1.313	6.896	7.962
9	1	-4.137	-3.488	-1.326	-1.338	-1.565	-.9	-2.173	-.895
	2	-1.832	-1.321	.723	1.238	1.684	.709	.065	4.755
	3	2.277	2.001	5.362	4.906	4.159	7.179	8.25	12.056

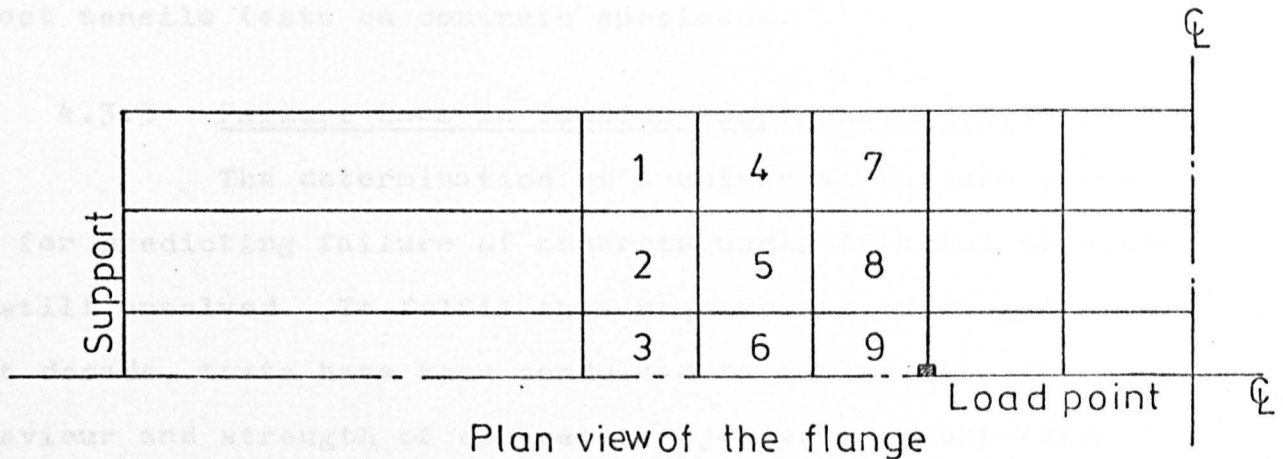
respectively, more details are given in Chapter 6. The location of the elements in the flange and the sampling points in each element are shown in Fig 4.3.

It can be seen from the tables that at least one of the principal stresses in the compression zone is tensile. Neither does the maximum compressive stress exceed 30% of the cube compressive stress for these beams (cube strength was 37.9, 37.5 and 36.4 N/mm² respectively). Thus, the compression zone of a T-beam failing in shear is under a state of tensile and compressive stresses. It was discussed before that for such stress states, where the tensile stresses are predominant, the linear brittle response for concrete can be considered. And hence cracks occur as a result of the existing tension or tension-compression stresses.

The failure laws used for this study are discussed in the following sections. The regions of failure are classified as tension or tension-compression zones.

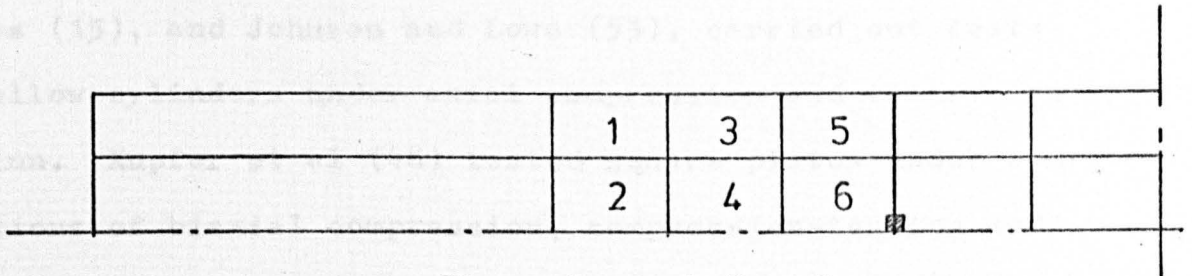
4.3.2 Failure Laws in Tension Zones

Many workers have proposed failure laws in multiaxial tensile stress states (49), (50). However, the most accepted failure theories for predicting cracking of concrete in tension is the maximum stress and maximum strain criterion. Concrete is assumed to behave linearly in tension with a limiting value equal to the tensile strength. These theories state that if a maximum principal tensile stress or strain in any direction reaches the tensile strength of concrete then a crack is assumed to occur in a direction perpendicular to the offending principal direction. The



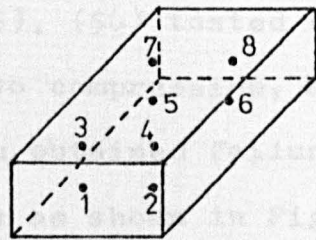
Plan view of the flange

Beams TBX-V & TBX-VIII



Plan view of the flange

Beam TBX-II



Sampling points for one element

FIG.4.3. ELEMENT NUMBERS

maximum tensile strength of concrete is determined from direct tensile tests on concrete specimens.

4.3.3 Failure Laws in Tension-Compression Zones

The determination of a universal failure criteria for predicting failure of concrete under triaxial stresses is still unsolved. To fulfil this requirement, during the last decade, tests have been conducted to investigate the behaviour and strength of concrete subjected to short-term multiaxial stress systems. More attention has been given to tests under biaxial and triaxial compression stress states.

Bresler and Pister (23), (51), Good and Helmy (52), Reeves (15), and Johnson and Lowe (53), carried out tests on hollow cylinders under axial compression and transverse torsion. Kupfer et al (48) tested square plates under combinations of biaxial compression, compression-tension and biaxial tension. They, also, measured multiaxial deformations. Mahmood and Hannant(54) carried out tests on cylinders for compression -compression-tension regions. Launay and Gashon (55), (56) tested cubes under triaxial compression and two compression, and one tension. Based on the information obtained failure envelopes were produced in stress space as shown in Figs 4.4 and 4.5.

From these tests it is difficult to obtain a consistent trend. This is due to the different shape and size of test specimens used and the conditions of loadings in each investigation.

A few failure theories have recently been presented for

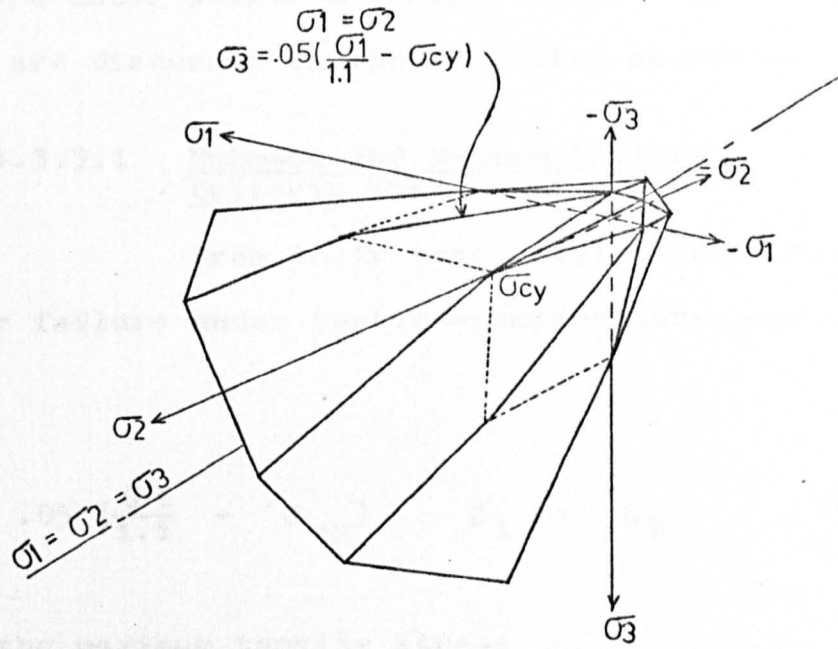


FIG. 4.4. FAILURE SURFACE FOR PLAIN CONCRETE
 SUBJECTED TO SHORT-TERM MULTIAXIAL
 STRESSES (After Mahmood , 54)

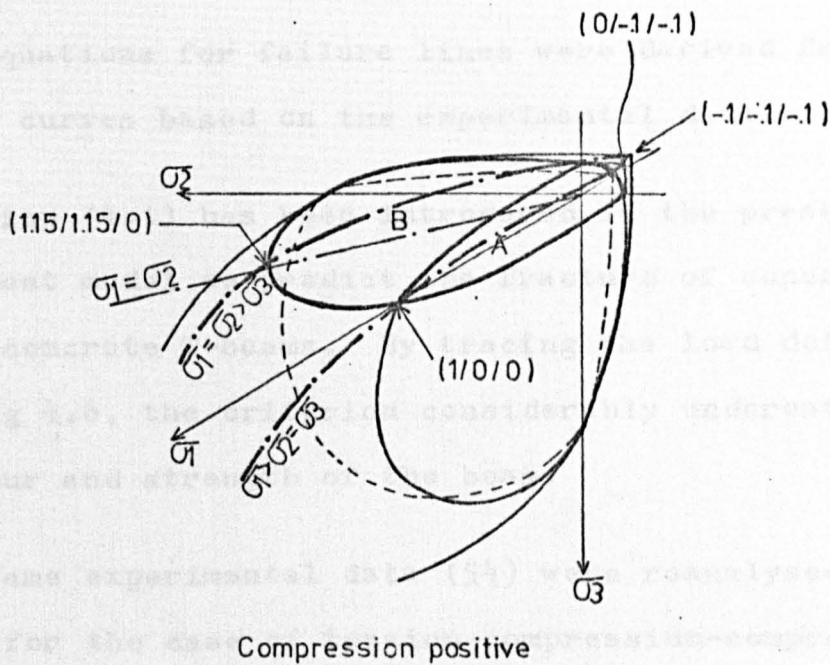


FIG. 4.5. FAILURE SURFACE FOR TENSILE
 STRESS STATES (After Cedolin , 58)

concrete fracture under combined tension-compression stress states. These are discussed in the following sections.

4.3.3.1 Mahmood and Hamant Failure Criteria (54)

From their test results they derived an equation for failure under tension-compression-compression as follows:

$$\sigma_3 = .05 \left(\frac{\sigma_1}{1.1} - \sigma_{cy} \right) \quad \sigma_1 = \sigma_2 \quad (4.1)$$

where σ_3 = the maximum tensile stress

σ_1 = the minimum compressive stress

σ_{cy} = concrete cylinder strength

A failure envelope in stress space for the multiaxial stress system is shown in Fig 4.4.

The equations for failure lines were derived from lower bound curves based on the experimental data.

Equation (4.1) has been introduced in the present finite element model to predict the fracture of concrete in reinforced concrete T-beams. By tracing the load deflection curve of Fig 4.6, the criterion considerably underestimates the behaviour and strength of the beam.

The same experimental data (54) were reanalysed in this study for the case of tension-compression-compression stress state. Two equations have been fitted to these data, a linear equation and a quadratic equation as shown in Fig 4.7.

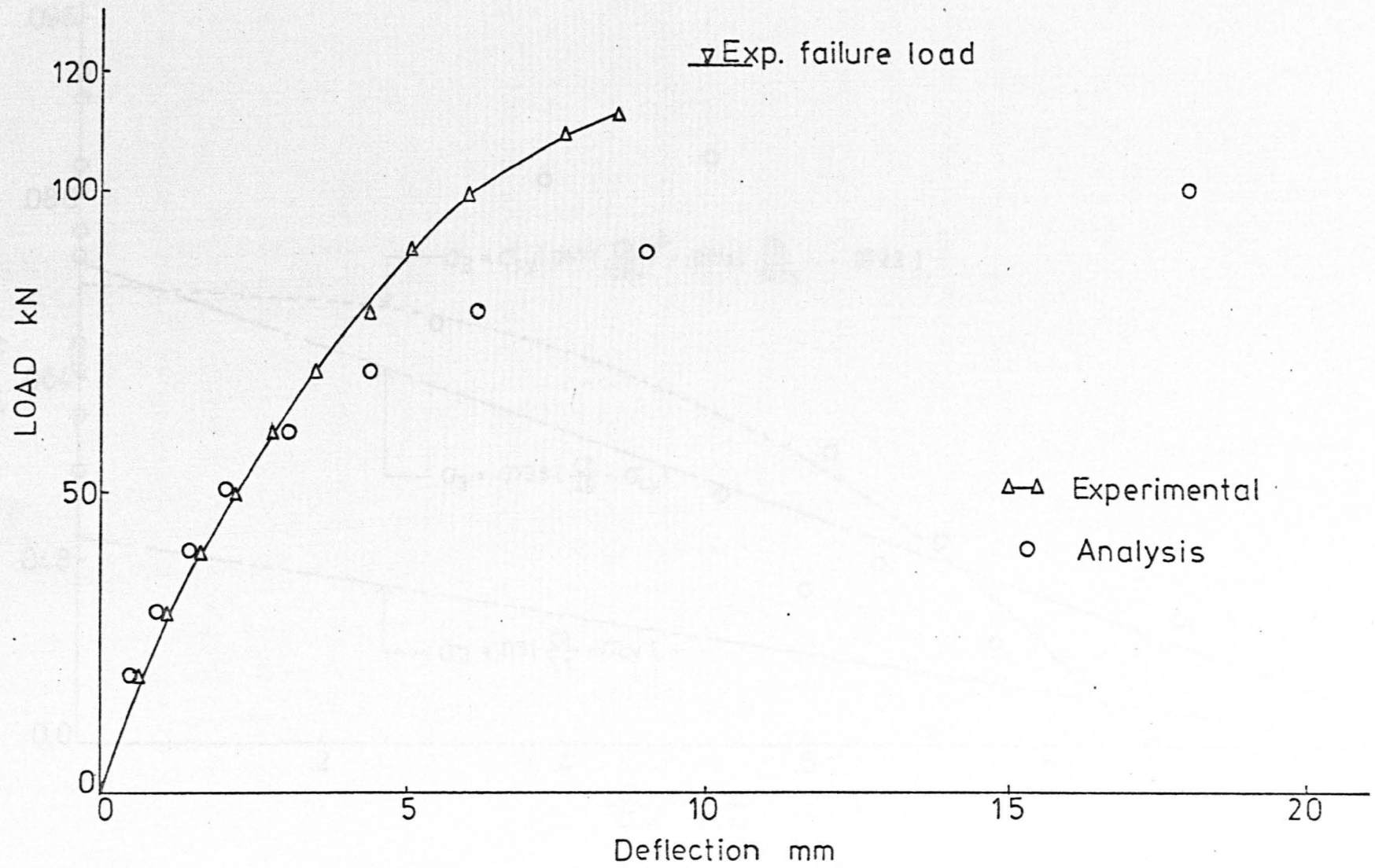


FIG.4.6. LOAD-DEFLECTION CURVE - BEAM TBX V - MAHMOOD & HANNANT FAILURE CRITERIA

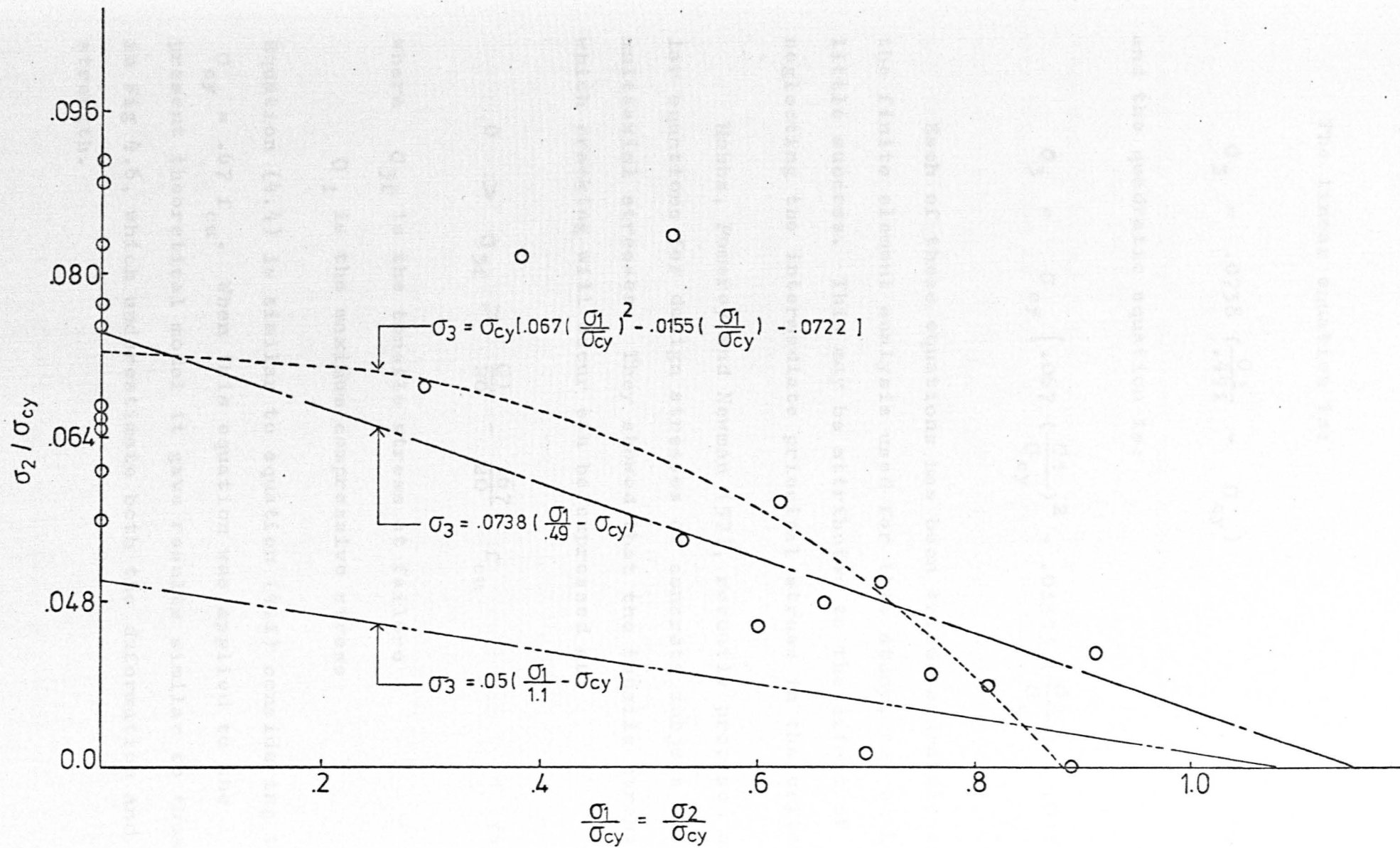


FIG.4.7. FAILURE EQUATIONS UNDER TENSION - COMPRESSION - COMPRESSION STRESSES

The linear equation is:

$$\sigma_3 = .0738 \left(\frac{\sigma_1}{.491} - \sigma_{cy} \right) \quad (4.2)$$

and the quadratic equation is:

$$\sigma_3 = \sigma_{cy} \left[.067 \left(\frac{\sigma_1}{\sigma_{cy}} \right)^2 - .01553 \left(\frac{\sigma_1}{\sigma_{cy}} \right) - .07217 \right] \quad (4.3)$$

Each of these equations has been tried separately in the finite element analysis used for this study, but with little success. This may be attributed to the effect of neglecting the intermediate principal stress in the criteria.

Hobbs, Pomeroy and Newman (57), recently proposed similar equations for design stresses of concrete subject to multiaxial stresses. They showed that the tensile stress at which cracking will occur can be expressed as:

$$0 > \sigma_{3f} > \frac{\sigma_1}{20} - \frac{.67}{20} f_{cu} \quad (4.4)$$

where σ_{3f} is the tensile stress at failure

σ_1 is the maximum compressive stress

Equation (4.4) is similar to equation (4.1) considering that

$\sigma_{cy} = .67 f_{cu}$. When this equation was applied to the present theoretical model it gave results similar to those in Fig 4.6, which underestimate both the deformation and strength.

4.3.3.2 Cedolin, Crutzen and Poli Failure Criteria (58)

From an analysis of the existing experimental data on triaxial stress states, stress-strain relationships were proposed for multiaxial compressive stresses and failure criteria for the ultimate strength of concrete under combined stresses. The failure criterion was formulated in terms of octahedral normal and shear stresses (σ_{oct} and τ_{oct} respectively). This type of failure criteria represents an improvement over the Mohr failure theory because it takes into account the intermediate principal stress.

The failure relationship takes the form:

$$\sigma_{oct} = f(\tau_{oct}) \quad (4.5)$$

or

$$F(I_1, I_2) = 0 \quad (4.6)$$

where I_1 and I_2 , the stress invariants are given by

$$I_1 = \sigma_1 + \sigma_2 + \sigma_3 \quad (4.7)$$

$$I_2 = \sigma_1 \sigma_2 + \sigma_2 \sigma_3 + \sigma_3 \sigma_1 \quad (4.8)$$

$$\sigma_{oct} = I_1/3 \quad (4.9)$$

$$\tau_{oct} = [2(I_1^2 - 3I_2)]^{1/2}/3 \quad (4.10)$$

In the octahedral normal and shear stress plane the

failure law of equation (4.5) can be represented by a linear or a quadratic equation according to the experimental information available and the application to structural elements.

Using the results of Kupfer (48) and Launay and Gashon (55), (56) a failure surface in the principal stress space has been drawn (58), Fig 4.5. Curve B is characterised by

$\sigma_1 = \sigma_2 > \sigma_3$ and represents the Launay and Gashon test data. While curve A corresponds to $\sigma_1 > \sigma_2 = \sigma_3$ and has been obtained by assuming the following hypothesis:

(1) rigid rotation of biaxial curve (2) intersection of the two planes $\sigma_2 = \sigma_t$, $\sigma_3 = \sigma_t$ ($\sigma_t =$ uniaxial tension).

Cedolin et al represented these curves through the octahedral shear and normal stresses Fig 4.8. Straight lines have been interpolated from this data for the limit conditions

$\sigma_1 > \sigma_2 = \sigma_3$ and $\sigma_1 = \sigma_2 > \sigma_3$. Cedolin et al fitted the following equations for these lines:

$$\sigma_1 > 0 \left\{ \begin{array}{l} \tau_{\text{oct}}/f'_c = 1.07 \sigma_{\text{oct}}/f'_c + .118 \quad \sigma_1 > \sigma_2 = \sigma_3 \\ \tau_{\text{oct}}/f'_c = 0.62 \sigma_{\text{oct}}/f'_c + .068 \quad \sigma_1 = \sigma_2 > \sigma_3 \end{array} \right\} \quad (4.11)$$

$$\sigma_1 < 0 \left\{ \begin{array}{l} \tau_{\text{oct}}/f'_c = 1.41 \sigma_{\text{oct}}/f'_c + .141 \quad \sigma_1 > \sigma_2 = \sigma_3 \\ \tau_{\text{oct}}/f'_c = .705 \sigma_{\text{oct}}/f'_c + .0705 \quad \sigma_1 = \sigma_2 > \sigma_3 \end{array} \right\} \quad (4.12)$$

Considering compression as positive, equations (4.11) represent the cases of one compression and two tensions or two compressions and one tension while equations (4.12) are adapted for three axial tensions.

Because these lines agree with experimental evidence (Fig. 4.8, from [10]), the octahedral failure law can be used to examine the failure mechanism of concrete under the cracking failure of concrete.

4.2 Crack Simulation

4.2.1 Introduction

Several ways have been used to study the effect of cracking in finite element models. Scordelis [59], [60], modeled existing and existing cracks at joints along a finite element and extent of the crack. The experimental results of Launay and Gashon [61] and Mahmood-Hannant [62] on both sides of the crack. The linkage between the crack and the boundary of the element is identical to the crack. The crack is produced between the element and the boundary of the element.

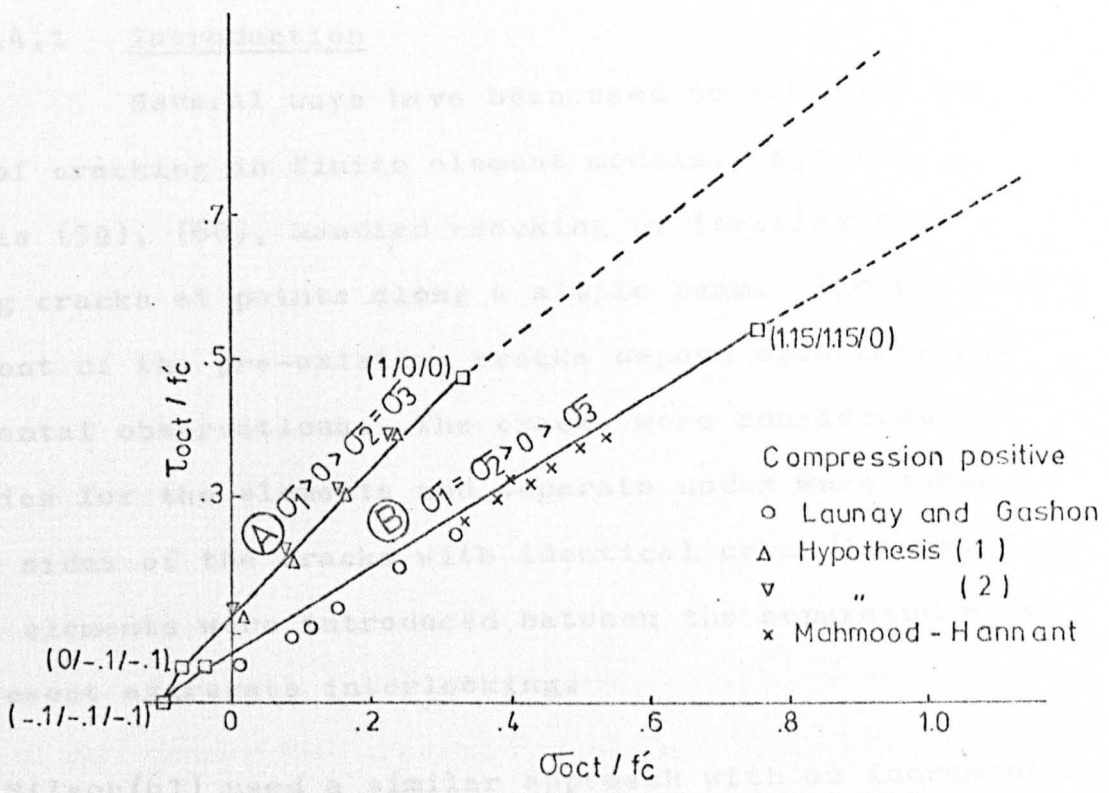


FIG.4.8. COMPARISON OF EXPERIMENTAL RESULTS AND PROPOSED EQUATIONS FOR TENSILE STRESSES

The elements near the crack tip are removed and replaced by twinning the nodal points. This technique is limited because cracks are allowed to form only along the element boundaries.

Leung [63], [64] used a similar method by using different topology in the region around the crack tip. He replaced the cracked element by four elements. And he used

Because these lines agree with the available experimental evidence Fig 4.8, from (48), (54), (55) & (56), the octahedral failure laws are used exclusively in this study to examine the tension-compression stress states and predict the cracking failure of concrete accordingly.

4.4 Crack Simulation

4.4.1 Introduction

Several ways have been used to simulate the effect of cracking in finite element models. Ngo and Scordelis (59), (60), handled cracking by locating pre-existing cracks at points along a simple beam. The position and extent of the pre-existing cracks depend upon previous experimental observations. The cracks were considered as boundaries for the elements and separate nodes were taken on both sides of the cracks with identical co-ordinates. Linkage elements were introduced between the separated nodes to represent aggregate interlocking.

Nilson(61) used a similar approach with an incremental solution of crack propagation. He considered a crack to occur between the edges of two elements if their average stress value exceeded the tensile strength of the concrete. The elements were then disconnected at their boundaries and renumbered by twinning the nodal points. This technique is limited because cracks are allowed to form only along the element boundaries.

Loove (62), (63) used a similar method by using different topology in the region around the crack tip. He replaced the cracked element by four elements, and separate

nodes were redefined on both sides of the crack. These approaches necessitate that cracks must follow element boundaries and for every crack, redefining of the topology and changing the FEM mesh is required. This introduces difficulties and increased costs in the computational process.

Another method used for tackling the cracking problem is by failure criteria. Cracks are initiated at certain points of the element according to specified failure criteria. The material properties are then adjusted in the cracked area by modifying the material matrix. In this way, natural crack directions can be obtained and more than one type of crack pattern can be simulated. The average properties of the cracked region are determined by this method, thus a high accuracy in the crack pattern can only be obtained by using fine meshes. This method seems to be common now among researchers to predict cracking of concrete. Zienkiewicz et al (30) used the maximum tensile strain criterion in a study for pressure vessels. Phillips (40), (42) applied maximum stress or strain criteria and octahedral failure laws in his study. Cervenka (64), (65), Cedolin (66), Cope (67), Buyukozturk (68), Robins (69), Suidan (35) and Mirza (70) did likewise in their studies.

4.4.2 Crack Initiation

In the present study, cracks are predicted by using two failure theories:

- (1) Maximum principal tensile stress criteria, and
- (2) Octahedral shear and normal stress criteria suggested by Cedolin et al (58).

The maximum stress criterion is used to determine cracking in tension zones where the concrete behaviour is linear elastic and local failure occurs by cracking. The basic assumptions of the failure is that when a principal tensile stress exceeds the limiting tensile strength of concrete, the material is assumed to have cracked in a plane normal to the offending principal direction. Thus for cracking:

$$\sigma_i \geq f'_t \quad (4.13)$$

The tensile stress in this principal direction cannot be supported after cracking, so the stress in this direction is reduced to a negligible value as shown in Fig 4.9. However, in a direction parallel to the crack, the material is assumed to be capable of sustaining stresses according to the biaxial stress state existing after cracking.

Further, it is assumed that no interaction occurs between the principal directions. It is possible that new cracks will occur due to the principal tensile stresses in the plane of the initial crack. The new cracks are assumed to be orthogonal to the first crack. So, for further cracking:

$$\sigma'_i \geq f'_t \quad (4.14)$$

The material is assumed homogeneous and isotropic before cracking, but it has orthotropic properties after cracking.

$$\frac{\sigma_{oct}}{f'_c} = 1.07 \frac{\sigma_{oct}}{f'_c} + 0.167 \frac{\sigma_{oct}}{f'_c}$$

$$\frac{\sigma_{oct}}{f'_c} = 0.62 \frac{\sigma_{oct}}{f'_c} + 0.167 \frac{\sigma_{oct}}{f'_c}$$

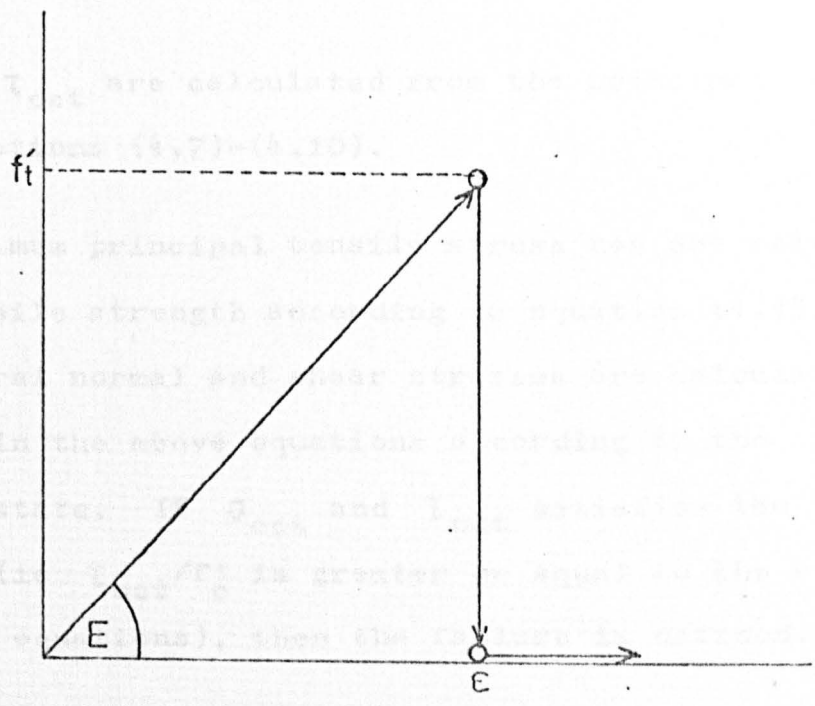


FIG.4.9. TENSILE STRESS- STRAIN RELATIONSHIP AND FRACTURE OF CONCRETE

In biaxial tension-compression stress states (Fig. 4.10) reported that under high tension in compression ratio, the fracture is characterized by a single all-ways fracture orthogonal to the principal tensile stress (Fig. 4.10). However, at lower tension to compression ratios, the fracture pattern takes the shape shown in Fig. 4.10. Johnson and Levy (13) have observed from their tests that the single cleavage fracture occurred when the compression to tension

Fracture in tension-compression zones is predicted by failure laws obtained on the octahedral normal and shear stress plane and which are expressed by the linear relationships given by equations (4.11) as follows:

$$\tau_{\text{oct}}/f'_c = 1.07 \sigma_{\text{oct}}/f'_c + .118 \quad \sigma_1 > \sigma_2 = \sigma_3$$

$$\tau_{\text{oct}}/f'_c = .62 \sigma_{\text{oct}}/f'_c + .068 \quad \sigma_1 = \sigma_2 > \sigma_3$$

where σ_{oct} and τ_{oct} are calculated from the principal stresses according to equations (4.7)-(4.10).

If the maximum principal tensile stress has not reached the limiting tensile strength according to equation (4.13), then the octahedral normal and shear stresses are calculated and substituted in the above equations according to the existing stress state. If σ_{oct} and τ_{oct} satisfies the above equations (ie τ_{oct}/f'_c is greater or equal to the right hand side of the equations), then the failure is defined.

No experimental evidence is available on the pattern of failure in multiaxial tension-compression stress states (2 compressions + 1 tension or 1 compression + 2 tensions). In biaxial tension-compression stress states Newman (44) reported that under high tension to compression ratios, the fracture is characterised by a single cleavage fracture orthogonal to the principal tensile stress (Fig 4.10). However, at lower tension to compression ratios, the fracture pattern takes the shape shown in Fig 4.10. Johnson and Lowe (53) have observed from their tests that the single cleavage fracture occurred when the compression to tension

ratio was less than 10, fracture pattern was similar to that of uniaxial tension. When the ratio was over 10, and an intermediate ratio, the fracture pattern was different from these values.

Lacey and Taylor (11) have noticed that the fracture pattern of concrete under compression is different from that of uniaxial tension. The fracture pattern is different from that of uniaxial tension and can be interpreted as that the failure of concrete under compression is a crushing type of failure.

The above failure pattern is observed in experimental results obtained from uniaxial tension tests, plates or slabs. The failure pattern is different from that of uniaxial tension. Thus their application to the structure is not forward. Realizing this and noting that the failure of concrete under compression is crushing type of failure, the authors have idealized the macroscopic fracture patterns in tension-compression zones.

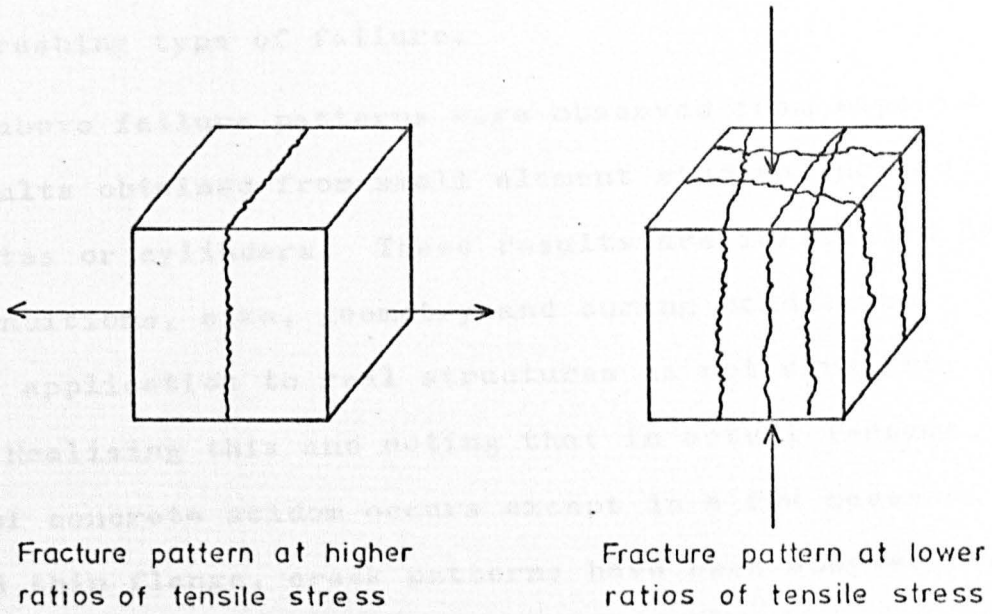


FIG. 4.10. IDEALIZATION OF MACROSCOPIC FRACTURE PATTERNS IN TENSION-COMPRESSION ZONES (After Vile)

4.4, Case 3.

(2) For lower principal tensile or compressive stress, failure, a multiple cleavage crack pattern of the type shown in Table 4.4, Case 3, is observed. These two cases have been adopted after Vile (11) in the finite element model by assuming different crack patterns and comparing the load-deflection curves for beams with the experimental ones. Fig. 4.11 shows load

ratio was less than 11, crushing failure occurred when this ratio was over 25, and an intermediate form of failure between these values.

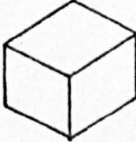
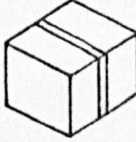
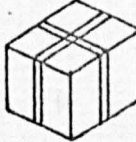
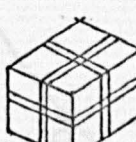
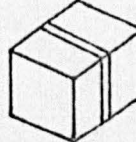
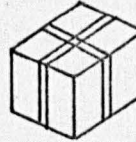
Launay and Gashon (55) have noticed from the tests on 2 compression + 1 tension that the strength of concrete was reduced considerably in this type of stress state. This can be interpreted as that the failure was of the cleavage type of fracture which occurs at lower energy requirement, than that for crushing type of failure.

The above failure patterns were observed from experimental results obtained from small element studies such as cubes, plates or cylinders. These results are influenced by testing conditions, size, geometry and curing conditions. Thus their application to real structures is not straightforward. Realising this and noting that in actual T-beams, crushing of concrete seldom occurs except in a few cases of narrow and thin flange, crack patterns have been adopted for the multiaxial tension compression stress states as follows:

- (1) For high principal tensile to compressive stress ratio, a single cleavage crack is assumed as shown in Table 4.4, Case 5.
- (2) For lower principal tensile to compressive stress ratios, a multiple cleavage crack pattern of the type shown in Table 4.4, Case 6, is assumed.

These two cases have been adopted after several trials in the finite element model by assuming different crack patterns and comparing the load-deflection curves for T-beams with the experimental ones. Fig 4.11 shows load

TABLE 4.4
CRACK PATTERNS

<u>Case No</u>	<u>Crack Pattern</u>	<u>Description</u>
1		Uncracked element
2		Concrete cracked in one direction due to max tensile principal stress (tension zone)
3		Concrete cracked in two directions due to max and intermediate tensile principal stresses
4		Concrete cracked in three directions due to max, intermediate and minimum tensile principal stresses
5		Concrete cracked in one direction due to combined tension-compression stresses
6		Concrete cracked in two directions due to combined tension-compression stresses

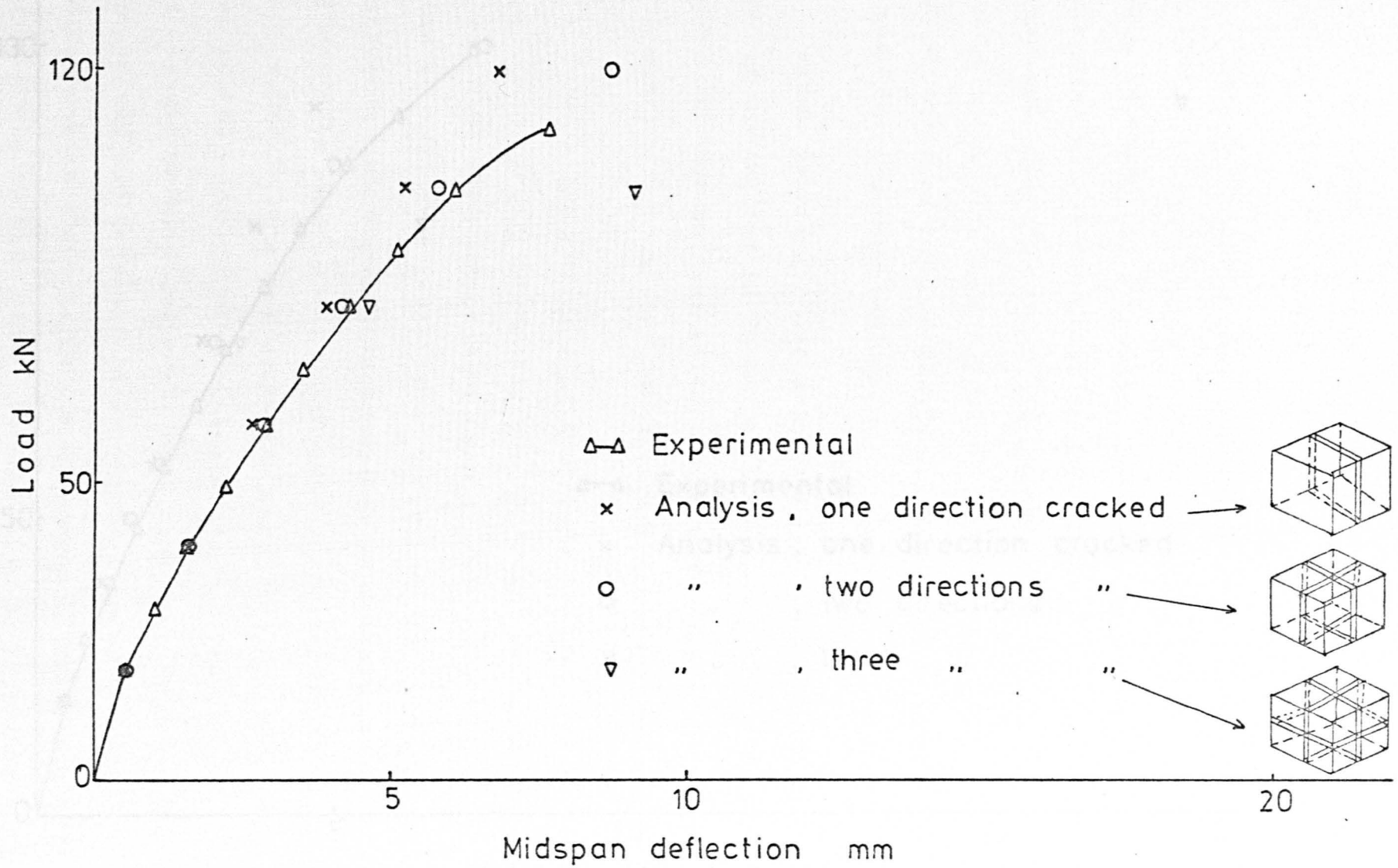


FIG. 4.11. a. LOAD - DEFLECTION CURVE - BEAM TBX - V

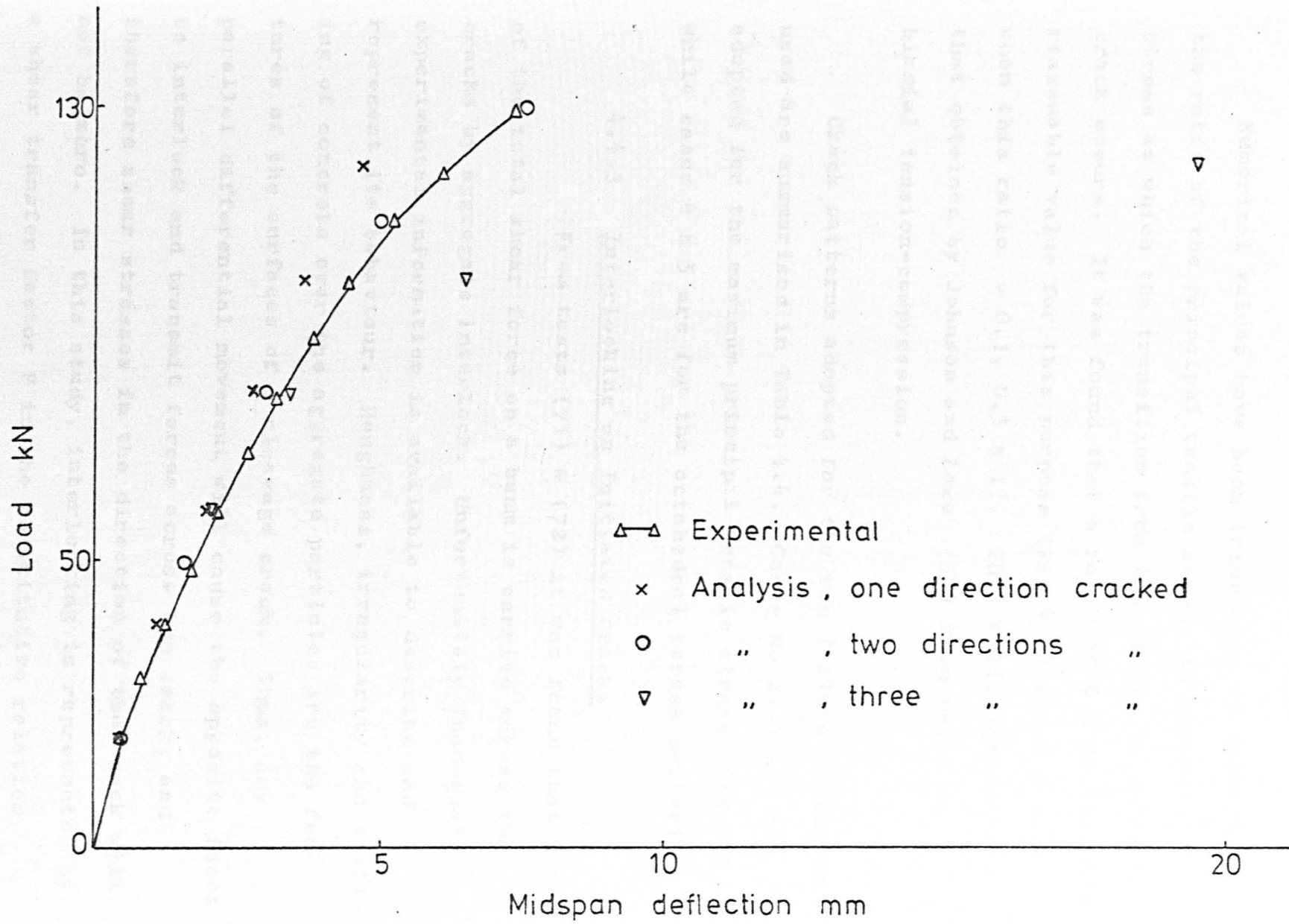


FIG.4.11.b. LOAD - DEFLECTION CURVE - BEAM TBX - VI

deflection curve for beam TBX V where 3 cases of assumed crack patterns are shown.

Numerical values have been tried also to determine the ratio of the principal tensile stress to compressive stress at which the transition from the single to multiple crack occurs. It was found that a ratio of 0.1 is the most reasonable value for this purpose (Fig 4.12 shows 3 cases when this ratio = 0.1, 0.3 & 1). This ratio agrees with that obtained by Johnson and Lowe (53) from tests on biaxial tension-compression.

Crack patterns adopted for the two failure criterion used are summarised in Table 4.4. Cases No 2, 3 & 4 are adopted for the maximum principal tensile stress criteria while cases 4 & 5 are for the octahedral stress criteria.

4.4.3 Interlocking on Initiated Cracks

From tests (71) & (72) it was found that part of the total shear force on a beam is carried across the cracks by aggregate interlock. Unfortunately inadequate experimental information is available to describe and represent its behaviour. Roughness, irregularity and spalling of concrete over the aggregate particles are the features of the surfaces of a cleavage crack. Thus, any parallel differential movement will cause the opposite faces to interlock and transmit forces across the crack, and therefore shear stresses in the direction of the crack will not be zero. In this study, interlocking is represented by a shear transfer factor F in the constitutive relation.

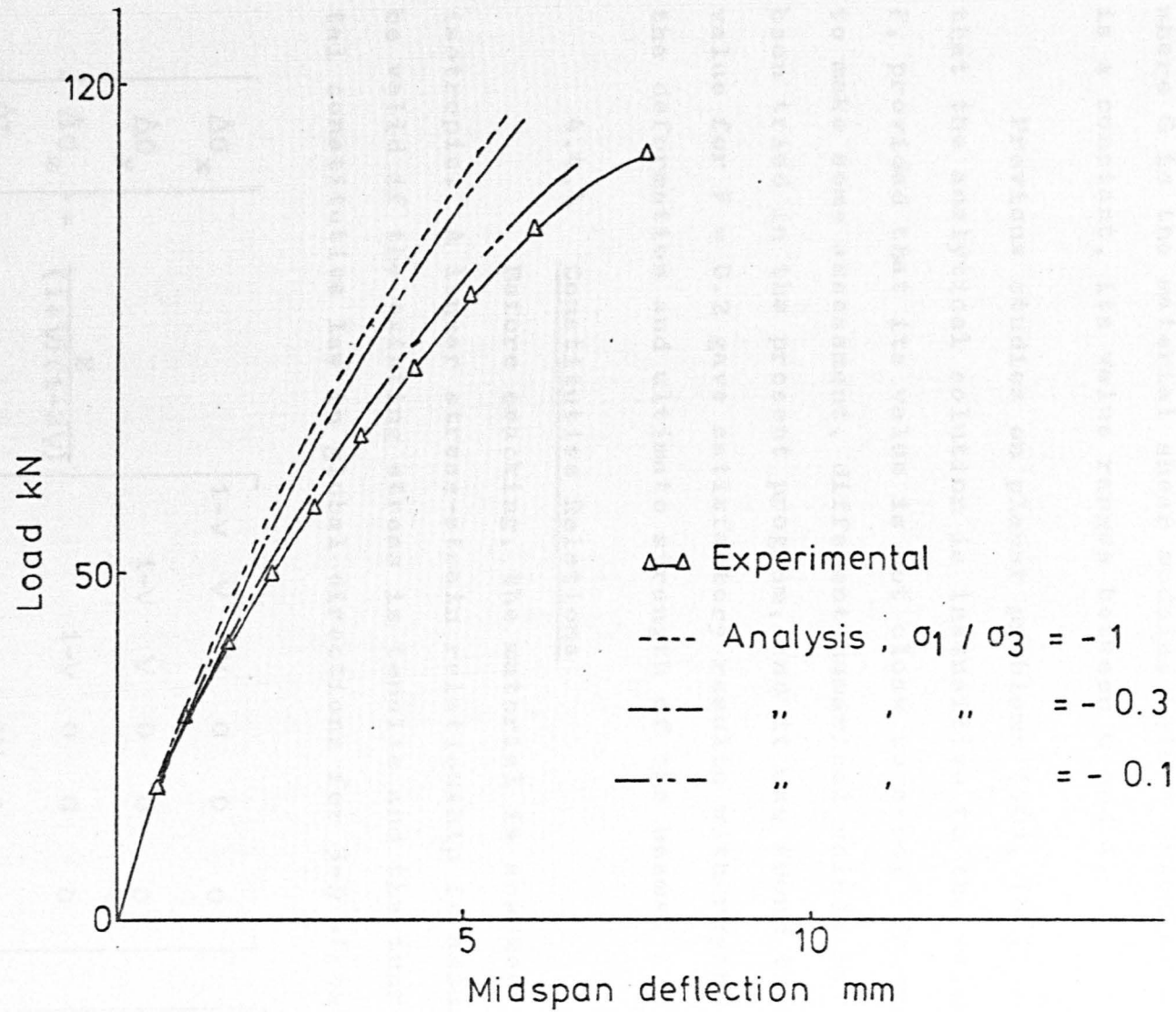


FIG. 4.12. LOAD - DEFLECTION CURVE - BEAM TBX - V

Thus, after cracking:

$$\tau^* = F G \gamma^* \quad (4.15)$$

where G is the material shear modulus before cracking and F is a constant, its value ranges between 0 and 1.

Previous studies on planar problems (40), (66), showed that the analytical solution is insensitive to the value of F , provided that its value is not close to zero. In order to make some assessment, different numerical values have been tried in the present program, and it was found that the value for $F = 0.2$ gave satisfactory results with regard to the deformation and ultimate strength of the beams.

4.4.4 Constitutive Relations

Before cracking, the material is assumed to be isotropic. A linear stress-strain relationship is assumed to be valid if the existing stress is tensile and the incremental constitutive law in global directions for 3-D stress are:

$$\begin{Bmatrix} \Delta\sigma_x \\ \Delta\sigma_y \\ \Delta\sigma_z \\ \Delta\tau_{xy} \\ \Delta\tau_{yz} \\ \Delta\tau_{zx} \end{Bmatrix} = \frac{E}{(1+\nu)(1-2\nu)} \begin{bmatrix} 1-\nu & \nu & \nu & 0 & 0 & 0 \\ & 1-\nu & \nu & 0 & 0 & 0 \\ & & 1-\nu & 0 & 0 & 0 \\ & & & \frac{1-2\nu}{2} & 0 & 0 \\ \text{Symm} & & & & \frac{1-2\nu}{2} & 0 \\ & & & & & \frac{1-2\nu}{2} \end{bmatrix} \begin{Bmatrix} \Delta\epsilon_x \\ \Delta\epsilon_y \\ \Delta\epsilon_z \\ \Delta\gamma_{xy} \\ \Delta\gamma_{yz} \\ \Delta\gamma_{zx} \end{Bmatrix} \quad (4.16)$$

$$\text{or } \{ \Delta\sigma \} = [D] \{ \Delta\epsilon \} \quad (4.17)$$

where E and ν are concrete modulus of elasticity and Poisson ratio respectively, and $[D]$ is the material properties or elasticity matrix.

After cracking, orthotropic conditions are introduced and the material matrix $[D]$ is applicable in the principal stress co-ordinate system. When a single cleavage crack occurs, the principal tensile stress orthogonal to the crack is reduced to zero. The corresponding terms in the material matrix are set to zero, while a shear constant F is included to represent the aggregate interlocking. The material matrix $[D]$ is then modified to:

$$[D]^* = \begin{bmatrix} 0 & 0 & 0 & 0 & 0 & 0 \\ 0 & D_{22} - \frac{D_{12}^2}{D_{11}} & D_{23} - \frac{D_{13}D_{12}}{D_{11}} & 0 & 0 & 0 \\ 0 & D_{32} - \frac{D_{31}D_{21}}{D_{11}} & D_{33} - \frac{D_{13}^2}{D_{11}} & 0 & 0 & 0 \\ 0 & 0 & 0 & F D_{44} & 0 & 0 \\ 0 & 0 & 0 & 0 & D_{55} & 0 \\ 0 & 0 & 0 & 0 & 0 & F D_{66} \end{bmatrix} \quad (4.18)$$

As the constitutive relationships are still linear-elastic after cracking, the material matrix $[D]^*$ represents a sudden change from one elastic state to another. This means that crack propagation is solved by a series of transitions from one instantaneous elastic stiffness to another. If no further cracking occurs during the cycling in which stiffnesses are updated, then convergence in displacements

would result immediately.

If multicreavage cracking occurs in two perpendicular directions, or a second cleavage crack forms orthogonal to the first crack, then the terms of $[D]$ corresponding to these two principal tensile stresses are set to zero and $[D]^*$ takes the form:

$$[D]^* = \begin{bmatrix} 0 & 0 & 0 & 0 & 0 & 0 \\ 0 & 0 & 0 & 0 & 0 & 0 \\ 0 & 0 & D_{33} & 0 & 0 & 0 \\ 0 & 0 & 0 & FD_{44} & 0 & 0 \\ 0 & 0 & 0 & 0 & FD_{55} & 0 \\ 0 & 0 & 0 & 0 & 0 & FD_{66} \end{bmatrix} \quad (4.19)$$

The zero values on the diagonals cause difficulties in the numerical solutions, thus the corresponding diagonal term is set to a small positive value.

The material matrix $[D]^*$ is in co-ordinate directions coincident with the angle of the crack, therefore it is essential to transform it back to the original global reference system for stiffness calculations.

The constitutive relationship in the global system is given by

$$\{\Delta\sigma\} = [D] \{\Delta\epsilon\} \quad (4.20)$$

and in the crack direction by

$$\{ \Delta \sigma \}^* = [D]^* \{ \Delta \epsilon \}^* \quad (4.21)$$

By applying the transformation rule, the strains can be expressed as:

$$\{ \Delta \epsilon \}^* = [T] \{ \Delta \epsilon \} \quad (4.22)$$

and [T] is defined by

$$[T] = \begin{bmatrix} a_{11}^2 & a_{12}^2 & a_{13}^2 & a_{11}a_{12} & a_{12}a_{13} & a_{11}a_{13} \\ a_{21}^2 & a_{22}^2 & a_{23}^2 & a_{21}a_{22} & a_{22}a_{23} & a_{21}a_{23} \\ a_{31}^2 & a_{32}^2 & a_{33}^2 & a_{31}a_{32} & a_{32}a_{33} & a_{31}a_{33} \\ 2a_{11}a_{21} & 2a_{12}a_{22} & 2a_{13}a_{23} & a_{11}a_{22} + a_{12}a_{21} & a_{12}a_{23} + a_{13}a_{22} & a_{11}a_{23} + a_{13}a_{21} \\ 2a_{21}a_{31} & 2a_{22}a_{32} & 2a_{23}a_{33} & a_{21}a_{32} + a_{22}a_{31} & a_{22}a_{33} + a_{23}a_{32} & a_{21}a_{33} + a_{23}a_{31} \\ 2a_{11}a_{31} & 2a_{12}a_{32} & 2a_{13}a_{33} & a_{11}a_{32} + a_{12}a_{31} & a_{12}a_{33} + a_{13}a_{32} & a_{11}a_{33} + a_{13}a_{31} \end{bmatrix} \quad (4.23)$$

where a_{ij} are the terms from the normalised modal matrix [A], (73)

where

$$[A] = \begin{bmatrix} a_{11} & a_{12} & a_{13} \\ a_{21} & a_{22} & a_{23} \\ a_{31} & a_{32} & a_{33} \end{bmatrix} \quad (4.24)$$

This matrix defines the direction cosines of the principal stress axes from the reference axes. A method for calculating matrix [A] is given in Appendix A.

Assuming that work done is independent of the co-ordinate system, then

$$\{ \Delta \epsilon \}^{*T} \{ \Delta \sigma \}^* = \{ \Delta \epsilon \}^T \{ \Delta \sigma \} \quad (4.25)$$

and substituting equations (4.20), (4.21) & (4.22) into equation (4.25) gives

$$[D] = [T]^T [D]^* [T] \quad (4.26)$$

4.5 Steel Behaviour

Steel reinforcement is usually used with concrete in the form of slender bars which can be assumed to be stressed only uniaxially.

The uniaxial stress-strain curve for different types of reinforcement steel are well known. A typical uniaxial stress-strain curve for high tensile steel is shown in Fig 4.13. The curve is linear elastic until the point 'P' called the 'proportional limit' is reached. After this point, increase in stress increases the strain but not in a linear relationship. The yield point known for normal types of steel is not well defined for this type. Thus, it is usually taken at fixed value of strain such as .002 and the stress is defined as 'proof stress'. After this the strain increases rapidly with small increases in stress and the material is defined to possess strain hardening. This continues until a maximum stress is reached 'V' and fracture occurs at point 'F' after a descending part on the curve.

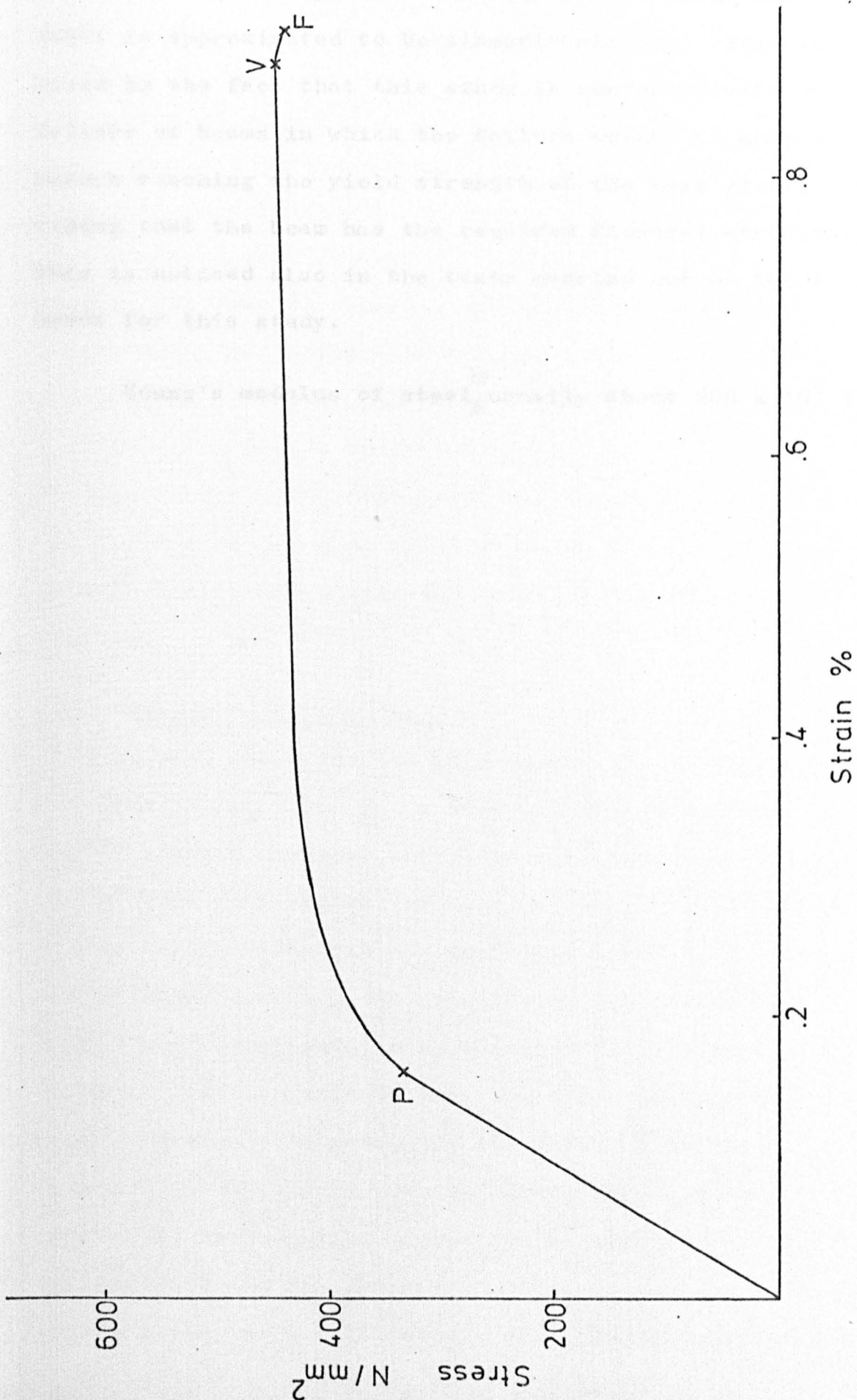


FIG. 4.13. TYPICAL STRESS - STRAIN CURVE FOR COLD - WORKED STEEL

For this study, the behaviour of the longitudinal steel is approximated to be linearly elastic. This is based on the fact that this study is concerned with shear failure of beams in which the failure occurs in most cases before reaching the yield strength of the main steel, providing that the beam has the required flexural strength. This is noticed also in the tests carried out on the T-beams for this study.

Young's modulus of steel^{is} usually about $200 \times 10^3 \text{ N/mm}^2$.

3.4 - Structure of the Program

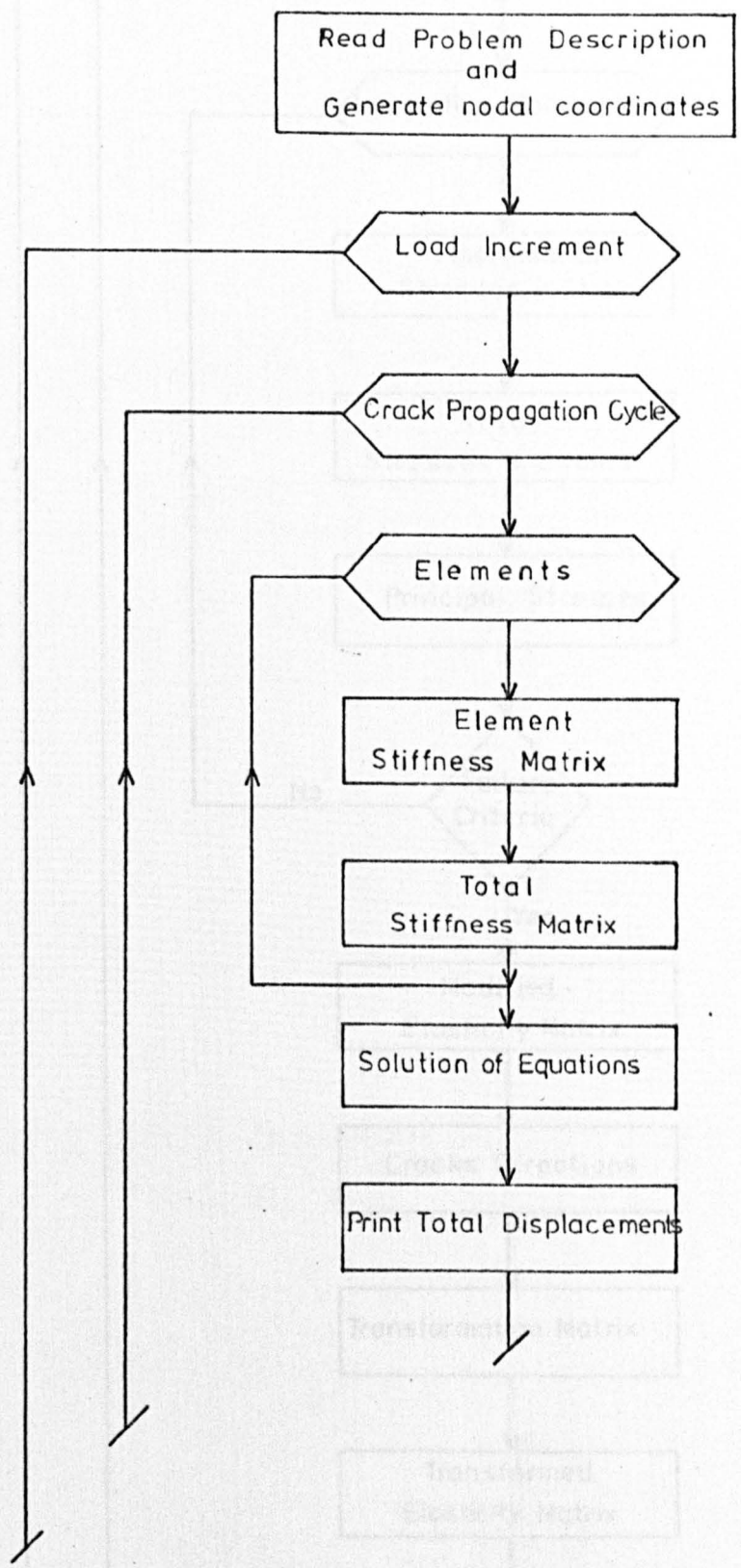
A flow chart for the main operations of the program is shown in Fig 3.1. In a finite element analysis there are four main operations that must follow in a logical sequence. These are (1) the formation of the stiffness matrix and incident load vectors for the entire structure, (2) the solution of the simultaneous load-displacement equations, (3) the application of the obtained displacements in the structure to determine internal stresses, and (4) checking the obtained stresses with the given failure law and making the necessary modifications in the material properties accordingly. The latter operation is the key for any non-linear analysis as it controls the incremental scheme and brings the finite element

5.1 Introduction

The main features of the computer program written and developed for this study are described in some detail in this chapter. The program is designed to handle the in-elastic incremental analysis of reinforced concrete T-beams using the finite element three dimensional stress analysis described in the foregoing chapters. The program consists of a series of computer segments written in Fortran IV for ICL 1906S computer. The main algorithm of the program in the form of flow charts and the consequence of computation process in each part is presented in this chapter.

5.2 Structure of the Program

A flow chart for the main operations in the program is shown in Fig 5.1. In a step-by-step non-linear finite element analysis there are four basic operations that must follow in a logical sequence. These are (1) the assembly of the stiffness matrix and increment load vector for the entire structure, (2) the solution of the incremental load-displacement equations, (3) the application of the obtained displacements to the elements to determine incremental internal stresses, and (4) checking the total stresses with the given failure law and making the necessary modifications in the material properties accordingly. The last operation is the key for any non-linear solution as it controls the incremental scheme and brings the final failure



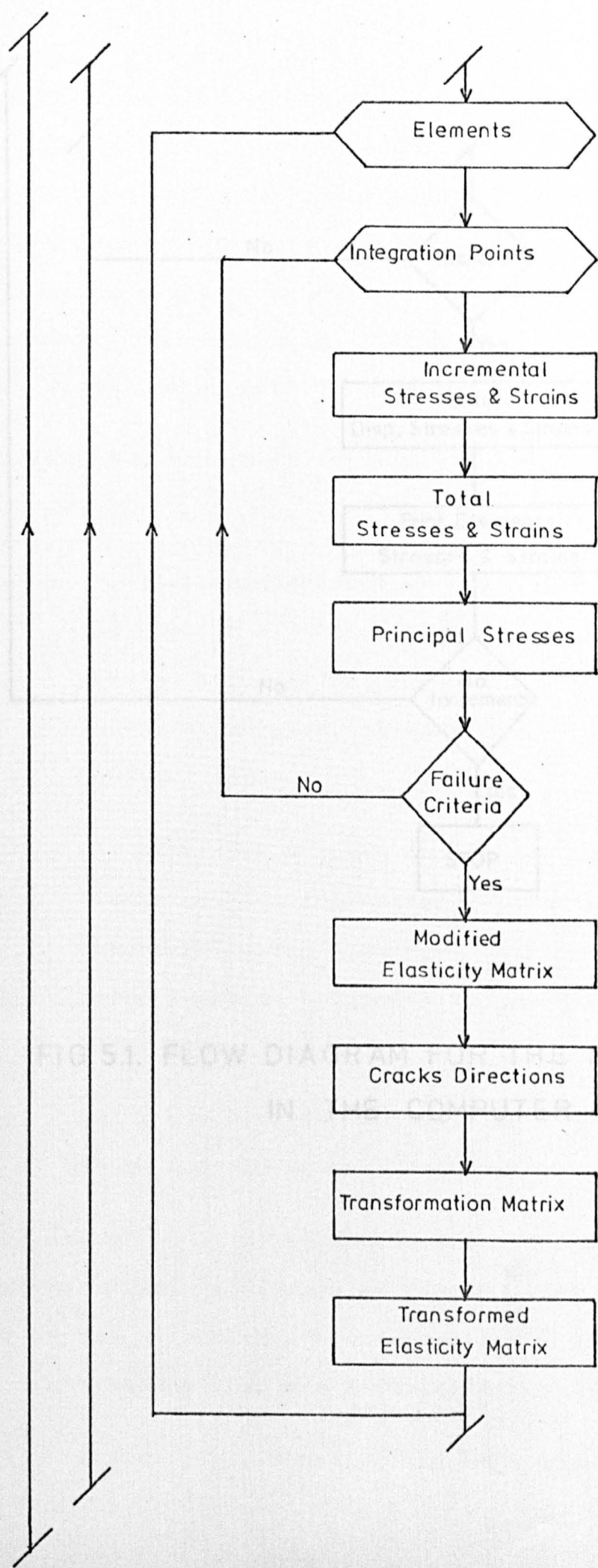


FIG. 5.1. FLOW DIAGRAM OF MAIN OPERATION IN THE COMPUTER PROGRAM

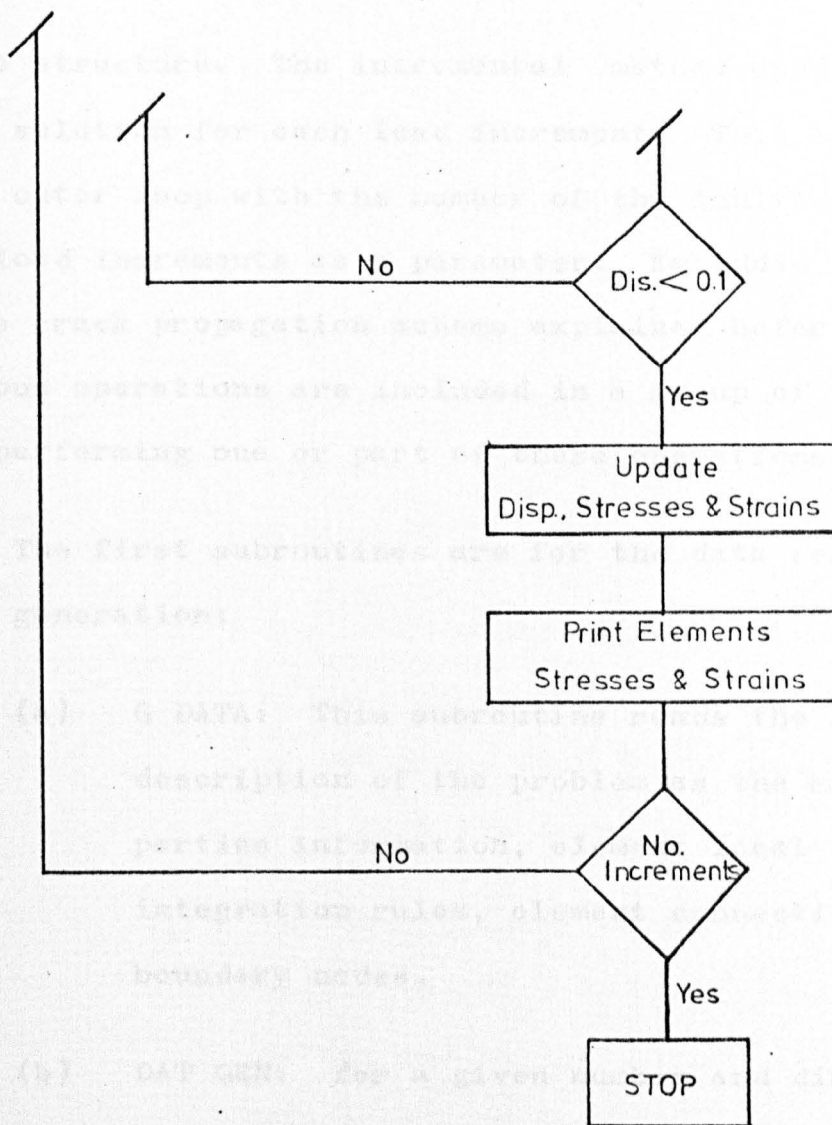


FIG. 5.1. FLOW DIAGRAM FOR THE MAIN OPERATIONS
IN THE COMPUTER PROGRAM

of the structure. The incremental method used repeats the whole solution for each load increment. This is characterised by an outer loop with the number of the individually specified load increments as a parameter. Embedded in this loop is the crack propagation scheme explained before. The previous operations are included in a group of subroutines, each performing one or part of these operations.

I The first subroutines are for the data readings and generation:

- (a) G DATA: This subroutine reads the general description of the problem as the material properties information, element local co-ordinates, integration rules, element connections and boundary nodes.
- (b) DAT GEN: for a given number and dimension of elements, this subroutine generates the X, Y & Z co-ordinates for each node in the mesh. Then it keeps these co-ordinates in dimensions block for later use.
- (c) LOAD: To read incremental load value and store it in one dimensional load vector.

II The second group of subroutines are for the evaluation of the elastic stiffness matrix for each element, then to transfer it/the assembled subroutine for the whole stiffness matrix. Five subroutines are incorporated in this block.

- (a) ELSTG: This contains the main loop for the

integration rule. At each integration point the following steps are performed:

- (1) In the first load increment, the initial material properties matrix is assembled from the elastic material constants given in the input data. In the subsequent increments it takes the previous modified matrix if it exists.
 - (2) The coefficients of the strain matrix are calculated by calling subroutines SFRI, JACOBIAN and FORM B and these are written on a tape for later use.
 - (3) The coefficients of the stress matrix are calculated from the material properties matrix and the strain matrix and are written on a tape for later use.
 - (4) Stiffnesses of the upper half of the element stiffness matrix are evaluated from the stress matrix, strain matrix, weighing integration coefficients and the determinant of the Jacobian matrix. The lower half is then filled by symmetry.
 - (5) The stiffnesses from each integration point are summed to give the element stiffness matrix.
- (b) SFRI: In this subroutine the parabolic shape

functions and its first derivatives are computed for the corner and midside nodes. Then it is stored in dimensions block.

- (c) JACOBIAN: Three operations are done in this subroutine: (1) The 3×3 Jacobian matrix is evaluated from the first derivatives of the shape functions and X, Y, Z nodal co-ordinates. (2) The determinant of this matrix is calculated. If this value is negative or very small, the program will terminate and send an error message. This indicates there is an error in the element connection data, the Cartesian co-ordinates or in the previous operations. (3) The inverse of the Jacobian matrix is formulated. This is used to evaluate the strain matrix.
- (d) FORM B: Terms of the strain matrix are calculated from the inverse of the Jacobian matrix and the first derivatives of the shape functions. Then these terms are arranged in the 6×60 strain matrix and written on a tape for later use.
- (e) STELEM: This subroutine evaluates the two or three node bar element. It enters the integration loop then it picks the appropriate shape functions, calculates the strain vector, the stress vector and writes them on a tape for later use. The bar stiffnesses are calculated from the contribution of stiffnesses at each integration point.

III The third group are for assemblage and solution. This has been done in the following routines:

- (a) FORM K: Assembles the total stiffness matrix for the structure. After every element stiffness matrix is evaluated, the individual coefficients are transferred into the total stiffness matrix node-by-node. The three equations associated with the given node are used from the proper storage location and the contribution of the current element are superimposed to the present values. The concrete stiffnesses are stored in a banded rectangular matrix form, then steel stiffnesses are added to it. Boundary conditions are inserted also after completing the assemblage. Each degree of freedom is examined and if it is restrained then a unity is inserted on the diagonal and zeros on the corresponding rows and columns.
- (b) SOLVE: The total load-displacement equations are solved using the direct elimination technique, resulting in a displacement vector. Practically, the routine solves, for any number of equations, bandwidth or load vectors, but with increasing bandwidth and number of unknowns, the solution time increases.

IV The final group is the subroutines for stresses, failure laws and updating stresses at the end of each load increment.

- (a) **STRESS:** The stresses and strains are calculated element-by-element at the incremental load level then it is added to the previous ones to obtain the total stresses or strains. The stress and strain matrices evaluated at the individual integration points, previously used during the calculation of the element stiffness matrix are re-read from tapes and used for the present evaluations of stresses and strains. The principal stresses are calculated at the 8 integration points of each element from the total stresses obtained at the load level considered.
- (b) **FCRITERIA:** The principal stresses are checked with the failure laws for concrete as described before at each individual sampling point of each element. According to the type of crack occurred, the program is directed to the appropriate stream to pick the corresponding factors required to modify the elasticity matrix. Terms from the previous elasticity matrix are re-arranged in a new 6 x 6 matrix after performing the necessary modifications on it. This matrix now is in the directions of the principal stresses and it has to be transformed into the global directions. The direction cosines of the principal stresses relative to the Cartesian directions are calculated and stored in a 5-dimensional array $-(3 \times 3 \times 8 \times 35 \times 2)$. Coefficients of the 6 x 6 transformation matrix are then arranged from the terms

of the direction cosines matrix. Transformation of the modified elasticity matrix is then performed using this transformed matrix and its transpose and the resulting terms are stored in a new 5-dimensional modulus matrix (6x6x8x35x2) to use in the next cycle or increment.

- (c) UPDAT: This is the last step, at the end of each load increment, the stresses, strains and direction cosines matrices are transferred and kept in a similar dimensions blocks, so it can be easily picked and used by the program in the following load increment.

5.3 Output of the Program

The displacements, stresses and cracked points for the structure are the most important results of any inelastic stress analysis. Accordingly, displacements at all nodes, principal stresses at each individual integration point and cracked points with the crack directions reference to X, Y, Z axis, are printed out after each cycle. The six components of stresses at the eight integration points are printed, also on the elemental level at the end of each load stage.

5.4 Concluding Remarks

The development of a three-dimensional stress analysis computer program to include non-linear conditions and failure laws is a lengthy and complex task. The difficulties arise in such programs with increasing the core-store and computation

time. In any finite element analysis program, and particularly for three dimensional stress systems, the core-store increases considerably due to: (1) the use of dimensions blocks with more than 2-dimensions in the process of modifying the material properties, (2) the augmentation of the number of unknowns and bandwidth of the total stiffness matrix of the structure. The dimension blocks used in the material modifications are minimised to the lowest level as a replacement system was used. The number of unknowns and bandwidth were limited by using a reasonable number of elements in the meshes. The computation time increases according to the number of increments and cycles performed in each increment. In each cycle a complete reformulation of element stiffness and solution of system of equations is performed. Most of the time was consumed in the stiffnesses calculations due to multiplications of large matrices. The method used in the program to multiply two matrices, for example, is to save the rows of the first matrix in a separate array, then multiply it by the columns of the second matrix to obtain the terms of the new matrix. This method saved time ^{compared} to the traditional way of multiplying matrices.

EXPERIMENTAL PROGRAMME

6.1 Introduction

In recent years research workers have shown growing interest to tackle the problem of shear failures in T-beams. The tests that have been conducted until now are not sufficient to give a clear understanding of the basic behaviour, failure mechanism or the way that the shear is resisted in such beams.

Experimental data (7), (8), (11) & (20) show that the ultimate shear force resisted by a T-beam is much higher than that of a comparable rectangular beam. Although it is believed now that the shear force is carried through aggregate interlock, dowel forces and concrete in the compression zone, there is little experimental information on the contribution of each shear component. Experimental investigations and shear theories on T-beams agree that the main part of the shear force is resisted by shear stresses in the uncracked concrete of the compression zone. Thus the assessment of the shear force carried by the compression zone in a T-beam is essential. Therefore this programme of work has been planned to conduct tests on large scale reinforced concrete T-beams to measure the shear force carried by the compression zone. This would need the elimination of the shear carried through aggregate interlock and dowel action. To achieve this, an inclined preformed crack within the web of the shear span has been used.

Two series of tests have been carried out. The first series was designed to study the effect on shear behaviour of the location of the preformed crack in the shear span. The second series was planned to assess the shear contribution of the flange. The main parameters to be studied in the second series are the flange width and thickness. The ratio of the area of steel in each beam to the area of steel required for the balanced section was kept constant at 0.3, as it gives reasonable amount of longitudinal reinforcement. A concrete mix design was carried out and the same mix was then used in all the beams to give a cube strength of about 35 N/mm^2 . The shear span to depth ratio was taken as 4.0 for all the beams.

The results from these tests are used in the next chapter for comparison with the analytical stress computations.

6.2 Properties of Materials

6.2.1 Concrete Mix Design

6.2.1.1 Introduction

A trial mix design was carried out to give an early strength suitable for the RC test members. Recently Pulverised Fly-Ash (PFA) has been incorporated in concrete as a fine material to obtain economic and strength advantages. In practice, PFA has been used in concrete in different ways, eg as a cement replacement, as an admixture, or as a replacement for sand.

Smith (74) considered the concrete containing fly-ash as a new type of concrete and designed accordingly. Jackson and Goodridge (75) achieved good early strength by combining

both sand and cement replacement. They found that in order to obtain both economic and strength advantages using PFA, it was best to replace up to 20% of the cement by weight and incorporate the rest of the PFA by volume replacement of sand.

The aim of this mix design was to obtain a fly-ash concrete mix to give the required early strength (cube strength) of about 35 N/mm^2 at 28 days, together with good flexural strength and degree of workability (slump between 50-75 mm).

6.2.1.2 Materials

6.2.1.2.1 Aggregates

The coarse aggregate used was 10 mm irregular gravel. The fine aggregate was washed and dried river sand. The percentages passing through the various BS sieves for both the sand and coarse aggregate are shown in Table 6.1.

The sieve analysis for sand indicates that it is a medium sand of zone 2, according to BS 882 (76).

The ratio of sand to gravel in all mixes was taken 1:1.33 according to grading curve 2 of Road Note No 4 (77).

6.2.1.2.2 Cement

Ordinary Portland cement considered to comply with BS 12 (78), was used throughout the experimental programme.

Table 6.1

Sieve Analysis of Available Aggregate

<u>BS Sieve Size</u>	<u>% Passing</u>
<u>¾" Coarse Aggregate</u>	
¾"	88
½"	25
3/16"	6.5
<u>Sand</u>	
3/16"	98.1
No. 7	82.4
No 14	66.6
No 25	51.5
No 52	31.4
No 100	1.6

6.2.1.2.3 P F A

The fly-ash used was produced by the Ferrybridge Power Station. The typical composition and sieve analysis given by the supplier is shown in Table 6.2, and was considered to comply with BS 3892 (79).

6.2.1.3 Mix Design Procedure

In the design of this mix, the intention was to replace both cement and sand by PFA. The replacement of cement was by weight and for sand by volume. The PFA/sand volume replacement factor and the PFA/cement ratio can be determined experimentally according to the materials used. The procedure used in the replacement was similar to that of Jackson and Goodridge (75).

The PFA/sand volume replacement factor can be selected as a reasonable value, normally between 0.4 to 0.6. As a guide in choosing this factor, a small mix consisting of aggregates and cement in any desired proportions is first made and the volume determined. A similar mix composed of the same materials in the same weight proportions but with only half the amount of the sand is then made and sufficient PFA is then added to yield the same volume as the PFA free mix. The PFA/sand volume replacement factor =

$$= \frac{\text{weight of PFA added}}{\text{weight of sand replaced}}$$

Table 6.2

Specifications of Fly-Ash Used

<u>Chemical Analysis</u>			
%	Silica	as SiO_2	50.5
%	Alumina	as Al_2O_3	26.9
%	Iron	as Fe_2O_4	9.6
%	Titenum	as TiO_2	0.9
%	Phosphorous	as P_2O_5	0.3
%	Calcium	as CaO	2.0
%	Magnesium	as MgO	1.1
%	Sodium	as Na_2O	2.4
%	Potassium	as K_2O	3.5
%	Sulphur	as SO_3	0.53
	Loss on Ignition		1.8

Sieve Analysis

BS Sieve	% Passing
No 52	99.98
100	96.90
200	80.34
300	74.34
Specific Surface	3990 cm^2/g
Density	2.17 gm/cm^2

To determine the PFA mix proportions the following steps can be followed:

- (1) A basic mix with suitable proportions by weight of cement and aggregates should be evaluated first.
- (2) The PFA/cement ratio ranges between 0.4 and 0.8, so a value should be chosen within this range for each mix.

It was suggested that the amount of cement to be replaced by weight should be up to 20%. So choosing a percentage for cement replacement, the amount of cement to be replaced and that remaining in the mix can be determined. Then the amount of PFA can be calculated using PFA/cement ratio. The balance of PFA replacing sand by volume can then be determined using PFA/sand volume replacement factor determined earlier.

- (3) The new mix proportions by weight can then be evaluated using the determined amounts of cement, PFA, sand, aggregate and water content.

Several PFA mixes should be made in which PFA/cement ratio and PFA/sand volume factor are varied, then the required ratios are those giving the highest early strength.

For this study, the amount of cement replaced by weight was between 10% and 20%. The PFA/sand volume replacement factors were chosen to be between 0.4 to 0.6. The total PFA/cement ratio was between 0.4 to 0.6. The basic mixes were designed according to Road Note No 4 (77).

Six trial mixes were carried out. The amount of cement replaced and the different factors of replacement

used in the mixes are summarised in Table 6.3.

The final proportions of the mixes and the weight of material per cubic metre for each mix are shown in Table 6.4.

6.2.1.4 Mixing and Casting

The mixing of the concrete was carried out in a horizontal type pan mixer with a capacity of 0.1 m^3 . The aggregate, cement and PFA were first mixed dry for one minute, then the water was added and mixed for another two minutes. The concrete was then poured into the moulds in two layers and compacted by a 25 mm dia vibrator. The moulds were covered with polythene sheeting and demoulded after one day. The specimens were then left under polythene sheets under internal uncontrolled temperature and humidity conditions until the day of testing.

6.2.1.5 Tests and Size of Test Specimens

For each mix the following tests were carried out:

- (1) The slump and VB test for fresh concrete.
- (2) Cube and flexure strength at 1, 3, 7 and 28 days.
- (3) Shrinkage strains up to 28 days.

Twelve cubes 100 mm size were used to measure the cube strength (3 cubes were tested at each age), while 8 prisms of size 100 mm x 100 mm x 500 mm were used for the flexural strengths (2 at each age). Two of these were instrumented

Table 6.3

Replacement Factors for PFA

<u>Mix No</u>	<u>Amount of Cement Replaced by Weight</u>	<u>PFA/Cement Ratio</u>	<u>PFA/Sand Volume Replacement Factor</u>
I	20%	0.6	0.6
II	10%	0.4	0.6
III	10%	0.4	0.6
IV	20%	0.6	0.6
V	10%	0.4	0.4
VI	10%	0.4	0.4

Table 6.4 Proportions of the Mixes and Weight of Material per Cubic Metre

Mix No	Basic Mix				Wt of Cem per cubic m Kg	Mix with PFA					Wt per Cubic m				
	C	S	G	W		C	PFA	S	G	W	(C+PFA)/Aggregate	W/(C+PFA)	Cement	PFA	Water
													Kg	Kg	Kg
I	1	2.15	2.85	0.53	352	1	0.6	2.1	3.55	0.65	1/3.6	0.405	285	171	185
II	1	2.6	3.4	0.61	300	1	0.4	2.4	3.8	0.7	1/4.5	0.50	272	109	190
III	1	2.6	3.4	0.61	300	1	0.4	2.4	3.8	0.72	1/4.5	0.515	270	108	194
IV	1	2.6	3.4	0.61	300	1	0.6	2.66	4.25	0.76	1/4.3	0.475	243	166	185
V	1	2.6	3.8	0.66	270	1	0.4	2.4	4.2	0.74	1/4.72	0.525	257.5	103	190.5
VI	1	2.8	3.6	0.66	277	1	0.4	2.4	4.0	0.74	1/4.58	0.515	263.5	105.5	195

by Demec discs to measure the shrinkage strains.

All the strength tests were carried out in a compression test machine supplied with frames for compression and flexural testing, and with a digital control console with a display unit for test results. The flexural and compression tests were carried out according to BS 188 (80).

6.2.1.6 Discussion of Results

Tables 6.5, 6.6 and Figs 6.1-6.3 summarise the results from the six mixes. Adequate workability and compaction of concrete are the most important properties for fresh concrete. The slump and VB tests were used to measure the characteristics of the fresh concrete. From table 6.4 it can be seen that mix III gave the highest slump, but this mix was bleeding after casting. Mixes I and IV gave lower slump and higher VB values, and it was noticed that they were less workable and needed more time in compaction. Mixes V and VI have the same degree of workability. From Table 6.5 and Figs 6.1 and 6.2 it can be seen that the cube and flexural strengths increase with decrease of $w/(c + PFA)$ ratio and $(c + PFA)/Aggregate$ ratio. Fig 6.3 shows the rapid increase in strength in the early days. Mix I gave higher cube strength than required. The increase in water percentage in mixes II, III and IV decreased the cube strength and improved the flexural strength, but the cube strength was slightly higher than required. The cube strength in mix V was lower due to the increase of water content and the aggregate ratios. This mix gave higher flexural strength at 1, 3 and 7 days as more sand was replaced by PFA. Mix VI

Table 6.5

Slump and VB for the Mixes

Mix No	I	II	III	IV	V	VI
Slump mm	37	56	68	43	62	62
V B Sec	4.5	3.5	3	4	3	3

Table 6.6 Compressive and Flexural Strength

Mix No	Compressive & Flexural Strength of PFA Mixes N/mm ²												Shrinkage Micro-Strain (28 Days)
	1 Day			3 Days			7 Days			28 Days			
	Comp	Flex	Flex/Comp	Comp	Flex	Flex/Comp	Comp	Flex	Flex/Comp	Comp	Flex	Flex/Comp	
I	12.3	1.56	.127	26.3	2.78	.105	38.1	3.36	.08	49	5.3	.108	291
II	10.6	1.15	.11	23.1	2.51	.109	29.7	2.88	.97	38.7	4.2	.109	292
III	9.8	1.3	.133	21.7	3.5	.161	30.9	3.44	.111	37.2	4.72	.127	292
IV	10.3	1.5	.14	20.7	3.6	.174	30.9	2.72	.88	37.2	4.64	.125	290
V	8.5	1.55	.182	18.1	3.4	.187	26.9	3.76	.14	33.8	4.22	.125	267
VI	10.2	1.4	.137	20.3	3.4	.168	27.9	3.66	.131	35.8	4.7	.131	293

- 108 -

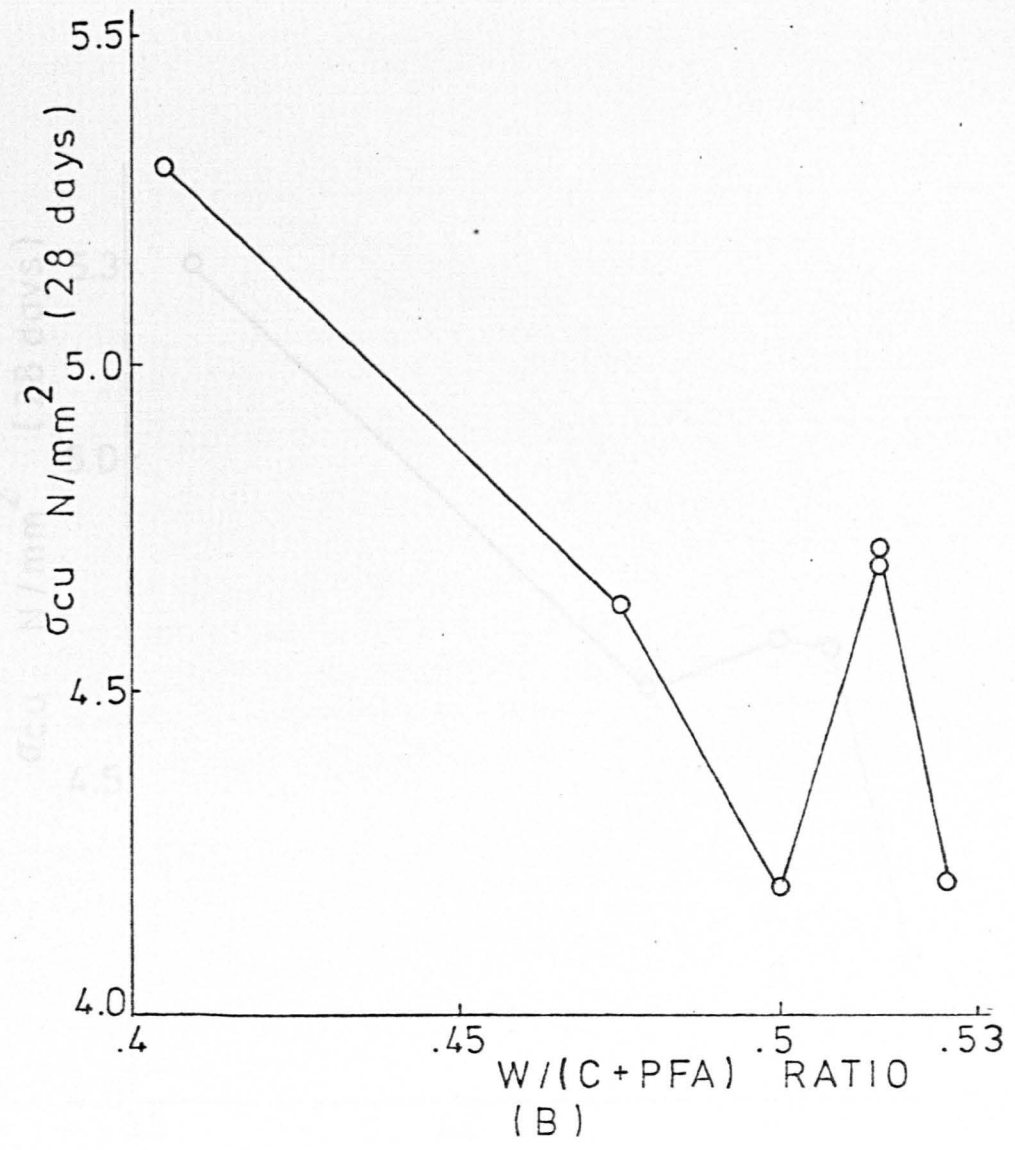
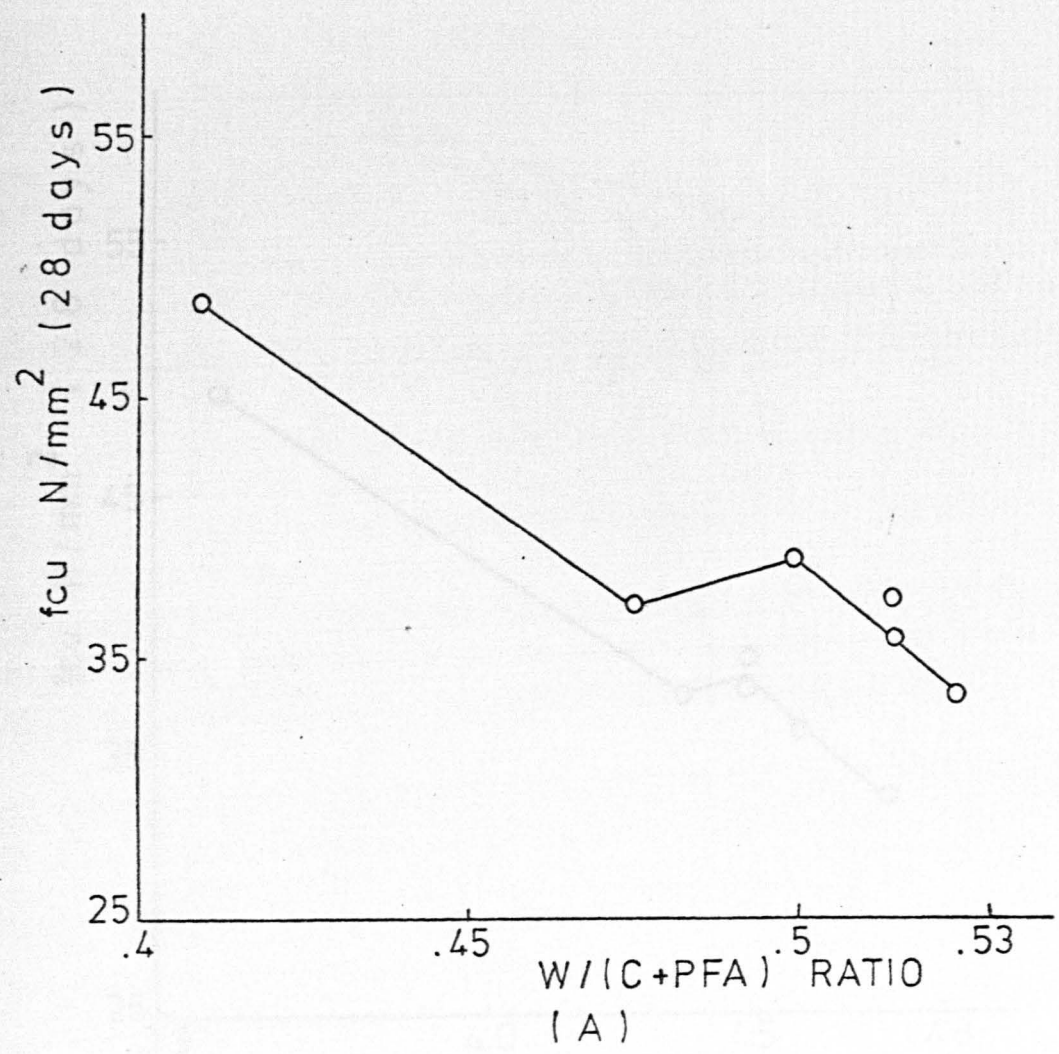


FIG. 6.1. INFLUENCE OF WATER/FINE MATERIAL RATIO ON CUBE AND FLEXURE STRENGTH

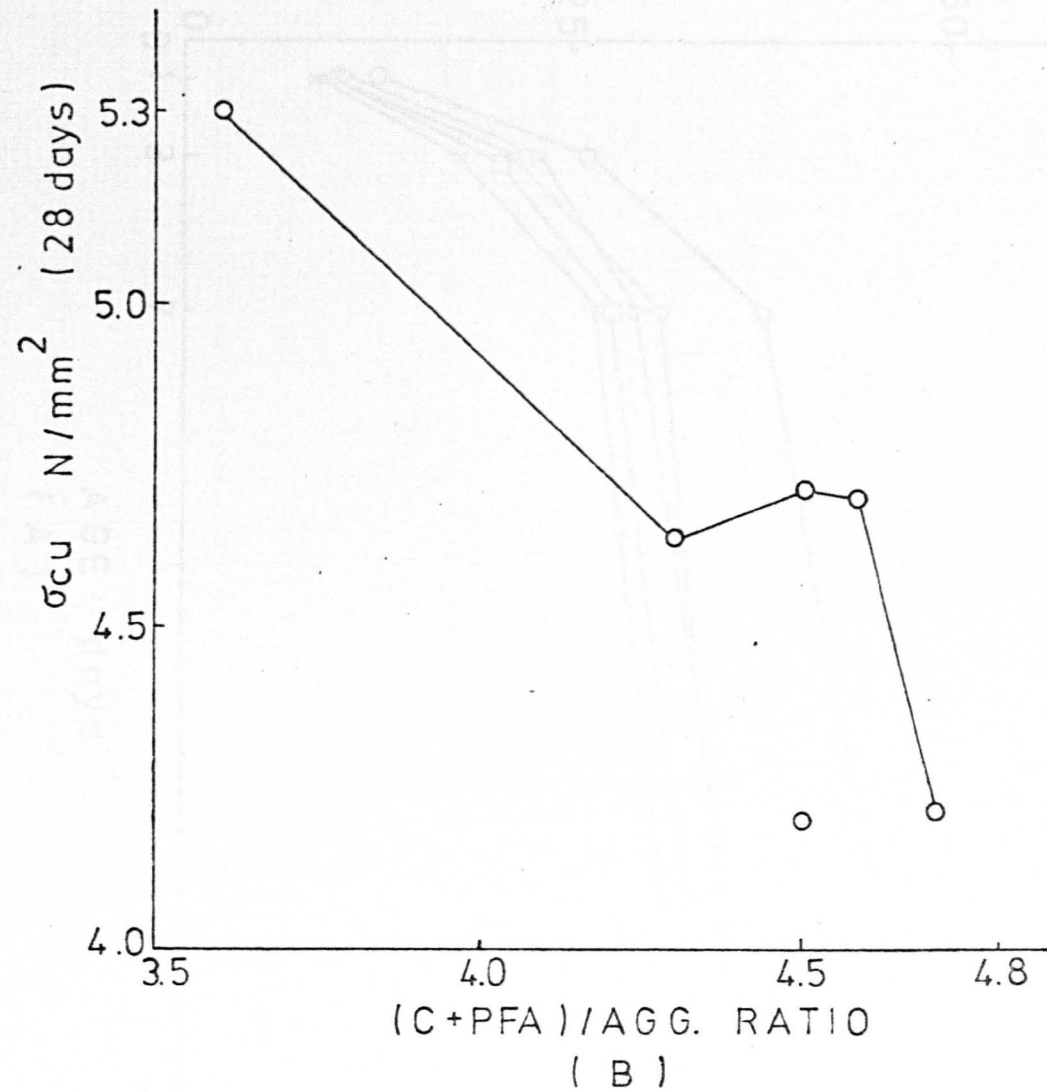
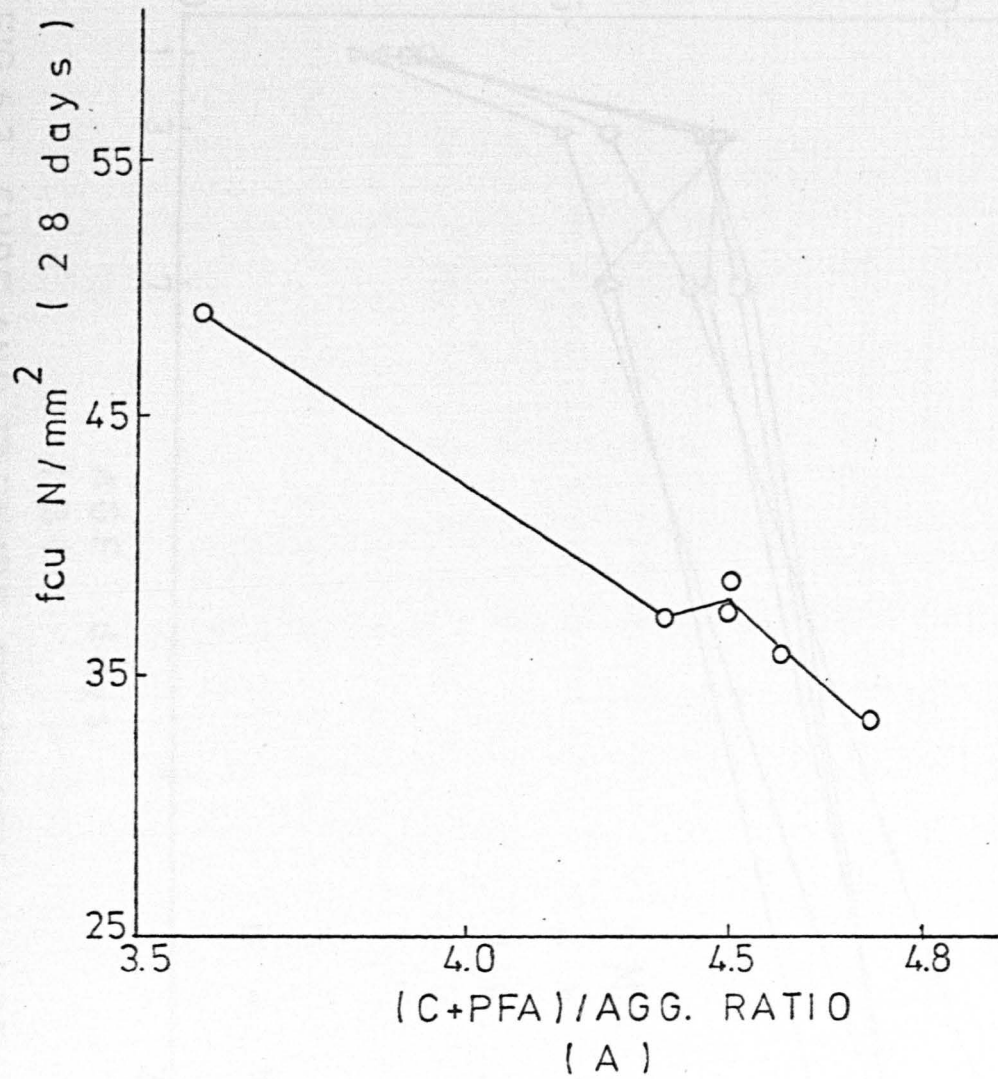


FIG. 6.2. INFLUENCE OF FINE MATERIAL / AGGREGATE RATIO ON CUBE AND FLEXURE STRENGTH

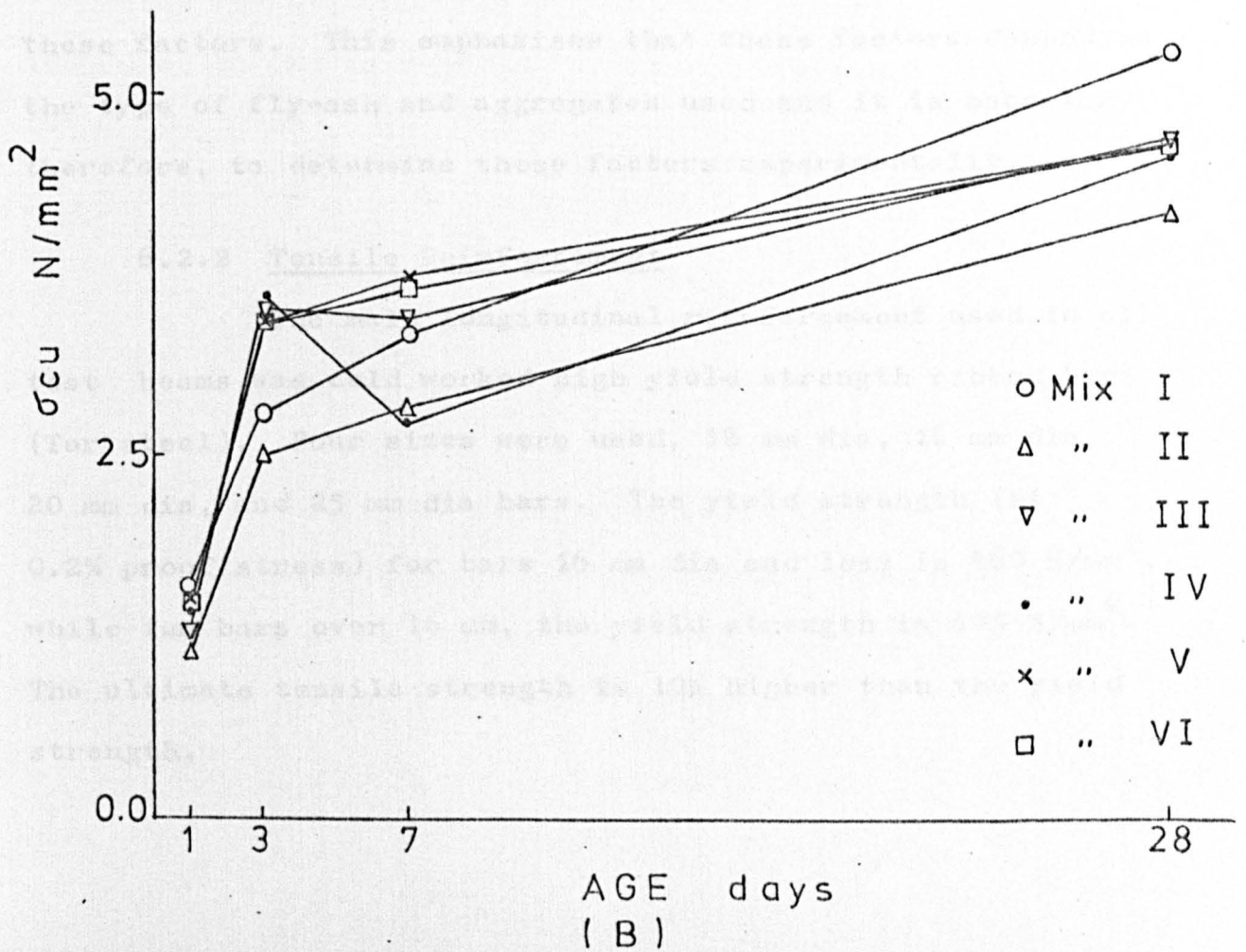
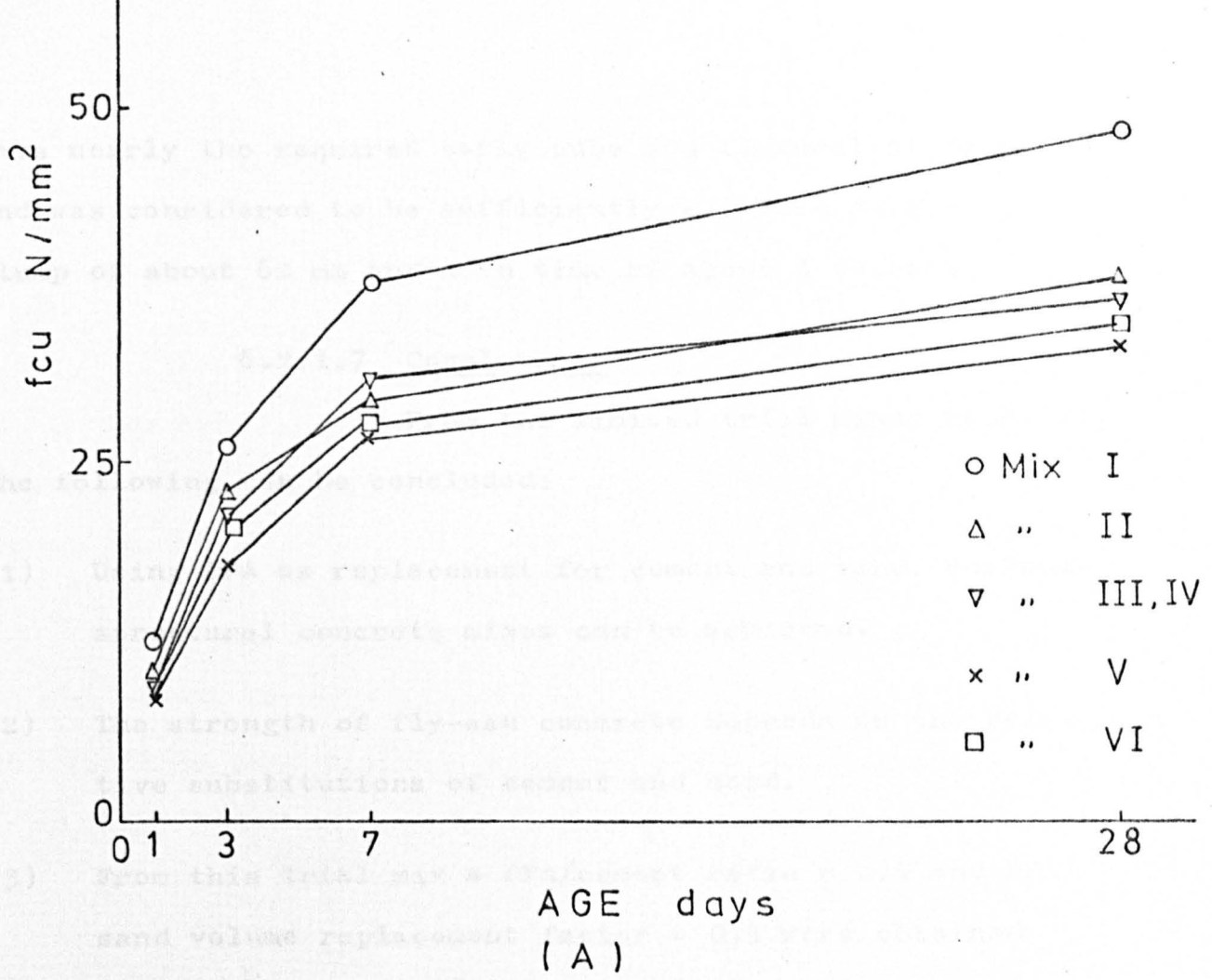


FIG. 6.3. CUBE AND FLEXURE STRENGTH vs. AGE

gave nearly the required early cube and flexural strength and was considered to be sufficiently workable as it gave a slump of about 62 mm and a VB time of about 3 seconds.

6.2.1.7 Conclusions

From the limited trial mixes reported, the following can be concluded:

- (1) Using PFA as replacement for cement and sand, workable structural concrete mixes can be achieved.
- (2) The strength of fly-ash concrete depends on the relative substitutions of cement and sand.
- (3) From this trial mix a PFA/cement ratio = 0.4 and PFA/sand volume replacement factor = 0.4 were obtained while Jackson and Goodridge (75) obtained a value of 0.6 for these factors. This emphasises that these factors depend on the type of fly-ash and aggregates used and it is necessary, therefore, to determine these factors experimentally.

6.2.2 Tensile Reinforcement

The main longitudinal reinforcement used in all test beams was cold worked high yield strength ribbed bars (Tor steel). Four sizes were used, 12 mm dia, 16 mm dia, 20 mm dia, and 25 mm dia bars. The yield strength (at 0.2% proof stress) for bars 16 mm dia and less is 460 N/mm^2 , while for bars over 16 mm, the yield strength is 425 N/mm^2 . The ultimate tensile strength is 10% higher than the yield strength.

6.3 Design of Beams

In all the beam tests, the web width (b_o), the effective depth (d), and the overall depth (h) were kept constant.

The area of longitudinal steel in the tension zone was taken as a percentage of the steel required for a balanced section.

The depth of the neutral axis was calculated according to the strain profile shown in Fig 6.4, which assumes that the steel is just yielding when the concrete crushes.

$$\text{ie } d_n = \frac{.0035 d}{.0035 + f_y/E_s}, \quad f_y = 425 \text{ N/mm}^2, \quad E_s = 200 \text{ kN/mm}^2$$

The force in the compression zone was calculated according to the assumptions of ultimate strength analysis (81).

$$C = C_1 + C_2$$

$$C_1 = K_1 K_3 f'_c b_o d_n$$

$$C_2 = K_1 K_3 f'_c (B - b_o) t$$

$K_1 K_3$ are the coefficients related to the magnitude of the internal compressive force in the concrete stress block.

From Hognestad et al results (82), the value of $K_1 K_3$ was taken as 0.74 for $f'_c = 28 \text{ N/mm}^2$. Thus,

$$A_{sb} = T/f_y$$

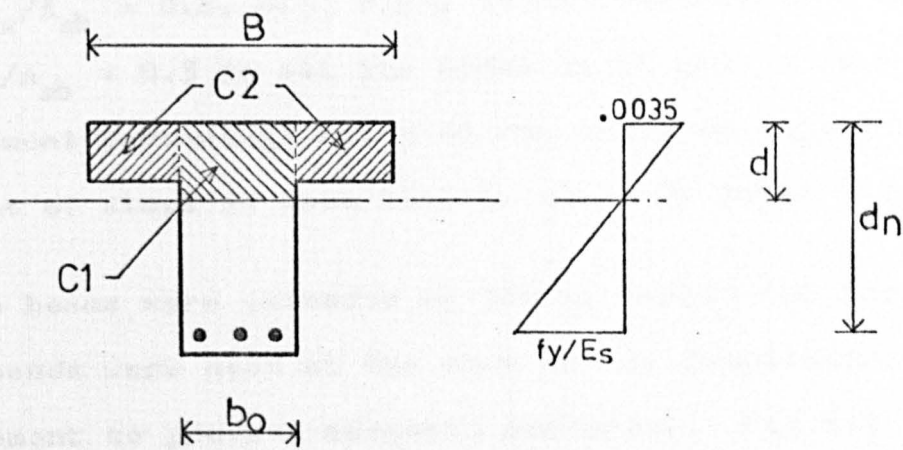


FIG. 6.4. STRAIN PROFILE FOR R.C. BEAMS

6.4

The tests were carried out on a series of beams. Tests were conducted to observe the behavior of the flange, diagonal preference of the concrete, and the steel bars used in the beams. The effects of aggregate type and size on the behavior of the beams were also studied. However, after carrying out a series of tests, it was found that the use of a single series of beams was not sufficient. A second series was used. This was to observe the behavior of the beams and for failure to occur in a different mode. Series I consisted of 12 beams in which the flange was

A_{sb} = Area of steel for balanced section

T = Tensile force in the main reinforcement

= The calculated compressive force C

f_y = yield strength of the main steel

The area of steel required for the balanced section was then calculated for each beam. Different percentages for the actual longitudinal steel (A_s) were calculated from A_{s_b} (eg $A_s/A_{sb} = 0.2, 0.3, 0.4$), it was then decided to choose $A_s/A_{sb} = 0.3$ in all the beams as it gave a reasonable reinforcement percentage based on the web area ($A_s/(b_o d)$). The amount of steel in each beam is shown in Table 6.7.

The beams were extended by 300 mm beyond the supports and 90° bends were used at the ends of the longitudinal reinforcement to provide adequate anchorage. Fig 6.5 shows a longitudinal section in the beam.

6.4 Description of Test Series

The tests were divided into two series. Since the tests were conducted to measure the contribution of the flange, diagonal preformed cracks and notches around the steel bars were used in both shear spans to eliminate the effects of aggregate interlock and dowel action as shown in Fig 6.5. However, after carrying out tests on the first series of beams, only one preformed crack in one shear span was used. This was to simulate the actual plane of failure and for failure to occur on one side of the beam only.

Series I consisted of five beams to investigate the effect

Table 6.7

Details of Beams

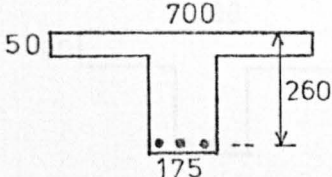
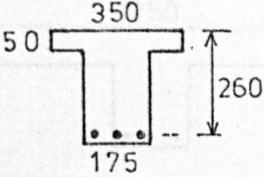
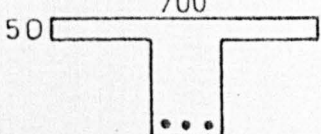
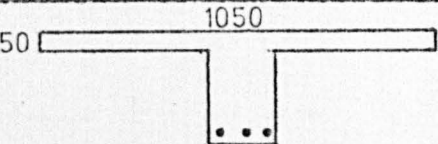
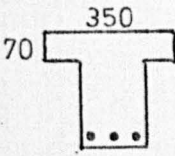
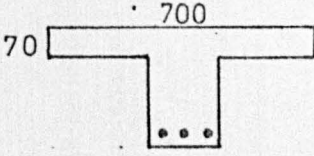
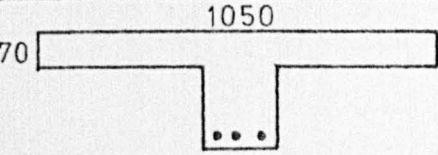
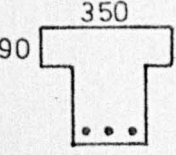
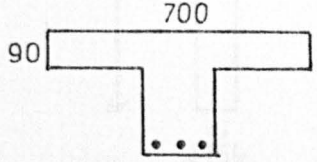
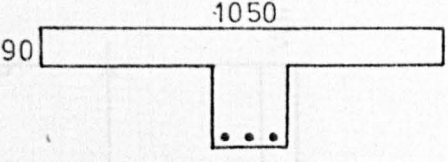
Beam No	Cross Section	No & Size of Bars (mm)	ρ %	$\frac{B}{b_o}$	$\frac{t}{h}$
TRB I II, II- III IV		2 ϕ 20 + 1 ϕ 12	1.78	4	.167
TBX-I		2 ϕ 16 + 1 ϕ 12	1.16	2	.167
TBX-II		2 ϕ 20 + 1 ϕ 12	1.78	4	.167
TBX-III		3 ϕ 20	2.25	6	.167
TBX-IV		3 ϕ 16	1.32	2	.233
TBX-V		2 ϕ 20 + 1 ϕ 16	1.92	4	.233
TBX-VI		2 ϕ 25 + 1 ϕ 20	2.9	6	.233
TBX-VII		2 ϕ 20	1.5	2	.3

Table 6.7 (Continued)

Beam No	Cross Section	No & Size of Bars (mm)	ρ %	$\frac{B}{b_o}$	$\frac{t}{h}$
TBX-VIII		3 ϕ 20	2.25	4	.3
TBX-IX		3 ϕ 25	3.25	6	.3

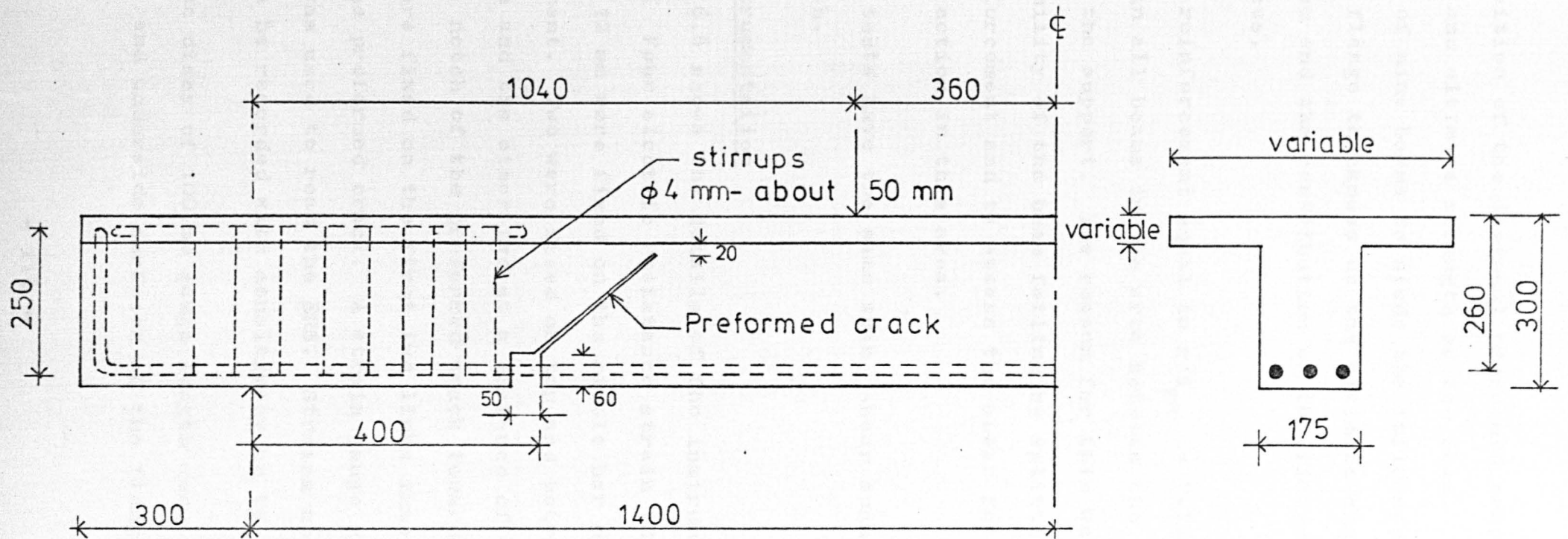


FIG.6.5. LONGITUDINAL AND CROSS SECTIONS OF BEAMS

of the position of the diagonal preformed crack on the behaviour and ultimate strength of the beam. Series II consisted of nine beams to study the influence of the flange width and flange thickness on the ultimate shear strength of the beam and the contribution of the flange in resisting shear forces.

Web reinforcement equal to $r'f_{yw} = 0.72 \text{ N/mm}^2$ was provided in all beams in the area between the preformed crack and the support. The reason for this was to decrease the possibility of the beam failing by splitting along the main reinforcement and to assess the shear force carried by the dowel action in this area.

All tests have the same span, shear span, web width and total depth.

6.5 Instrumentation

Fig 6.6 shows the details of the instrumentation for each beam. Four electric resistance strain (ERS) gauge of length 12 mm were fixed on the middle bar of the main reinforcement. Two were fixed on top and bottom of the bar at midspan and the other two at a distance of 50 mm from the end of the notch of the preformed crack towards the support. Six ERS were fixed on the first two links immediately adjacent to the preformed crack. A strain gauge recorder of 10 channels was used to read the ERS. Strains up to 30,000 μ strains can be recorded with sensitivity up to 5 μ strains.

Demec discs of 100 mm gauge length were fixed on the top, side, and underside surfaces of the flange at four

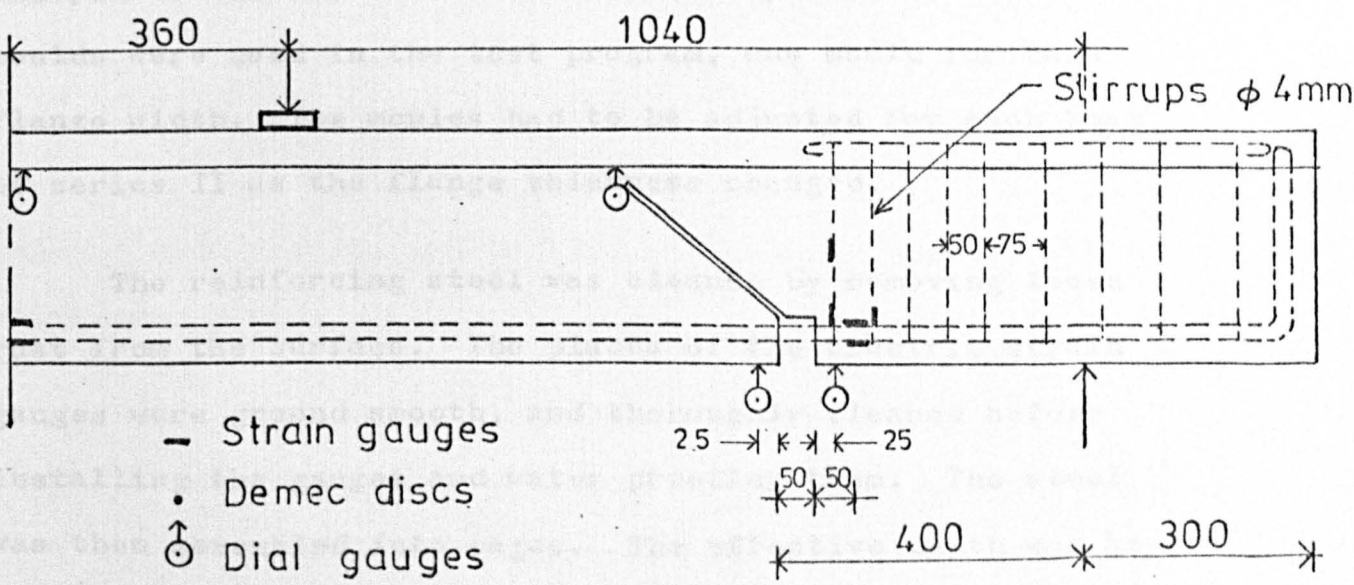
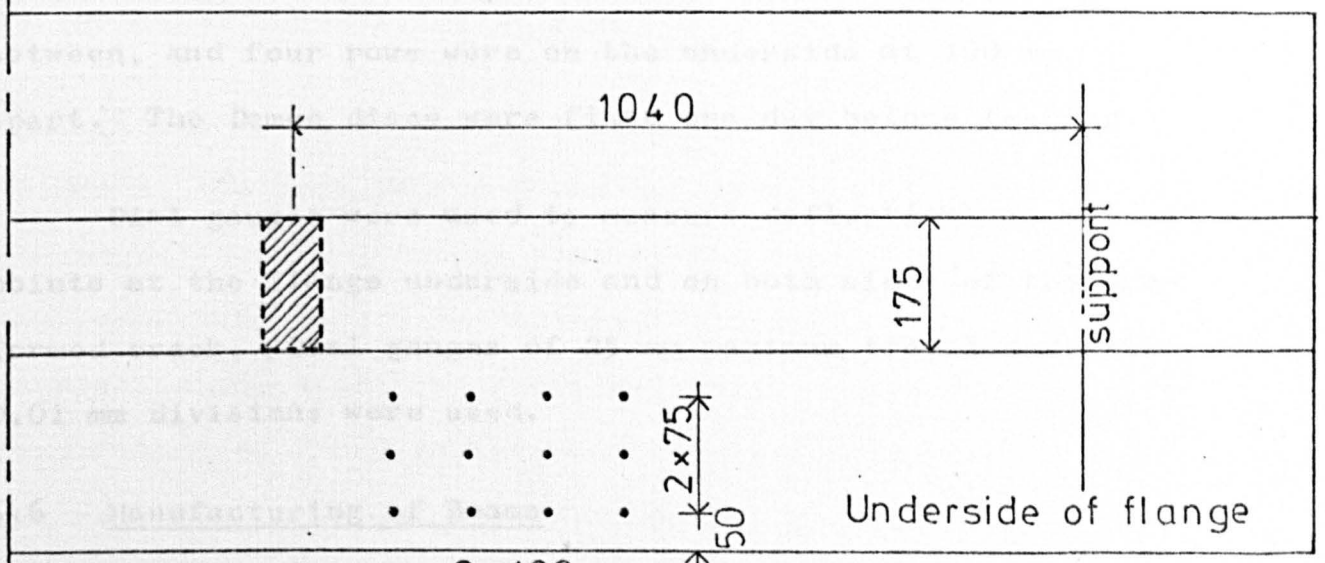
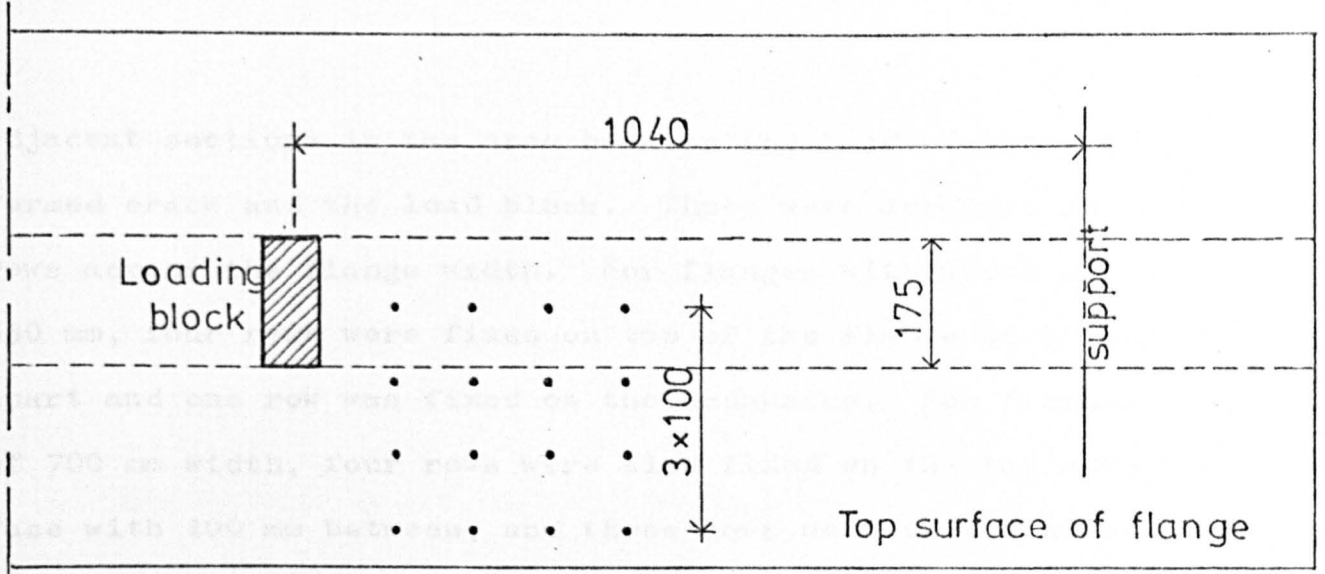


FIG. 6.6. DETAILS OF INSTRUMENTATION
 (No. of demec discs varies with the flange width)

adjacent sections in the area between the head of the pre-formed crack and the load block. These were arranged in rows across the flange width. For flanges with width of 350 mm, four rows were fixed on top of the flange at 50 mm apart and one row was fixed on the underside. For flanges of 700 mm width, four rows were also fixed on the top surface with 100 mm between, and three rows were on the underside surface 75 mm apart. For flanges of 1050 mm width, six rows were fixed on the top surface at distance 100 mm in between, and four rows were on the underside at 100 mm apart. The Demec discs were fixed one day before testing.

Dial gauges were used to measure deflections at several points at the flange underside and on both sides of the pre-formed crack. Dial gauges of 25 mm maximum travel and with 0.01 mm divisions were used.

6.6 Manufacturing of Beams

Steel moulds fabricated from standard channels, angles and plates were used to cast the test specimens. Three moulds were used in the test program, one mould for each flange width. The moulds had to be adjusted for each beam of series II as the flange thickness changed.

The reinforcing steel was cleaned by removing loose rust from the surface. The places of the electric strain gauges were ground smooth, and thoroughly cleaned before installing the gauges and water proofing them. The steel was then assembled into cages. The effective depth was kept constant for all beams, so steel chairs with different heights were used in each beam.

The steel crack formers, Fig 6.7 were covered with polystyrene sheets on both faces using wall paper paste. Polystyrene sheets of 50 mm thickness with three holes to allow the steel to go through were used for the preformed crack around the bars.

The reinforcement cage was placed first in the mould, then the crack formers were fixed with screws to the sides of the mould. The 50 mm thick polystyrene sheets were stuck to the mould using sticking tape.

Casting was carried out in layers with batches of concrete. Between four and six batches were required to fill the mould according to the size of the beams. Each layer was compacted using 25 mm internal vibrator. Care was taken in placing and vibrating the first layer to ensure the penetration of concrete between the steel bars and to fill the required cover underneath. Special attention was taken in the areas of the electrical strain gauges to prevent any harm or damage being done to them throughout the casting process. The top surface of the concrete was smoothed after the completion of compaction. Cubes and prisms for control tests were cast and compacted at the same time. After casting the beam and its control specimens were covered with polythene sheets.

After three days, the side screws fixing the steel crack formers were taken off and then the beam was stripped from the mould. The crack formers were taken out and the preformed crack was cleaned by removing the polystyrene in

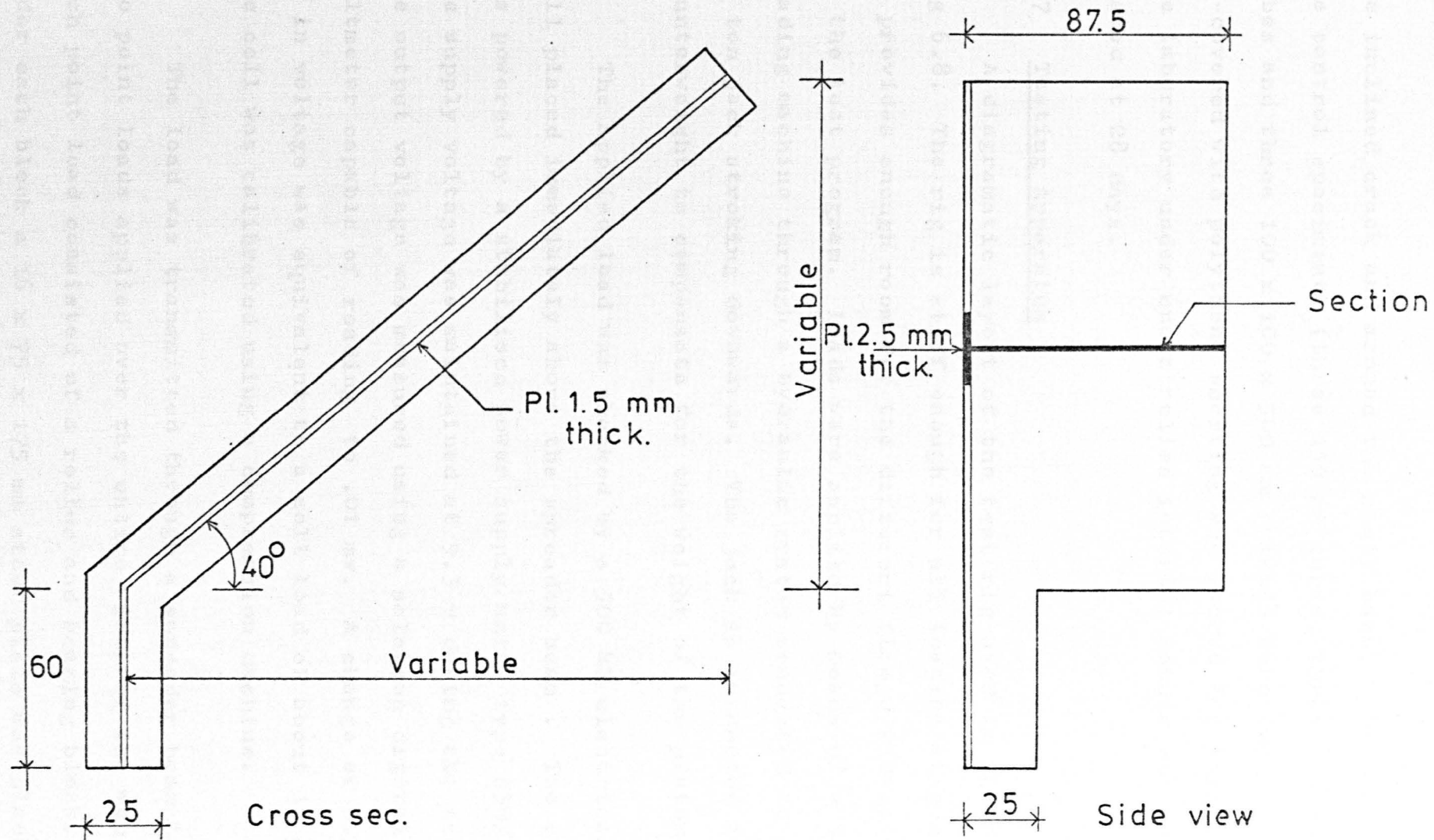


FIG. 6.7. DETAILS OF CRACK FORMERS

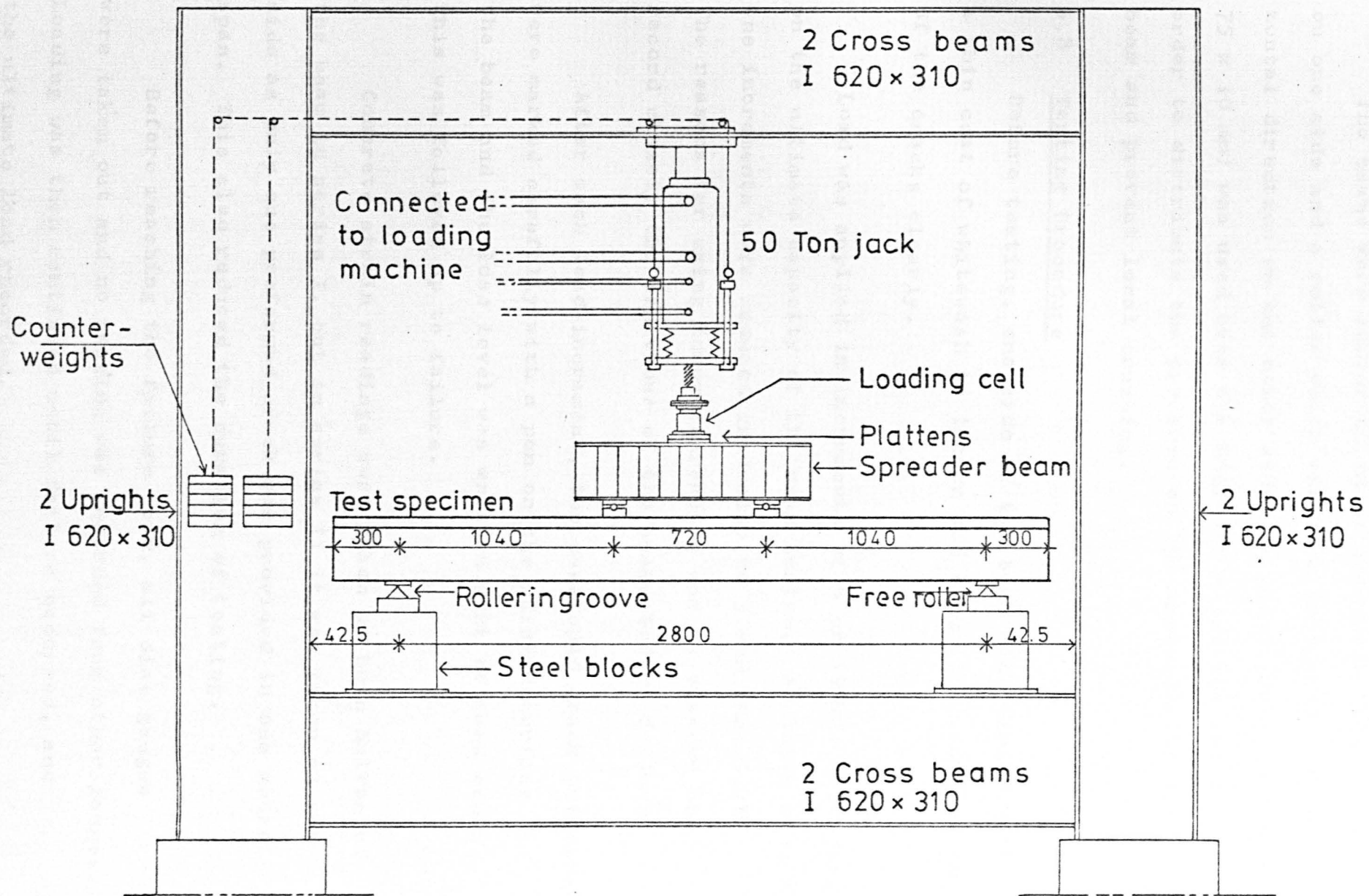
the inclined crack and around the steel bars. The beam and the control specimens (three 150 mm cubes, three 100 mm cubes and three 100 x 100 x 500 mm prisms) were then re-covered with polythene sheeting and stored for curing in the laboratory under uncontrolled internal conditions until tested at 28 days.

6.7 Testing Apparatus

A diagramatic layout of the test rig used is shown in Fig 6.8. The rig is stiff enough for all loading stages and it provides enough room for the different flange widths used in the test program. Loads were applied by means of a 500 kN loading machine through a hydraulic system connected to a 50 ton jack stroking downwards. The jack is connected to a counterweight to compensate for the weight of the piston.

The applied load was checked by a 500 kN electrical load cell placed immediately above the spreader beam. The cell was powered by a stabilised power supply unit type E30/1. The supply voltage was maintained at 9.3 v during the test. The output voltage was measured using a solatron digital voltmeter capable of reading to .01 mv. A change of 0.3 mv in voltage was equivalent to a cell load of about 10 kN. The cell was calibrated using a compression machine.

The load was transmitted through a spreader beam to two point loads applied over the entire width of the web. Each point load consisted of a roller and bearing block. Under each block a 16 x 75 x 175 mm steel plate was placed to distribute the pressure evenly.



SCHEMATIC LAYOUT OF TEST RIG - FIG.6.8.

The beams were supported on an immovable knife-edge on one side and a roller which can move freely in the horizontal direction on the other side. A steel plate (175 x 75 x 10 mm) was used over the knife-edge and the roller in order to distribute the pressure on the underside of the beam and prevent local crushing.

6.8 Testing Procedure

Before testing, one side of the beam was painted with a thin coat of whitewash to locate and study the propagation of the cracks clearly.

Load was applied in increments of 5 or 10 kN, depending on the ultimate capacity of the beam tested. At later stages the increments were reduced gradually to 5 and then 3 kN. The reasons for using lower increments was to observe and record closely the behaviour of the beams before failure.

After each load increment, the developed crack patterns were marked carefully with a pen on the painted surface of the beam and the load level was written next to each crack. This was followed up to failure.

Concrete strain readings were taken on both halves of the beam in series I, but in series II it was taken on one side as only one preformed crack was provided in one shear span. This also reduced the duration of testing.

Before reaching the failure load, all dial gauges were taken out and no reading was recorded from other gauges. Loading was then continued until failure occurred, and the ultimate load recorded.

The beams were photographed after failure and then taken out.

Control specimens were also tested on the concrete compression machine until failure.

6.9 Investigation for the Location of the Preformed Crack

6.9.1 Introduction

It is very difficult to predetermine the failure plane in a beam failing in shear. Placas (14) noticed that there is more than one shear crack in the shear span and usually two or more will widen more than the others with increasing load depending on the shear span length. Previous test results show that the main diagonal cracks appear within the middle third of the shear span. Bahia (83) related the location of the failure plane to the mode of failure. He reported that beams failing in diagonal tension failed at planes away from the loading block, while beams failing in shear or shear compression failed at planes very close to the loading block. However, in his tests, there were beams which failed in shear or shear compression and their planes were away from the loading blocks and the location of the preformed crack he used.

Having recognised this, it was felt necessary to investigate the location of the preformed crack and its influence on the shear strength and behaviour of the beam.

6.9.2 Details of Tests

Five beams were cast and tested in this series. Beam A was cast without preformed crack and referred to as

TRB I in the tests. Beams AI (TRB II) and BI (TRB II-) had preformed crack at location (1) and beams BII (TRB III) and BIII (TRB IV) had preformed cracks at locations (2) and (3) respectively as shown in Fig 6.9. These locations were chosen within the middle third of the shear span where the main failure planes take place. The inclination of these cracks was taken at about 27° . The percentage of longitudinal reinforcement in each beam was $\rho = 1.78\%$ ($A_s/A_{sb} = 0.3$). The flange width was 700 mm and flange thickness was 50 mm.

6.9.3 Discussion of Results

6.9.3.1 Load-deflection Relations

Load-deflection curves for the full beam and the beams with different location for the preformed crack are shown in Fig 6.10. At low load stages beams A, AI, BI and BII showed little difference in deflection, while beam BIII gave higher deflections. The difference in deflections increased with the increase in load level and in particular in beam BIII. The curves are linear until the appearance of the first flexural cracks, then they continue approximately as linear but with different inclination until about 80% - 90% of the ultimate load where they deviate from linearity. The excessive increase in deflections before failure is probably due to the rapid decrease in stiffness of the beams after the formation of shear cracks. Beam BIII sustained higher deflections and failed at a higher load than AI, BI and BII. The stiffness of the beams decreased as the preformed crack moves towards the load points as shown from

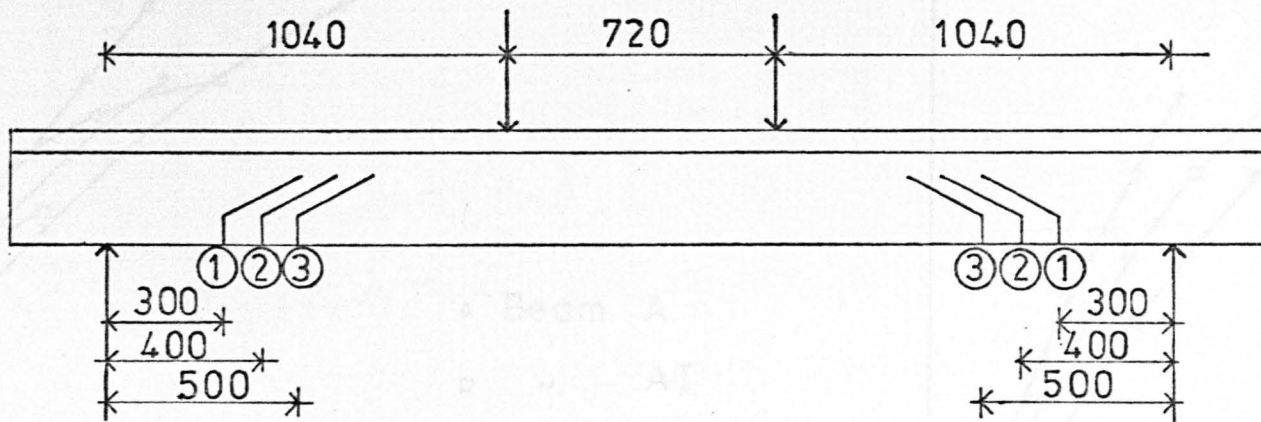


FIG. 6.9. LOCATIONS OF PREFORMED CRACKS FOR BEAMS OF SERIES I

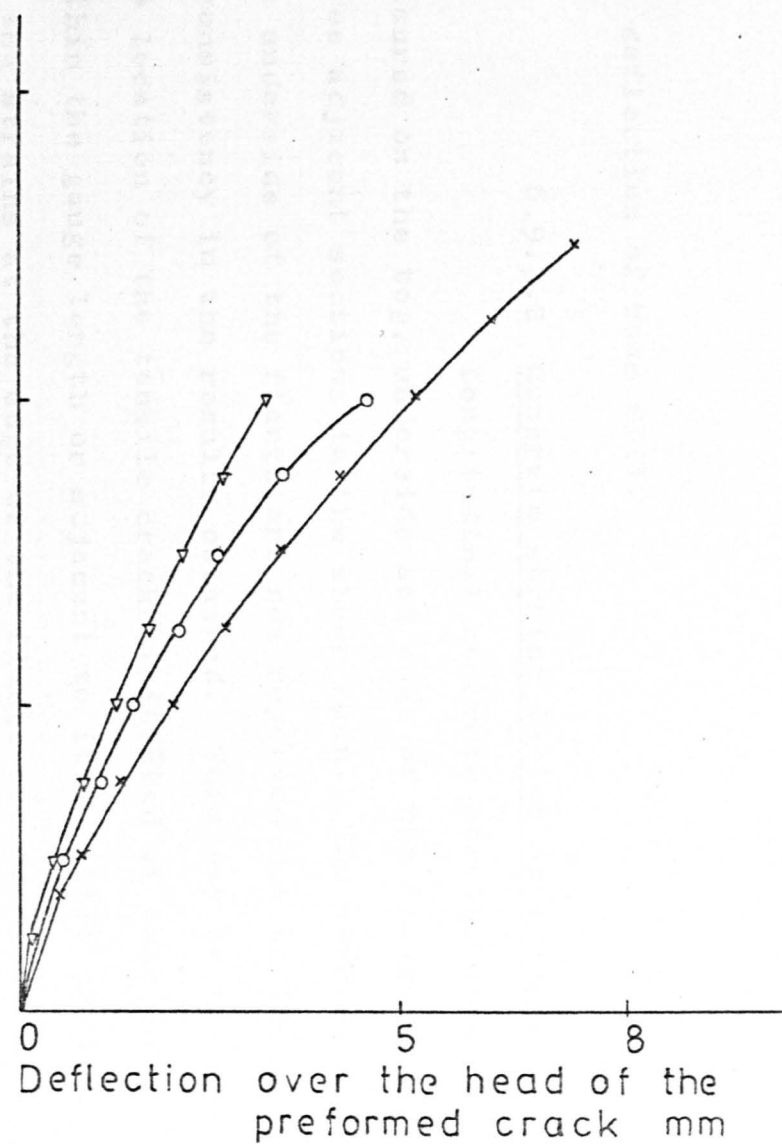
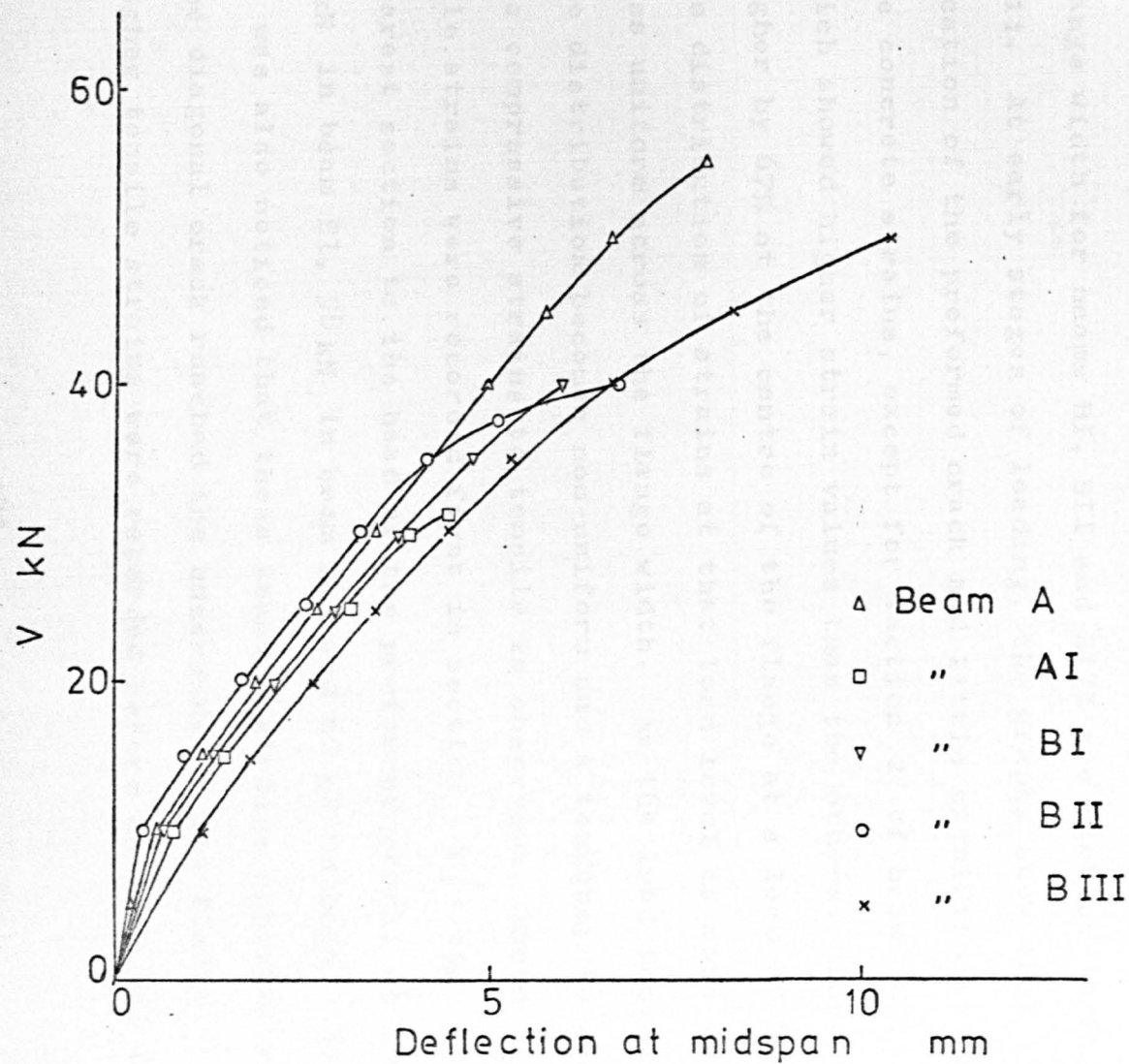


FIG. 6.10. SHEAR FORCE - DEFLECTION CURVES

the deflection of beam BIII.

6.9.3.2 Concrete strains in the Shear Span

Longitudinal concrete strains were measured on the top, underside and edge of the flange in three adjacent sections in the shear span. The strains at the underside of the flange are not reported due to the inconsistency in the results obtained. This may be due to the location of the tensile cracks initiated at this face within the gauge length or adjacent to it. Little change in the strains at the edge of the flange occurred, so this data is also not reported here.

The distributions of the concrete strains across the flange width for beams BI, BII and BIII are plotted in Fig 6.11. At early stages of loading, the graphs show that the location of the preformed crack had little significance on the concrete strains, except for section 2 of beam BIII which showed higher strain values than the others. They are higher by 67% at the centre of the flange at a load of 40 kN. The distribution of strains at that load level is more or less uniform across the flange width. As the load increases the distribution becomes non-uniform and a tendency to change the compressive strains to tensile is observed. These tensile strains were recorded first in section 3, the nearest section to the head of the preformed crack, at load 50kN in beam BI, 58 kN in beam BII and 60 kN in beam BIII. It was also noticed that these tensile strains appeared when the diagonal crack reached the underside of the flange. Higher tensile strains were recorded before failure but they

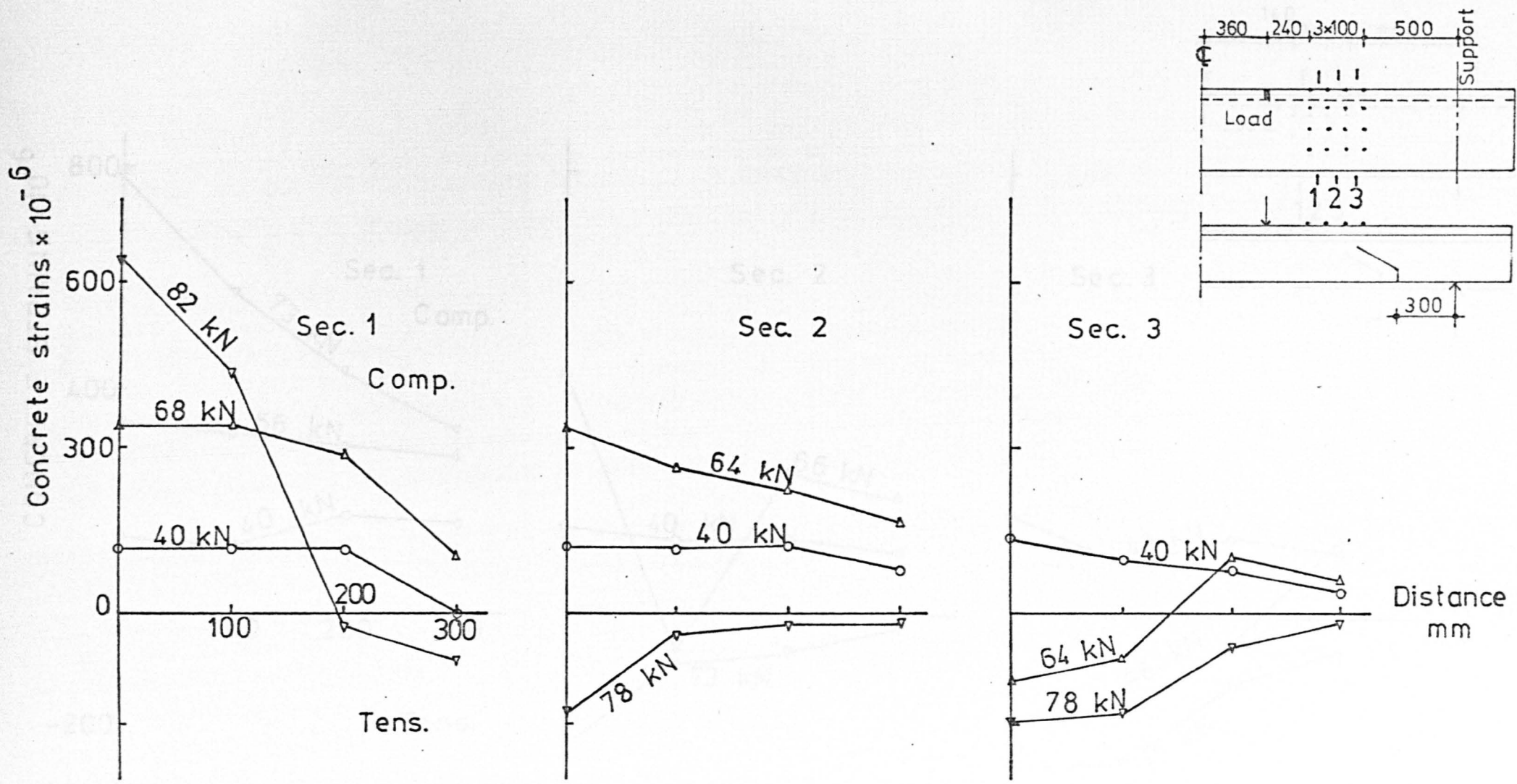


FIG. 6.11. a. CONCRETE STRAINS ACROSS THE FLANGE WIDTH OF BEAM BI

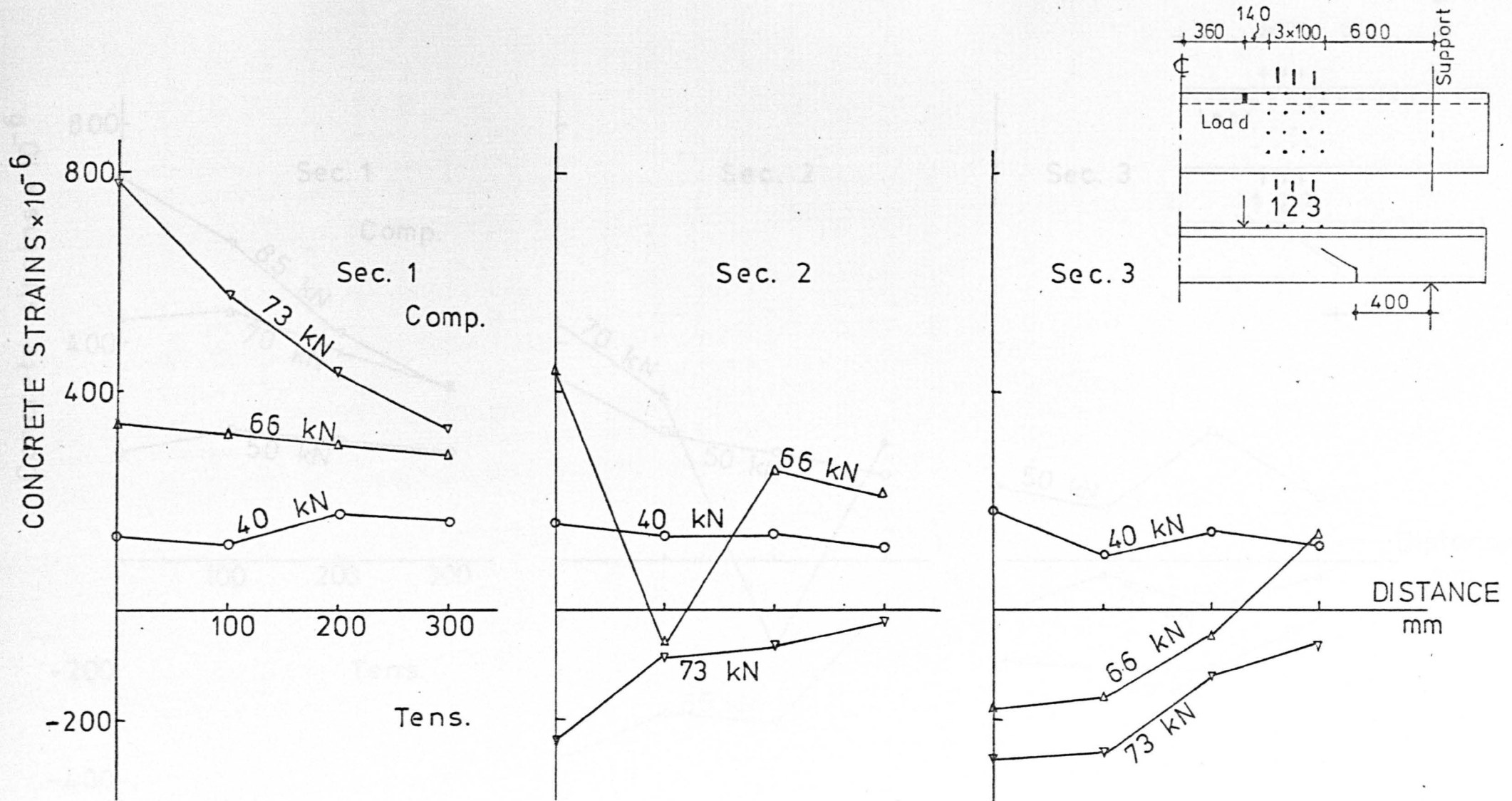


FIG. 6.11. b. CONCRETE STRAINS ACROSS THE FLANGE WIDTH OF BEAM B II

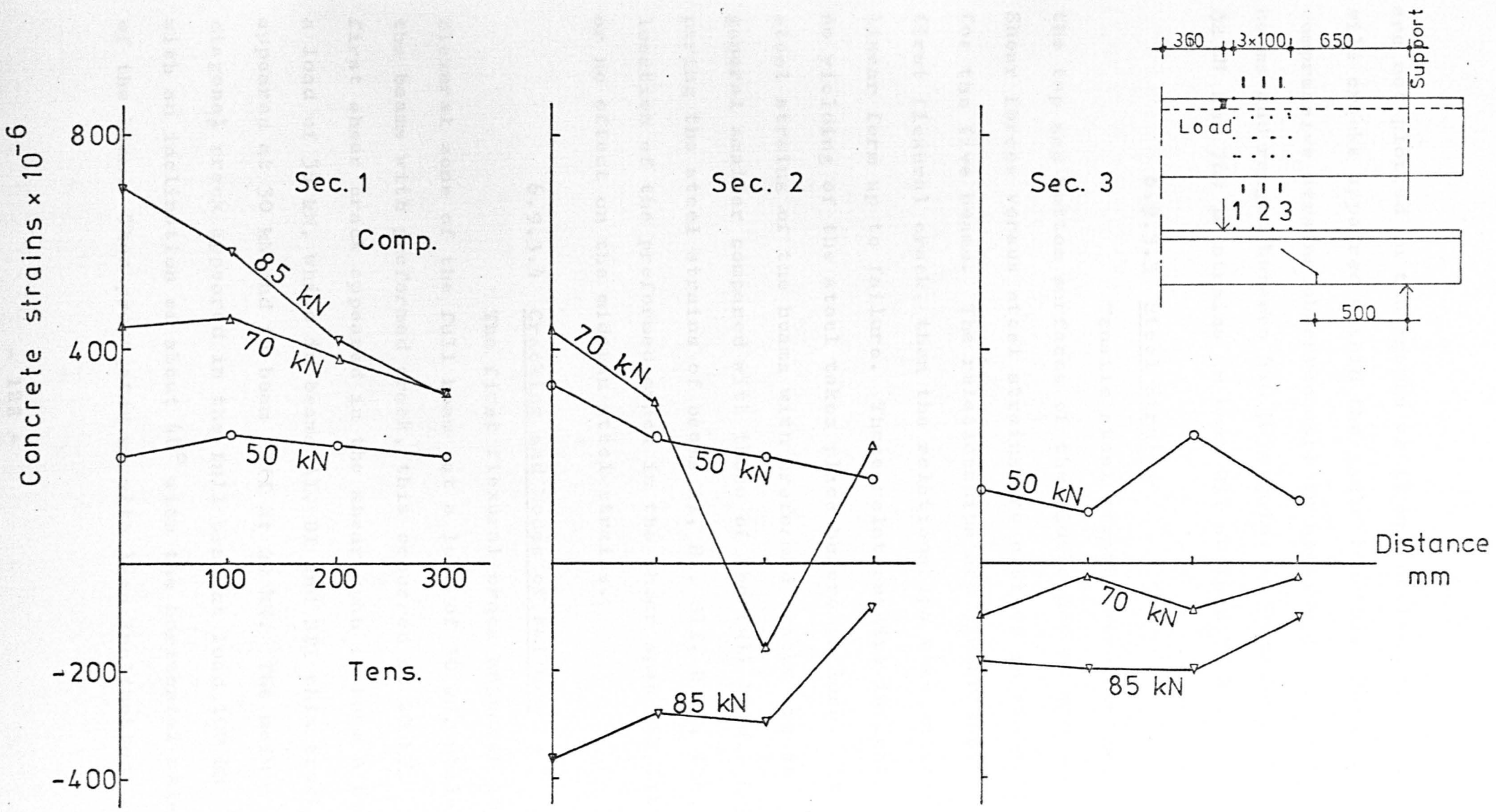


FIG. 6.11. c. CONCRETE STRAINS ACROSS THE FLANGE WIDTH OF BEAM BIII

are not plotted on the graphs as it was noticed that tensile cracks appeared within the gauge lengths. The maximum compressive strains observed were in section 1 in the three beams and ranged between 640 μ strains in beam BI at load 82 kN and 780 μ strains in beam BII at load 73 kN.

6.9.3.3 Steel Strains

Tensile steel strains were measured on the top and bottom surfaces of the middle bar at midspan. Shear forces versus steel strains are plotted in Fig 6.12 for the five beams. The relationships are linear until the first flexural crack, then the relationships take another linear form up to failure. These relationships indicate that no yielding of the steel takes place before failure. The steel strains of the beams with preformed cracks are in general smaller compared with those of the full beam. Comparing the steel strains of beams AI, BI, BII, BIII, the location of the preformed crack in the shear span has little or no effect on the midspan steel strains.

6.9.3.4 Cracking and Modes of Failure

The first flexural crack appeared in the flexural zone of the full beam at a load of 30 kN, while in the beams with preformed crack, this occurred at 20 kN. The first shear crack appeared in the shear span in beam A at a load of 35 kN, while in beams AI, BI and BII this crack appeared at 30 kN and in beam BIII at 20 kN. The main diagonal crack appeared in the full beam at load 100 kN with an inclination of about 40° with the horizontal axis of the beam. Then propagated up with less inclination

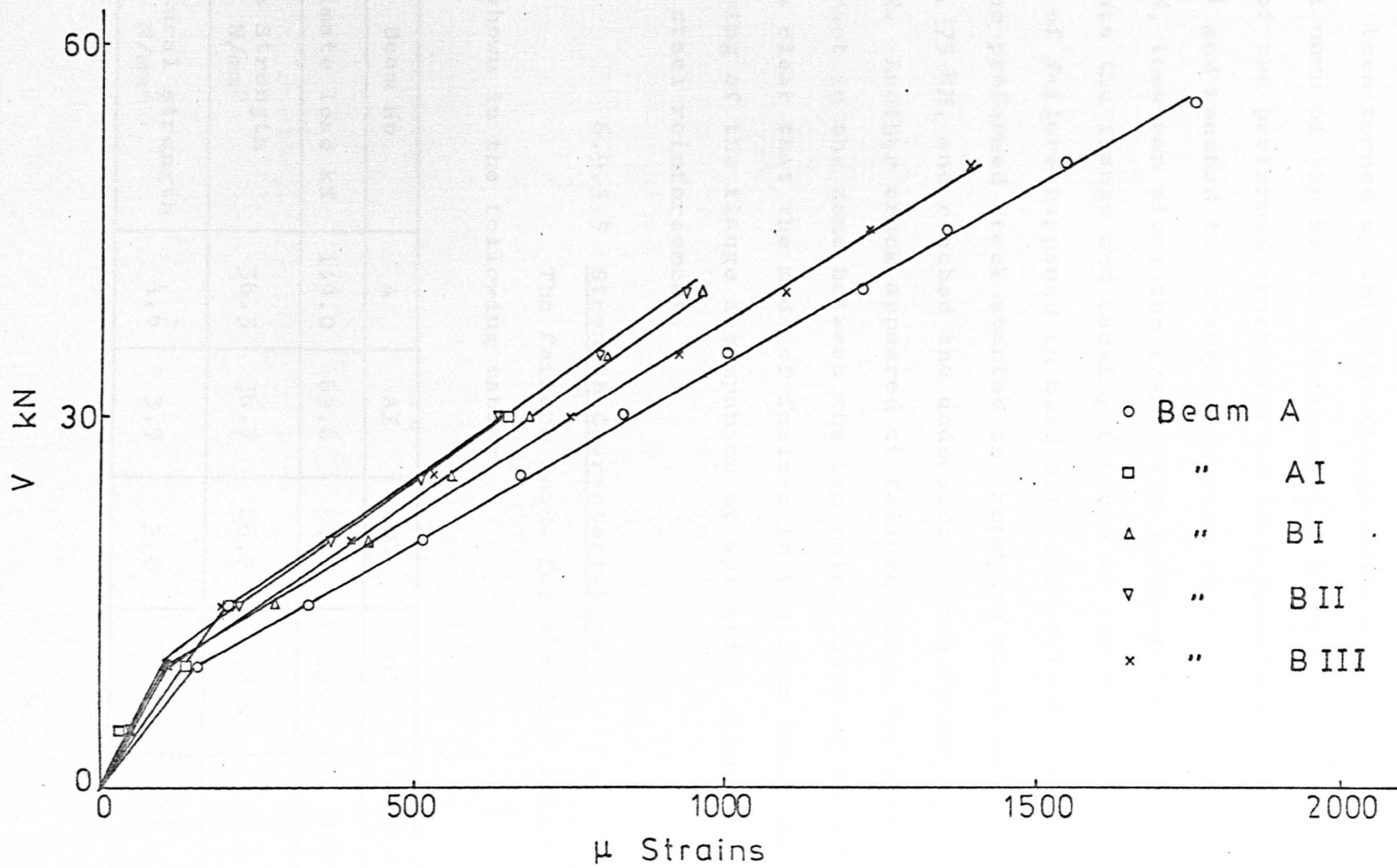


FIG. 6.12. SHEAR FORCE vs. STEEL STRAINS AT MID-SPAN

(about 30°) and down along the main reinforcement. The top end of the diagonal crack extended along the web/flange junction then turned up into the flange initiating the final break down of the beam. For beams AI, BI and BII the top end of the preformed crack started to propagate at a load of 40 kN and reached the flange underside at a load of about 55 kN, then ran along the flange/web junction before turning up into the flange and causing failure of the beam. The same mode of failure happened in beam BIII except that the top end of the preformed crack started to propagate at an earlier load, 75 kN, and reached the underside of the flange at 45 kN. Another crack appeared at failure along the flange/web root in the zone between the two point loads of this beam. It is clear that the mode of failure in the four beams is shearing of the flange accompanied by splitting along the main steel reinforcement.

6.9.3.5 Strength Characteristics

The failure loads for the five beams are shown in the following table:

Beam No	A	AI	BI	BII	BIII
Ultimate load kN	119.0	69.6	84.0	85.5	106
Cube Strength N/mm ²	36.3	36.7	26.7	38.4	37.4
Flexural strength N/mm ²	4.6	3.9	3.0	-	3.7

Since beam A is a full beam, the total shear force at any stage of loading is a combined contribution of compression zone, aggregate interlock and dowel action. The rest of the beams have preformed cracks in the shear span, so the total shear force is a combined contribution of compression zone and partially of the dowel forces.

6.9.4 Location of the Preformed Crack for the Next Tests

The strength and modes of failure of the beams with preformed cracks have been compared with the full beam. Fig 6.13 shows the three locations of the preformed crack and the main failure plane of beam A. It was decided to adopt location (2) of beam BII for the next tests of the programme. The reasons for this were:

- (1) This crack is at the same location as the main crack in beam A as shown in Fig 6.13.
- (2) For location (1) of beams AI and BI, the distance between the crack and the support is a minimum i.e., at the edge of the middle third of the shear span. Not many beams fail in this position.
- (3) Location (3) of beam BIII, the failure plane extended to the point load and the area around the load block was cracked. Another crack appeared at failure along the flange/web root in the flexural zone. The beam might fail in a shear-flexural mode of failure rather than the required shear failure.

The inclination of the preformed crack in these beams

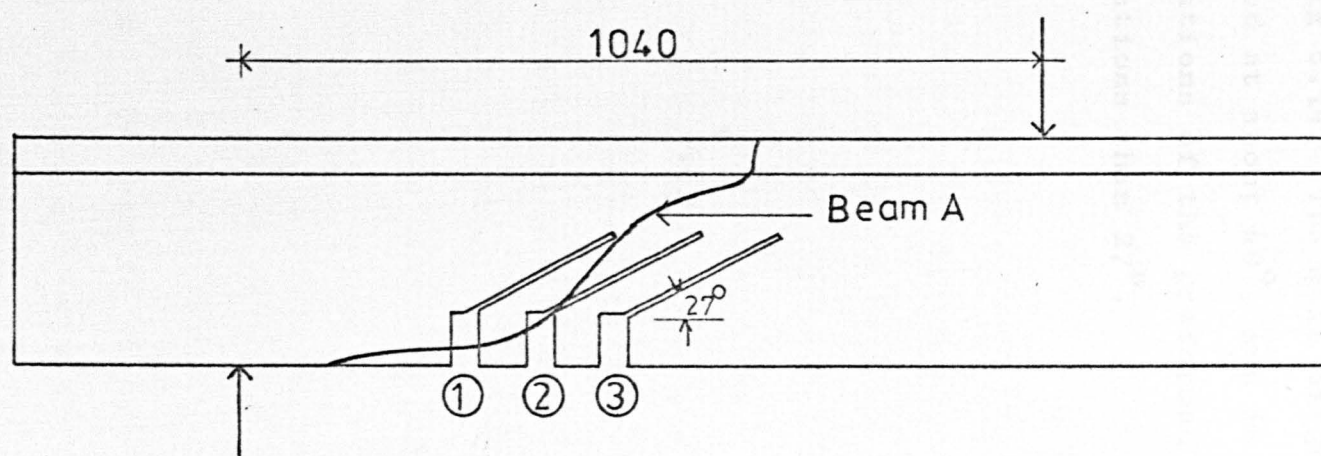


FIG. 6.13. LOCATION OF FAILURE PLANES

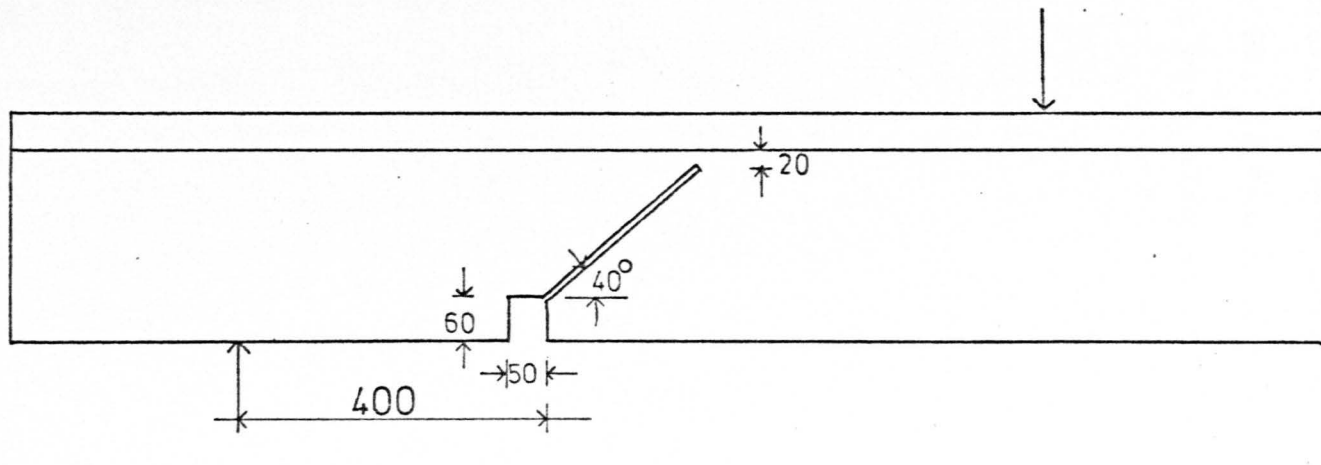


FIG. 6.14. SUGGESTED LOCATION AND INCLINATION OF PREFORMED CRACK

was taken as about 27° according to Al-Alusi (6) and Placas (14) who pointed out that the main diagonal cracks generally appeared at lower inclination than 30° . However, as a result of the test on beam A the inclination was modified to about 40° , Fig 6.14. The main diagonal crack in this beam was inclined at about 40° , and in beams BI, II and III, the propagations of the preformed cracks were also at steeper inclinations than 27° .

In this chapter a comparison of the results obtained from the analysis with the actual behaviour from the test results is presented. In spite of the vast amount of experimental data available, the failure mechanism for this type of fracture is not completely understood. The aim of this study is to evaluate the accuracy of the solution in predicting the behaviour. However, it must be remembered that the analytical solution neglects some aspects which may influence the ultimate behaviour of the beam, such as the bond between steel and concrete, local effects of beam supports, etc.

Results from tests of reinforced concrete beams are compared with those from the analysis in the following sections. Two series of tests are used for this purpose. The test series are described in sections 3.1 and 3.2. The results are compared with those from the analysis in section 3.3. All the beams are tested until failure.

CHAPTER 7

COMPARISON OF COMPUTER ANALYSIS RESULTS WITH EXPERIMENTAL DATA

7.1 Introduction

In Chapters 3, 4 and 5, a 3-dimensional finite element model was developed to analyse the problem of inelastic behaviour of reinforced concrete T-beams failing in shear. In this chapter a comparison of the results from the analysis with the actual behaviour from tests is carried out. In spite of the vast amount of experimental work which has been carried out on beams failing in shear, the behaviour and failure mechanism for this type of failure is still not completely understood. The aim of this study is to investigate the accuracy of the solution in reflecting the beam behaviour. However, it must be remembered that the theoretical solution neglects some aspects which are thought to influence the ultimate behaviour of the beam, such as bond between steel and concrete, dowel effect of main reinforcement, etc.

Results from tests on reinforced concrete T-beams are compared with those from the analysis in the following sections. Two series of beams are used for this study. The test series are described in Sections 6.3 and 6.4. The results are compared with those from the analysis in Section 7.2. All the beams are tested until failure under two point loads with constant shear span/depth ratio = 4 and $A_s/A_{sb} = 0.3$.

7.2 Comparison

7.2.1 Method of Analysis

Each beam had two symmetrically loaded shear spans. Beams of series one had a preformed crack in each shear span, except beam TRB-I which had no preformed crack. Beams of series two had only one preformed crack in one shear span. Due to symmetry one quarter of the beam has been solved analytically. This quarter is formed by the two symmetrical planes, namely, the midspan plane and the longitudinal plane as shown in Fig 7.1.

All boundary nodes located on the midspan plane are constrained horizontally in direction X, and free to move in directions Y and Z, while boundary nodes located on the longitudinal plane are constrained in Z-direction and free in X and Y directions. The nodes at the support are constrained in Y and Z directions and free in X-direction.

The actual shearing force $P/2$ acting on each shear span is simulated by an equivalent nodal load $P/4$ in the analytical solution.

The idealisation of the different flange widths for finite element analysis is shown in Fig 7.2. The main reinforcement is approximated by bar elements lying on the bottom surface of the beam.

The initial elastic modulus E_c for concrete is taken 30 N/mm^2 and Poisson's ratio ν is taken 0.15. The modulus of elasticity for steel is taken 200 kN/mm^2 .

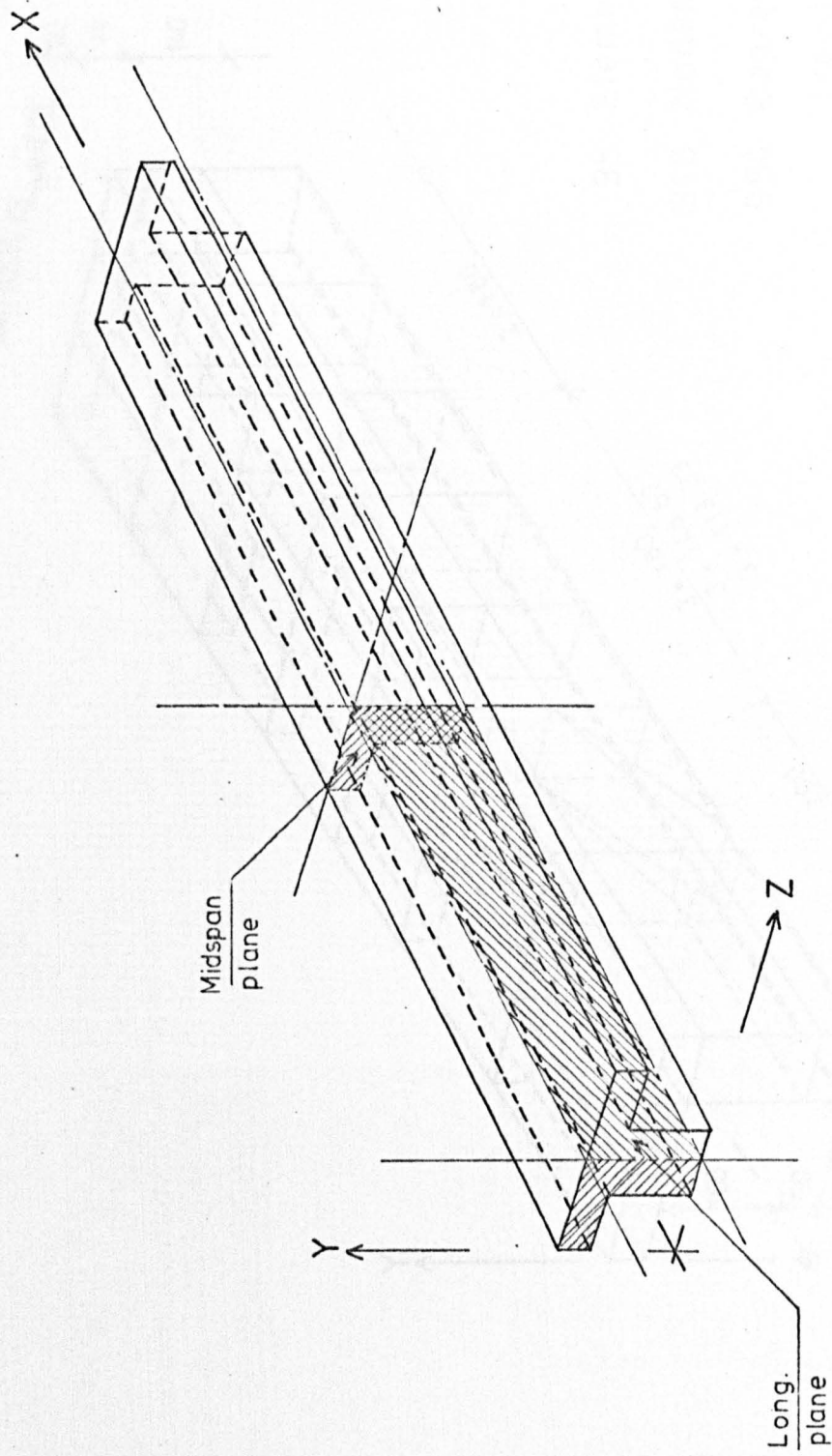
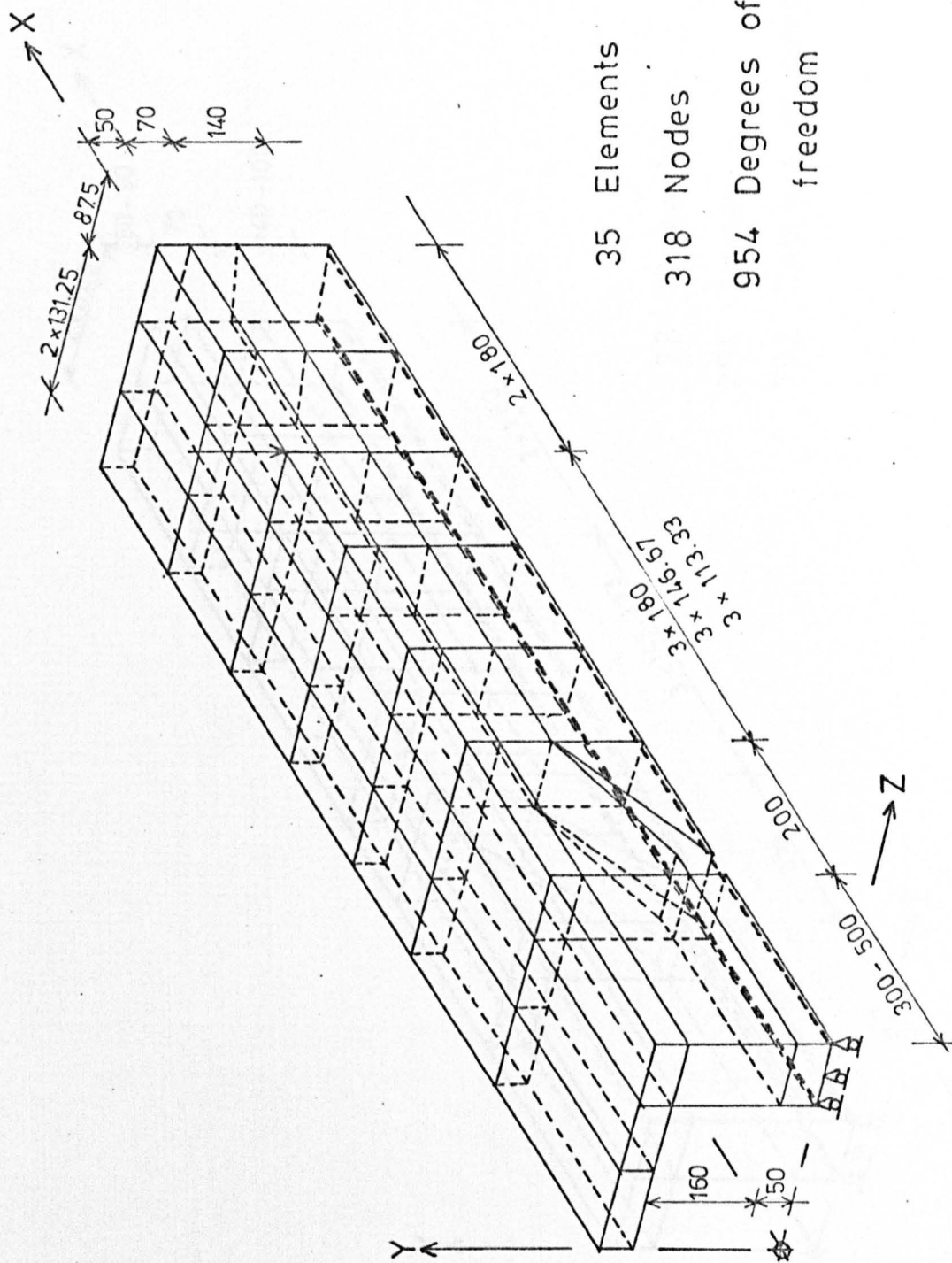
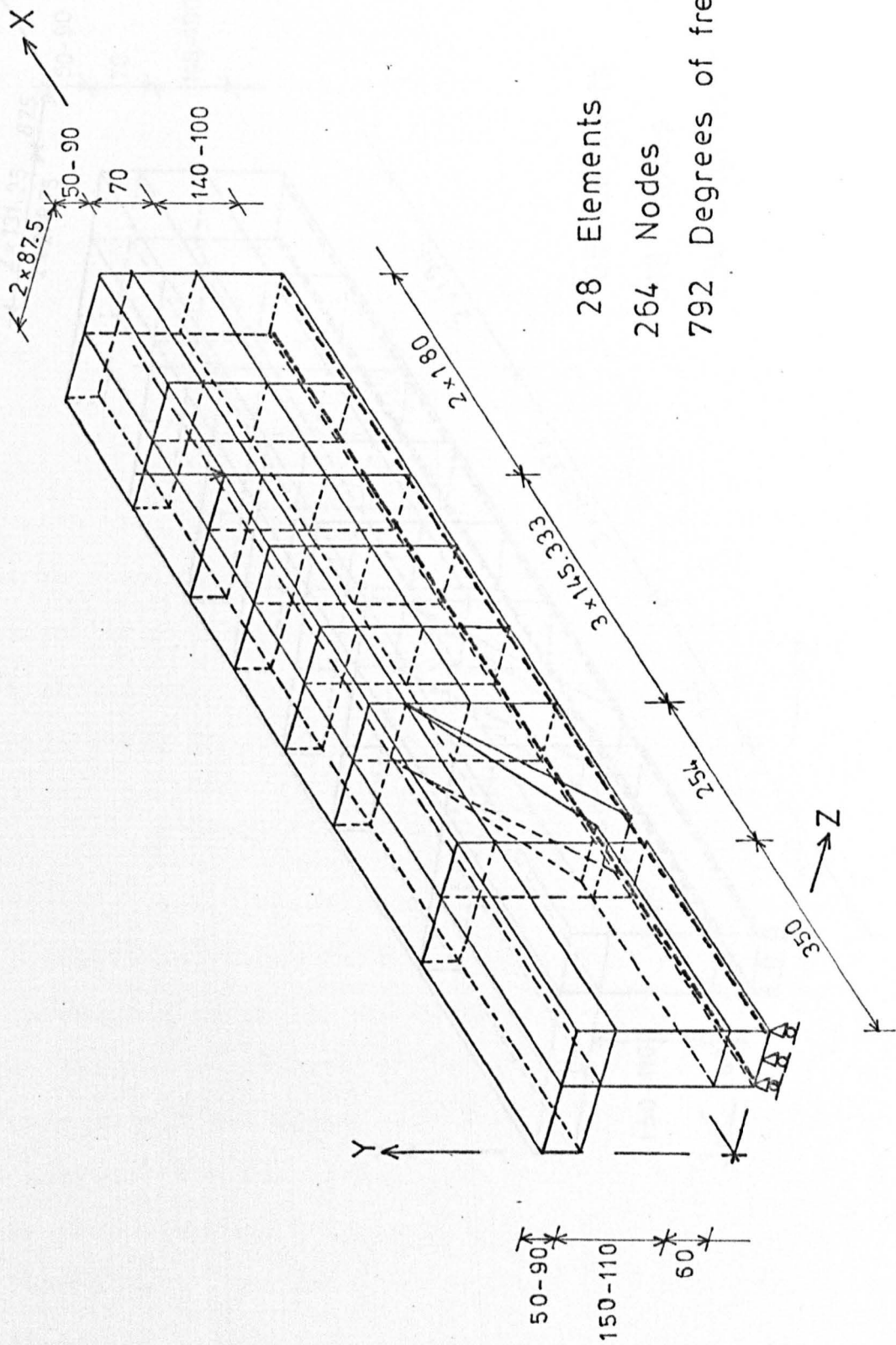


FIG. 7.1. PART OF THE BEAM TO BE ANALYSED BY F. E. M.



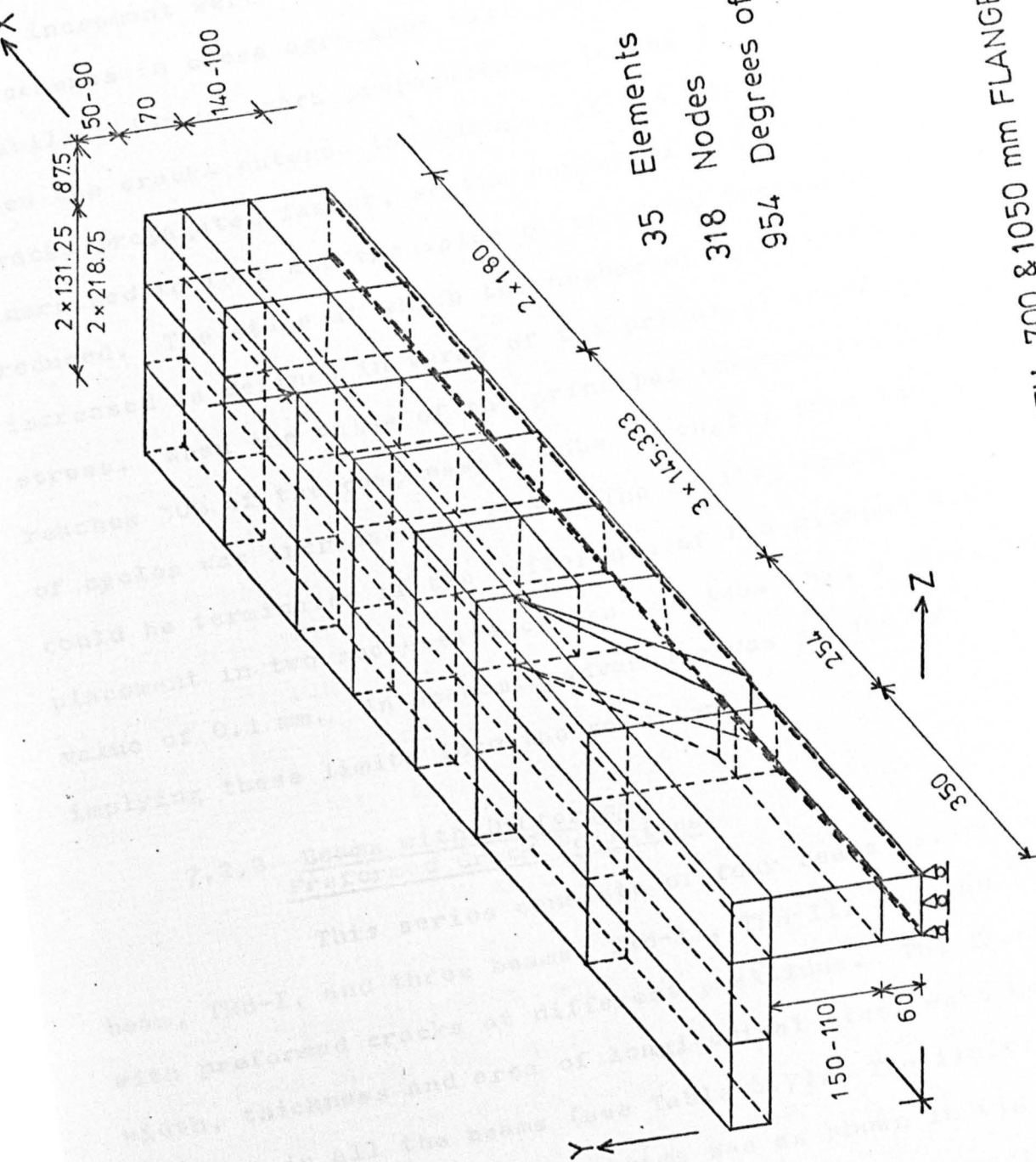
35 Elements
 318 Nodes
 954 Degrees of freedom

FIG.7.2.a. FINITE ELEMENT MESH FOR BEAMS OF SERIES I



28 Elements
 264 Nodes
 792 Degrees of freedom.

FIG.7.2.b. FINITE ELEMENT MESH FOR BEAMS WITH 350 mm FLANGE WIDTH
 (Series II)



35	Elements
318	Nodes
954	Degrees of freedom

FIG. 7.2.c. FINITE ELEMENT MESH FOR BEAMS WITH 700 & 1050 mm FLANGE WIDTHS
(Series II)

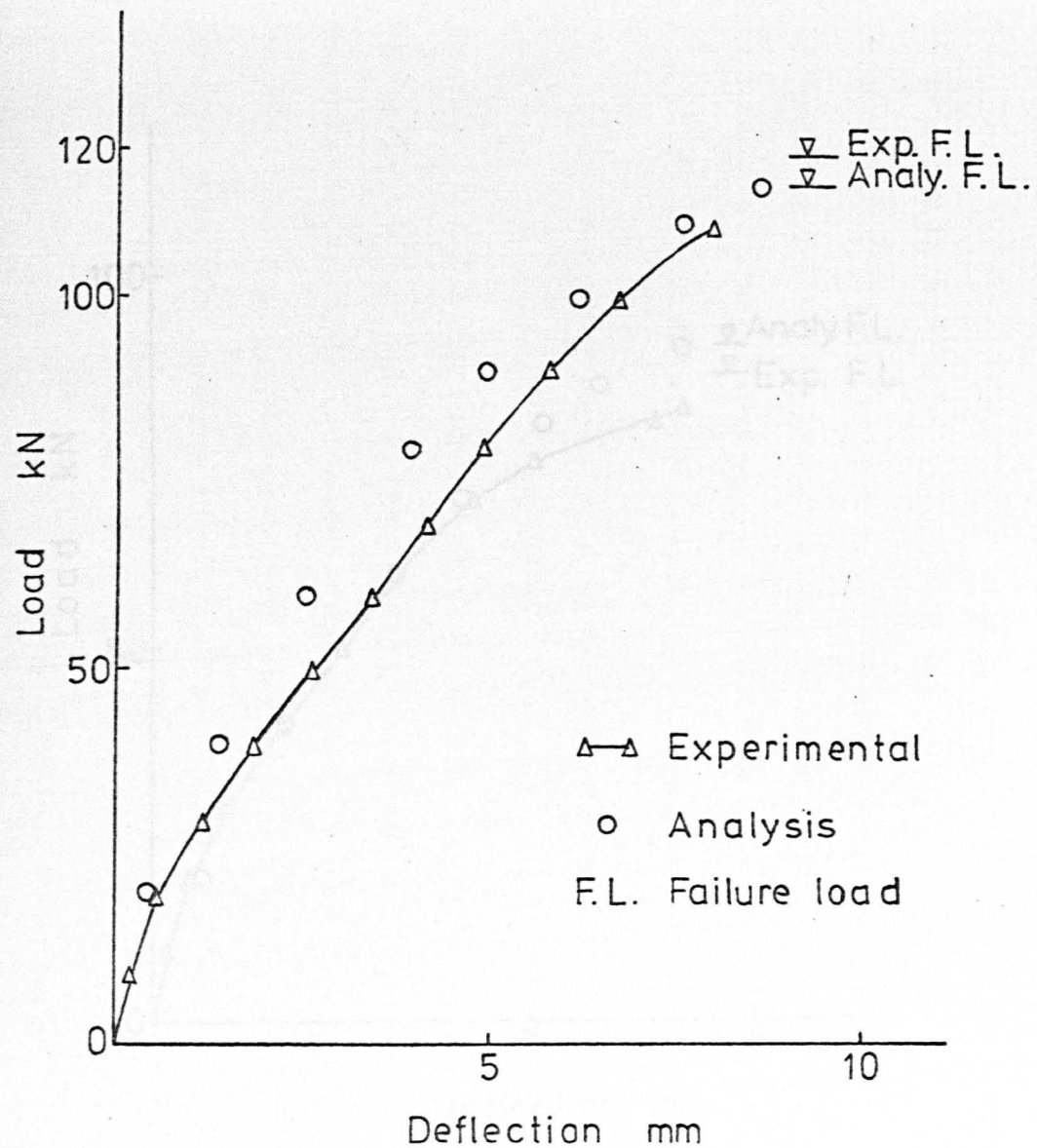
In the early stages of analysis, two cycles for each load increment were found to be sufficient to bring the displacements in close agreement with the experimental ones and stabilisation of crack propagation. In the later stages, when the cracks entered the flange, it was noticed that cracks propagated faster, so the number of cycles was increased to four and the value of the load increment was reduced. The stage at which the number of cycles was increased is defined in terms of the principal compressive stress. When the value of the principal compressive stress reaches 30% of the compressive cube strength, then the number of cycles was increased to four. The cycling operation could be terminated if the difference of the midspan displacement in two successive cycles was less than a prescribed value of 0.1 mm. An economic advantage was gained by implying these limits into the solution.

7.2.2 Beams with Different Preformed Crack Positions

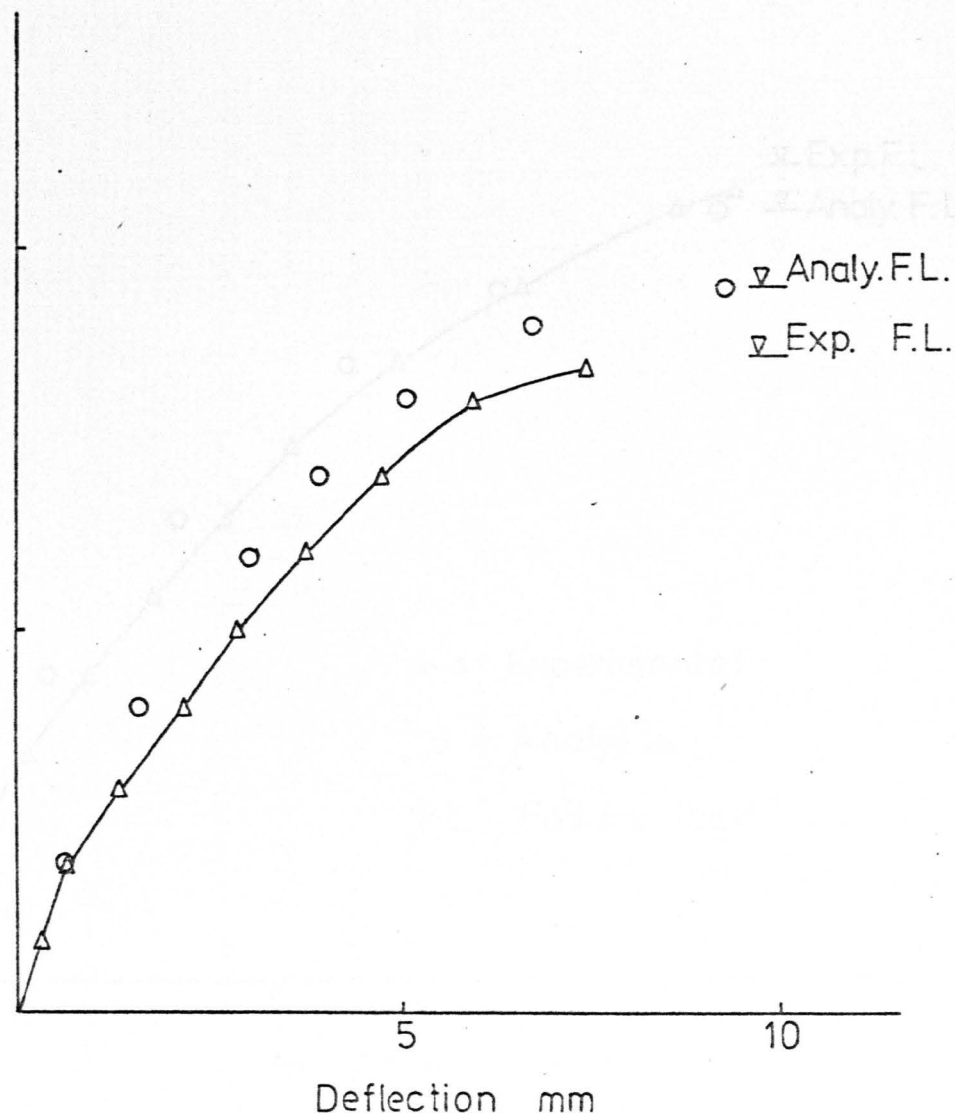
This series consists of four beams, an uncracked beam, TRB-I, and three beams, TRB-II, TRB-III and TRB-IV, with preformed cracks at different positions. The flange width, thickness and area of longitudinal steel were kept the same in all the beams (see Table 6.7). The finite element idealisation for these beams was as shown in Fig 7.2a. Thirty-five elements were used to represent the quarter of the beam shown. The load was applied in 7 increments and the number of cycles used for each increment was two, until approaching the ultimate load when the number was increased to four.

Load-deflection curves at the midspans of the beams are plotted in Fig 7.3. The analytical solutions are in good agreement with the experimental curves, but the stiffnesses were overestimated in the early stages of loading for beam TRB-I and in the later stages for beams TRB-II and TRB-III. This is probably due to the stiffening effect between steel and concrete which is neglected in the analysis.

The ultimate strength predicted from the analysis underestimates the experimental values for beams TRB-I and TRB-IV by 3% and 6% respectively, and overestimates the values for beams TRB-II and TRB-III by 12% and 5% respectively. This shows that the ultimate strengths for the four beams were reasonably predicted by the analysis. However, the difference in strength shown between the analytical and experimental could be related to the preformed crack location which changes the element size in the mesh for each case. This can be observed from the mesh size in the area between the preformed crack and the load point where the failure occurs in this area. In beam TRB-II, the mesh division in this area was 180 mm (Fig 7.2a) which is the coarsest mesh size in the three cases with preformed crack, and hence the ultimate strength of the beam was overestimated by 12% than the experimental value. In beam TRB-III the mesh division in the same area was reduced to 146.67 mm, the strength was overestimated by 5% than the experimental one. In the last beam TRB-IV, the mesh division in the same area was the smallest to be 113.33 mm, and the strength of this beam was underestimated by 6% of the experimental value. However,



(1) - Beam TRB I



(2) - Beam TRB II

FIG. 7.3. MIDSPAN LOAD - DEFLECTION CURVES

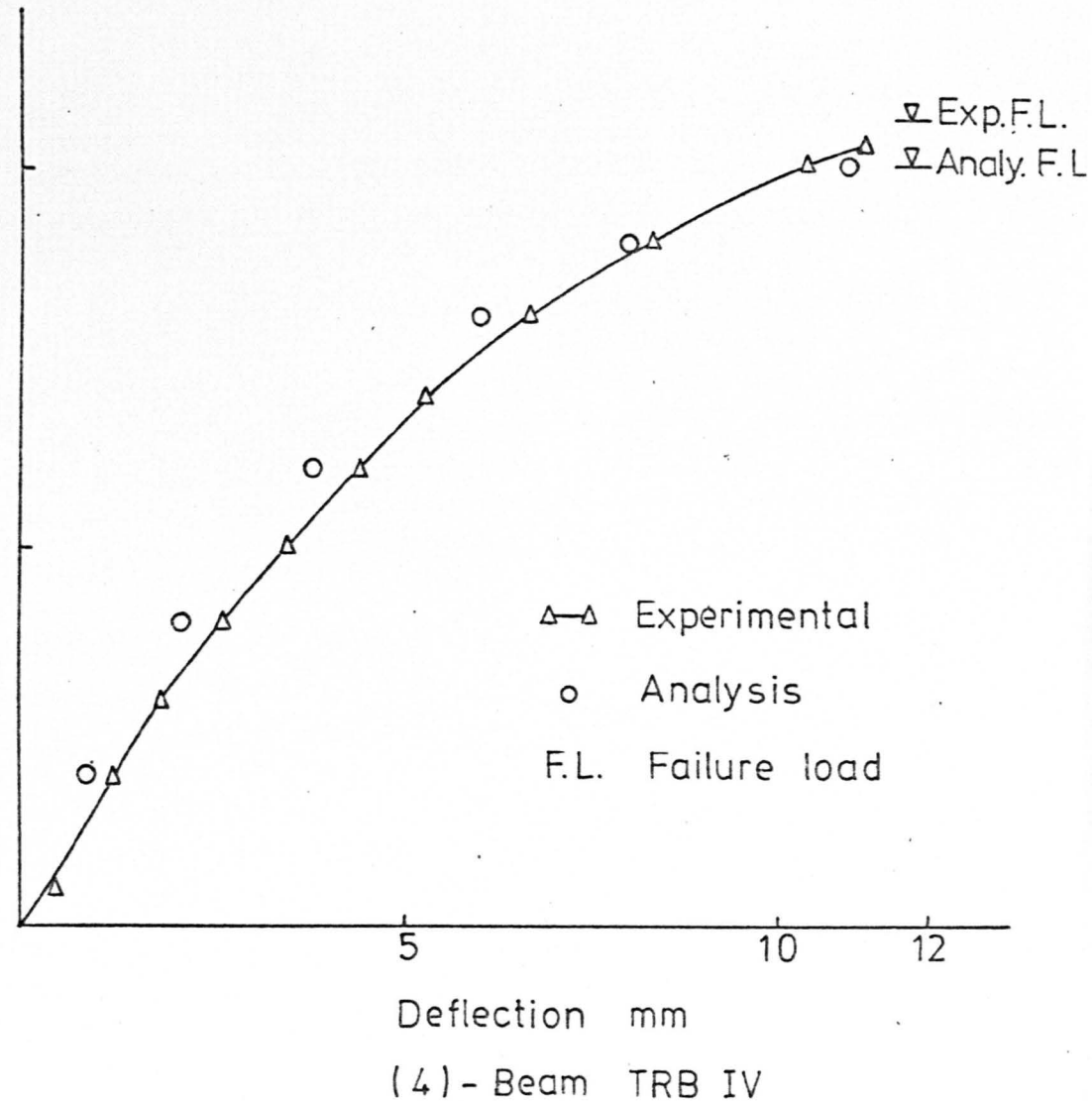
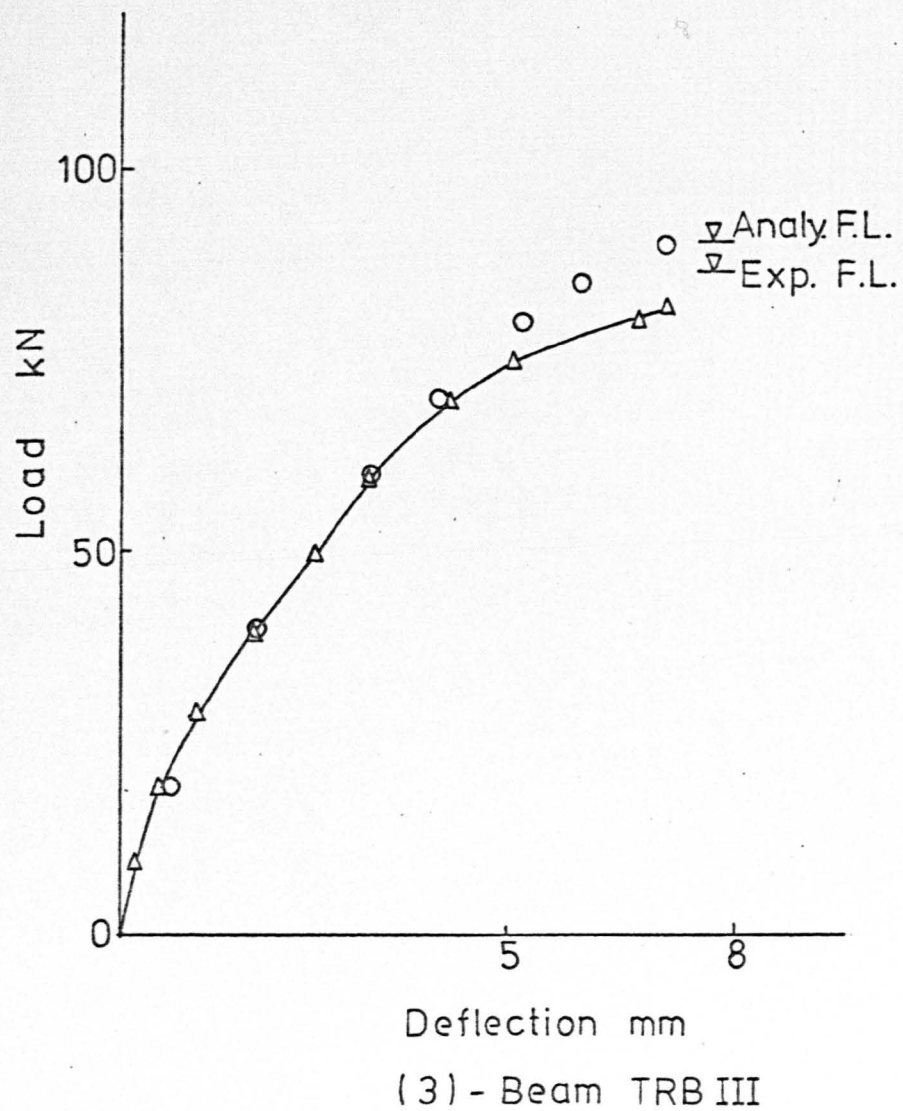


FIG. 7.3. Continued

this discussion is only on three beams, but it shows to some extent the effect of mesh size on predicting the ultimate strength of the beam, particularly in the areas where failure occurs.

Fig 7.4a, b, c and d, shows the crack patterns obtained from the analysis for beams TRB-I, TRB-II, TRB-III and TRB-IV respectively, while Fig 7.5a, b, c and d, shows the actual failure modes for the four beams respectively. The crack patterns from the analysis are plotted at intermediate load stage (60kN) and at ultimate load. As it has been discussed in Chapter 4, the stresses were calculated at the sampling points of the integration rule, hence cracking occurs at these points after checking the stresses with the failure laws. Thus each sampling point represents a cracked region of the element. The cracks were assumed to be perpendicular to the principal tensile stress. A crack at the sampling point is represented in the drawing by parallel lines \parallel in the direction of the crack and representation for the location of the sampling points and the cracks are shown in Fig 7.4a for one element in the 2-dimensional case.

In the experiment the cracks first appeared in the four beams at the tension side of the web and propagated vertically towards the flange with increasing load. Cracks also appeared at the head of the preformed crack and propagated diagonally towards the underside of the flange until it reached the flange-web junction and extended along it as the load increased. Before reaching the ultimate stage the flange began to crack and failure occurred by the rapid

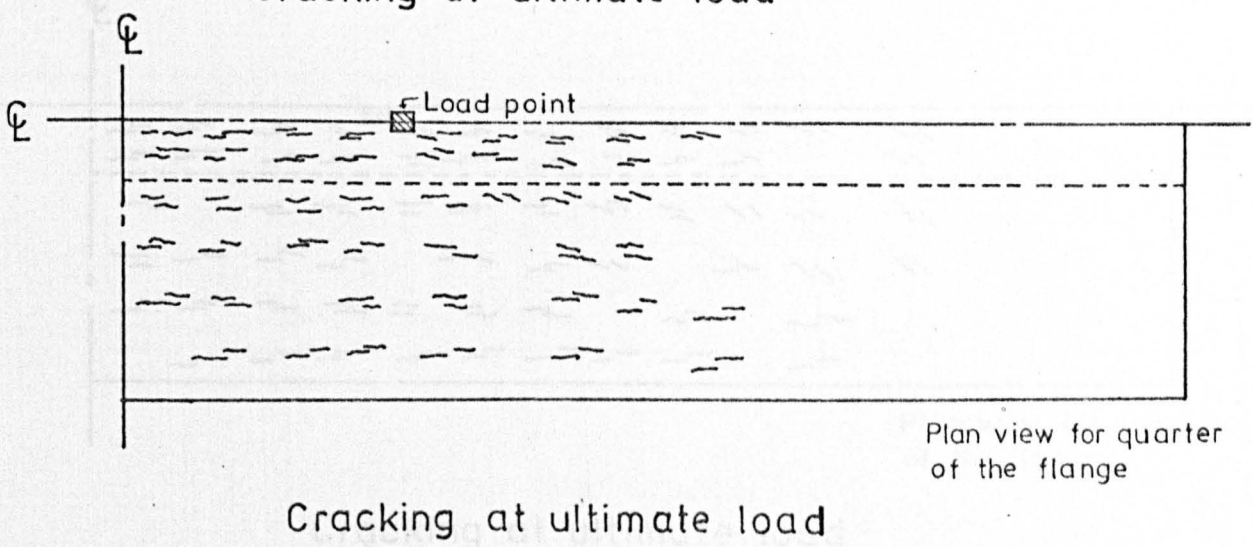
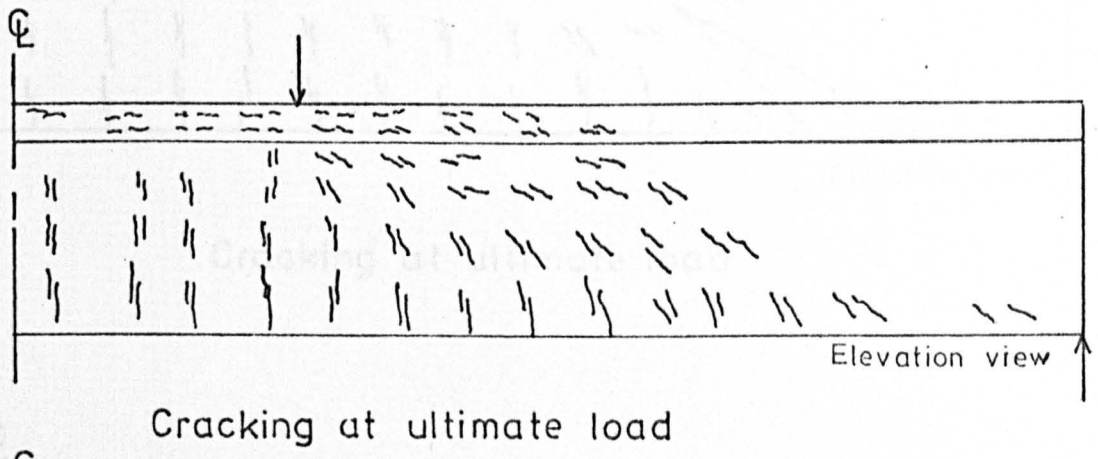
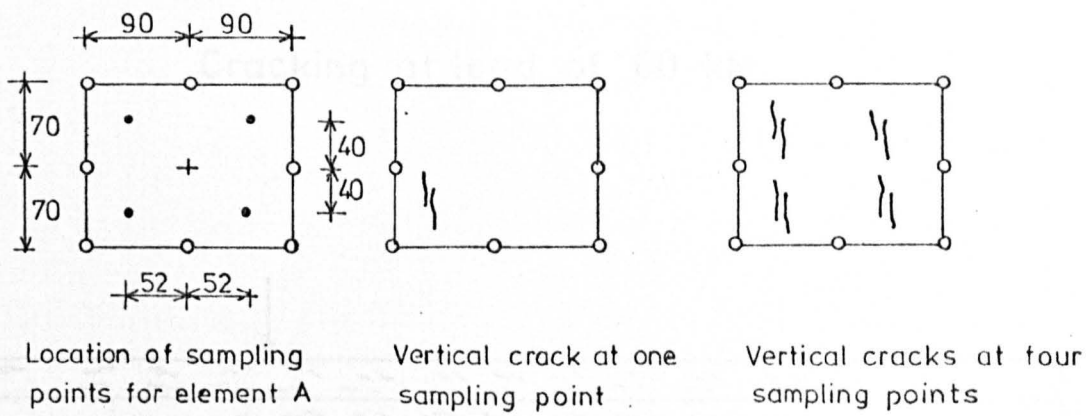
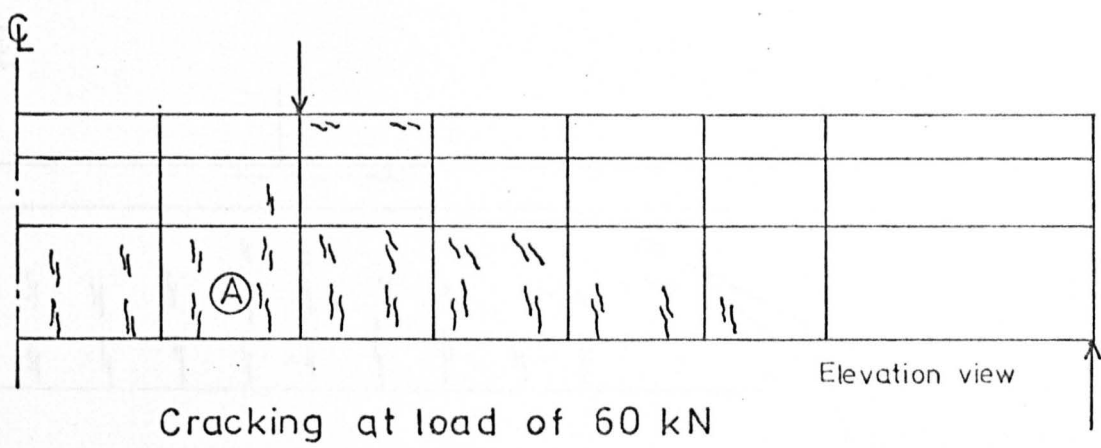
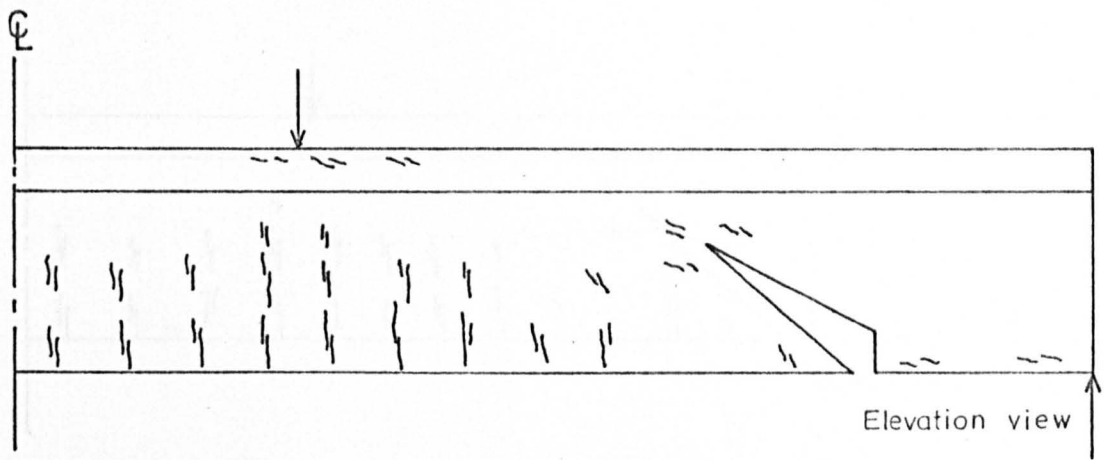
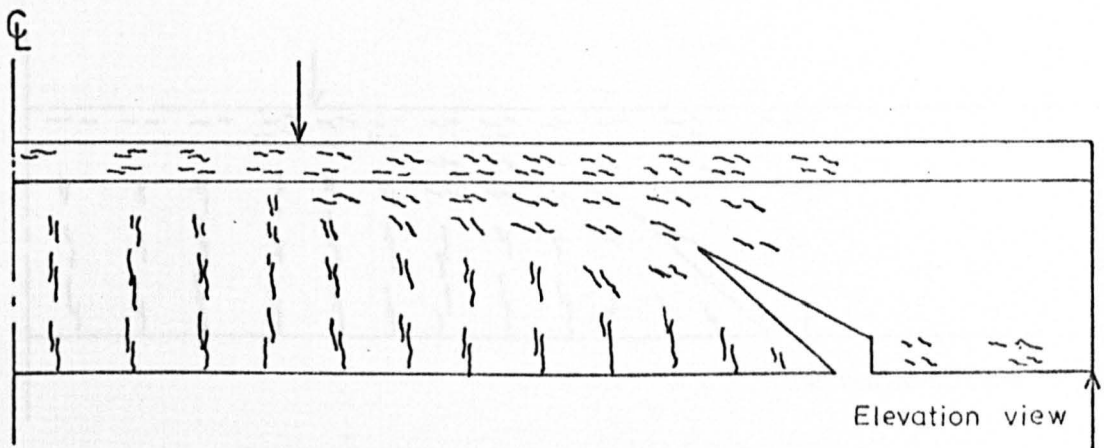


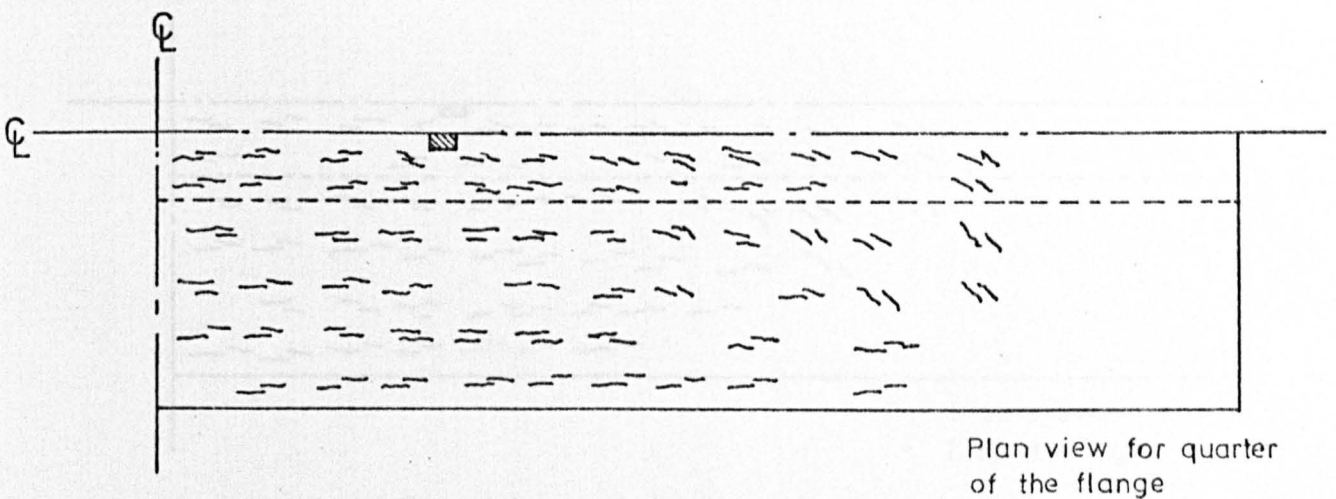
FIG.7.4. a. CRACK PATTERNS RESULTING FROM ANALYSIS - BEAM TRB-I



Cracking at load of 60 kN

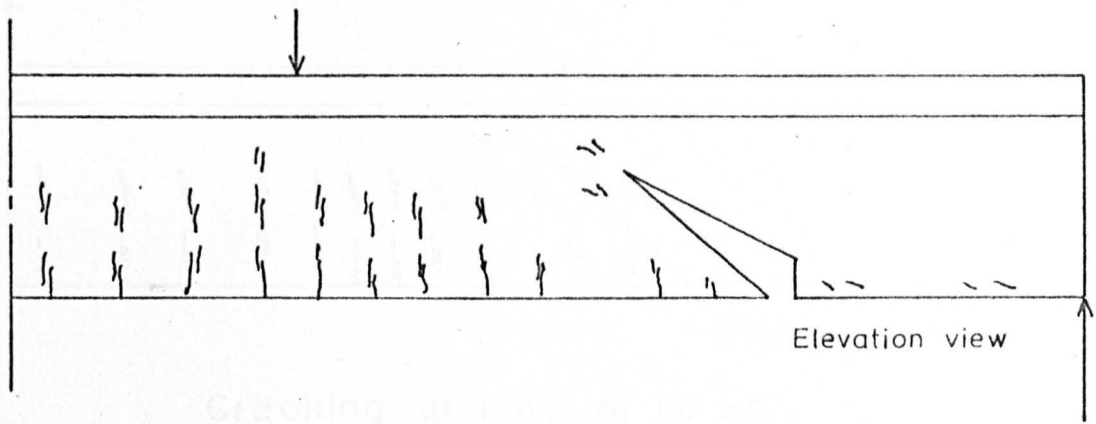


Cracking at ultimate load

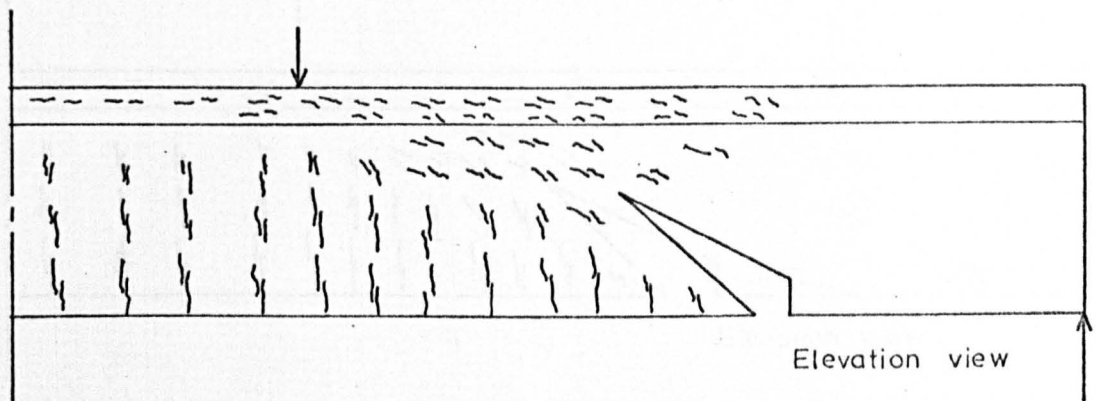


Cracking at ultimate load

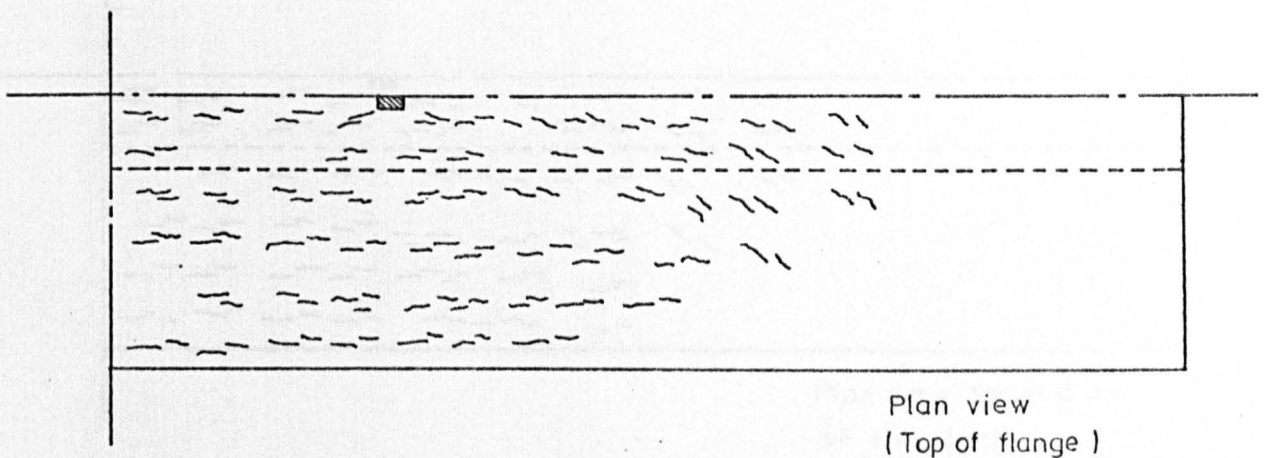
FIG.7.4. b. CRACK PATTERNS RESULTING FROM ANALYSIS - BEAM TRB - II



Cracking at load of 60 kN

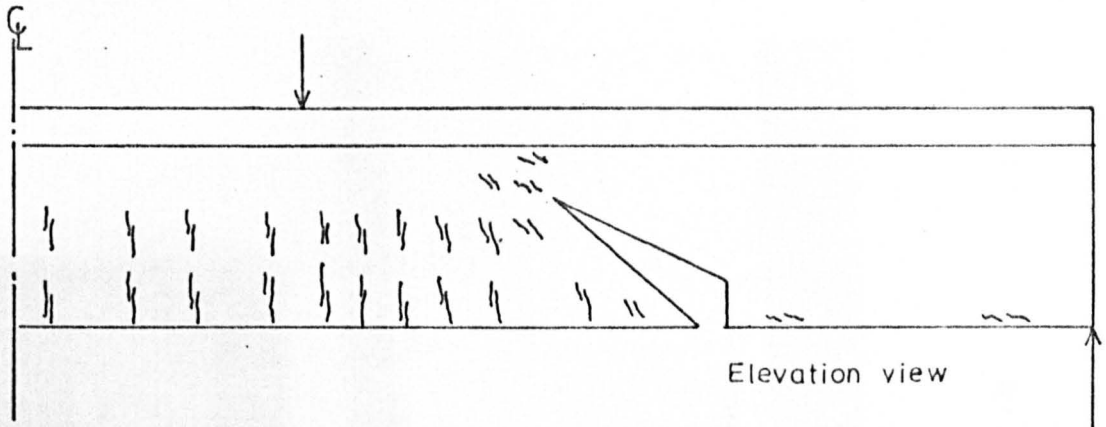


Cracking at ultimate load

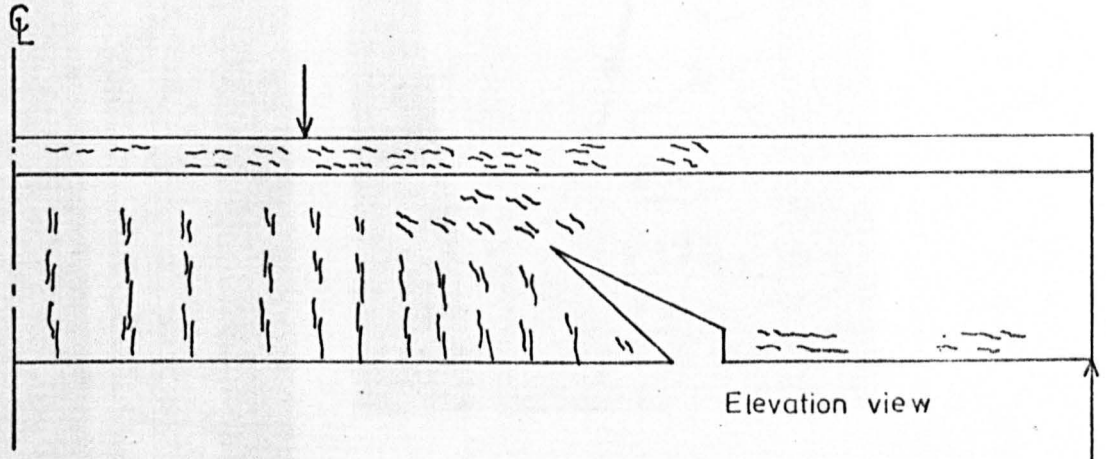


Cracking at ultimate load

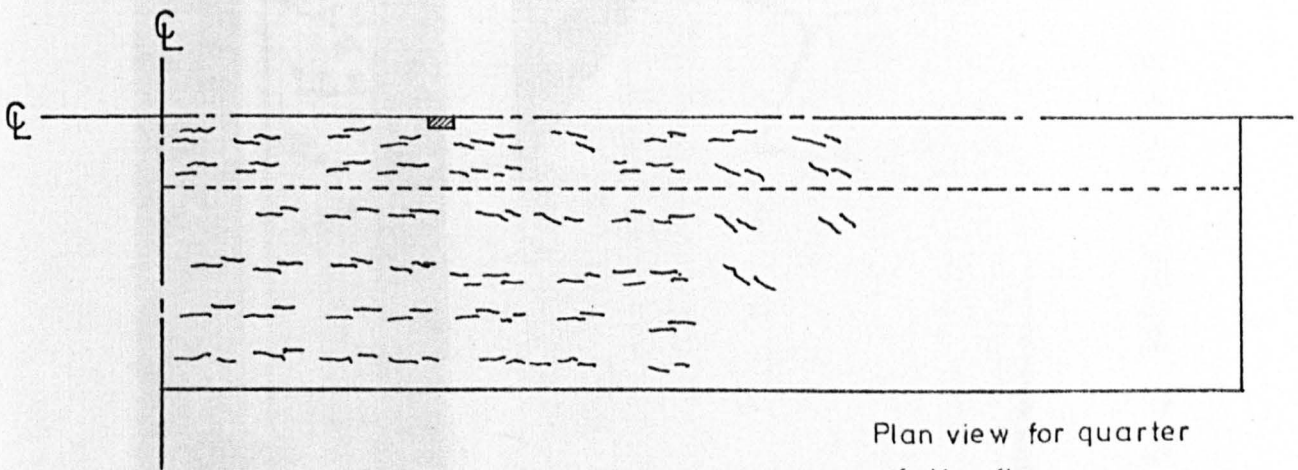
FIG.7.4. c. CRACK PATTERNS RESULTING FROM ANALYSIS - BEAM TRB - III



Cracking at load of 60 kN



Cracking at ultimate load



Cracking at ultimate load

FIG.7.4. d. CRACK PATTERNS RESULTING FROM ANALYSIS - BEAM TRB-IV

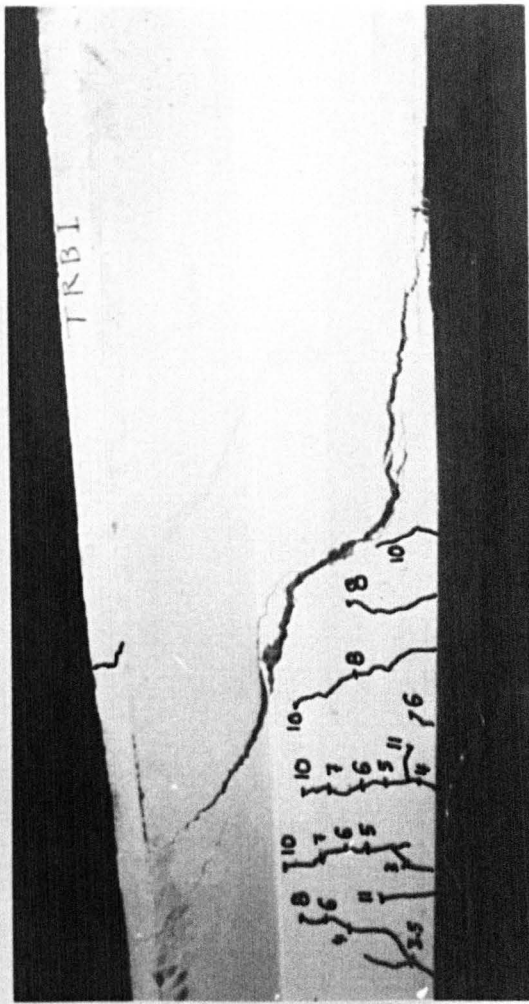
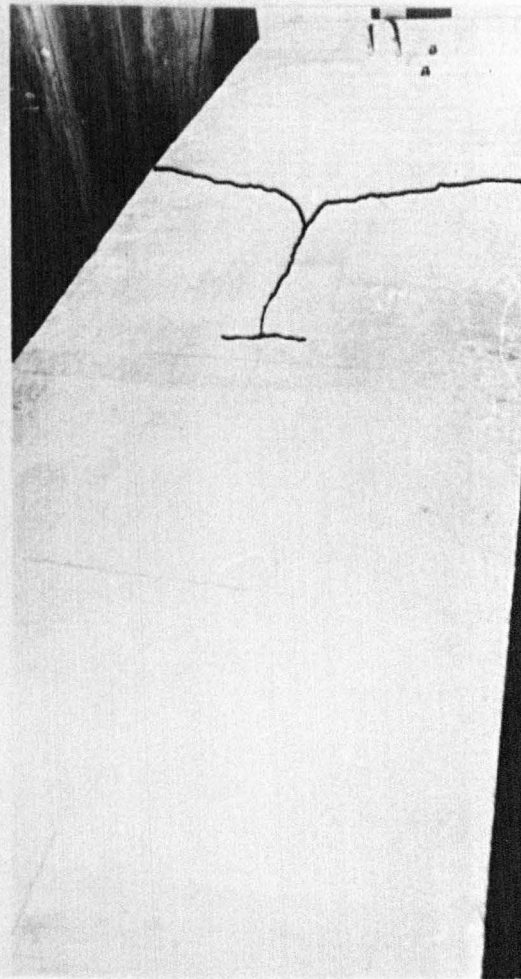
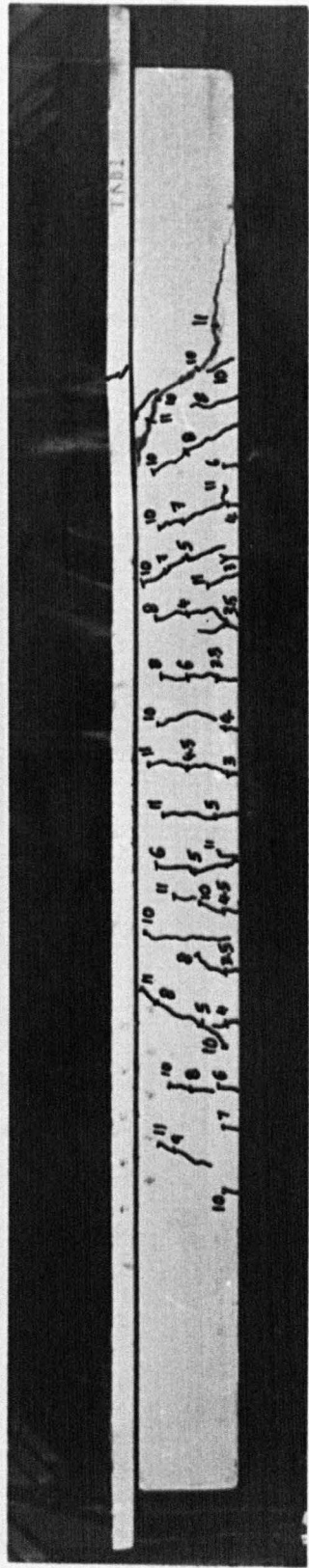


FIG.7.5. a. MODES OF FAILURE - BEAM TRB I , $B/b_0 = 4$ & $t/h = 0.167$

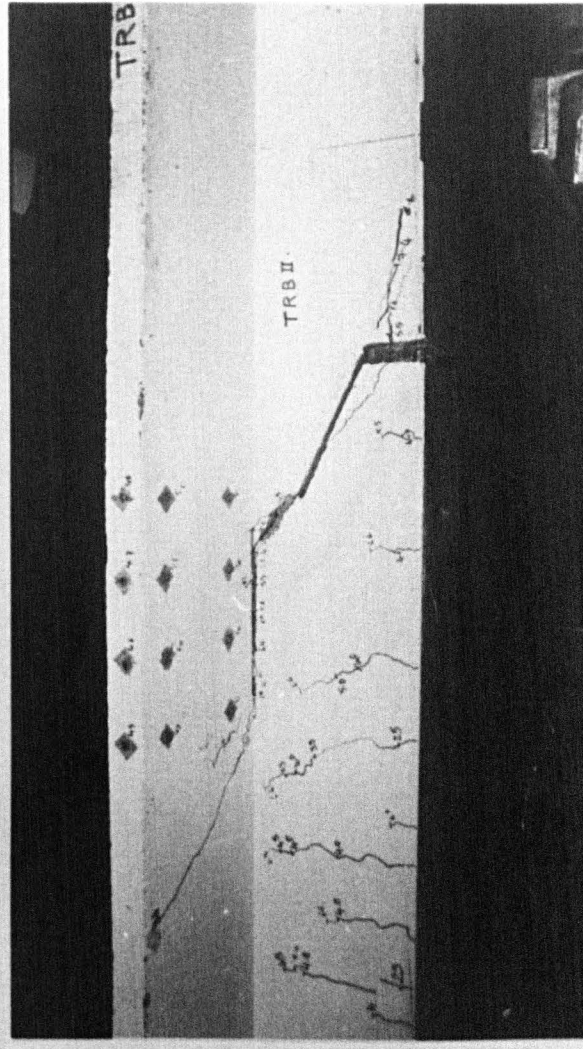
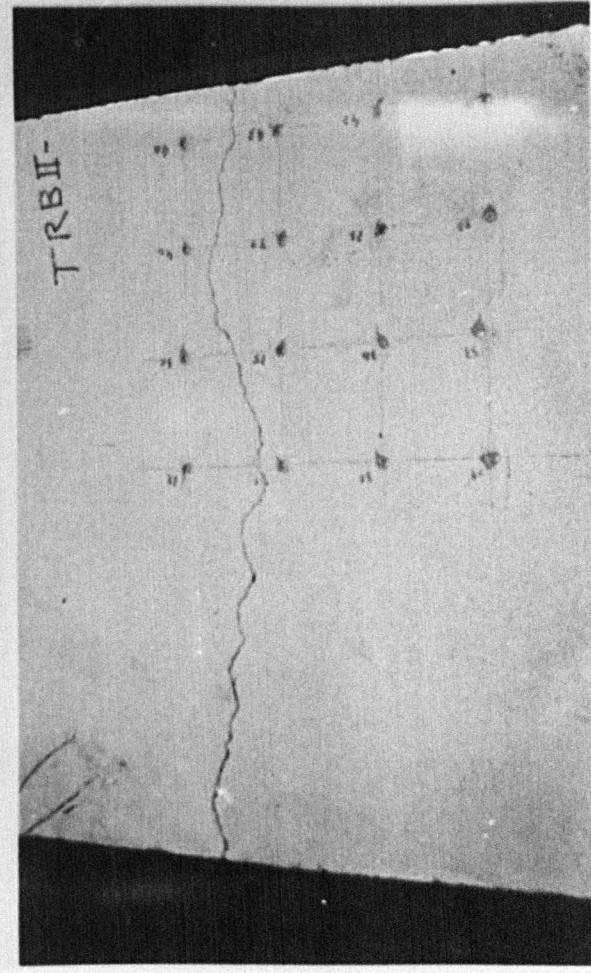
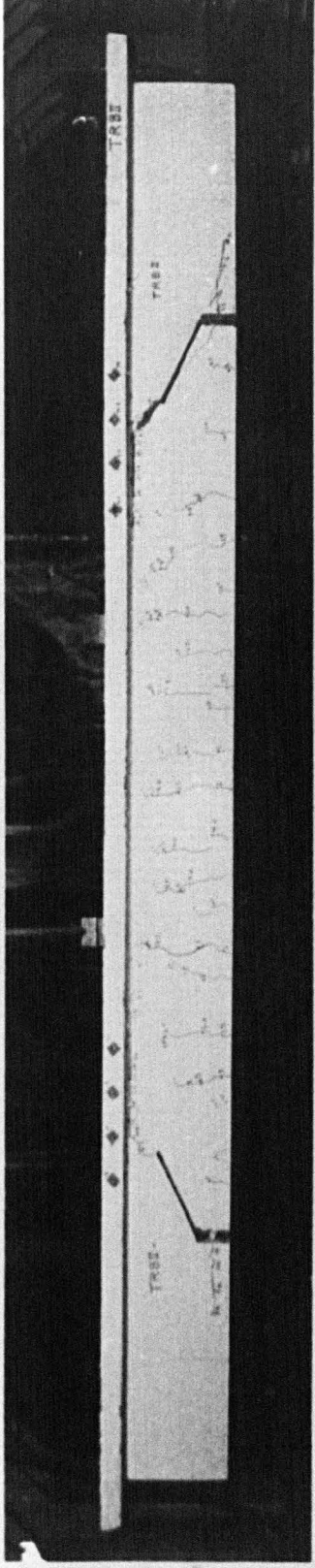


FIG. 7.5. b. MODES OF FAILURE - BEAM TRBII , $B/b_0 = 4$ & $t/h = 0.167$

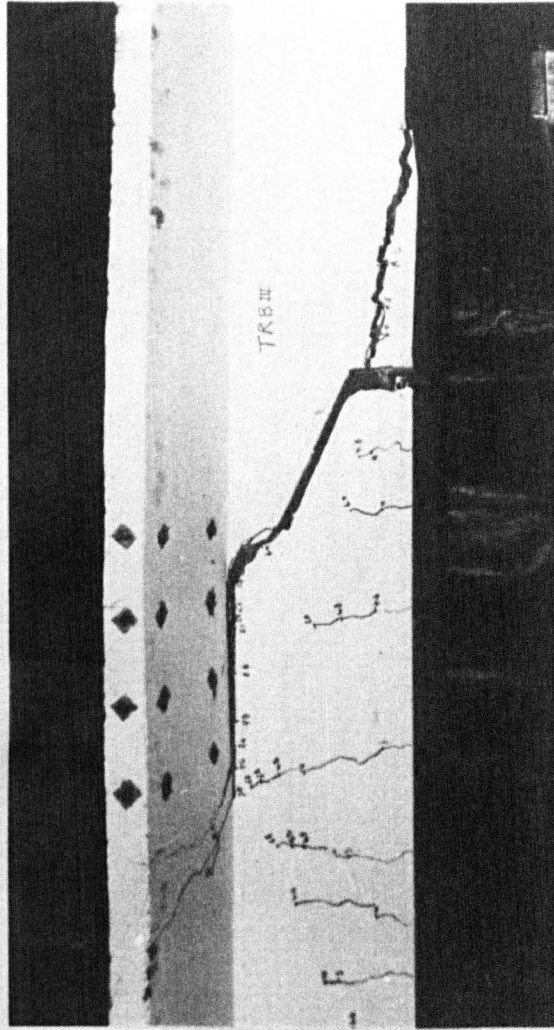
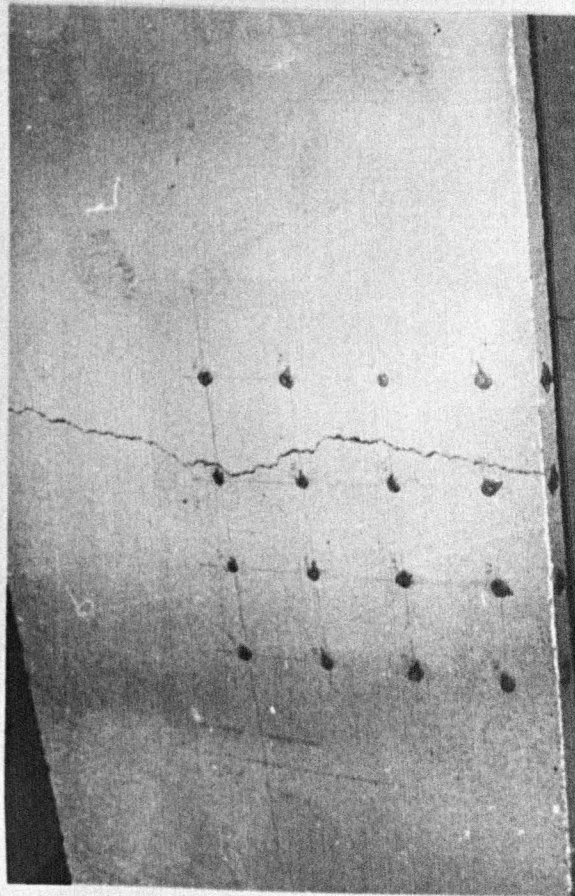
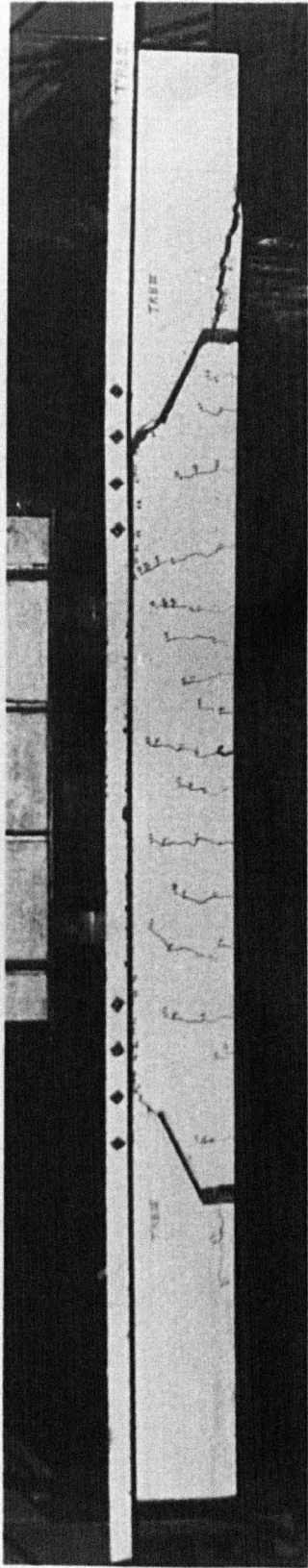


FIG. 7.5.c. MODES OF FAILURE - BEAM TRBIII, $B/b_0 = 4$ & $t/h = 0.167$

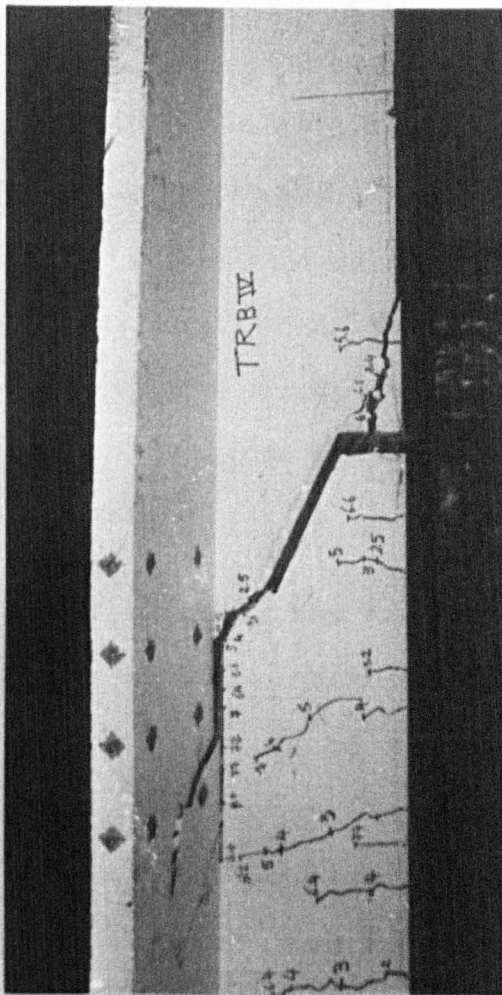
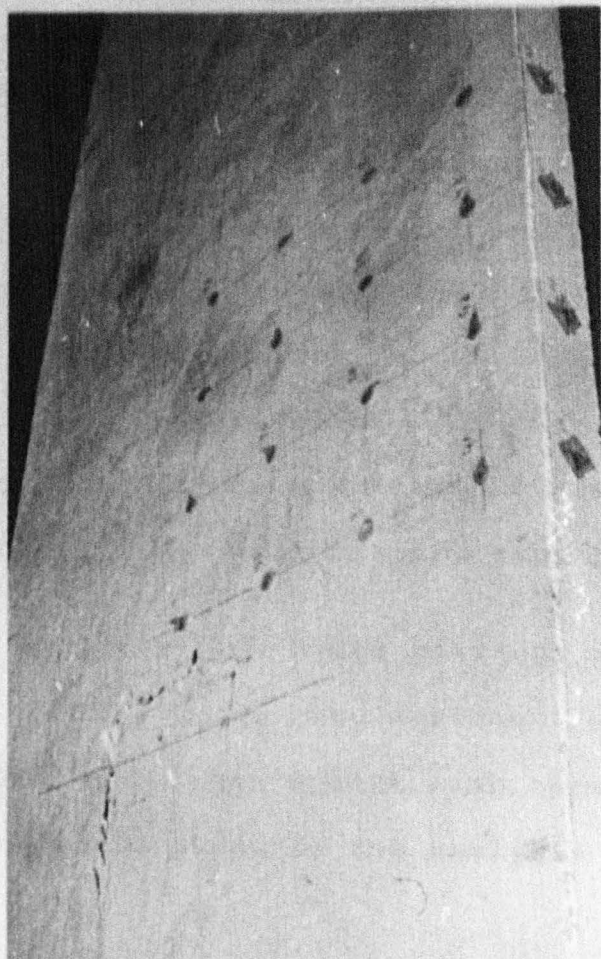
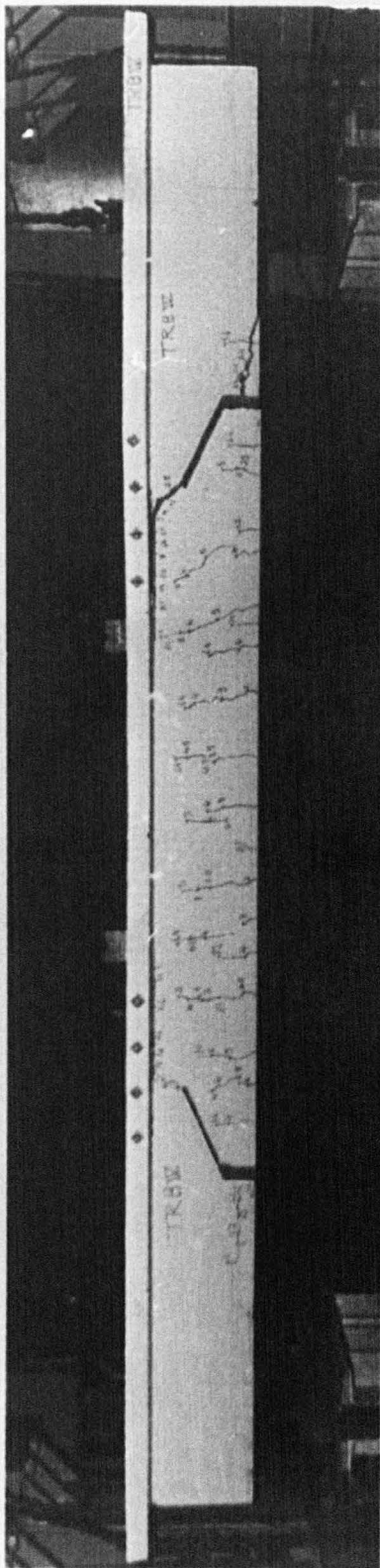


FIG. 7.5. d. MODES OF FAILURE - BEAM TRB IV, $B/b_0 = 4$ & $t/h = 0.167$

development of the cracks in the area of flange between the load and the preformed crack. In the full beam the main diagonal crack appeared at 100kN, propagated upwards until it reached the flange, then it turned up in the flange causing the failure. Horizontal splitting across the flange width occurred at the instant of failure. This splitting was due to the upward bending of the part of the flange over the preformed crack.

The crack patterns resulting from the analysis (Fig 7.4) for the four beams indicates that cracking at early stages of loading was in the tension side of the web, then extended upwards. As discussed above, cracks are defined to be at certain sampling points of the element, thus the distribution of cracks in the tension zone is regular. The cracks also, in this context, have an average meaning due to each sampling point representing the average material properties for a part of the element. In the actual beam the distribution of cracks is irregular due to the fact that the concrete is a non-homogeneous material and the appearance of the surface cracks depends on the internal microcracks. Remembering the assumptions in the analysis and the factors governing the appearance of cracking in the actual beam, it is difficult to compare the number and spacing of cracks between both the analysis and experiment.

The directions and shape of the crack patterns in the web resulting from the analysis is in good agreement with those from the experiments. Inclined cracks also appeared around the head of the preformed crack in the analysis and

this simulates the propagation of cracks diagonally along the preformed cracks in the actual beams. With increasing the load, cracks appeared in the area of the web between the head of the preformed crack and the load point with inclination very close to the horizontal and these are analogous to the extension of the cracks along the web flange junction in the tests. At the same time cracks start to occur in the flange with inclination in the area over the preformed crack and tend to be in horizontal direction in the areas near the load point. These cracks continued in the flange resulting in increased displacements until the solution diverges indicating the failure of the beam. The horizontal splitting across the flange width appeared at failure in the tests, has not been predicted explicitly in the analysis. This splitting could be a local effect of the failure of this part of the beam due to the separation and bending up of this part of the flange from the web. Another reason could be that the cracks in the flange are predicted by the failure criteria based on octahedral normal and shear stresses which do not define a certain direction for the fracture pattern and it is adopted in the analysis by assuming the cracks to be perpendicular to the direction of the principal tensile stresses as discussed in Chapter 4. In the full beam, the crack pattern from the analysis showed inclined cracks representing the actual diagonal crack. These cracks appeared in the analysis at load 110 kN, while in the test, the diagonal crack appeared at 100 kN.

7.2.3 Beams with Different Flange Width and Thickness

This series of beams has been classified into three groups. Each group contains three beams with the same flange width but of different thicknesses. The finite element idealisation for these groups is shown in Figs 7.2.b and 7.2c.

7.2.3.1 Group 1

The flange width for these beams was 350 mm ($B/b_o = 2$), and the thickness ranged from 50 to 90 mm ($t/h = .167 - .3$). The beams are referenced TBX I, TBX IV and TBX VII. Twenty-eight elements were used in the finite element model of the quarter beam. Six load increments were applied in the analysis with two cycles in each, until the last two increments, where the number of cycles increased to four.

The comparison of the experimental and analytical load-deflection curves is shown in Fig 7.6, where it can be seen that satisfactory agreement was achieved. In the case of beam TBX VII, the analytical solution underestimated the experimental results. The discrepancy in deflection and strength before failure is believed to be due to the effect of dowel action which was ignored in the analysis. This is especially true for beams with stiffer reinforcement bars such as beam TBX VII of this group (y 20).

The crack patterns and the spread of the crack zones resulting from the analysis at intermediate load stage and at ultimate load are shown in Fig 7.7. The actual cracking

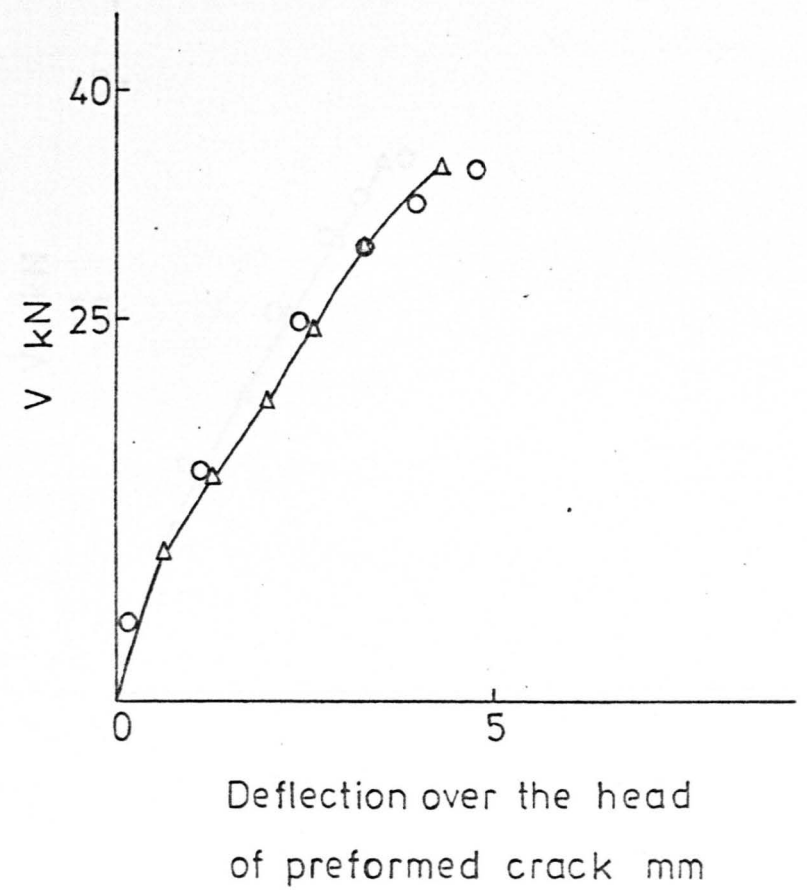
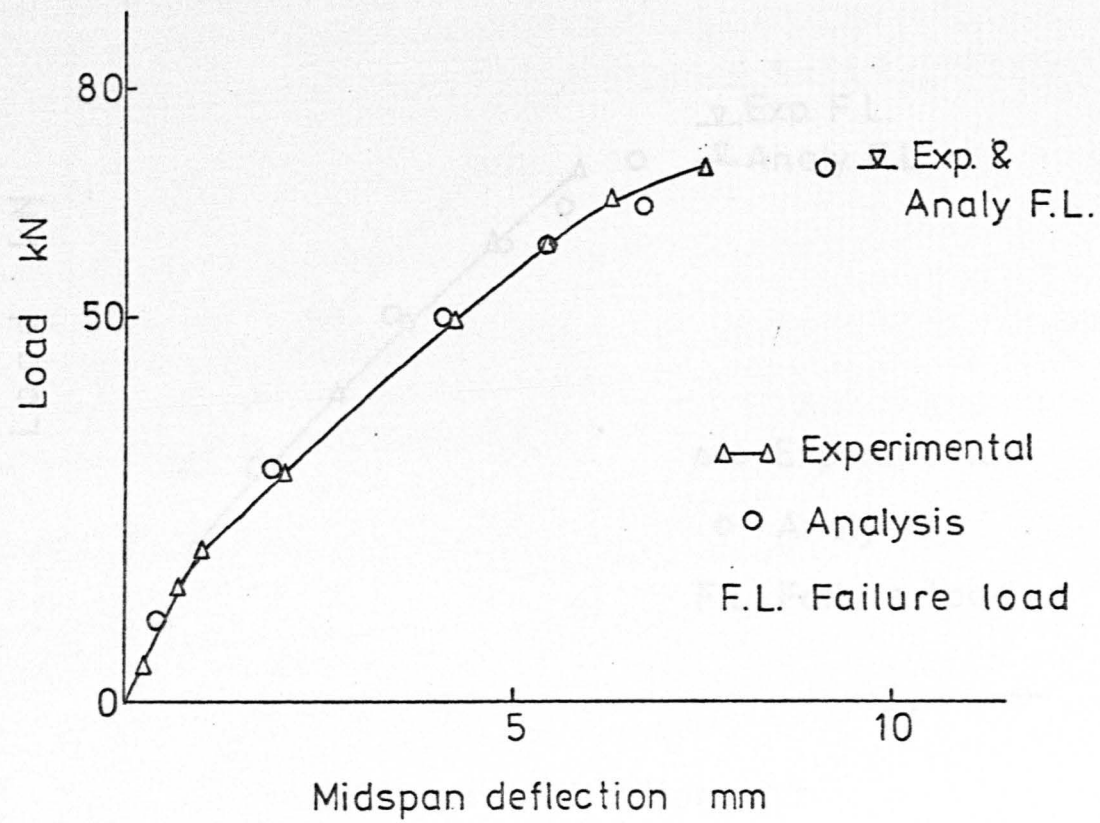


FIG. 7.6.a. LOAD - DEFLECTION CURVES - BEAM TBX - I

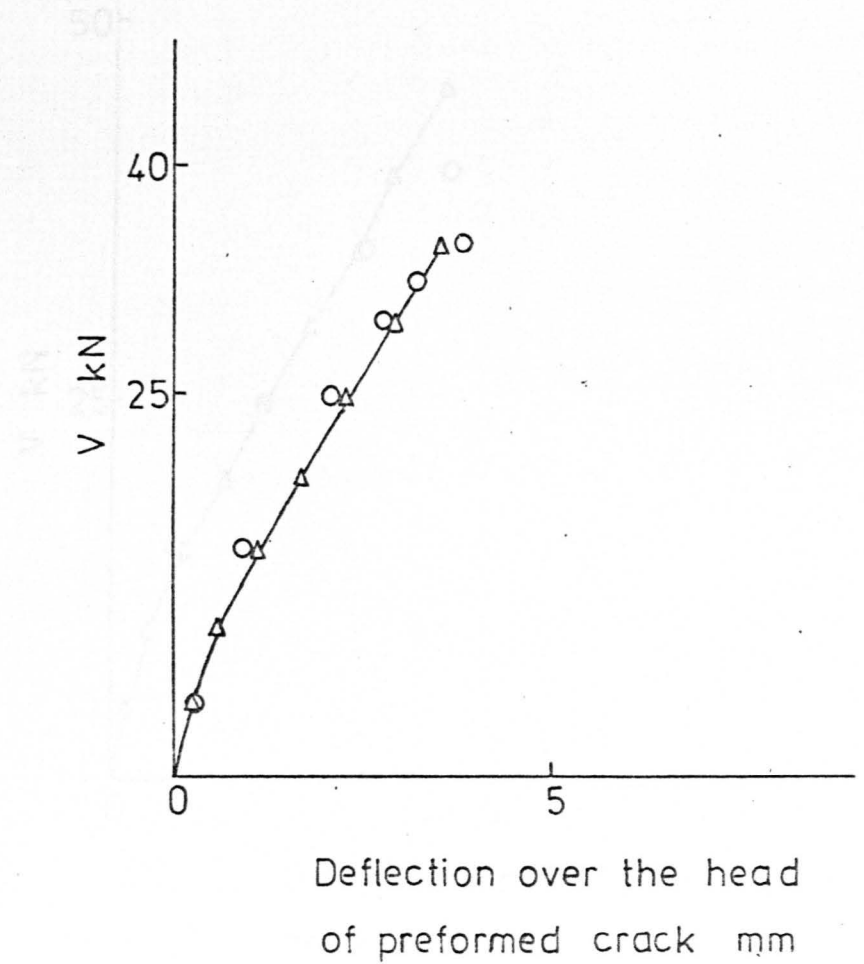
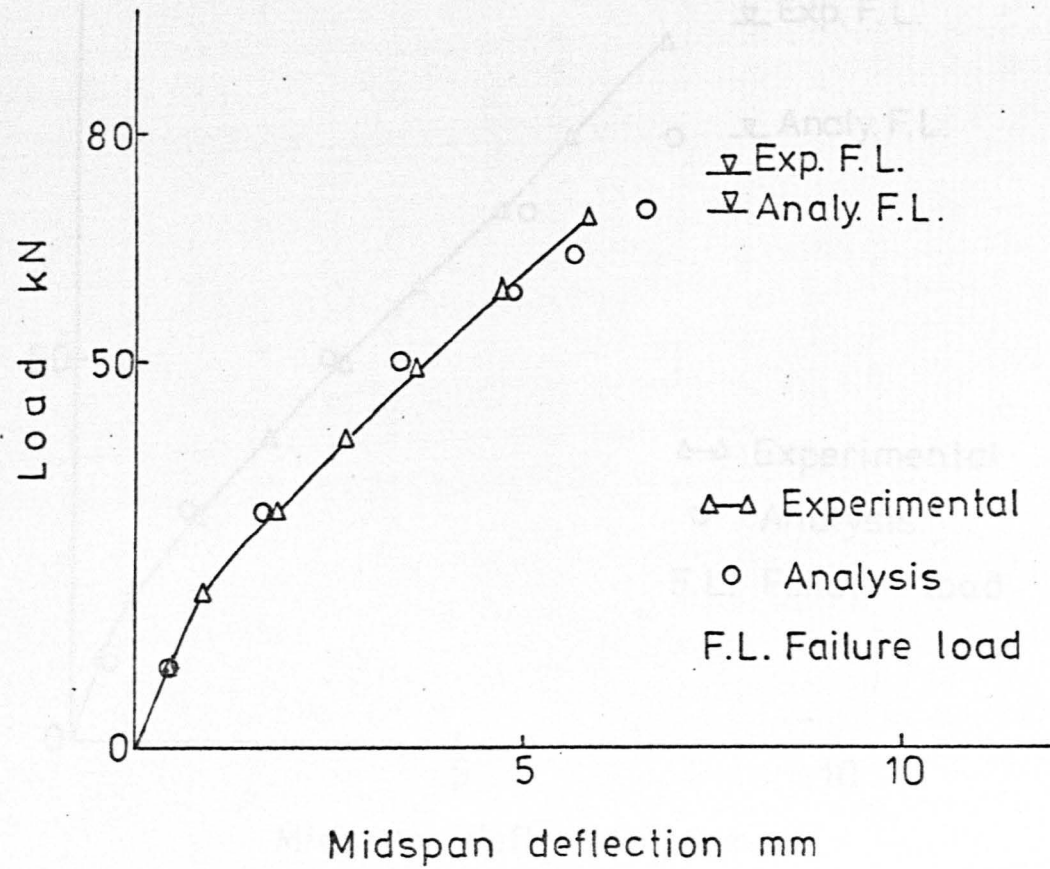


FIG.7.6.b. LOAD - DEFLECTION CURVES - BEAM TBX - IV

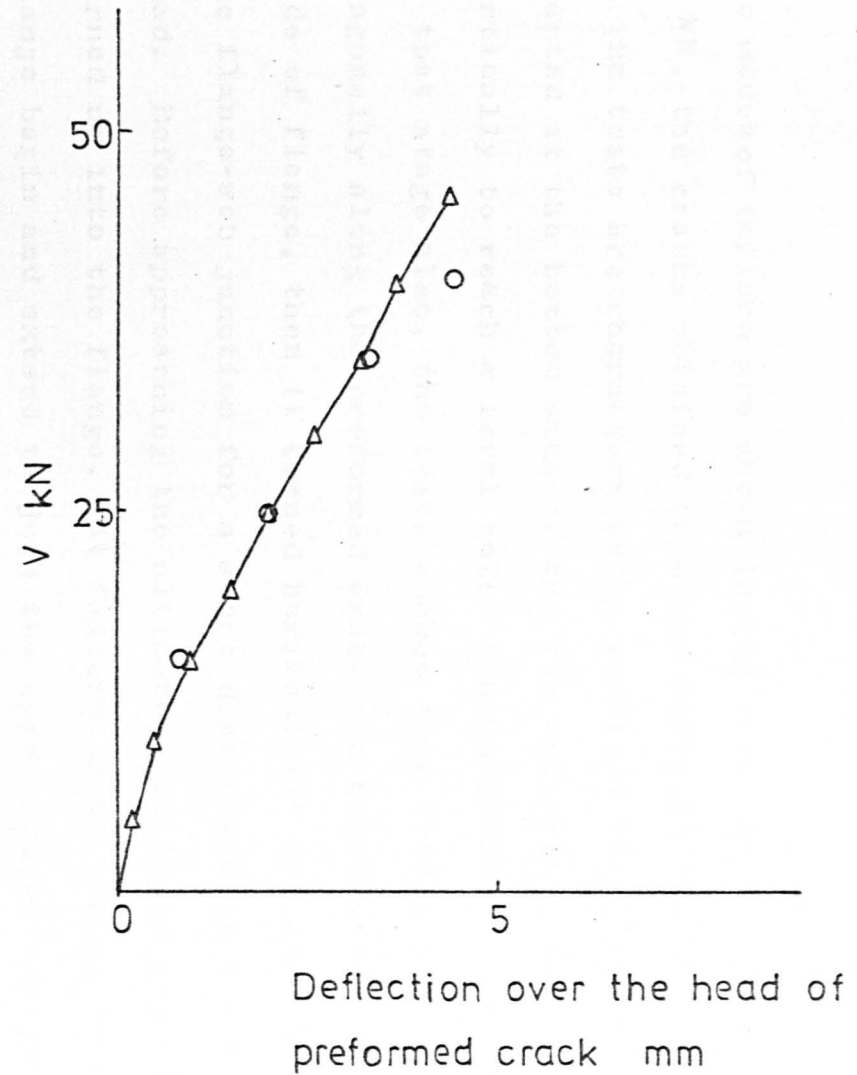
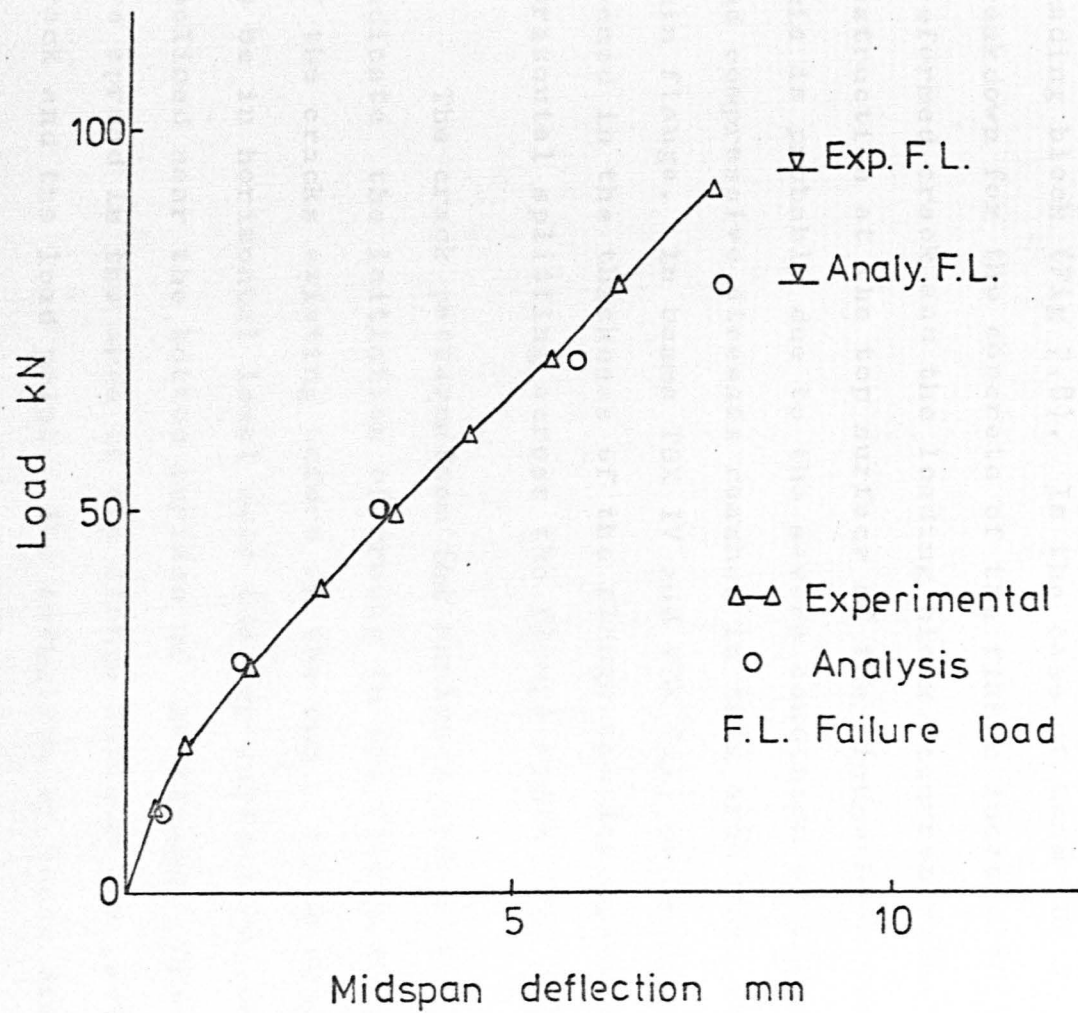
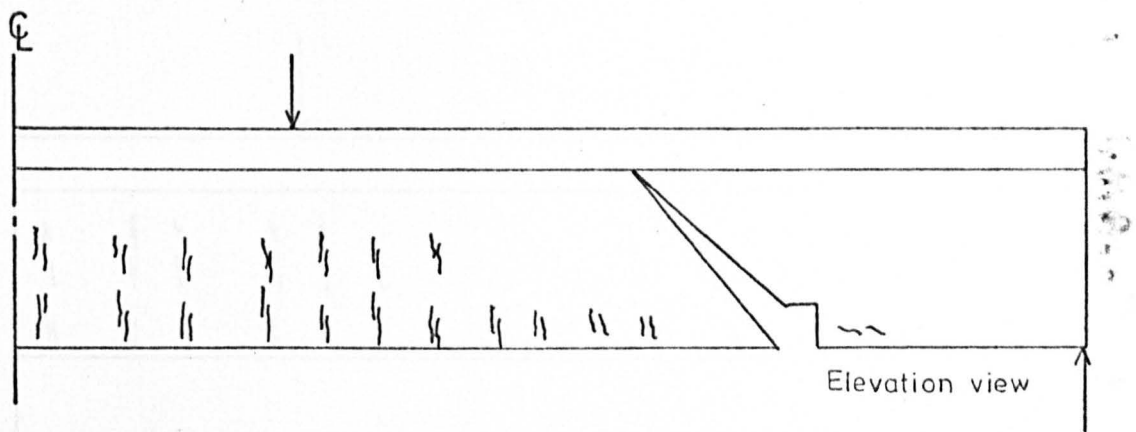


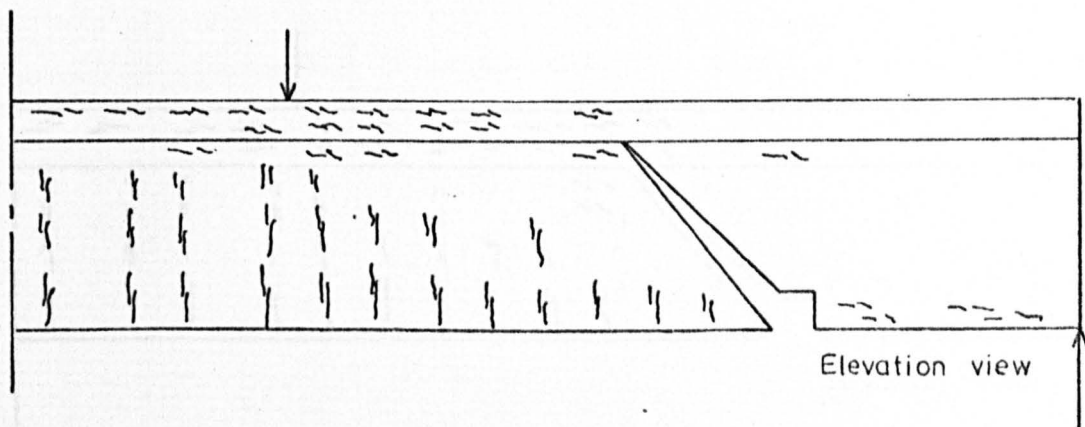
FIG. 7.6. c. LOAD - DEFLECTION CURVES - BEAM TBX-VII

and modes of failure are shown in Fig 7.8. At load level of 50 kN, the cracks obtained from the analysis and observed in the tests are characterised by vertical flexural cracks started at the bottom side of the web and propagated vertically to reach a level below the underside of flange. At that stage also, the tests showed that cracks propagated diagonally along the preformed crack and reached the underside of flange, then it turned horizontally and ran along the flange-web junction for a short distance with increasing load. Before approaching the ultimate load these cracks turned up into the flange. At failure shear cracks in the flange begin and extend to join the upper end of the preformed crack and the top surface of the flange near the loading block (Fig 7.8). In the case of beam TBX I, a breakdown for the concrete of the flange located between the preformed crack and the loading block occurred with little destruction at the top surface of the flange near the load. This is probably due to the severe condition of shearing and compressive stresses reached in this area with short and thin flange. In beams TBX IV and TBX VII, an inclined crack opened in the thickness of the flange and accompanied by a horizontal splitting across the flange width (Fig 7.8).

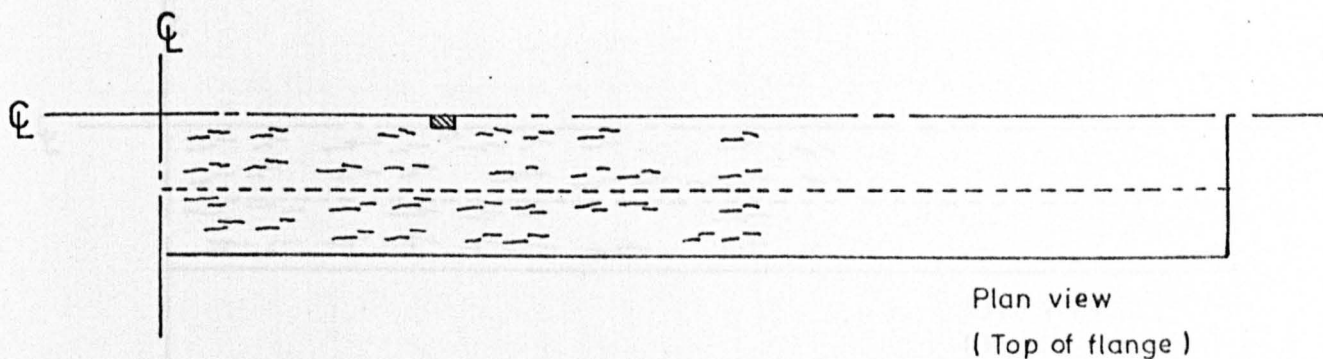
The crack patterns from the analysis shown in Fig 7.7 indicate the initiation of cracks in the flange separately of the cracks existing before in the web. These cracks tend to be in horizontal level near the top surface and slightly inclined near the bottom surface of the flange. Cracks are spread in the area of the flange between the preformed crack and the load point. The formation of these cracks



Cracking at load of 50 kN



Cracking at ultimate load



Cracking at ultimate load

FIG.7.7.a. CRACK PATTERNS RESULTING FROM ANALYSIS - BEAM TBX- I

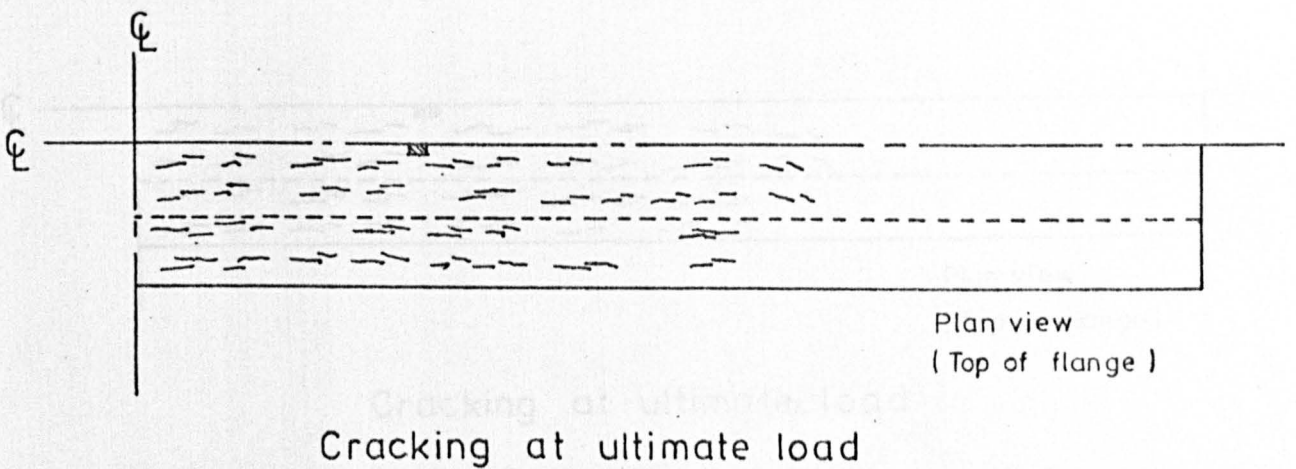
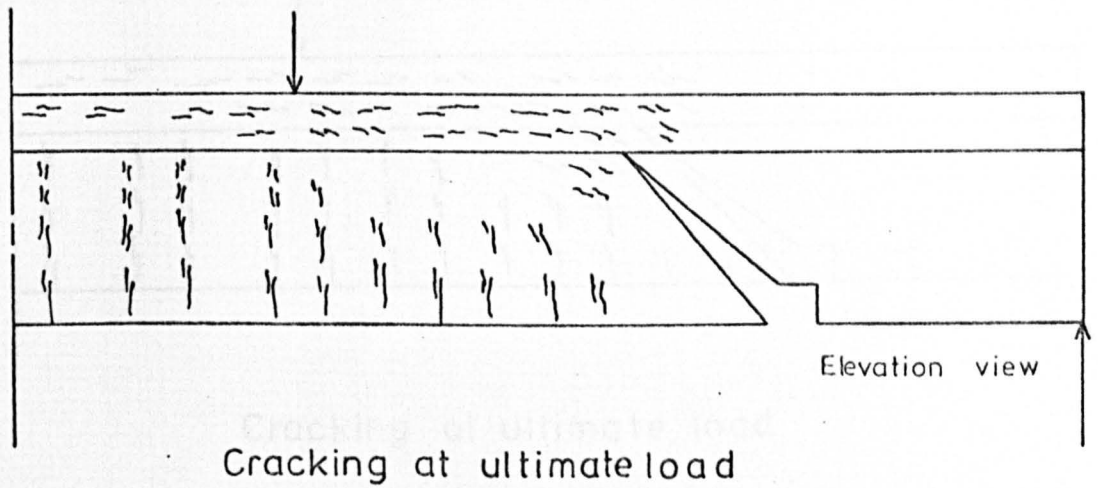
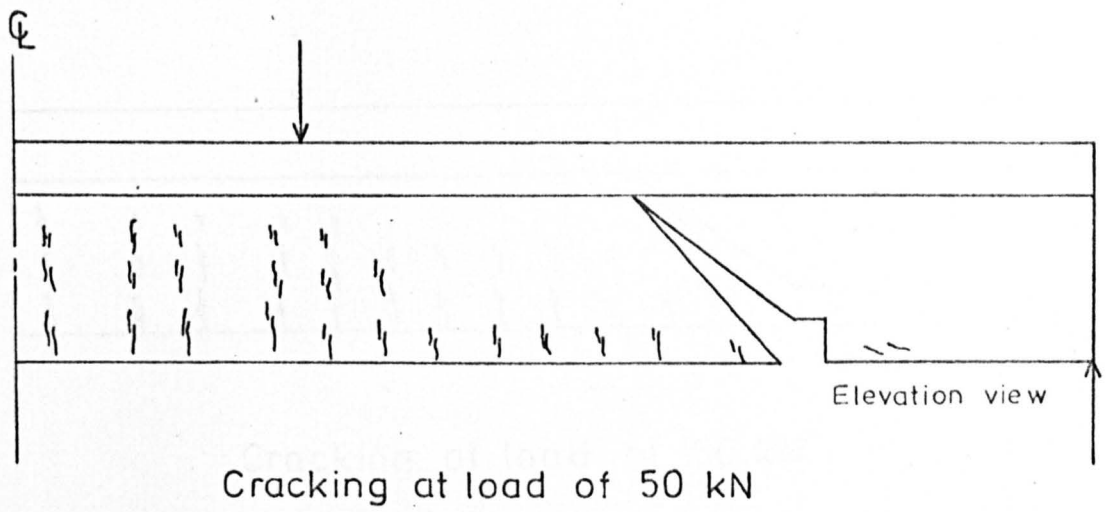
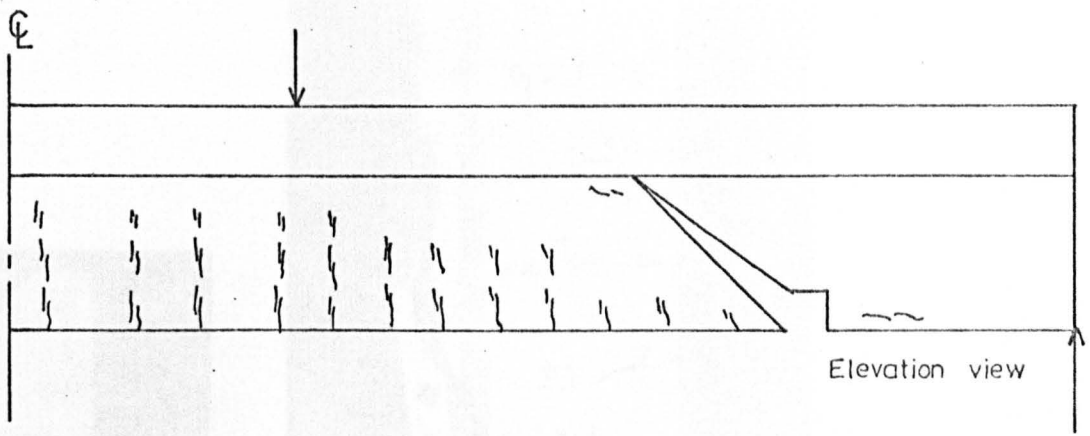
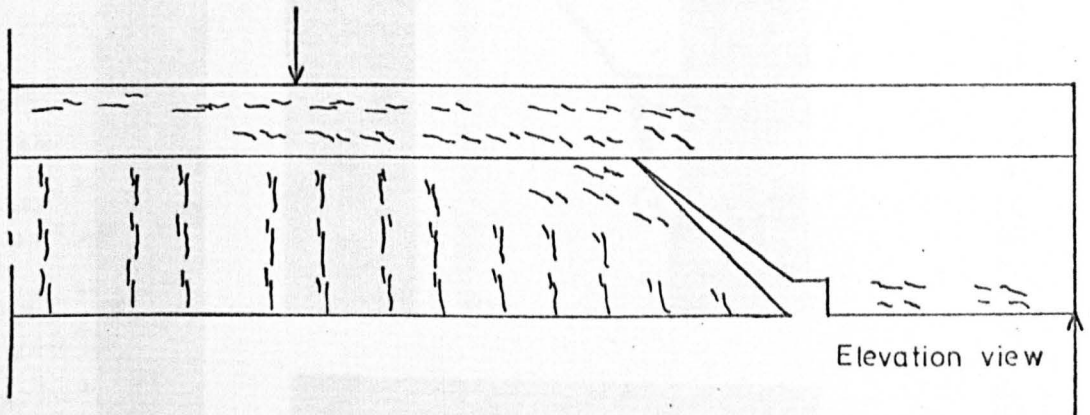


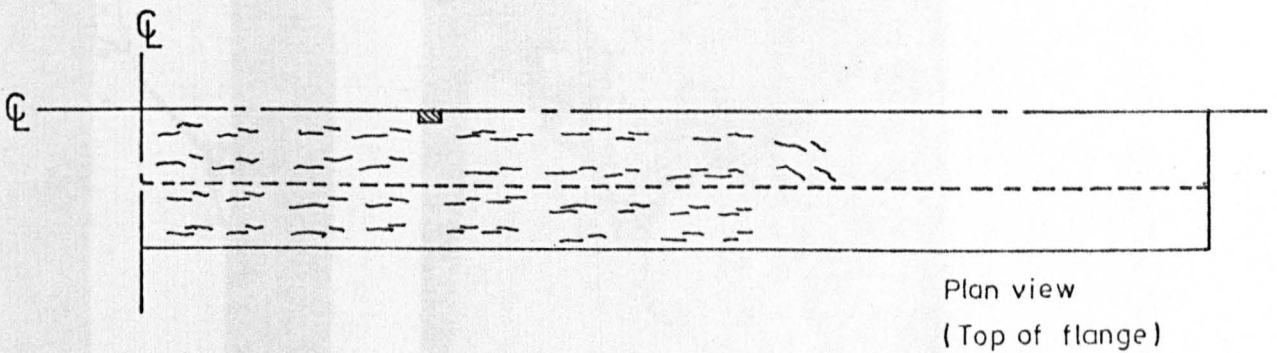
FIG. 7.7. b. CRACK PATTERNS RESULTING FROM
ANALYSIS - BEAM TBX - IV



Cracking at load of 50 kN



Cracking at ultimate load



Cracking at ultimate load

FIG. 7.7. c. CRACK PATTERNS RESULTING FROM ANALYSIS - BEAM TBX - VII

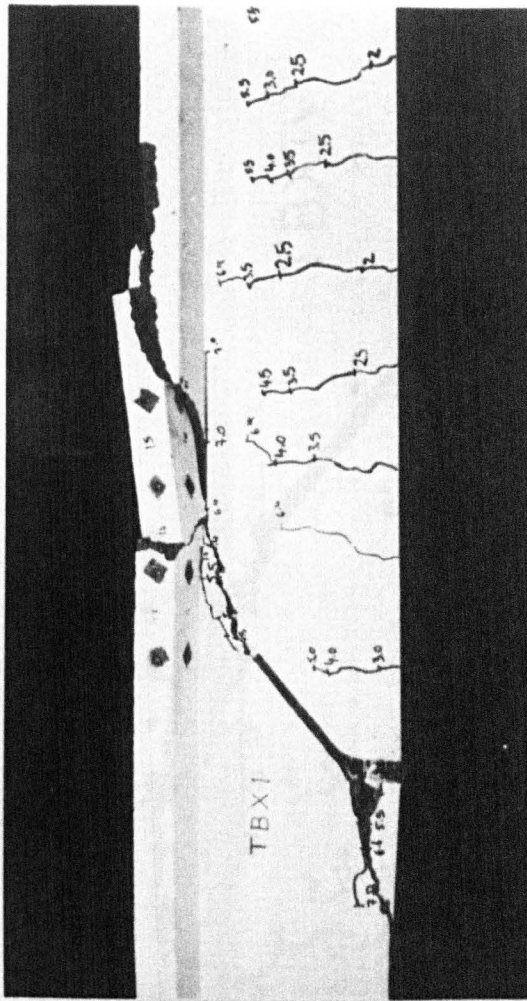
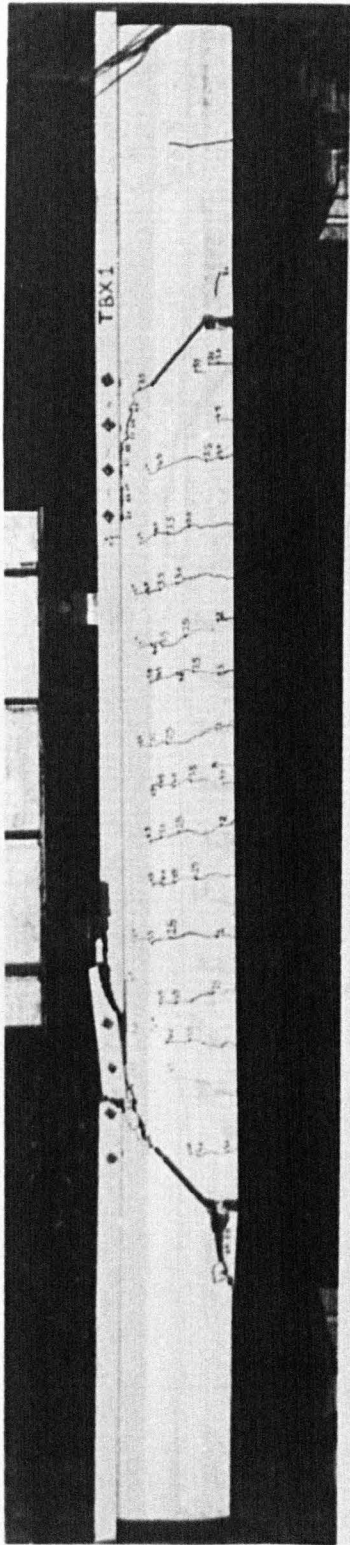


FIG. 7. 8. a. MODES OF FAILURE - BEAM TBX - I , $B/b_0 = 2$ & $t/h = 0.167$

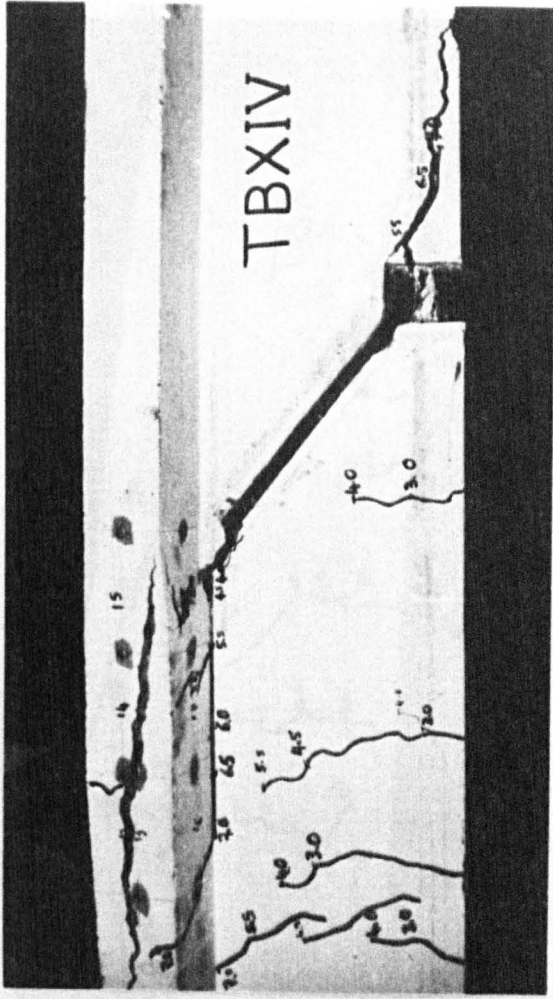
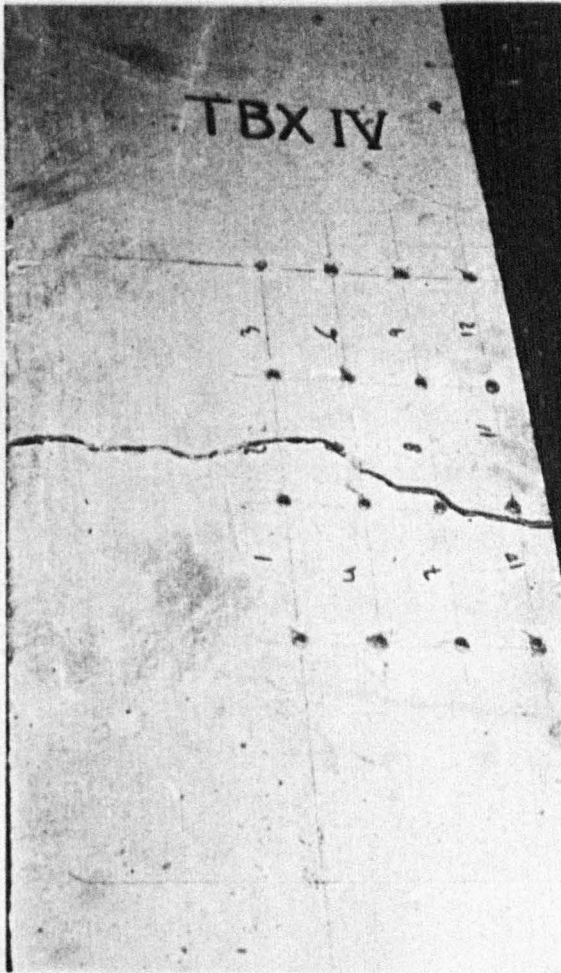
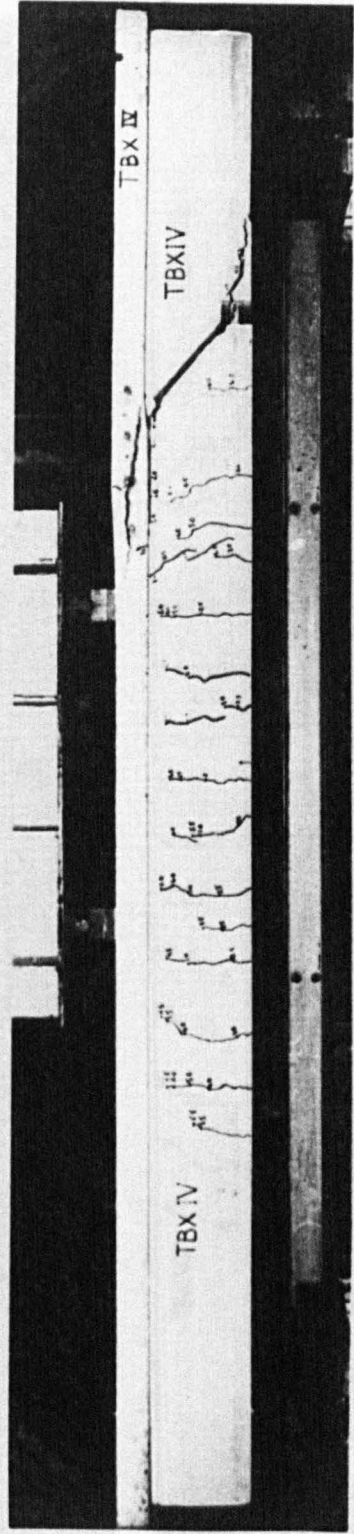


FIG. 7. 8. b. MODES OF FAILURE - BEAM TBX-IV , $B/b_0 = 2$ & $t/h = 0.233$

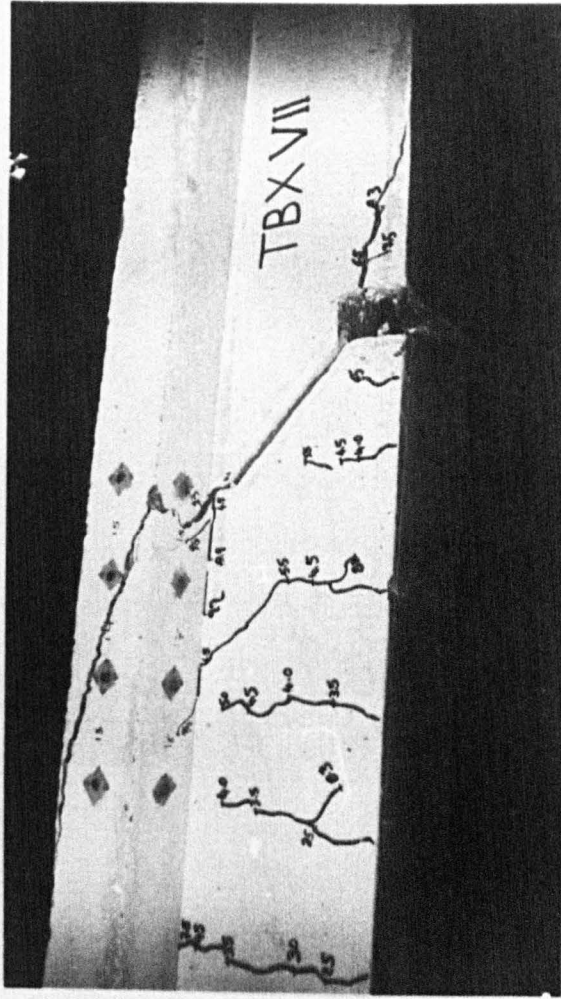
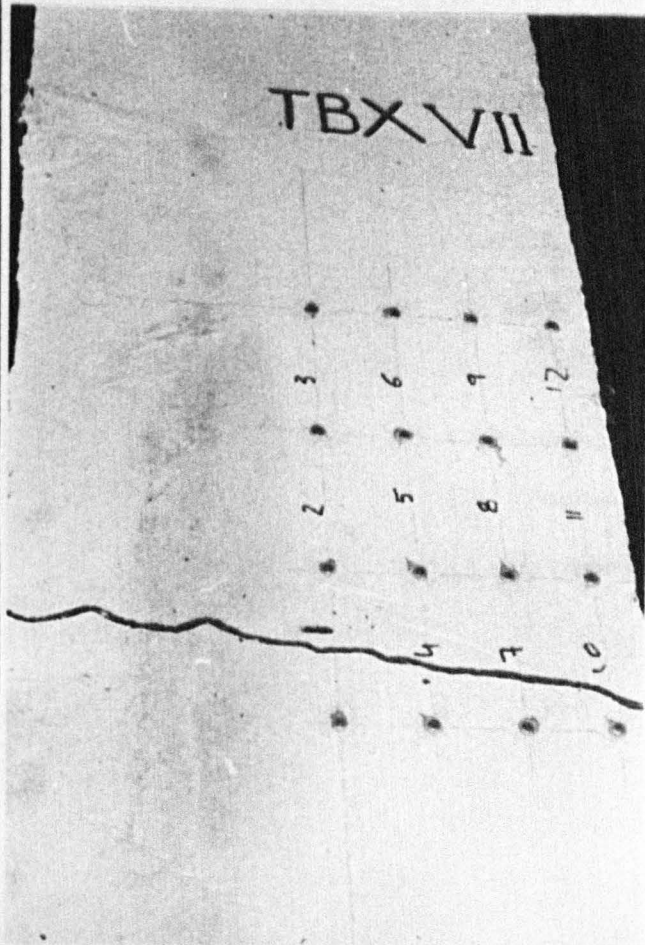
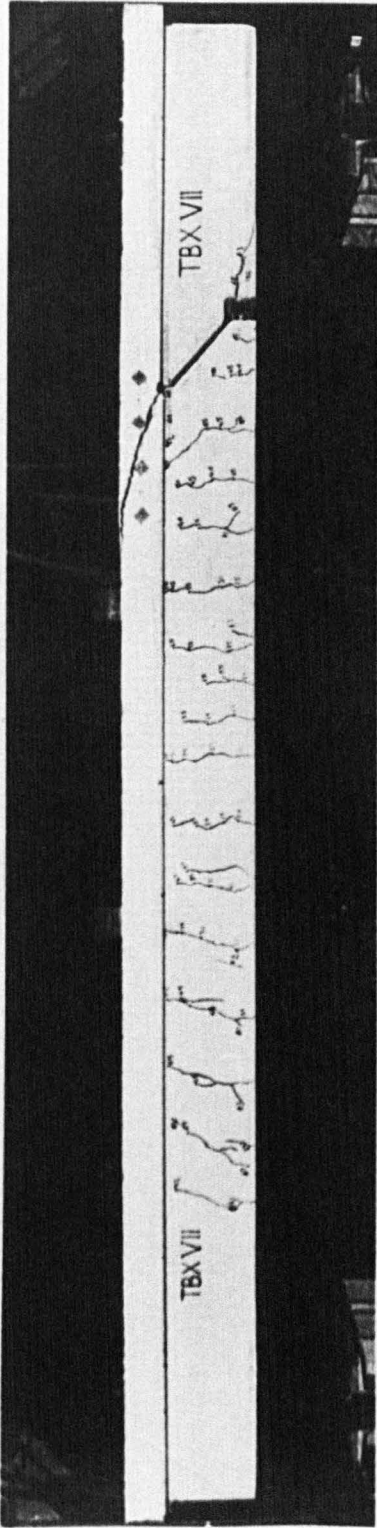
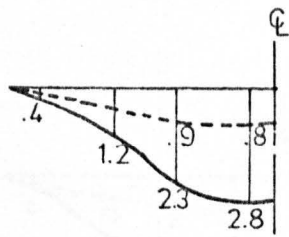


FIG. 7.8. c. MODES OF FAILURE - BEAM TBX - VII, $B/b_0 = 2$ & $t/h = 0.3$

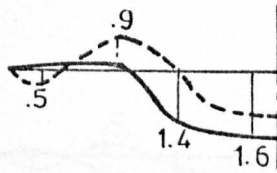
in the last load increment shows that failure occurred in the flange due to their appearance.

The measured steel strains from the tests and those calculated in the analysis showed that the main tensile reinforcement had not yielded.

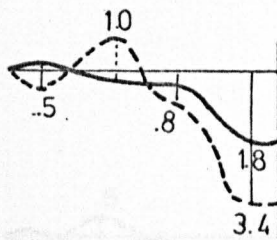
A plot for the shear stress distributions obtained from the analysis before failure is shown in Fig 7.9. The shear stresses are plotted at three sections across the half flange width in the shear span. Section 1, at a distance of 550 mm from the support, is located over the head of the preformed crack. Section 2 was at 860 mm from the support and Section 3 was at 1010 mm from the support, ie very near to the load point. The full line represents the shear stresses near the bottom surface of the flange and the dotted line near the top surface of the flange. The shearing force resisted by the flange was calculated by integrating the shear stresses at sec 1 across the flange width and taking an average stress value through the flange thickness. Table 7.1 shows the shearing forces for the three beams calculated from the analytical results and the shearing forces estimated from the experiments. The experimental values are the actual shear forces on the beams reduced by the forces carried by the shear links existing in the area between the preformed crack and the support. More details will be given in Chapter 8 about calculating these forces.



Sec.1 at 550 mm from the support



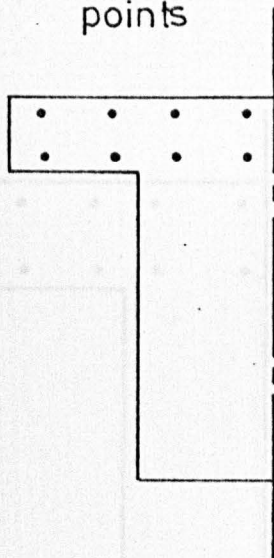
Sec.2 at 860 mm from the support



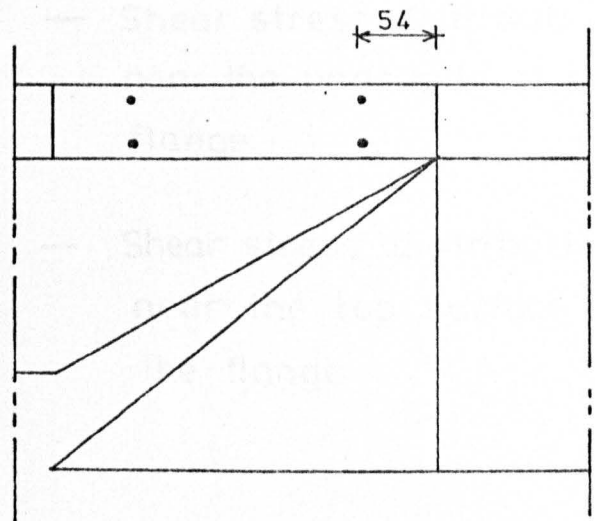
Sec.3 at 1010 mm from the support

The values shown on the graphs are shear stresses in N/mm^2

- Sampling points

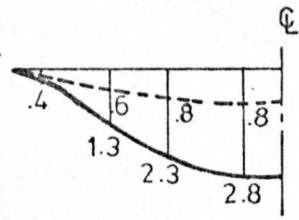


Cross sec.

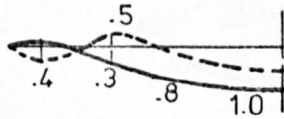


Elevation view

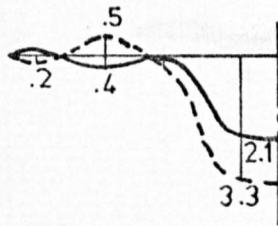
FIG.7.9. a. SHEAR STRESS DISTRIBUTION BEFORE FAILURE - BEAM TBX - I



Sec. 1



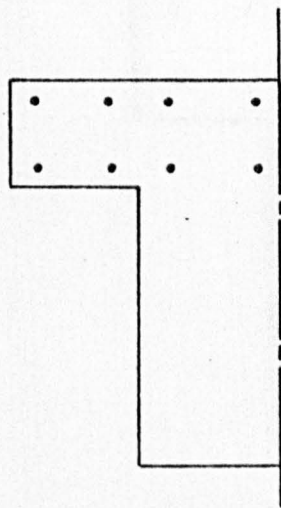
Sec. 2



Sec. 3

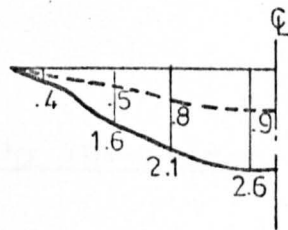
— Shear stress distribution near the underside of the flange

-- Shear stress distribution near the top surface of the flange



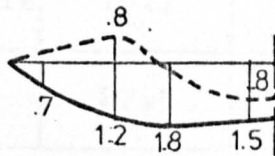
Cross sec.

FIG. 7.9.b. SHEAR STRESS DISTRIBUTIONS BEFORE FAILURE - BEAM TBX-IV

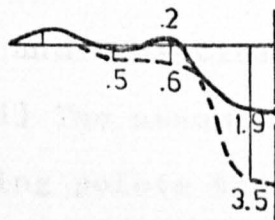


Sec. 1

Beam No.	
Cube strength N/mm ²	
Shearing Force kN	



Sec. 2



Sec. 3

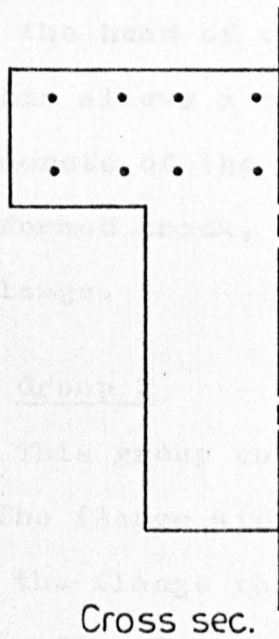


FIG. 7.9. c. SHEAR STRESS DISTRIBUTIONS
BEFORE FAILURE - BEAM TBX-VII

Table 7.1

Shear Forces carried by the Flange

Beam No		TBX-I	TBX-IV	TBX-VII
Cube strength N/mm ²		36.1	37.9	34.8
Shearing Force kN	Analysis	19.7	28.8	36.2
	Exp	27.5	29.8	38.1

From the above Table it can be seen that the shear forces obtained from the analysis and the tests are in good agreement for beams TBX IV and TBX VII. The disparity between the experimental and analytical values for beam TBX I may be referred to: (1) The assumed linear stress distribution between the two sampling points through the flange thickness. (2) The location of the sampling points inside the element boundaries and not at the head of the preformed crack as shown in Fig 7.9a. This allows a part of the shear force to be resisted by the concrete of the web between the underside of flange and the preformed crack, noting that this beam has narrow and thin flange.

7.2.3.2 Group 2

This group contained the beams TBX II, TBX V And TBX VIII. The flange width for these beams was 700 mm ($B/b_o = 4$) and the flange thickness ranged from 50 mm to 90 mm ($t/h = .167 - .3$). The finite element mesh used for this group is shown in Fig 7.2c, in which 35 elements were used. Six load increments were performed for each beam

with two iteration cycles for each increment except in the last two where four cycles were used.

Fig 7.10 shows the midspan load-deflection curves and, also, the vertical displacement at the underside of the flange near the head of the preformed crack, against the shearing force. The analytical results agree closely with the experimental curves. The difference in strength between the experimental and analytical solution in beams TBX V and TBX VIII is mainly due to the dowel action of the 20 mm diameter reinforcement bars.

The crack patterns resulted from the analysis at intermediate load stage (60 kN for beams TBX II and TBX V, 80 kN for beam TBX VIII) and at ultimate load are shown in Fig 7.11. The modes of failure obtained from the experiments are shown in Fig 7.12. The cracks appeared first in the lower side of the web in both the experiment and analysis, then spread vertically towards the underside of the flange. In the tests cracks extended diagonally from the head of the preformed crack towards the underside of flange and continued along the web-flange junction. At failure these cracks turned up into the flange, propagated to the loading area and lifted up the part of flange between the preformed crack and the loading block. In the case of beam TBX II, the failure was accompanied by transverse splitting on the top of flange over the head of preformed crack, then extended longitudinally parallel to the flange-web junction until it reached the loading block. In beams TBX V and TBX VIII, the failure was accompanied also by transverse splitting on

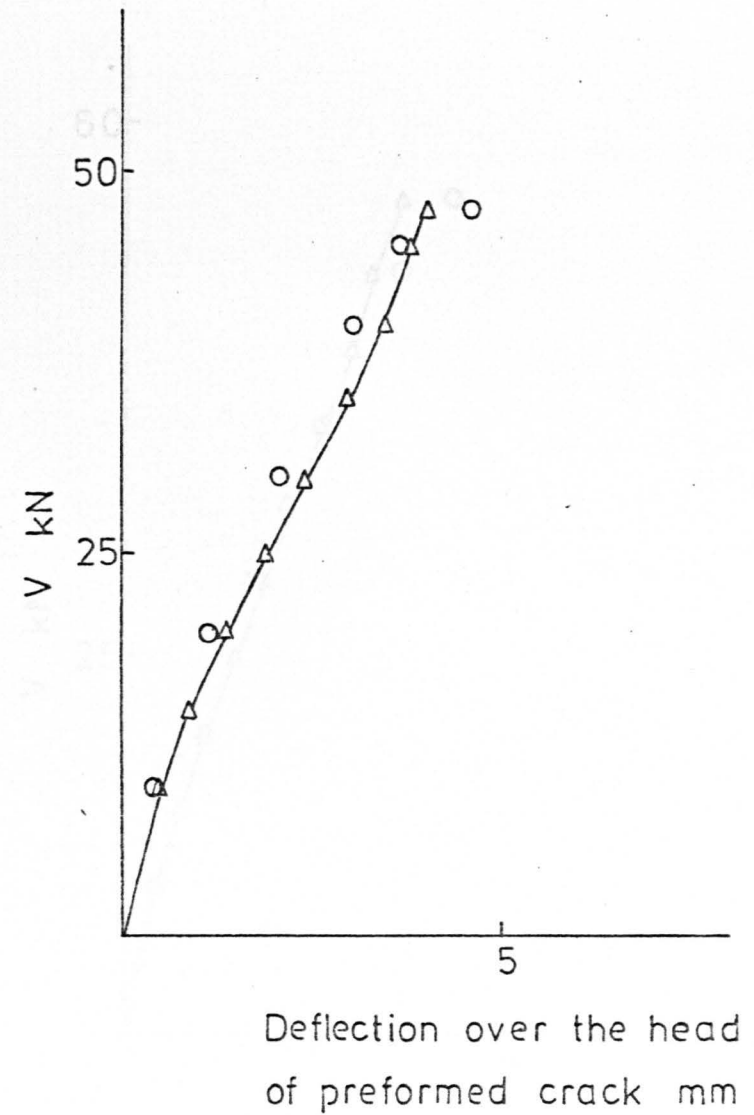
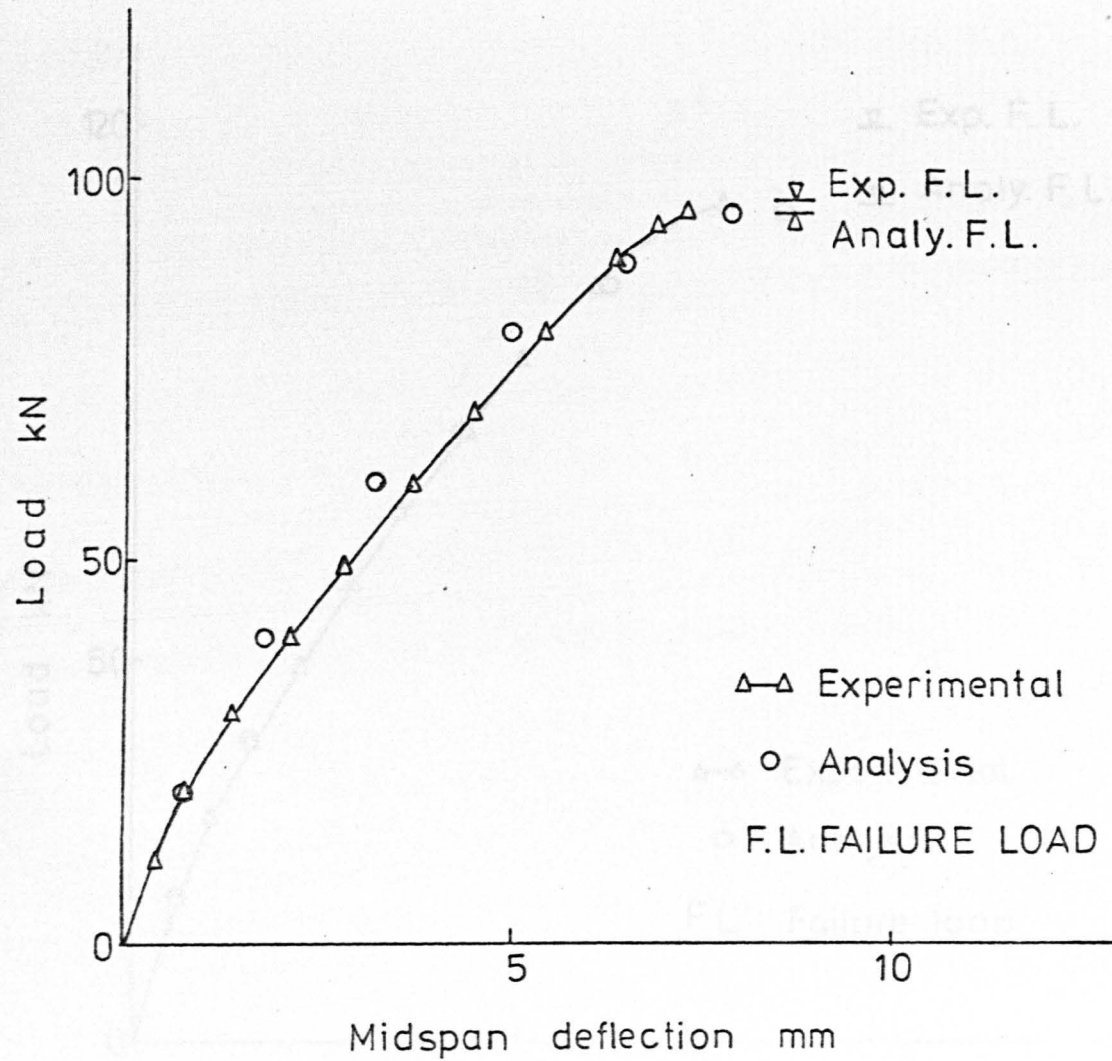


FIG.7.10. a. LOAD - DEFLECTION CURVES - BEAM TBX - II

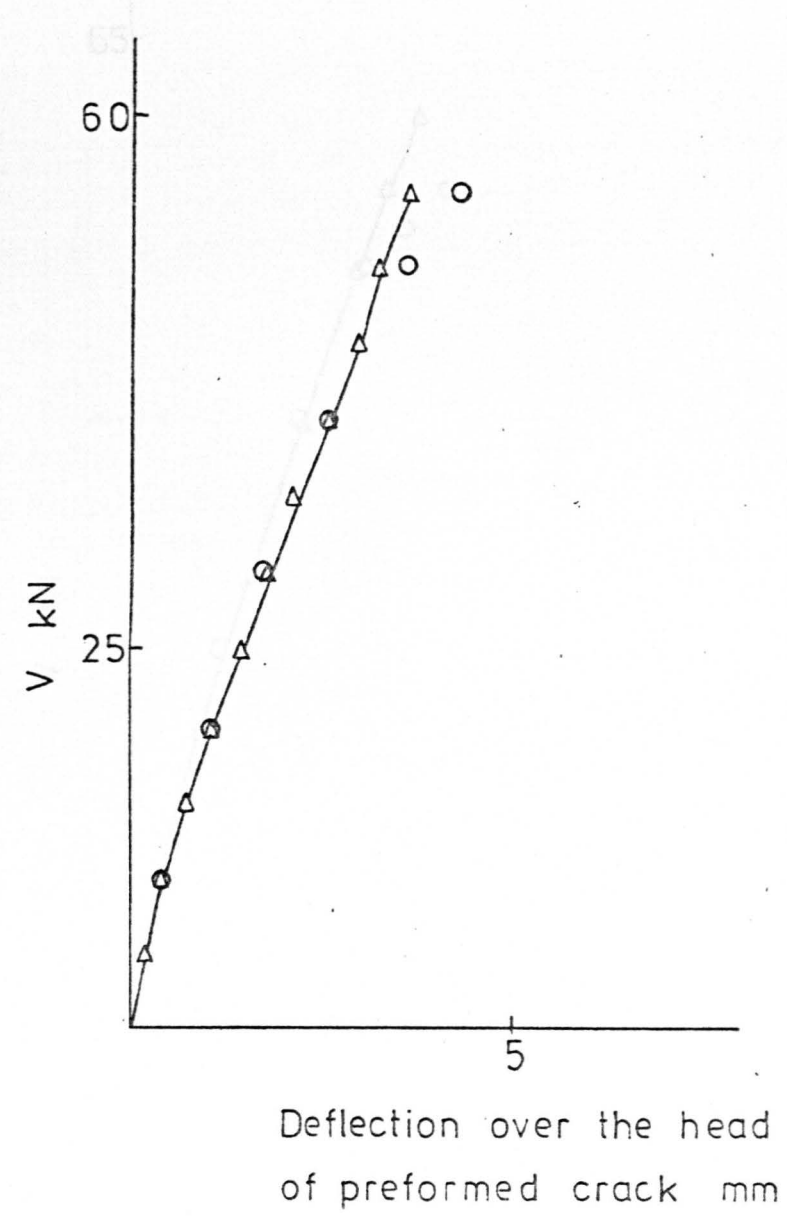
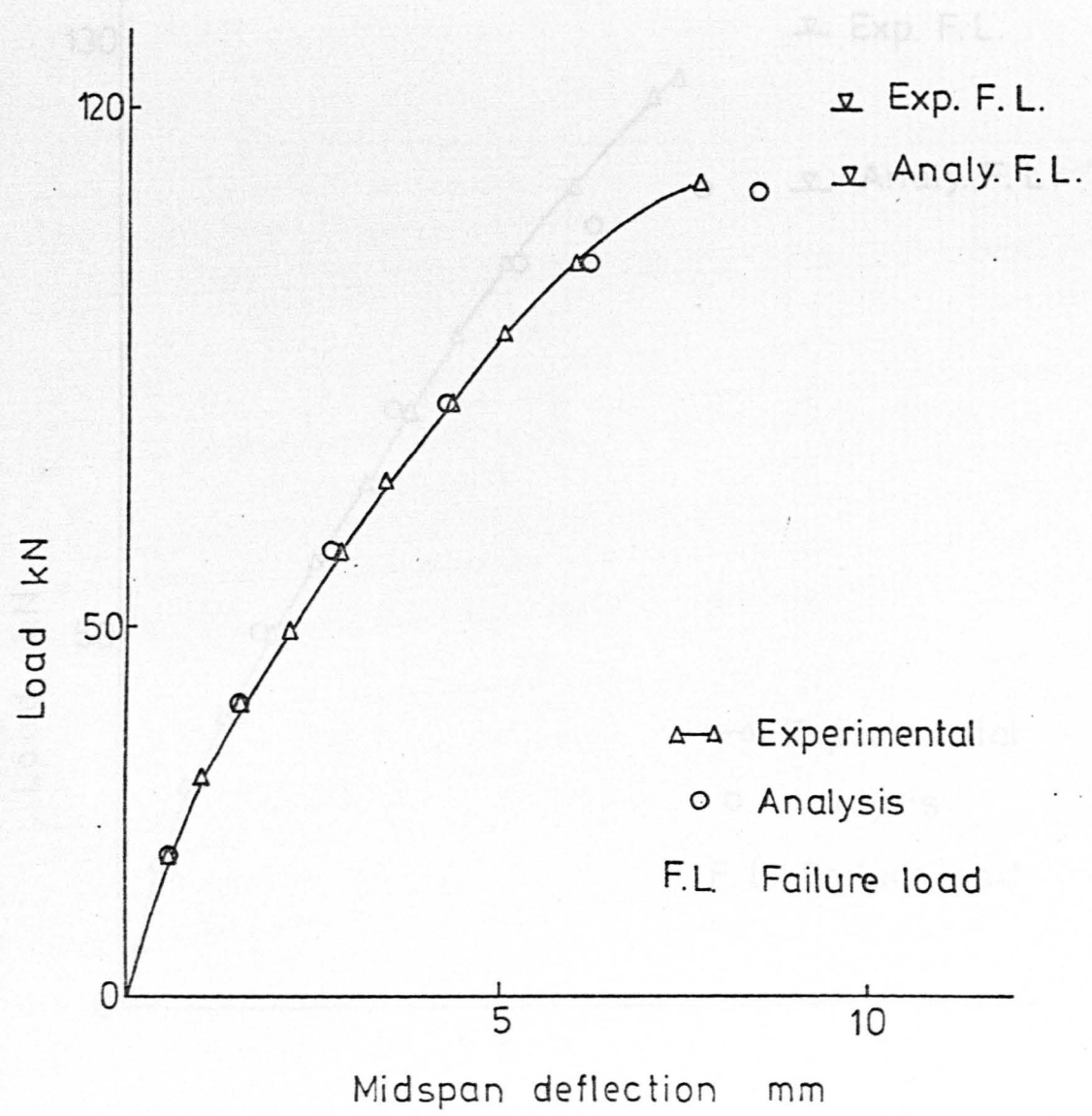


FIG.7.10.b. LOAD - DEFLECTION CURVES - BEAM TBX - V

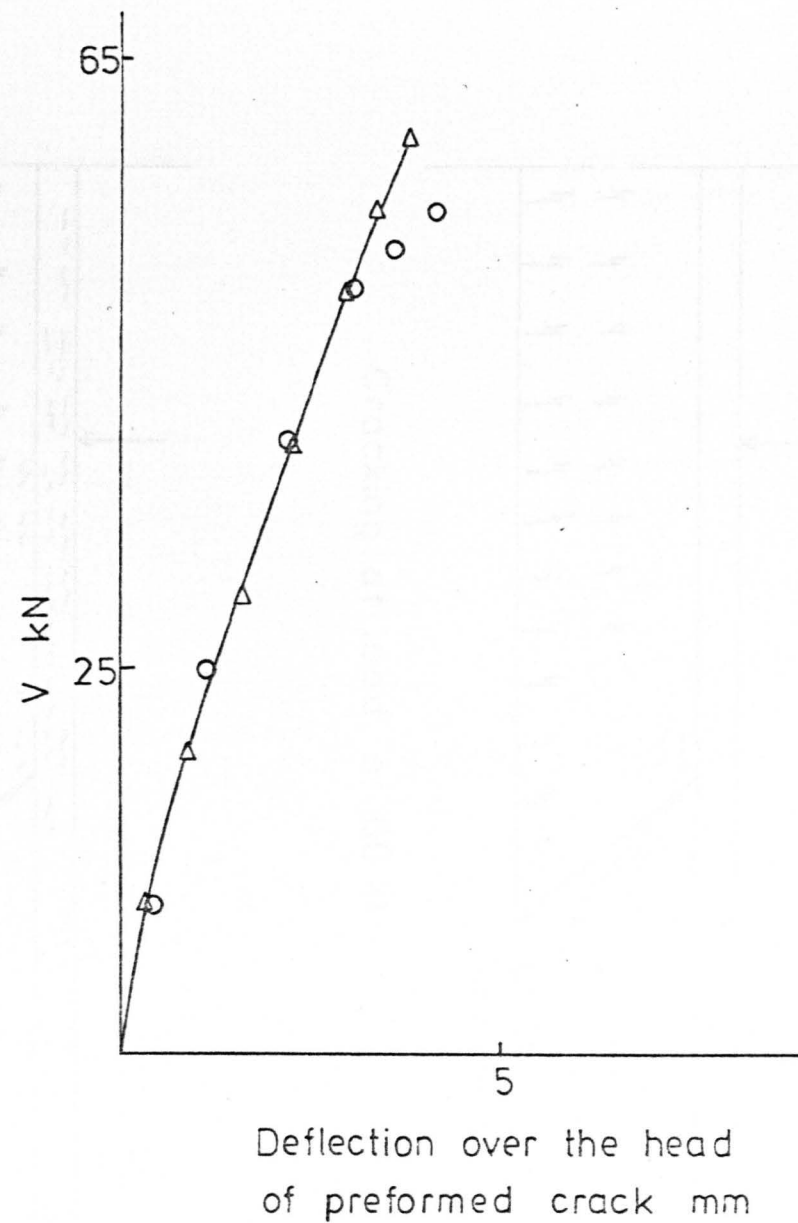
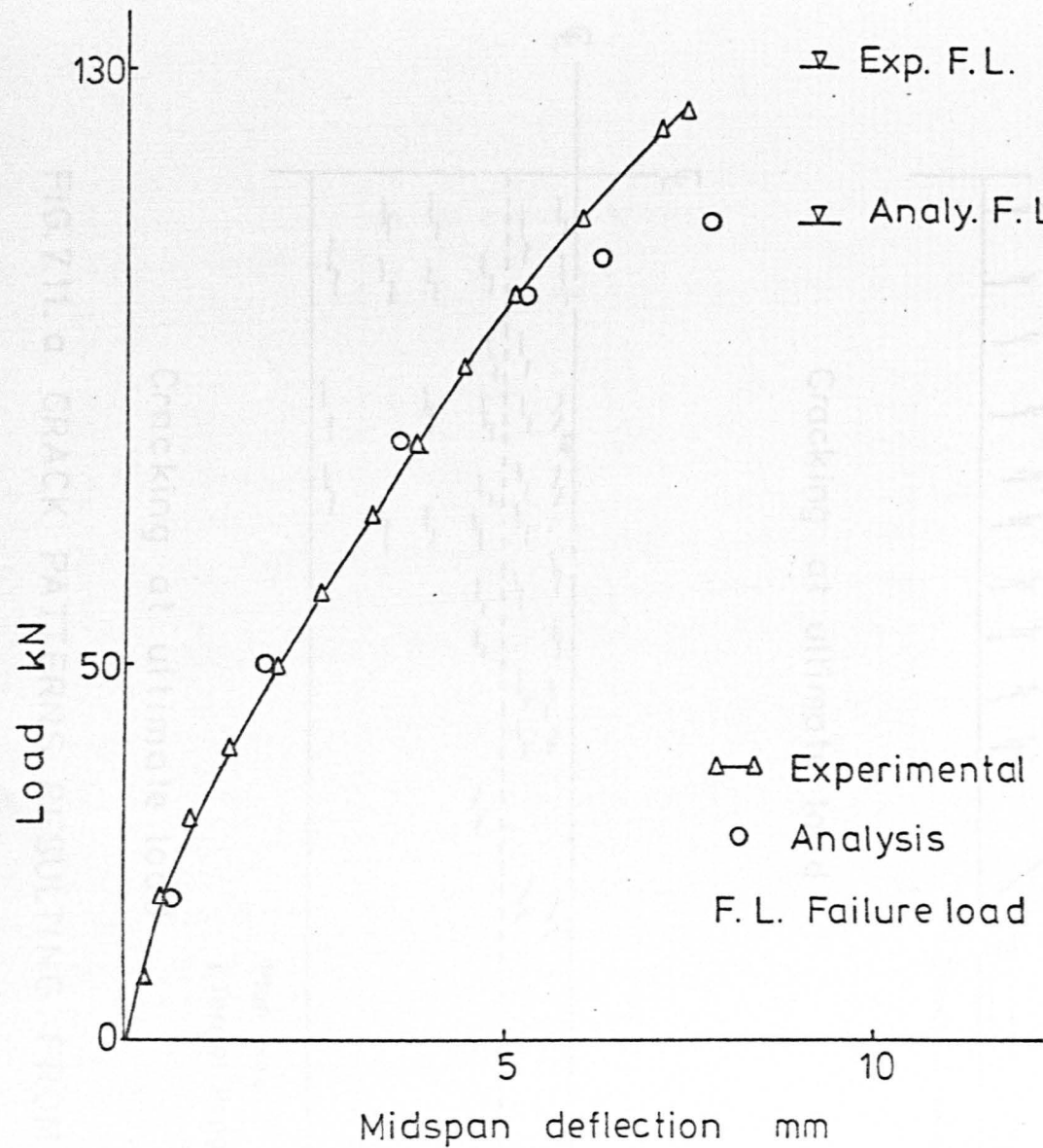
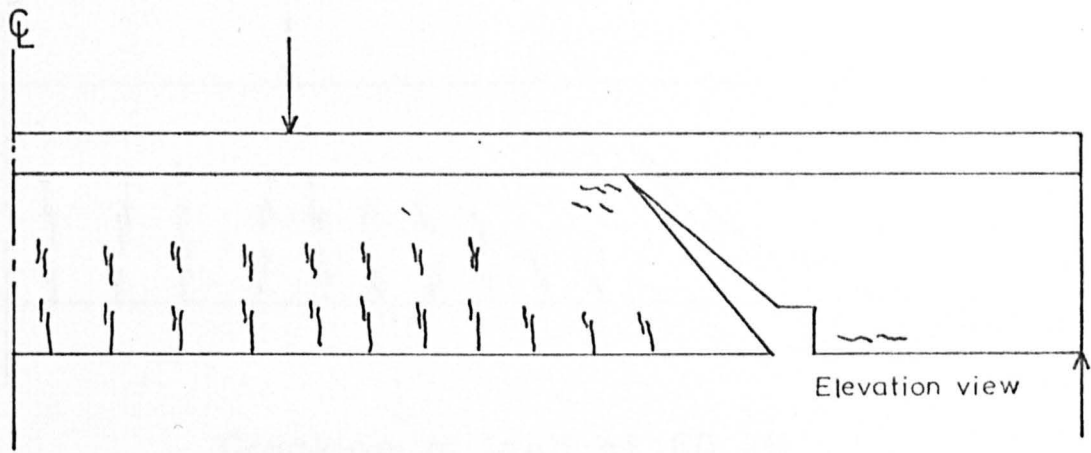
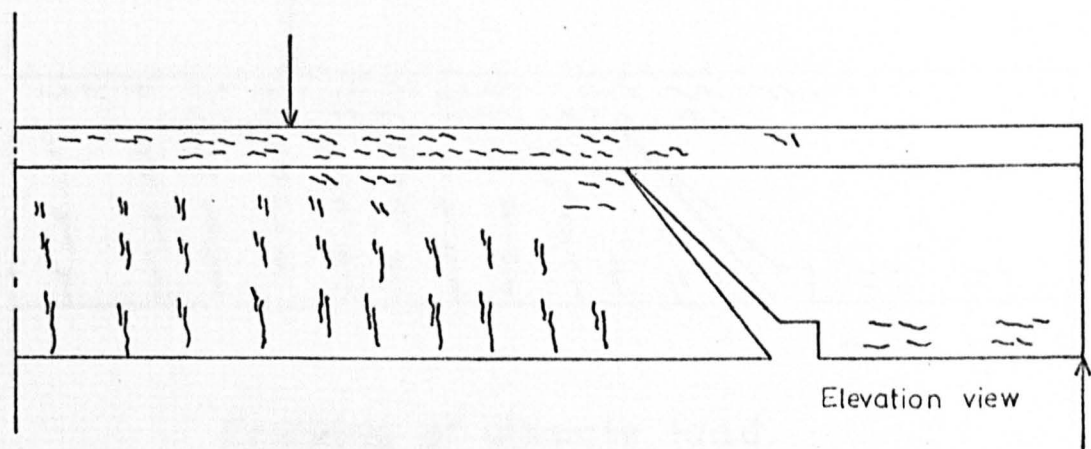


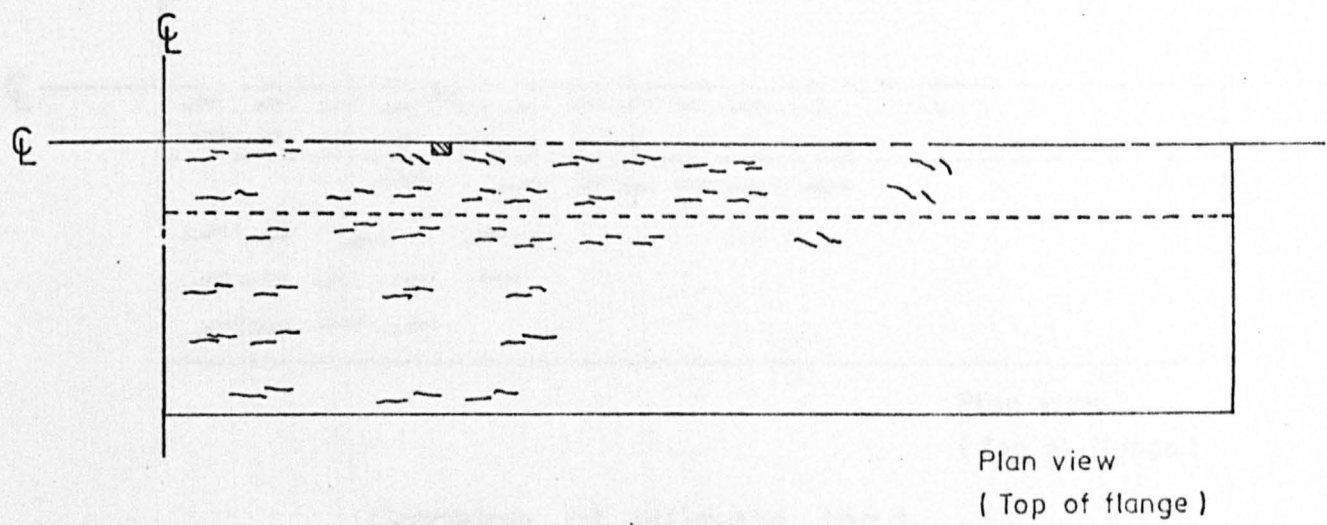
FIG. 7.10.c. LOAD - DEFLECTION CURVES - BEAM TBX - VIII



Cracking at load of 60 kN

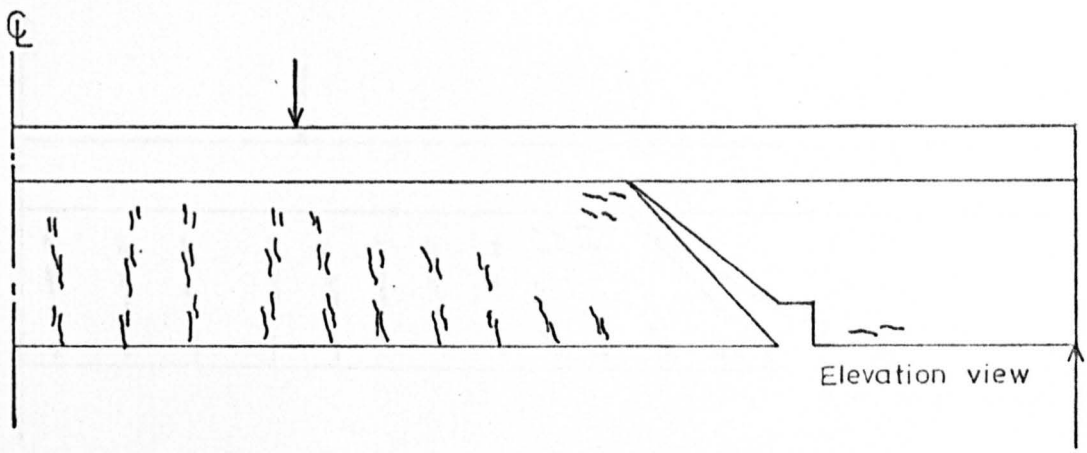


Cracking at ultimate load

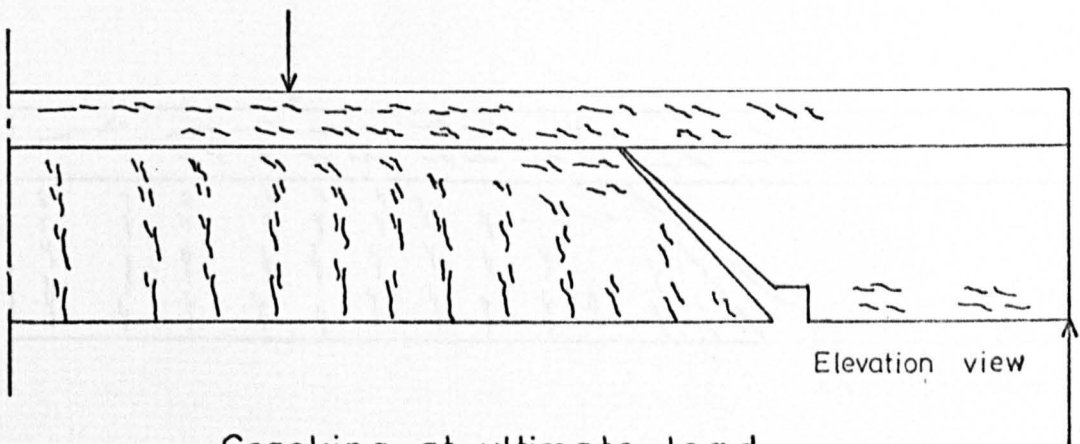


Cracking at ultimate load

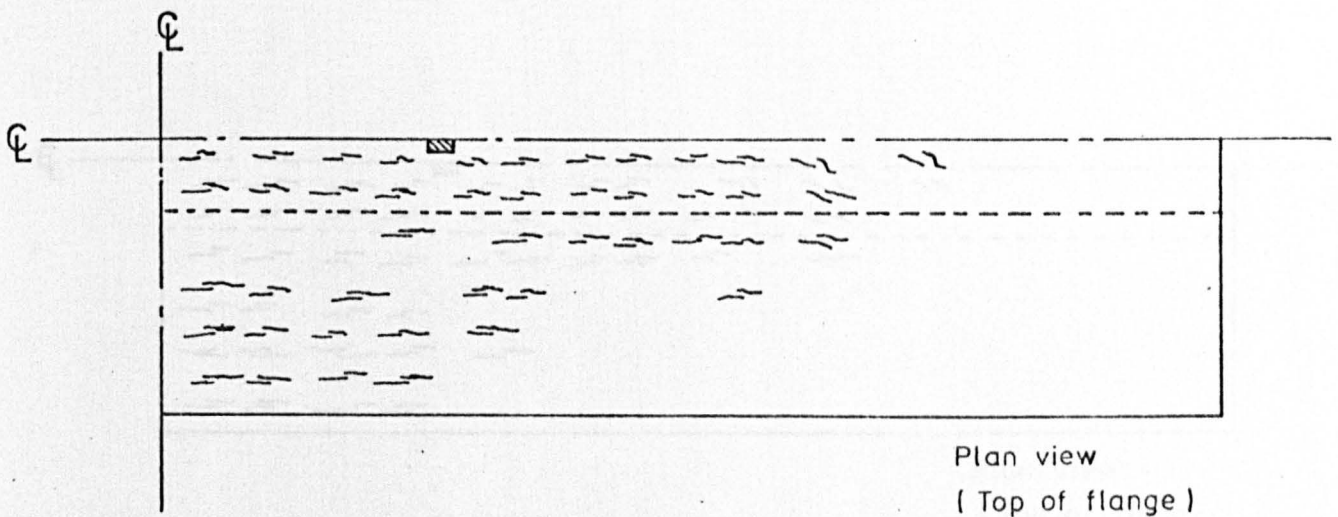
FIG. 7.11. a. CRACK PATTERNS RESULTING FROM ANALYSIS - BEAM TBX - II



Cracking at load of 60 kN

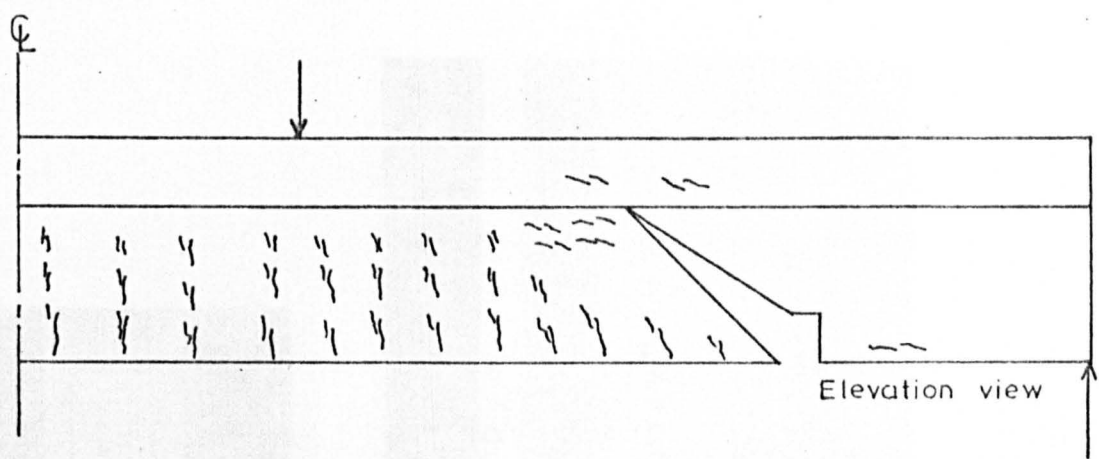


Cracking at ultimate load

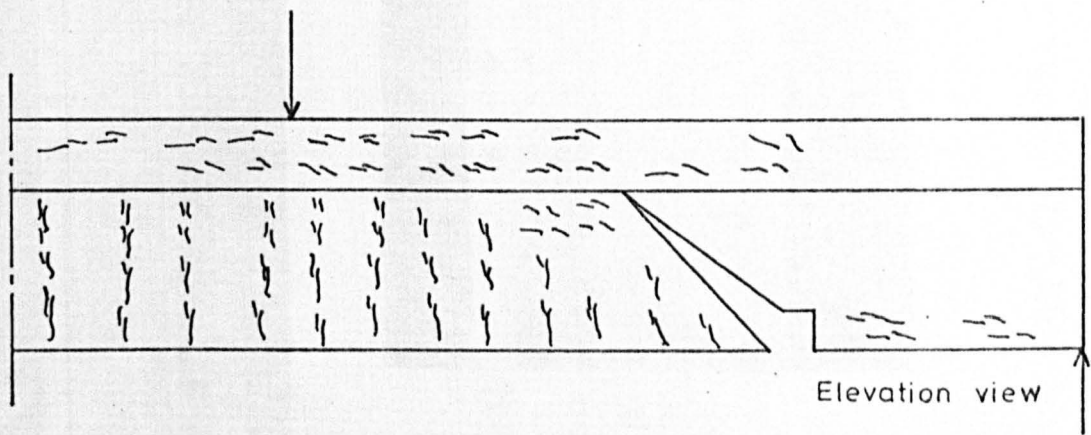


Cracking at ultimate load

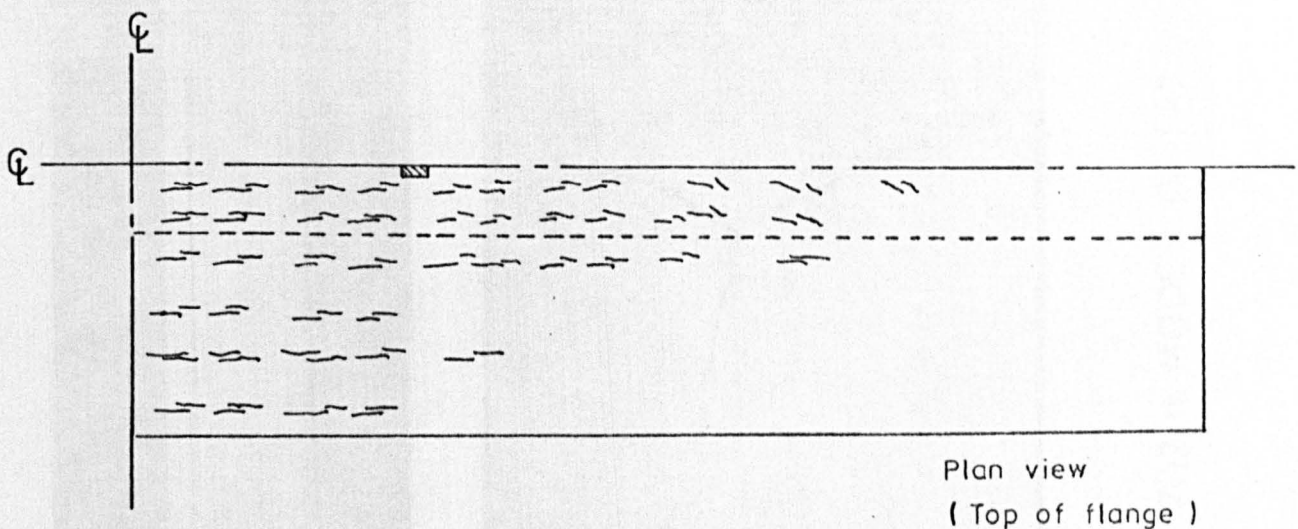
FIG.7.11.b. CRACK PATTERNS RESULTING FROM ANALYSIS - BEAM TBX - V



Cracking at load of 80 kN



Cracking at ultimate load



Cracking at ultimate load

FIG.7.11. c. CRACK PATTERNS RESULTING FROM ANALYSIS - BEAM TBX - VIII

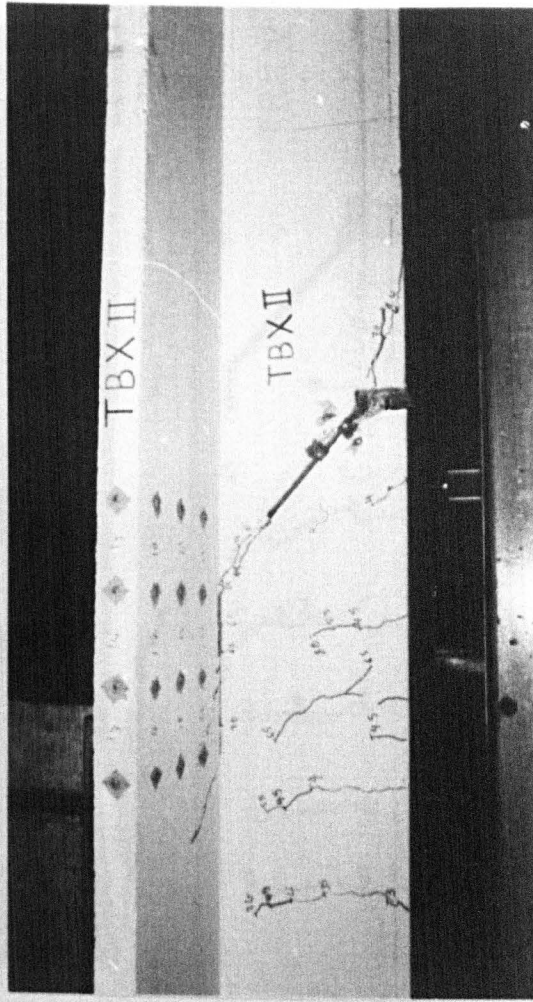
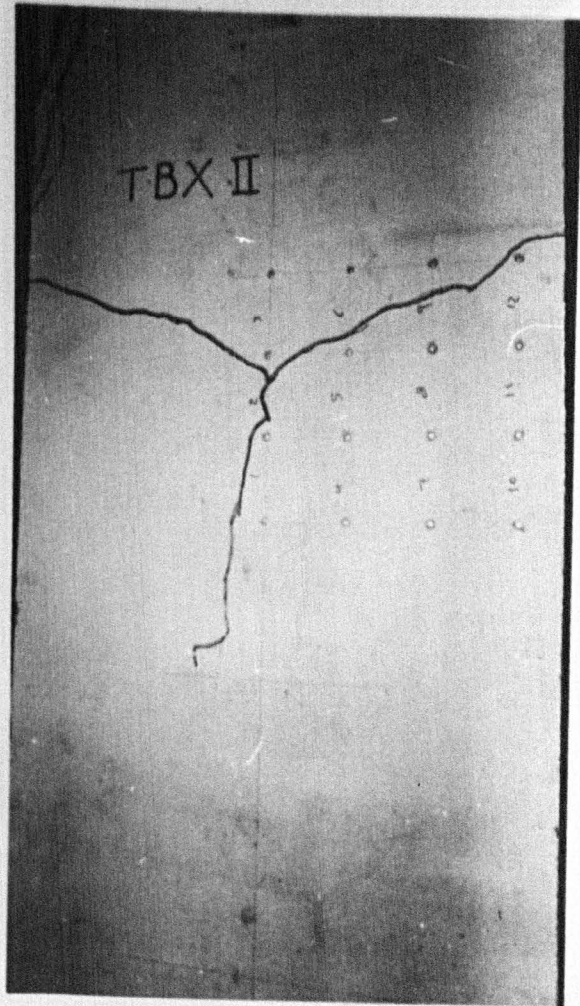
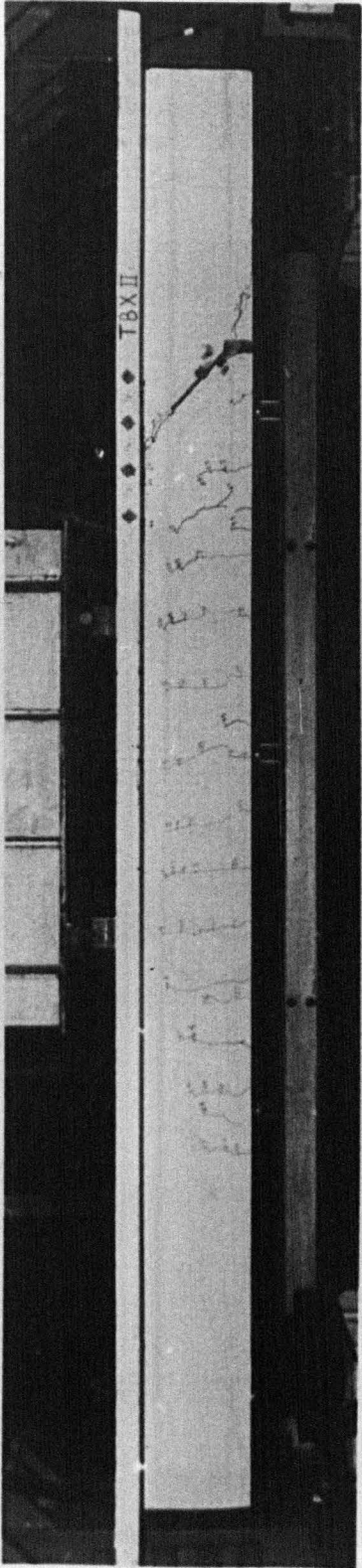


FIG. 7.12. a. MODES OF FAILURE - BEAM TBX - II , $B/b_0 = 4$ & $t/h = 0.167$

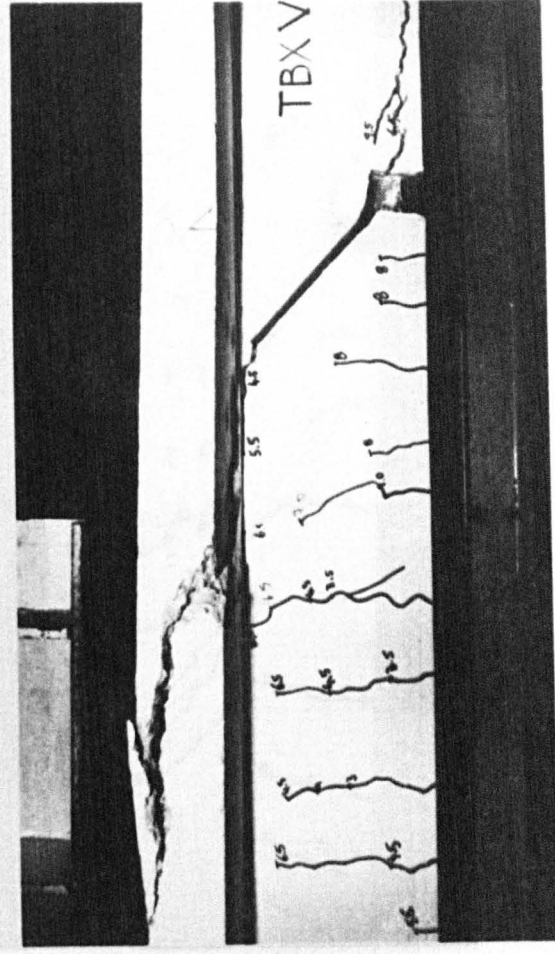
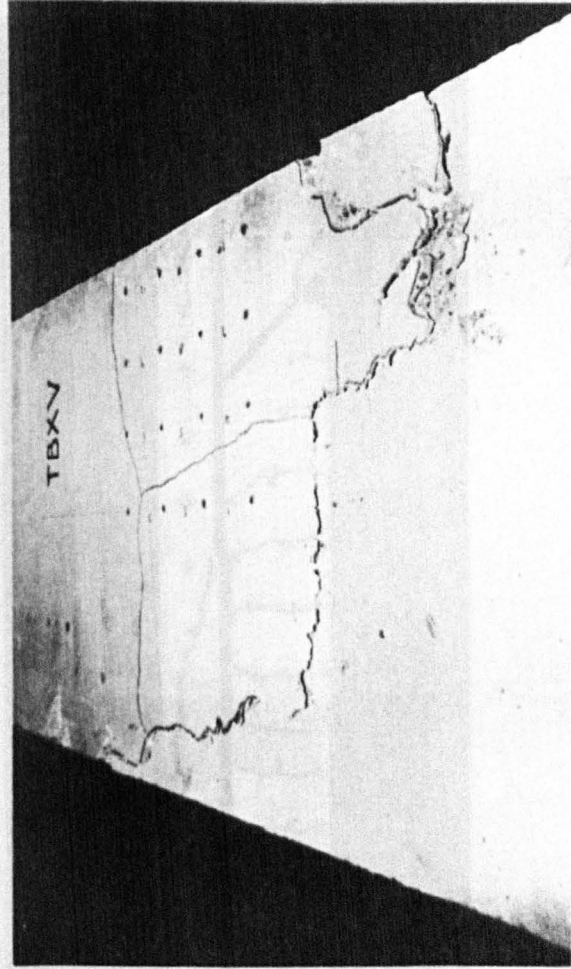
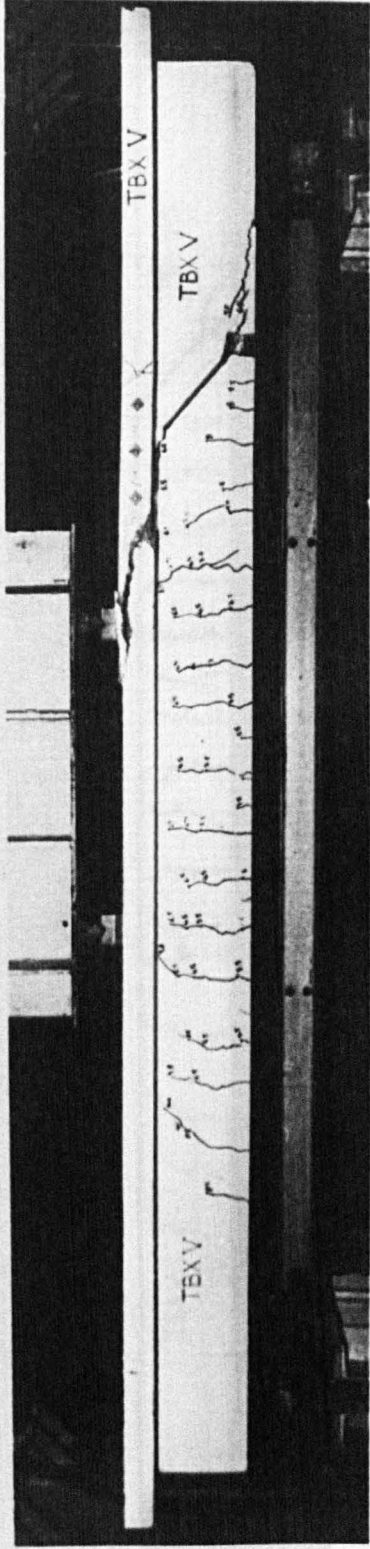


FIG. 7.12. b. MODES OF FAILURE - BEAM TBX - V , $B/b_0 = 4$ & $t/h = 0.233$

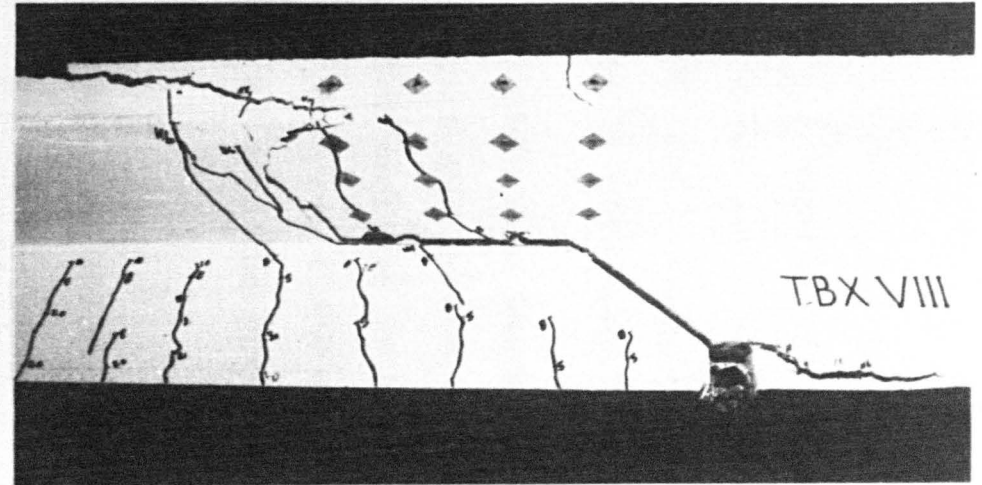
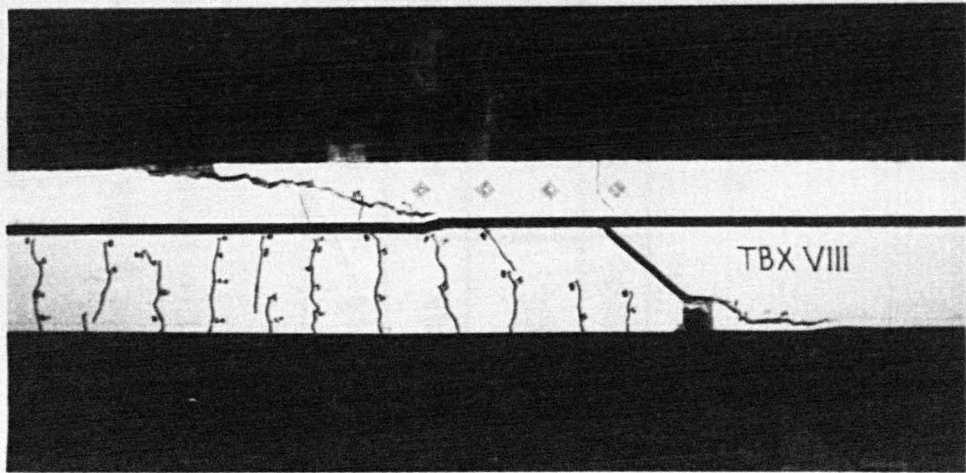
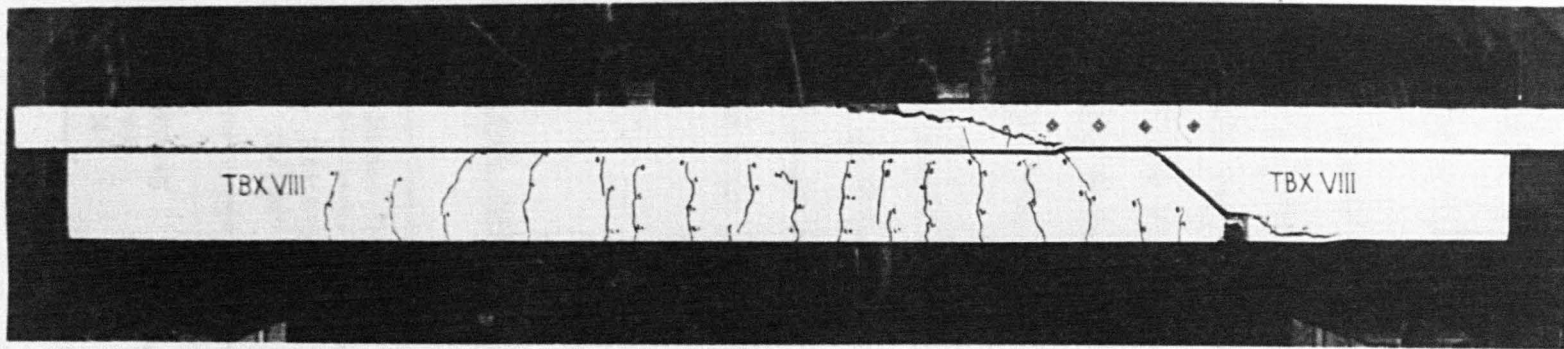


FIG. 7.12.c. MODES OF FAILURE - BEAM TBX-VIII, $B/b_0 = 4$ & $t/h = 0.3$

top of the flange and longitudinal splittings parallel to the flange-web junction. These longitudinal splittings extended around the loading block and then to the flexural zone of the flange between the two loading blocks causing destruction of part of flange in this area, Fig 7.12.

The crack patterns obtained from the analysis, Fig 7.11, at failure, show the initiation and spread of cracks in the flange near the top and bottom surfaces in the area between the preformed crack and the load point and in the flexural zone. This shows agreement between the predicted crack pattern and the actual one.

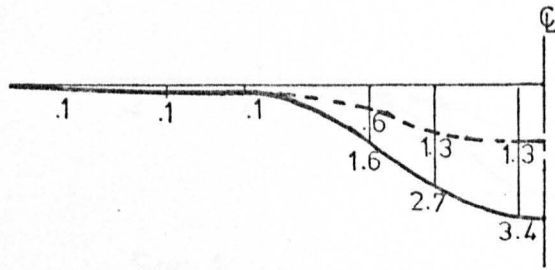
The shear stress distributions across the flange width are plotted in Fig 7.13, for the three beams at three different sections in the shear span. Table 7.2 shows the calculated and the actual shearing forces resisted by the flange.

Table 7.2

Shear Forces carried by the Flange

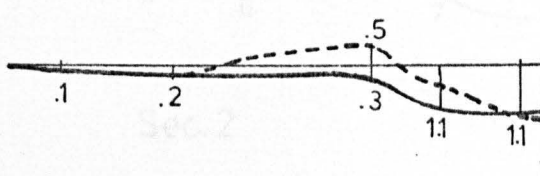
Beam No		TBX II	TBX V	TBX VIII
Cube Strength N/mm ²		38.6	37.5	36.1
Shearing Force kN	Analysis	28.9	44.1	50.0
	Exp	35.4	44.2	50.2

The experimental and analytical values for the shear strength of the flanges of beams TBX V and TBX VIII are

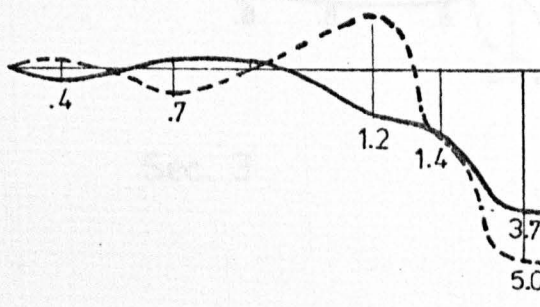


Sec.1 at 550 mm from the support

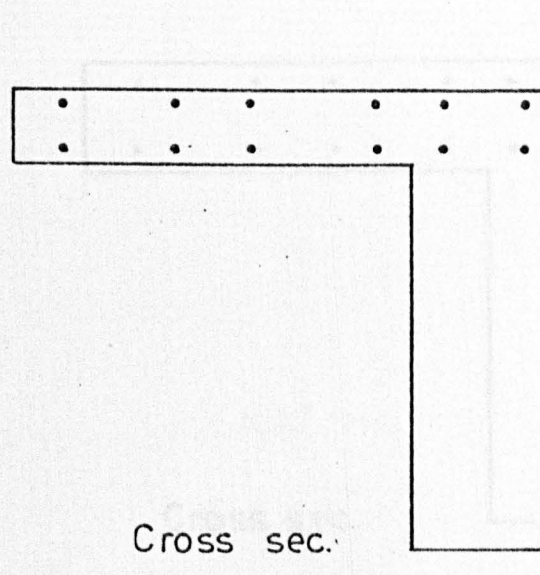
The values shown on the graphs are shear stresses in N/mm^2



Sec.2 at 860 mm from the support

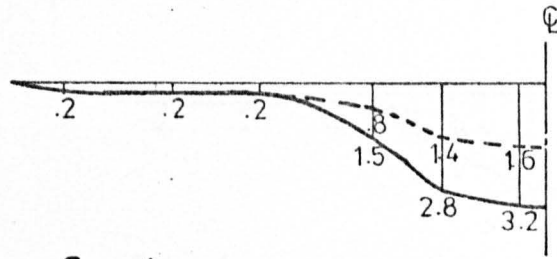


Sec.3 at 1010 mm from the support

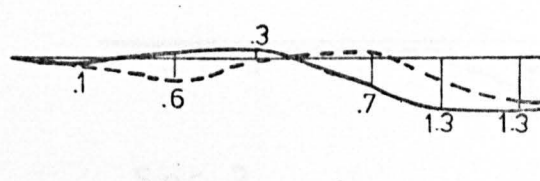


- Shear stresses near the underside of the flange
- Shear stresses near the top surface of the flange
- Sampling points

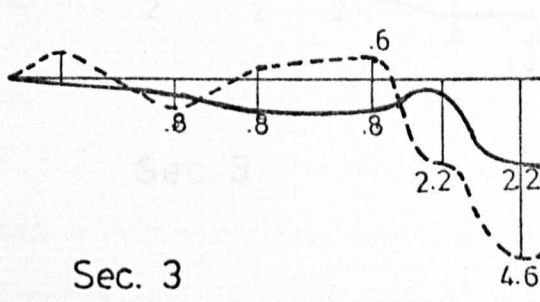
FIG. 7.13. a. SHEAR STRESS DISTRIBUTIONS BEFORE FAILURE - BEAM TBX-II



Sec. 1



Sec. 2



Sec. 3

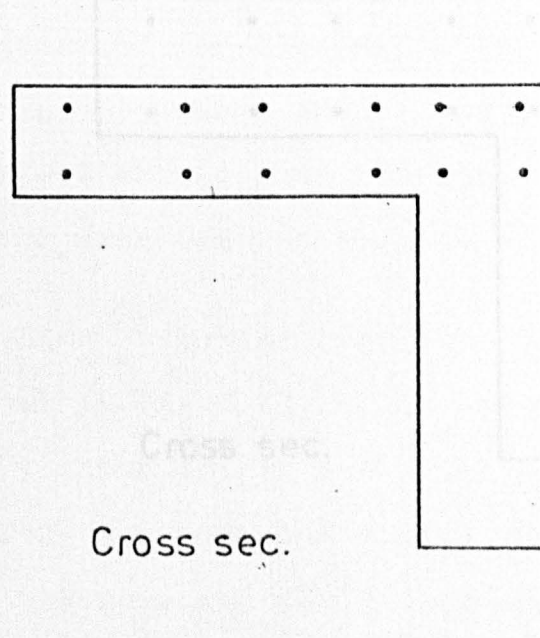
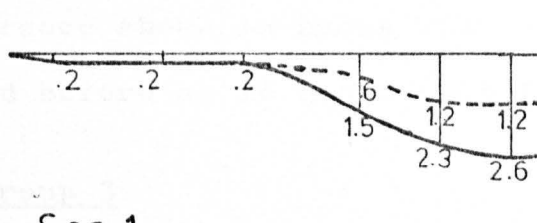
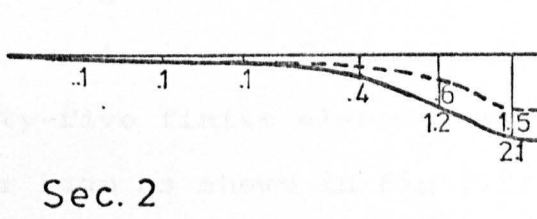


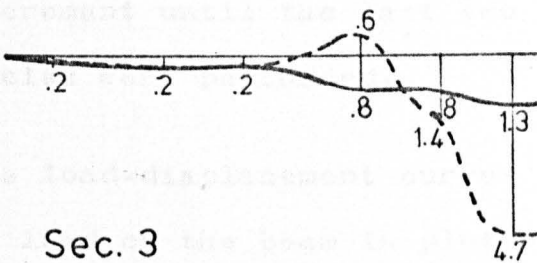
FIG. 7.13.b. SHEAR STRESS DISTRIBUTIONS BEFORE FAILURE - BEAM TBX-V



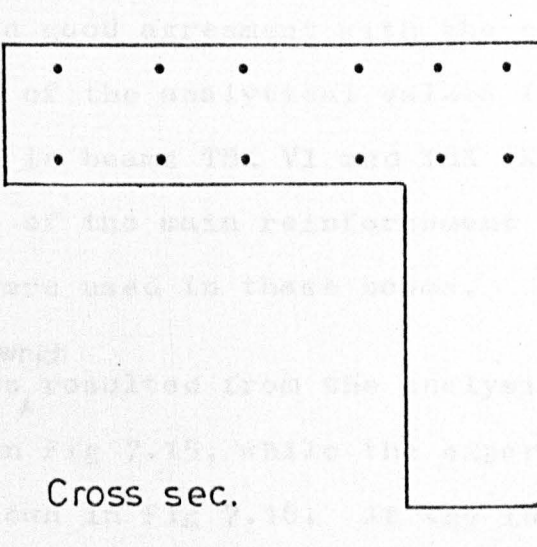
Sec. 1



Sec. 2



Sec. 3



Cross sec.

FIG. 7.13. c. SHEAR STRESS DISTRIBUTIONS BEFORE FAILURE - BEAM TBX-VIII

coincident. The difference shown in beams TBX II is due to the reasons discussed before as it has a thin flange.

7.2.3.3 Group 3

The beams of this group are TBX III, TBX VI and TBX IX. The flange width is 1050 mm ($B/b_o = 6$) and the flange thickness varies from 50 mm and 90 mm ($t/h = .167 - .5$). Thirty-five finite elements were used in the model of the quarter beam as shown in Fig 7.2c. Six load increments were used in the analysis with two iteration cycles for each increment until the last two increments where four iteration cycles were performed.

Fig 7.14 shows the load-displacement curves for the three beams. The total load on the beam is plotted versus the midspan-deflection. The shear force is plotted against the vertical displacement of the underside of flange near the head of the preformed crack. The displacements obtained from the analysis are in good agreement with the experimental curves. The divergence of the analytical values from the experimental at failure in beams TBX VI and TBX IX is mainly due to the dowel effect of the main reinforcement as bars of 20 and 25 mm diameter were used in these beams.

which

The crack patterns, ^Aresulted from the analysis for two load stages are shown in Fig 7.15, while the experimental modes of failure are shown in Fig 7.16. At the intermediate load stage, the crack locations and directions from the experiment and the analysis are in good agreement. Up to that load level the cracks are vertical and distributed in the web. With increasing load in the tests, cracks ran

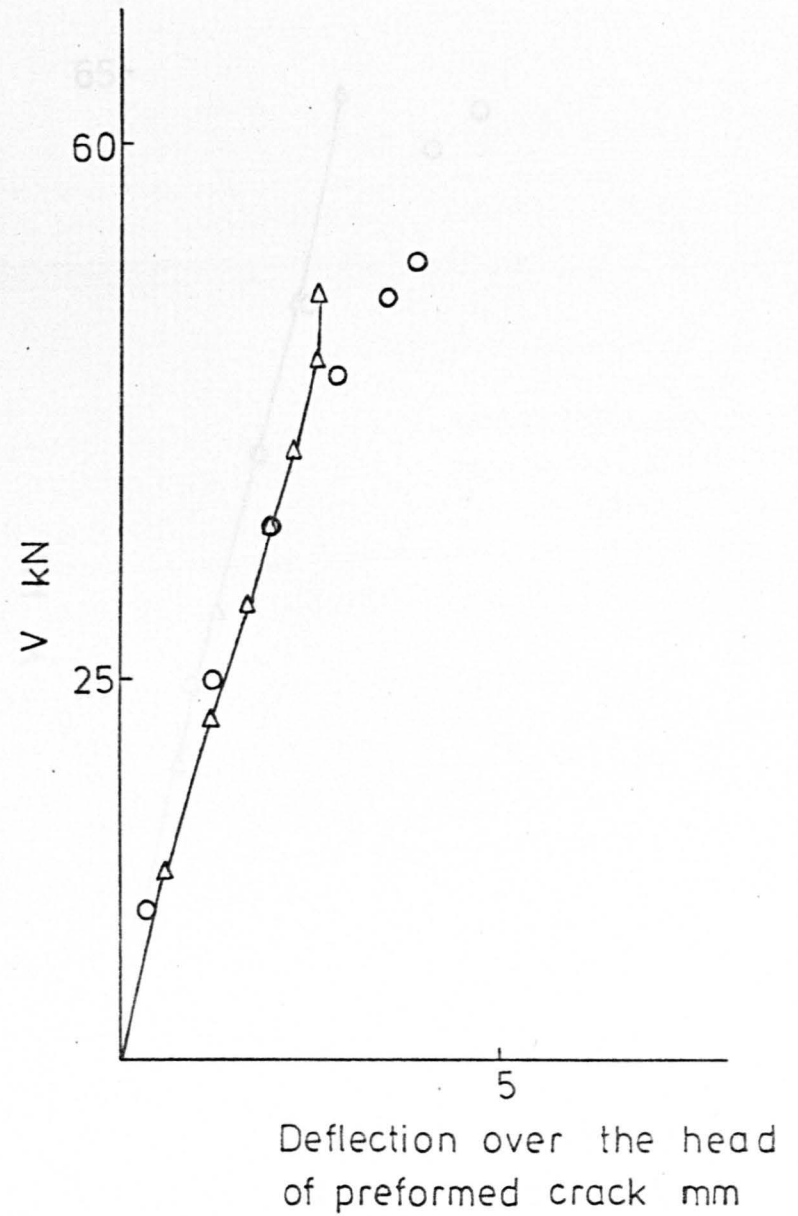
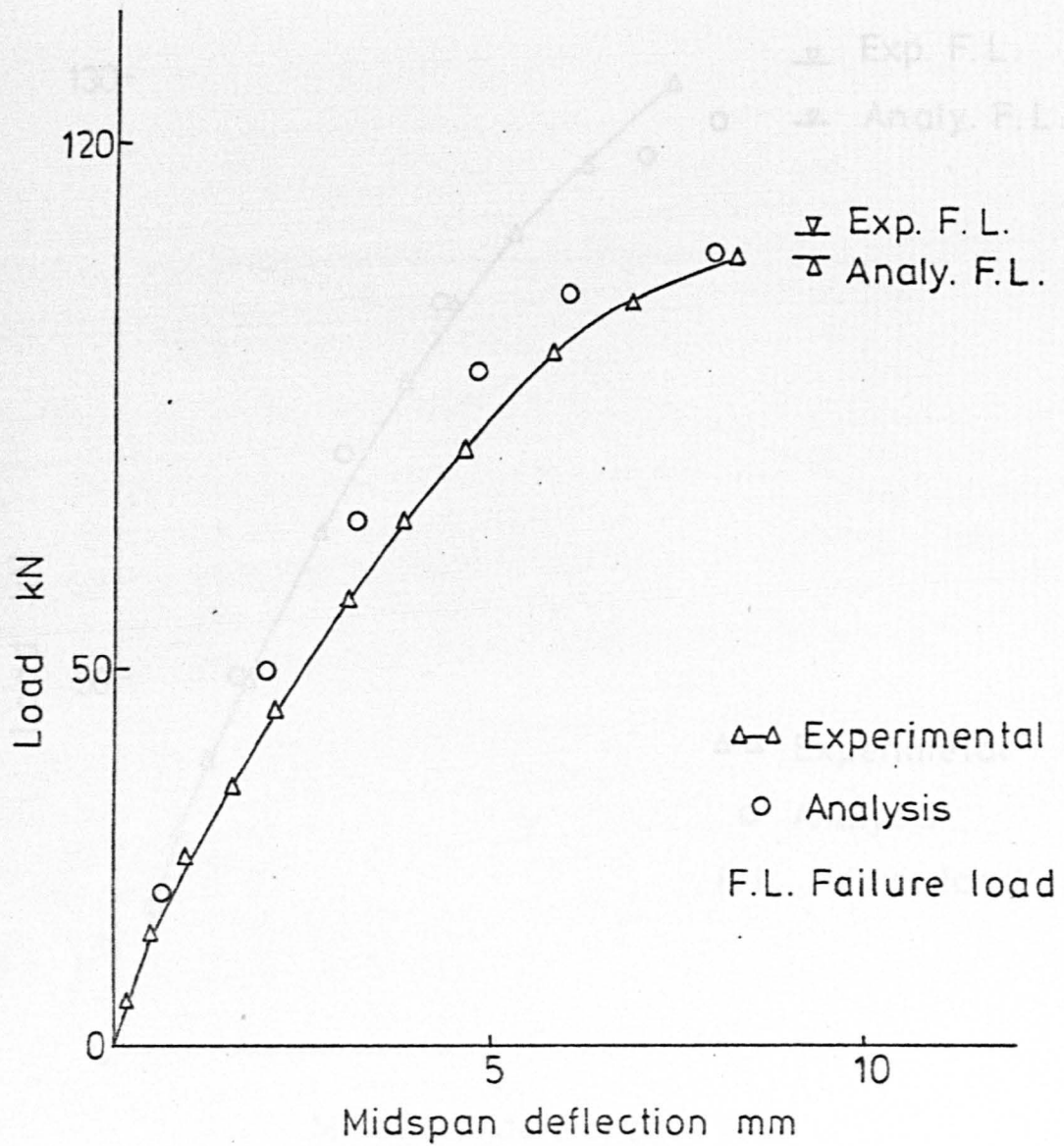


FIG. 7.14.a. LOAD - DEFLECTION CURVES - BEAM TBX-III

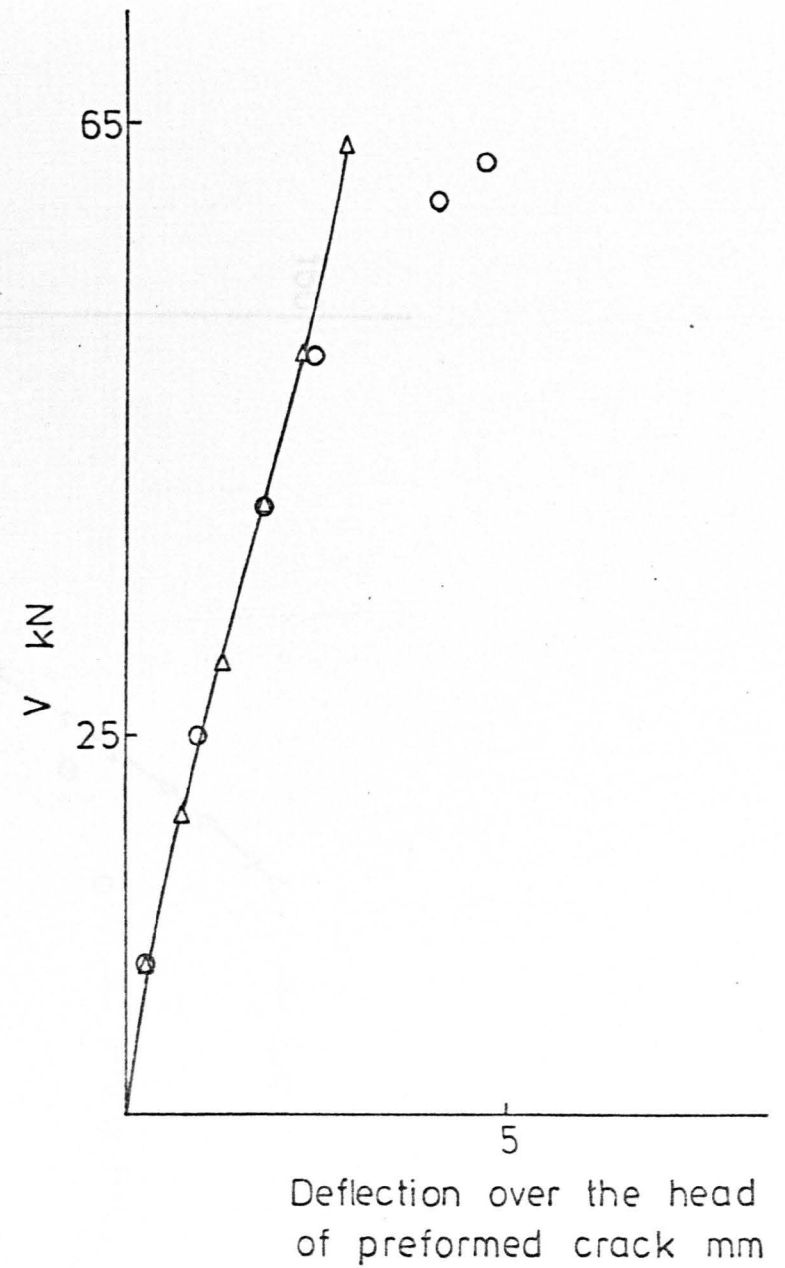
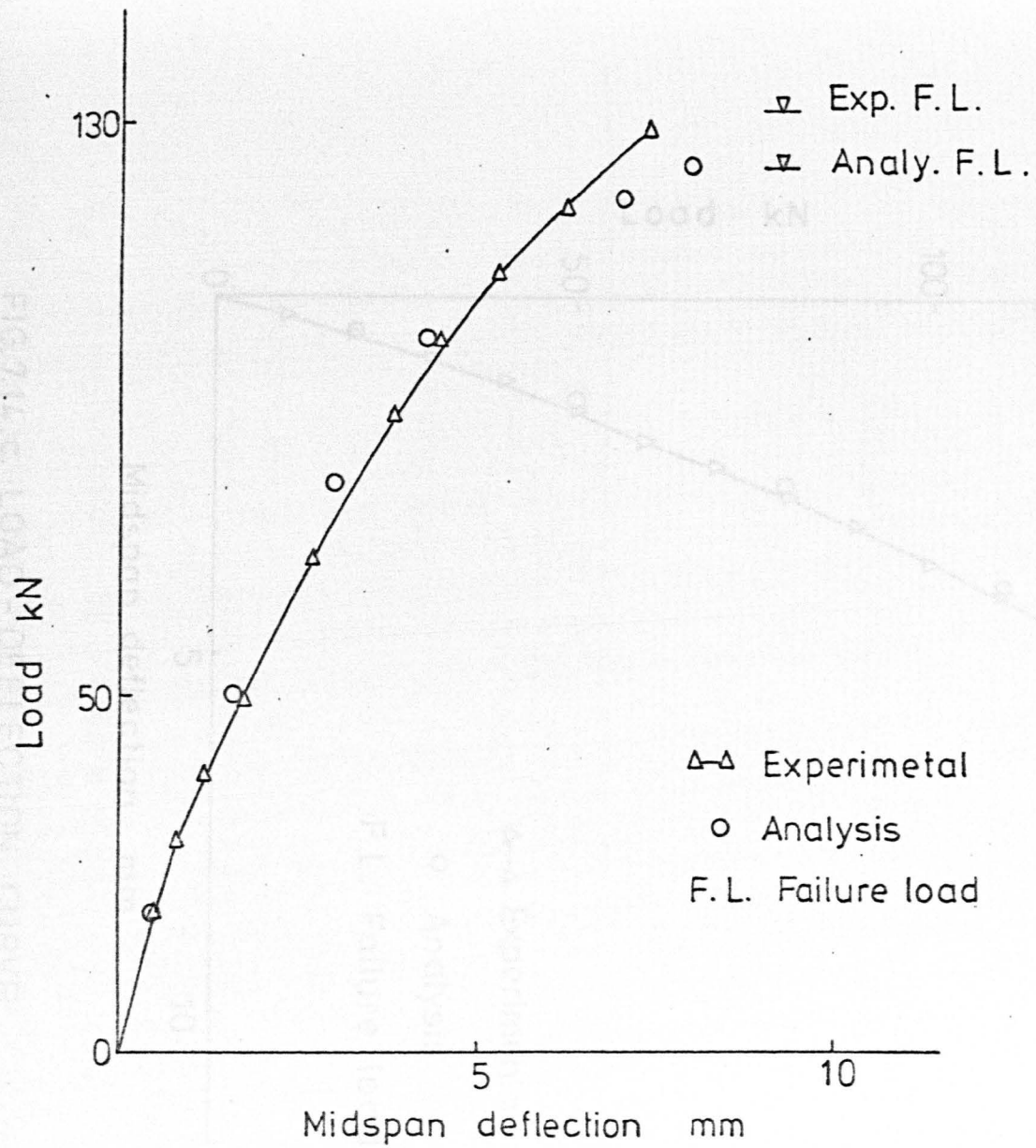


FIG. 7.14. b. LOAD - DEFLECTION CURVES - BEAM TBX-VI

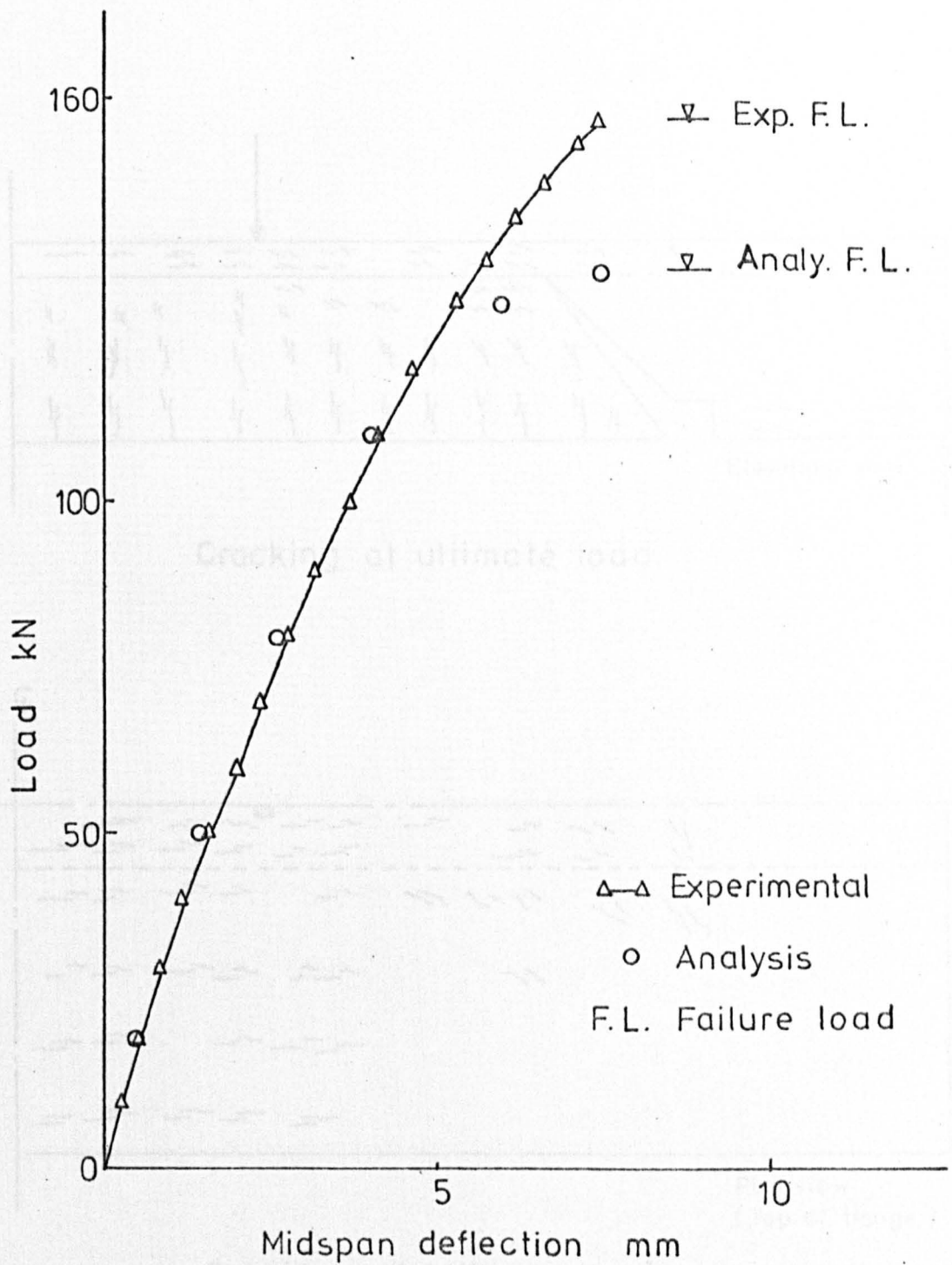


FIG. 7.14.c. LOAD - DEFLECTION CURVE FROM

BEAM TBX-IX

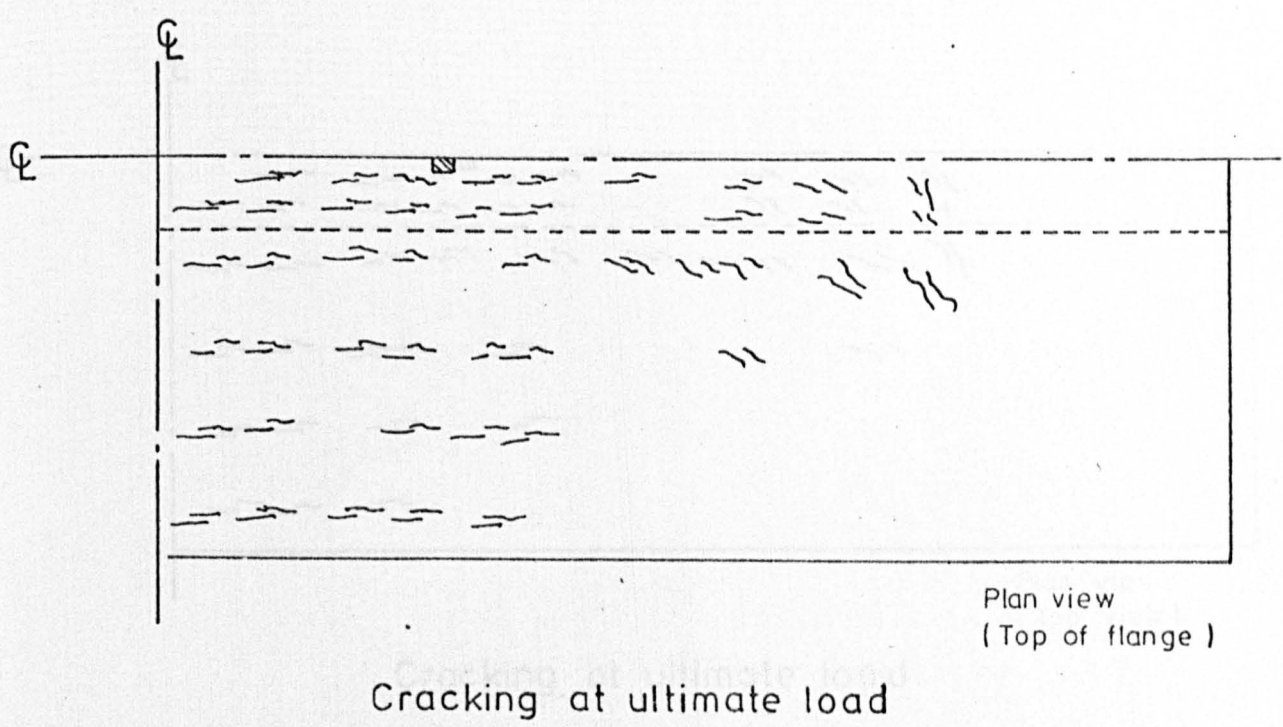
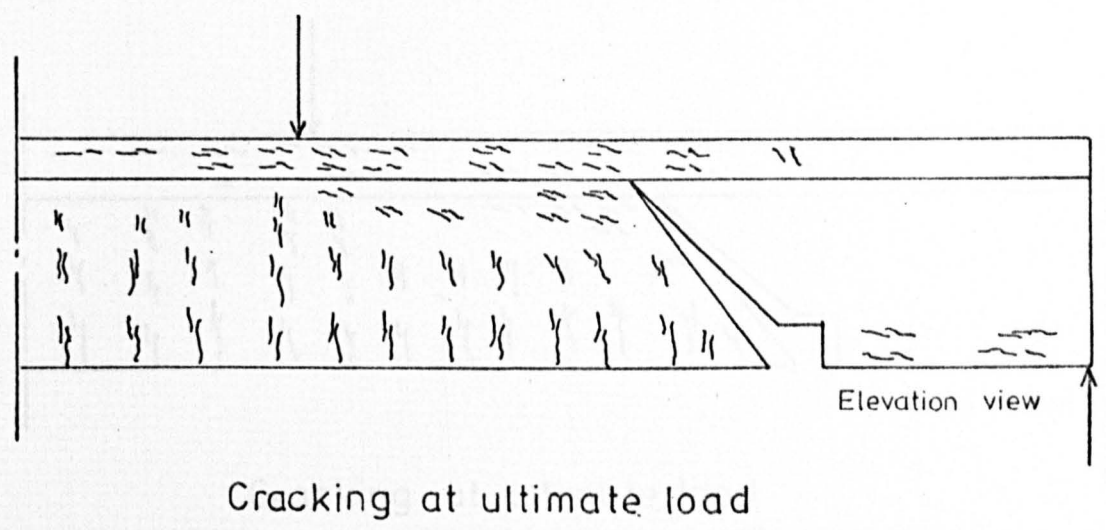
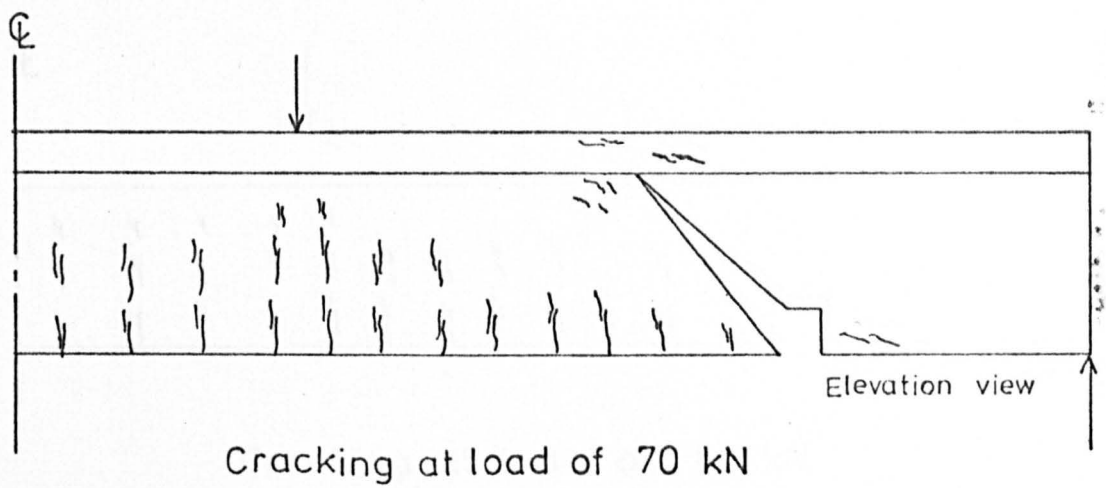


FIG. 7.15.a. CRACK PATTERNS RESULTING FROM ANALYSIS - BEAM TBX-III

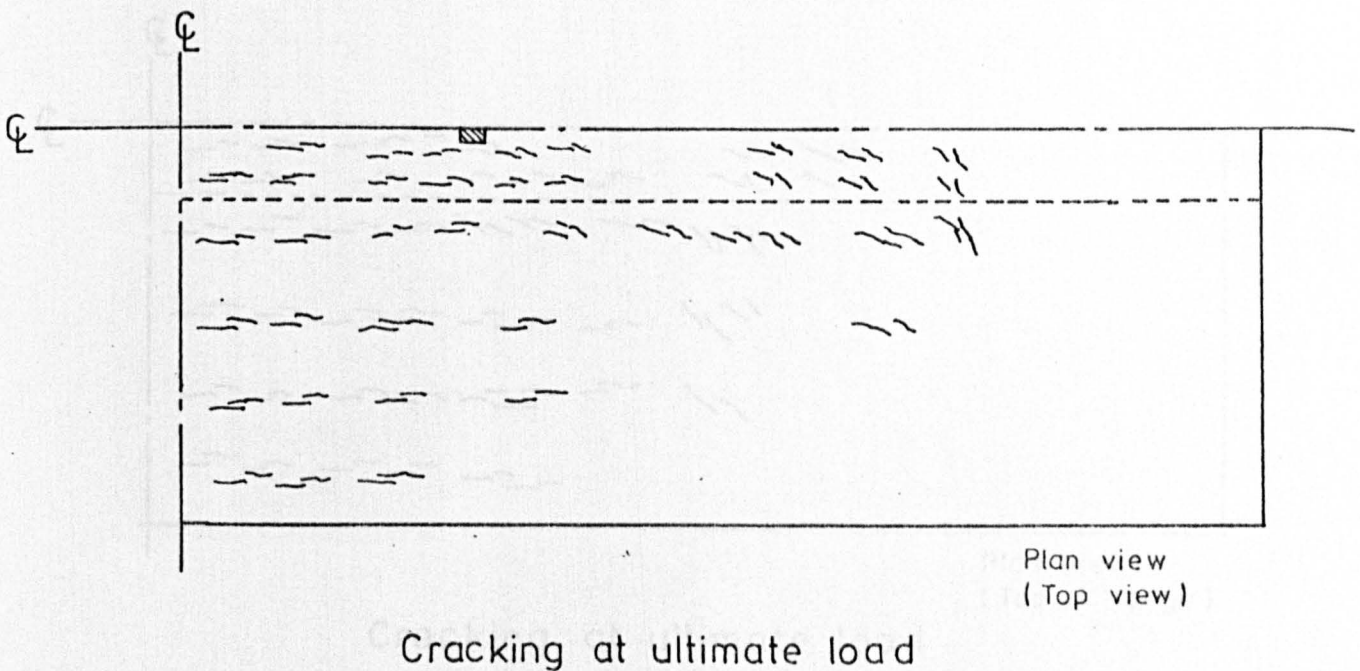
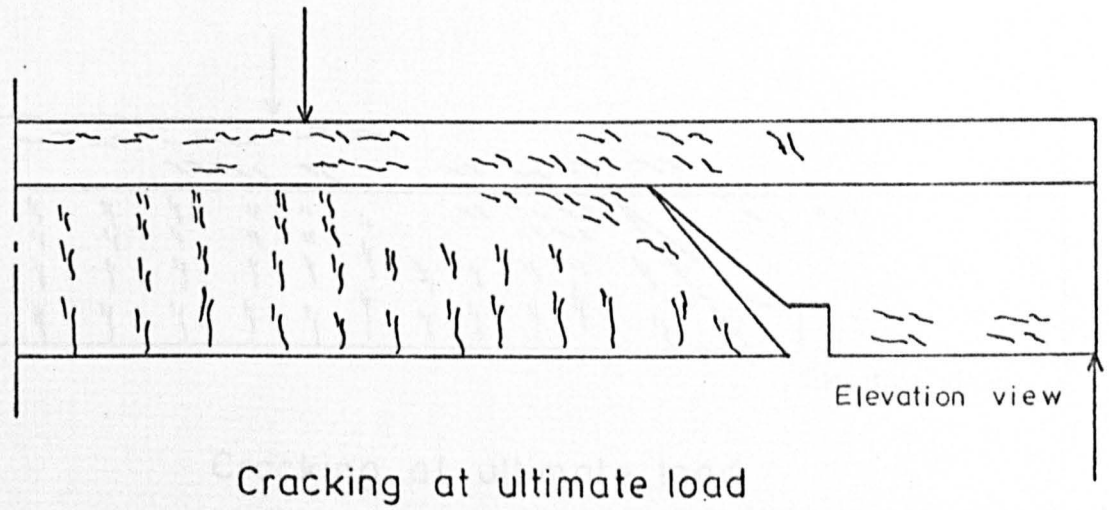
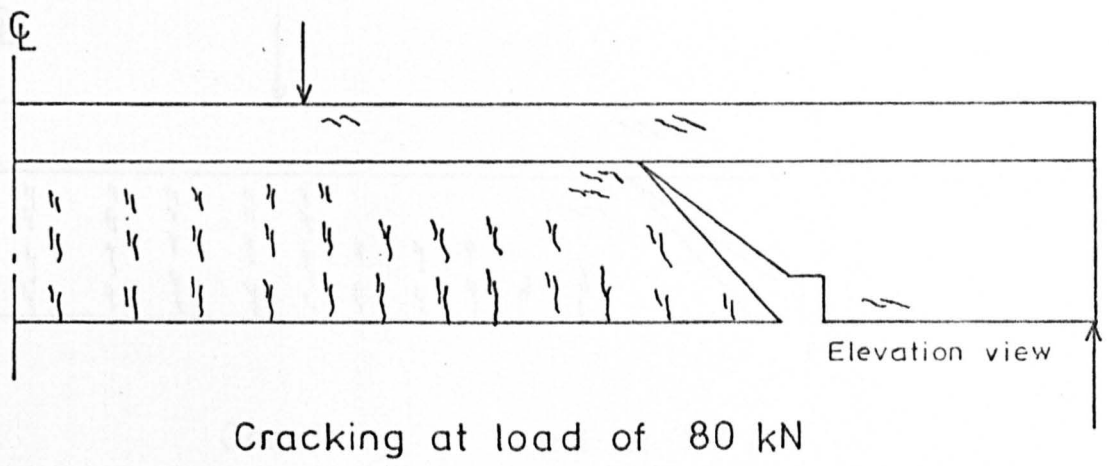
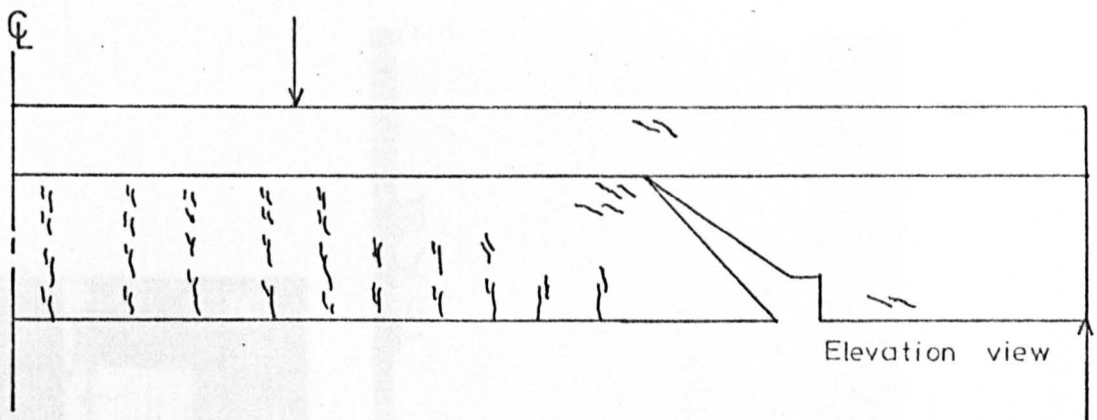
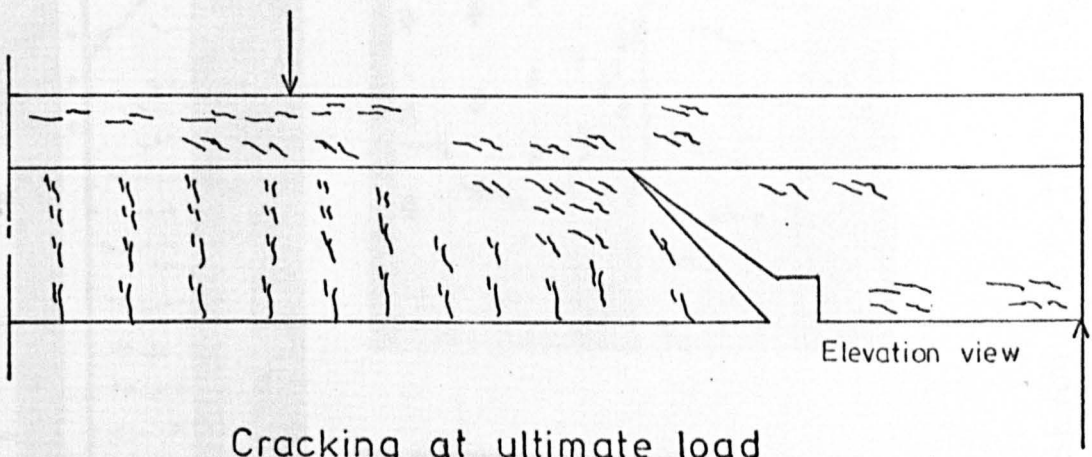


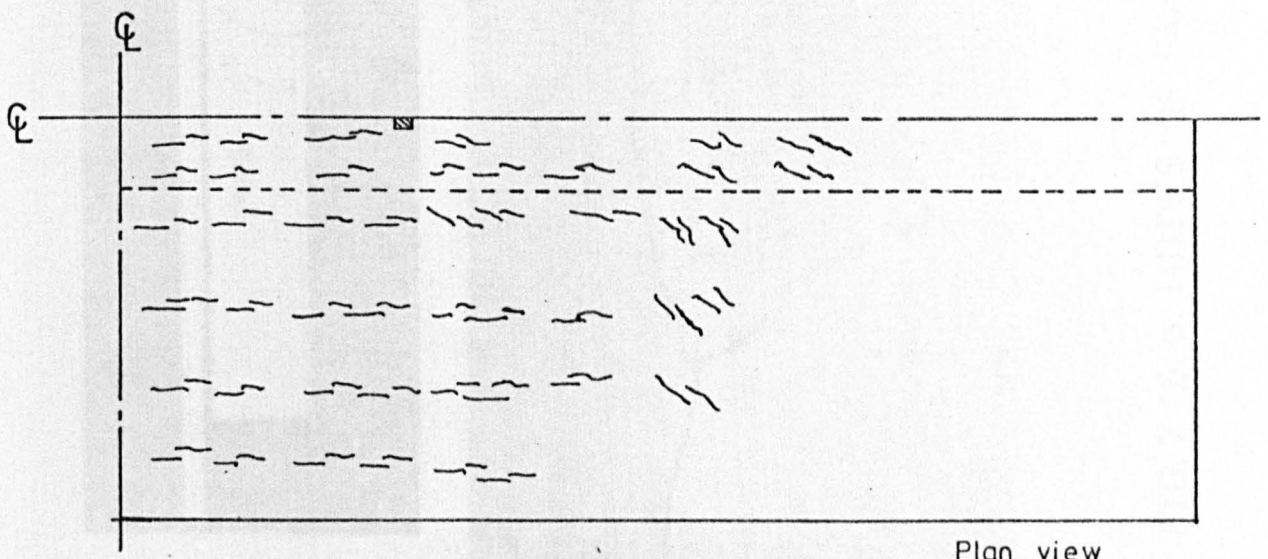
FIG. 7.15. b. CRACK PATTERNS RESULTING FROM ANALYSIS - BEAM TBX - VI



Cracking at load of 80 kN



Cracking at ultimate load



Cracking at ultimate load

Plan view
(Top of flange)

FIG. 7.15.c. CRACK PATTERNS RESULTING FROM ANALYSIS - BEAM TBX - IX

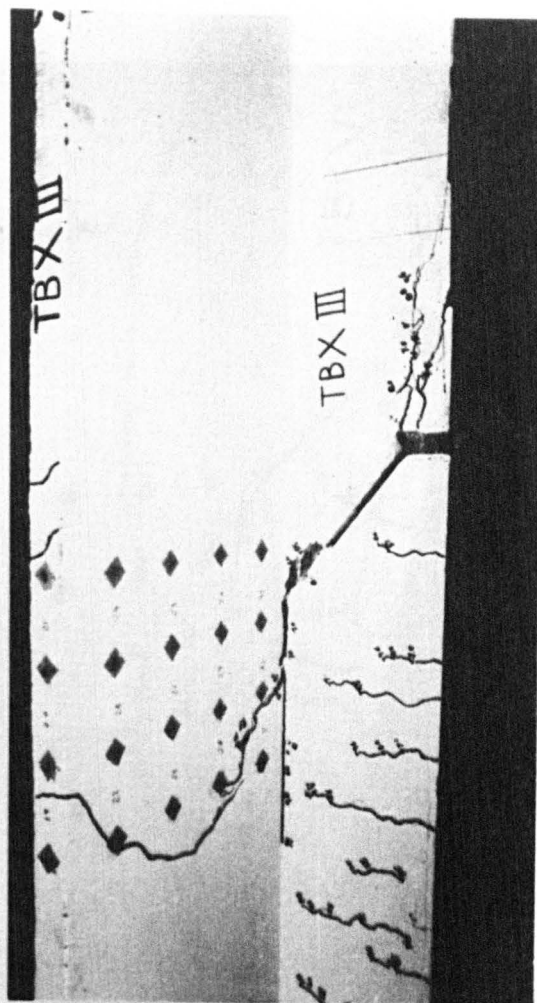
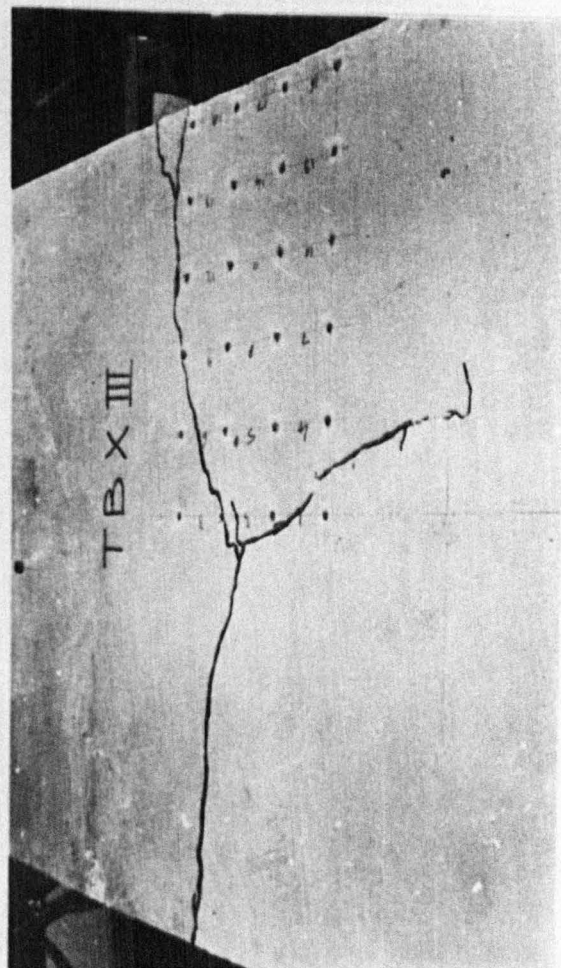
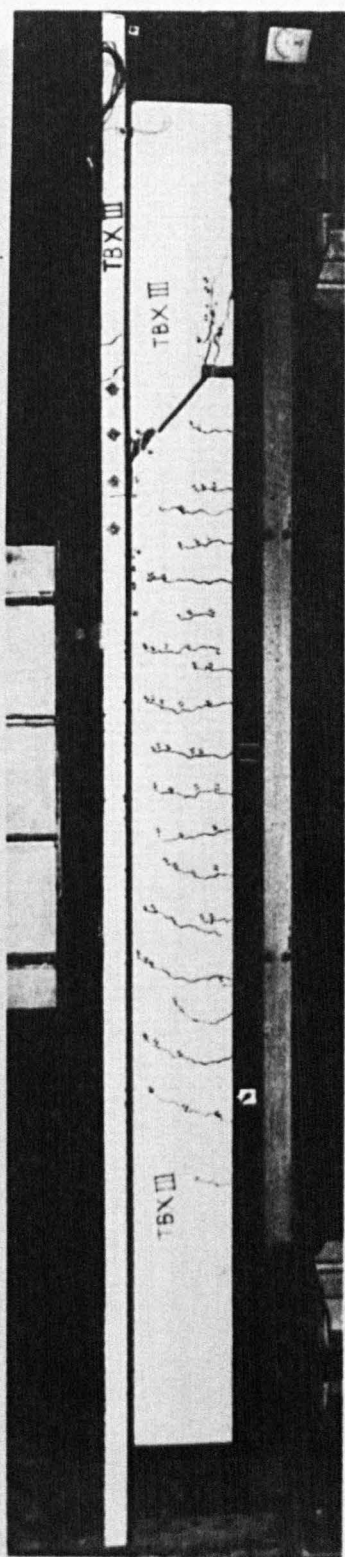


FIG. 7.16. a. MODES OF FAILURE - BEAM TBX - III , $B/b_0 = 6$ & $t/h = 0.167$

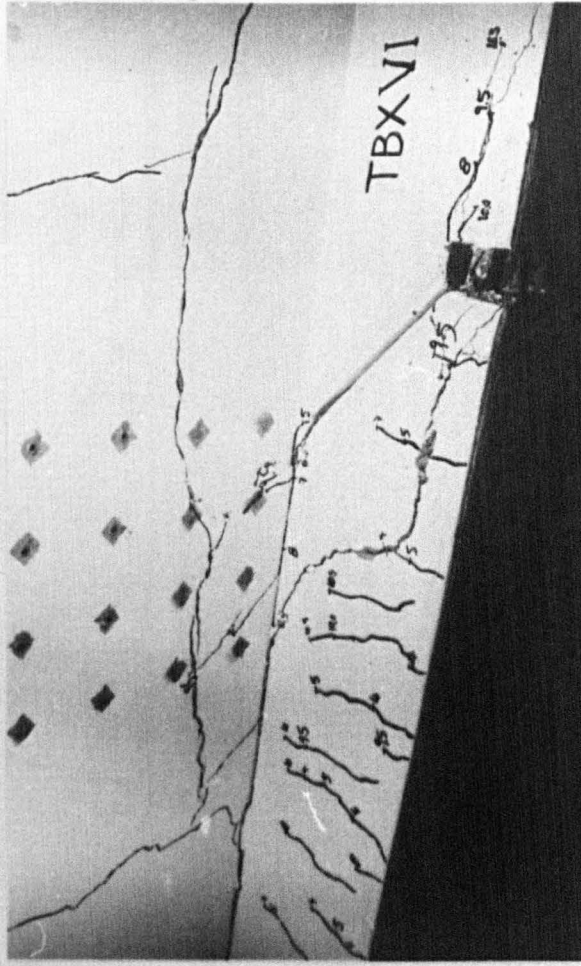
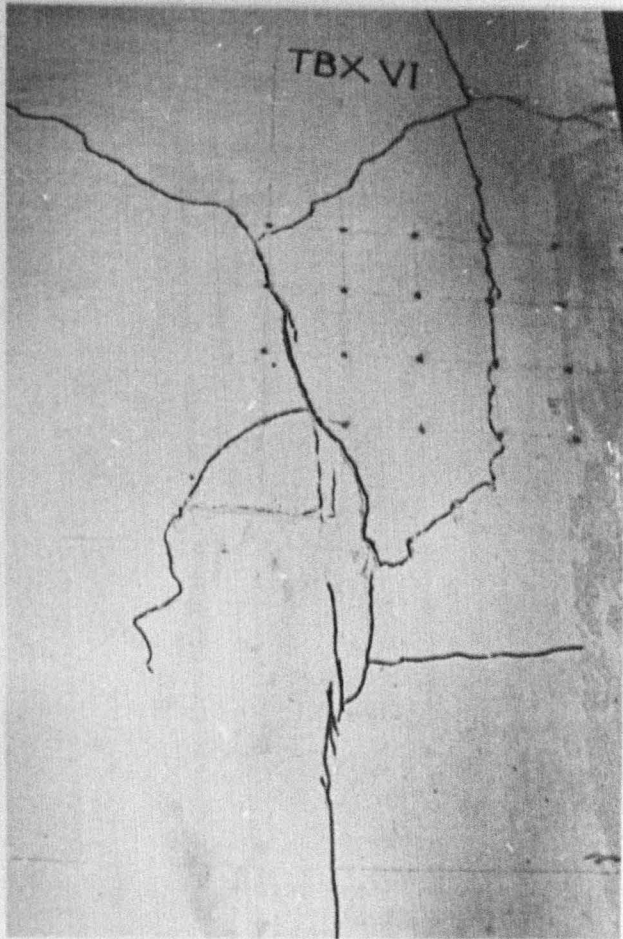
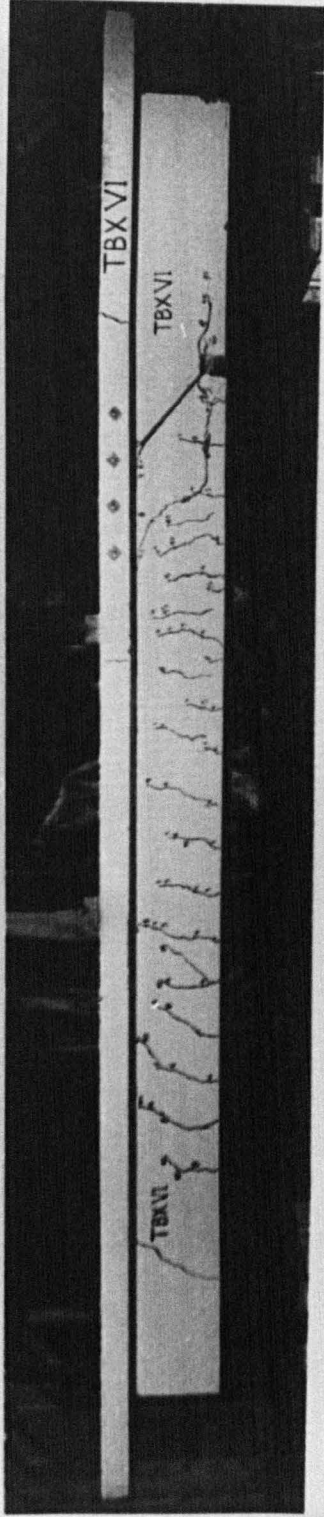


FIG. 7.16. b. MODES OF FAILURE - BEAM TBX - VI , $B/b_0 = 6$ & $t/h = 0.233$

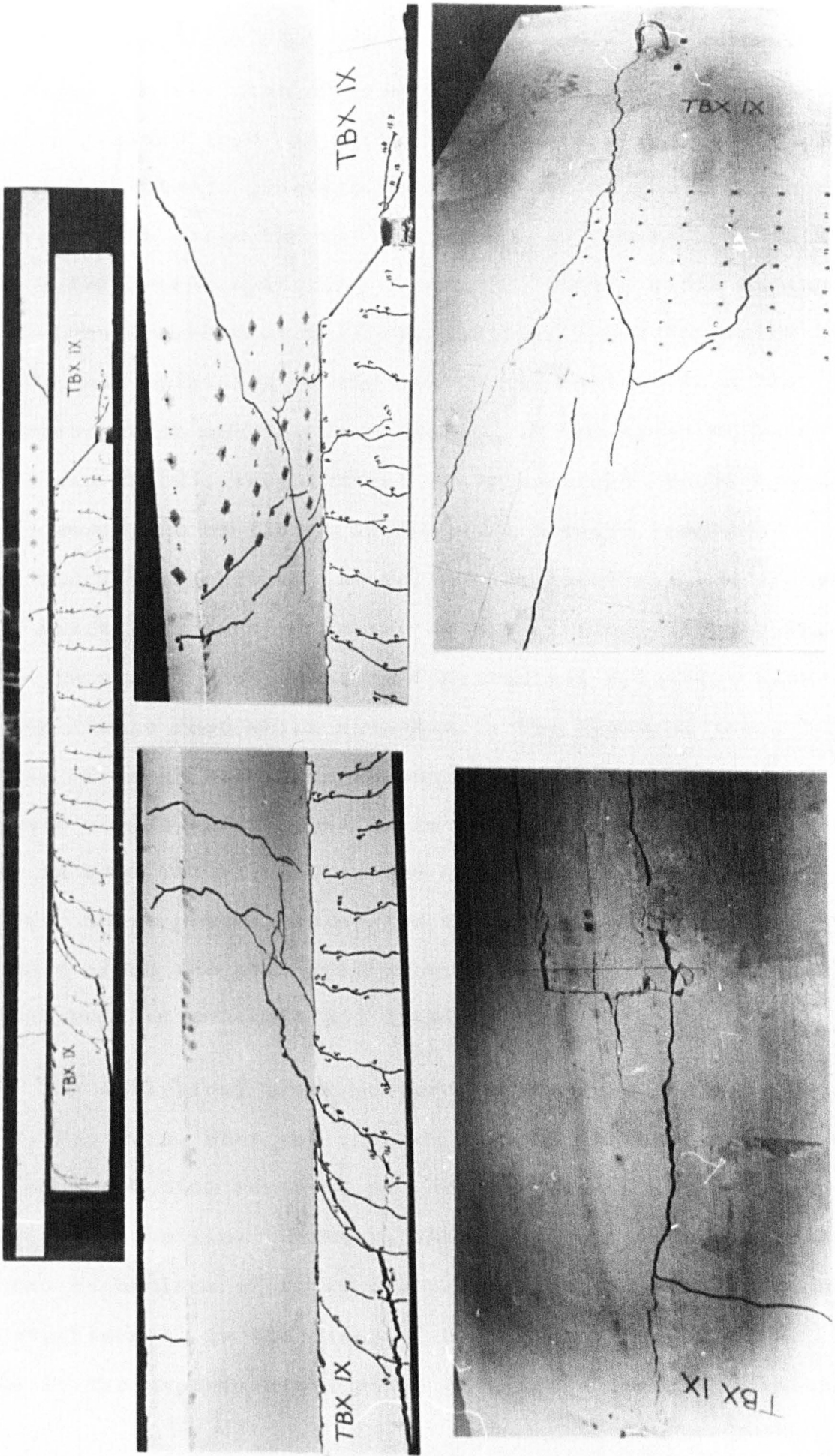


FIG. 7.16. c. MODES OF FAILURE - BEAM TBX - IX, $B/b_0 = 6$ & $t/h = 0.3$

along the flange-web root and turned to enter the underside of flange. In the case of beam TBX III, (with thin flange), when the failure load was approached, a crack propagated from the web-flange junction near the head of the preformed crack and penetrated through the flange thickness. In this beam, a transverse splitting across the flange width at the top surface occurred at failure, and this was accompanied by longitudinal splitting of the web/flange root between the transverse crack and the load block. In the cases of beams TBX VI and TBX IX, longitudinal and transverse cracks appeared in the underside of flange in the area between preformed crack and loading block. At failure longitudinal and transverse splittings took place at the top of flange in the shear span. This was accompanied by longitudinal splitting along the web-flange root which extended to the flexural zone. Failure of these beams was accompanied, also, by secondary diagonal cracks which appeared in the web near the preformed crack in beam TBX VI, and in the other shear span in beam TBX IX. These cracks propagated upward to the flange and downward along the main reinforcement causing the breakdown of bond between concrete and steel.

The analytical crack patterns at failure for these beams, Fig 7.15, show the cracked regions in the flange near the top and bottom surfaces and longitudinally along the flange-web junction. However, there is a difference between the two mechanisms of failure obtained from the analysis and the experiments, in the cases of beams TBX VI and TBX IX. While in the experiments a plane of failure initiated in the

web by a secondary diagonal crack, the analysis shows cracking of flange is the main cause of failure. The deficiency of the finite element in predicting these secondary cracks is probably due to the average meaning for cracking discussed before and the large zones of cracked areas represented by one element. More refined meshes may help to define closely the zones of cracking. Nevertheless, following the order of formation of cracks in the last unstable load increment of the analysis and the observations of cracking in the tests, shows that failure was precipitated by the crack propagation in the flange.

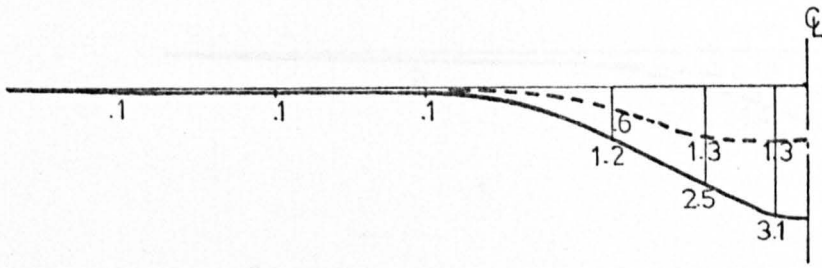
The shear stress distributions across the flange width within the shear span, for the three beams is shown in Fig 7.17. The shearing force resisted by the flange calculated for Section 1, is compared with the experimental values in Table 7.3.

Table 7.3 at 1010 mm from the support

Shear Forces carried by the Flange

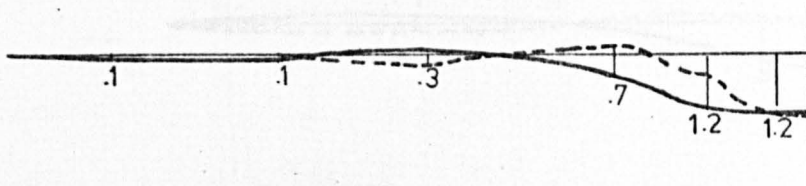
Beam No		TBX III	TBX VI	TBX IX
Cube Strength N/mm ²		38.9	36.4	37.0
Shear Force kN	Analysis	33.3	50.4	62.1
	Exp	38.2	49.7	62.7

FIG 7.17 a. SHEAR STRESS DISTRIBUTION BEFORE FAILURE

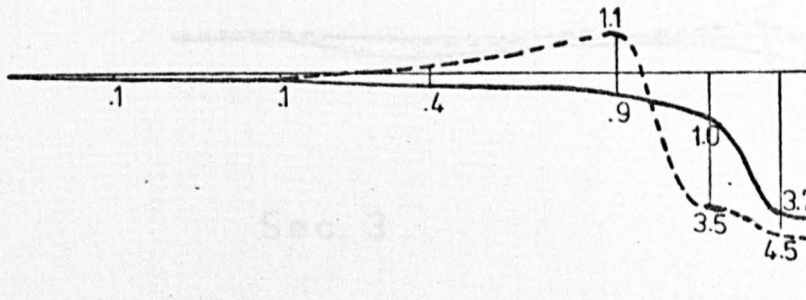


Sec. 1 at 550 mm from the support

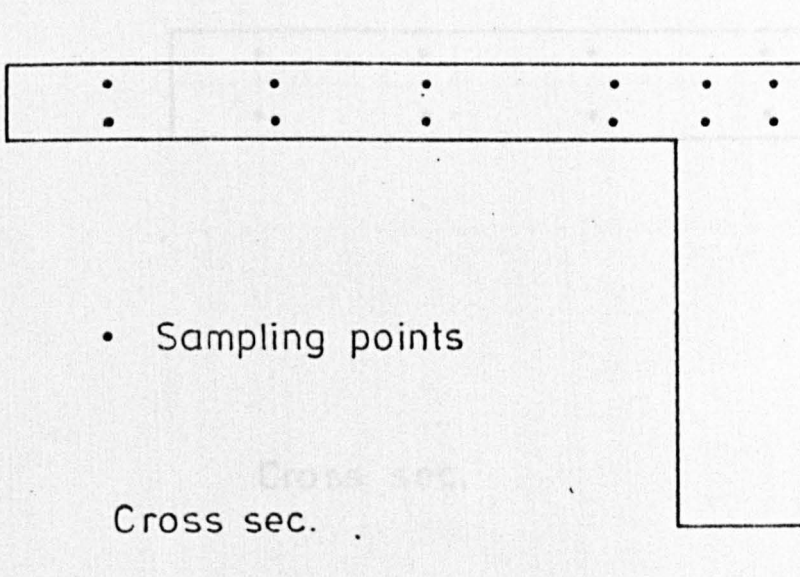
The values shown on the graphs are shear stresses in N/mm^2



Sec. 2 at 860 mm from the support



Sec. 3 at 1010 mm from the support



- Shear stresses near the underside of the flange
- Shear stresses near the top surface of the flange

FIG. 7.17.a. SHEAR STRESS DISTRIBUTION BEFORE FAILURE
BEAM TBX-III

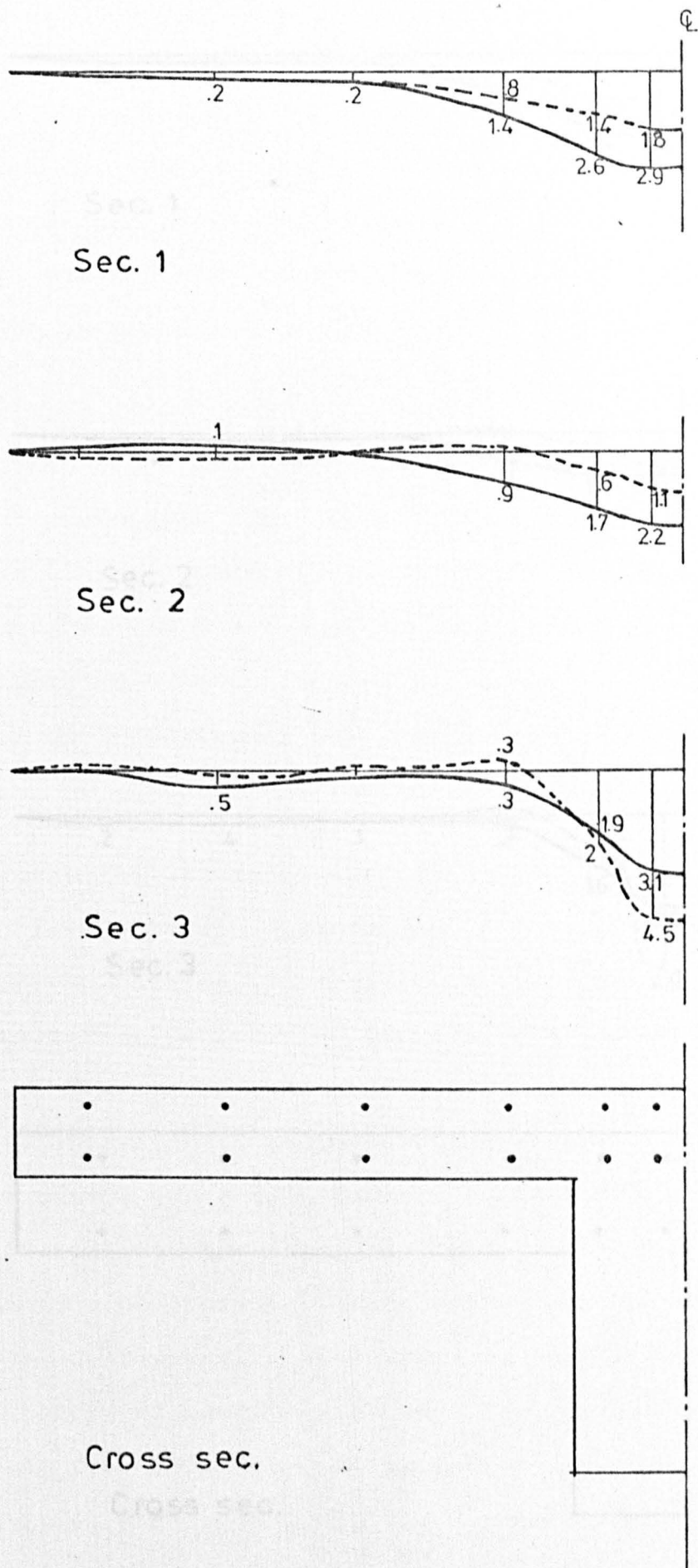
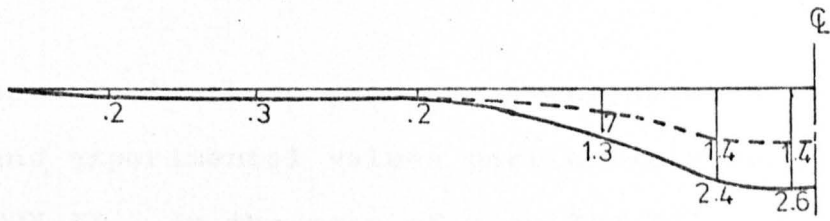
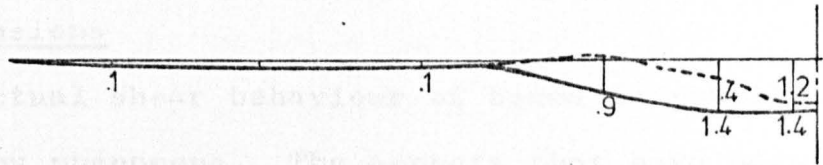


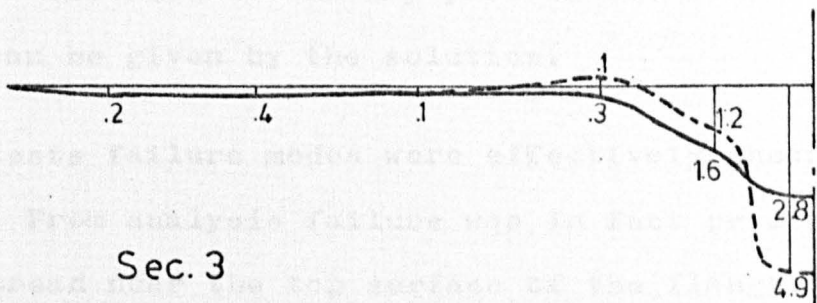
FIG. 7.17. b. SHEAR STRESS DISTRIBUTIONS BEFORE FAILURE - BEAM TBX - VI



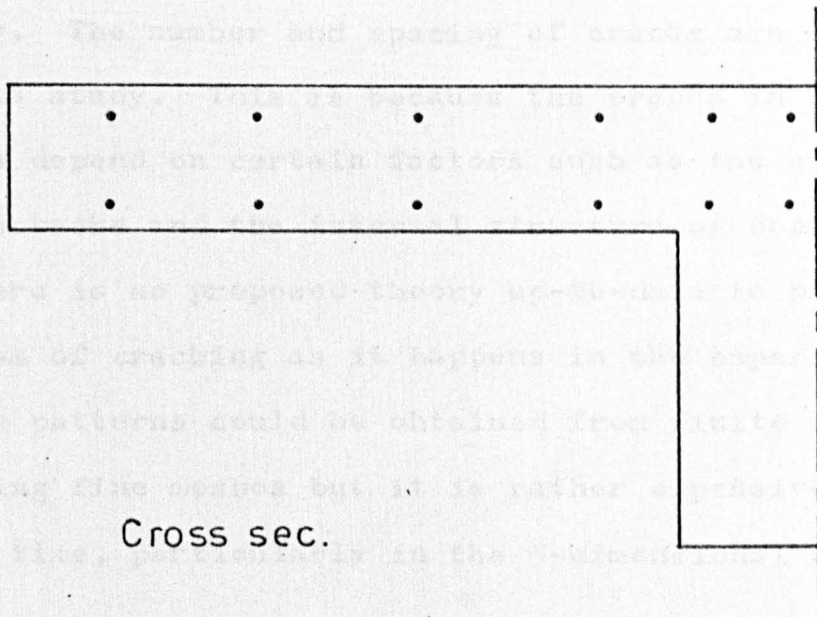
Sec. 1



Sec. 2



Sec. 3



Cross sec.

FIG. 7.17. c. SHEAR STRESS DISTRIBUTIONS BEFORE FAILURE - BEAM TBX - IX

The above Table shows good agreement between the analytical and experimental values particularly for beams TBX VI and TBX IX. In the case of beam TBX III, the analytical value underestimates the experimental. This beam has a thin flange and probably part of the shear force is resisted by the web as discussed before.

7.3 Conclusions

The actual shear behaviour of beams is complex and involves many phenomena. The aspects that have been introduced in this theoretical analysis enabled to predict the history of deformation and the crack propagation for beams failing in shear with enough accuracy. A complete picture of the stress distribution in any part of the beam at any load level can be given by the solution.

From tests failure modes were effectively shearing in the flange. From analysis failure was in fact precipitated by cracks spread near the top surface of the flange. In general quantitative correlation between crack zones are satisfactory. The number and spacing of cracks are not compared in this study. This is because the cracks in the actual beams depend on certain factors such as the existence of pre-microcracks and the internal structure of concrete. In fact, there is no proposed theory up-to-date to predict the mechanism of cracking as it happens in the experiments. Better crack patterns could be obtained from finite element analysis using fine meshes but it is rather expensive in computation time, particularly in the 3-dimensional case.

In some beams cracks propagated from the preformed

crack towards the support point at a lower load level in the analysis than the experiment. This may have been due to the links provided in this area in the tests and have not been introduced in the analysis.

In some beams, the calculated load-displacement curves overestimate the observed ones. This may be due to some extent to the assumed material constants. Also it could be due to the large values of the load increments and the coarseness of the mesh used.

By investigating the shear stress distributions in the area of the flange between the preformed crack and the load point, it was noticed that some values are not consistent (ie they have opposite signs to what they should be). This may be due to (1) The irregular changes in the material properties in that area of flange due to the spreading of cracking in it. (2) The shear retention factor (0.2) that has been used, a more accurate study should be made to investigate its effect on the shear stress distribution. (3) The crude mesh that has been used. (4) The reduced integration rule used in evaluating the stiffnesses.

CHAPTER 8

EFFECTIVE WIDTH AND SHEAR RESISTANCE OF THE FLANGE

8.1 Introduction

It has been stated in Chapter 2 that the strength and behaviour of T-beams depend on a number of factors. The exact analysis of T-beams subject to shear is too time-consuming for the practising engineer and therefore the use of an 'effective width' concept in the calculation of the shear strength of the flange would have distinct advantages.

Several research workers have presented solutions for the effective widths of T-beams for use in bending problems (84)-(91). These studies defined the 'effective width' as a function of the longitudinal stress at the top surface or the middle surface of the slab. However, although there are several studies on the shear strength of T-beams, very little work has been done on the concept of using an 'effective width' in the assessment of the shear force carried by the flange of T-beams. Placas and Regan (13) predicted the effective area of the flange resisting shear as $t (b_o + 6")$, but in the discussion in Section 2.3, it was shown that this value was rather conservative in many cases. Swamy and Quereshi (21) have taken the full width of the flange (B/b_o in their tests was 3), but reduced the neutral axis depth to fall within the flange thickness.

Experimental results (7), (8), (11), (14) and (20) indicate that there is an increase in the shear strength of T-beams with an increase in the flange width, flange thickness

and percentage of main longitudinal reinforcement.

In this chapter an investigation of the 'effective width' to be used in shear, together with the factors influencing the shear strength of the flange, is reported. The Finite Element Analysis described in Chapters 3, 4 and 5 was used to determine the theoretical stress distribution in the flange. This was used exclusively in this study in an attempt to obtain a satisfactory assessment for the 'effective width' and the contribution of the flange in resisting shear forces.

8.2 Effective Width of the Flange

8.2.1 Shear Stresses in the Flange

In general the shear stress distribution in an isolated flanged beam is not constant, but varies across the width of the flange with higher values over the rib and lower values at the edges as shown in Fig 8.1. The stress also varies through the thickness of the flange with higher values near the underside.

The shear stress distribution in the flange was obtained from the non-linear Finite Element Stress Analysis discussed in Chapters 3, 4, and 5. In this Finite Element model, the analysis of reinforced concrete structure in 3-dimensional stress state was presented. The brick-type hexahedron isoparametric elements (20 nodes) were used throughout to represent the concrete and bar elements were also used to simulate the tensile reinforcement.

The progressive cracking of concrete in tension and

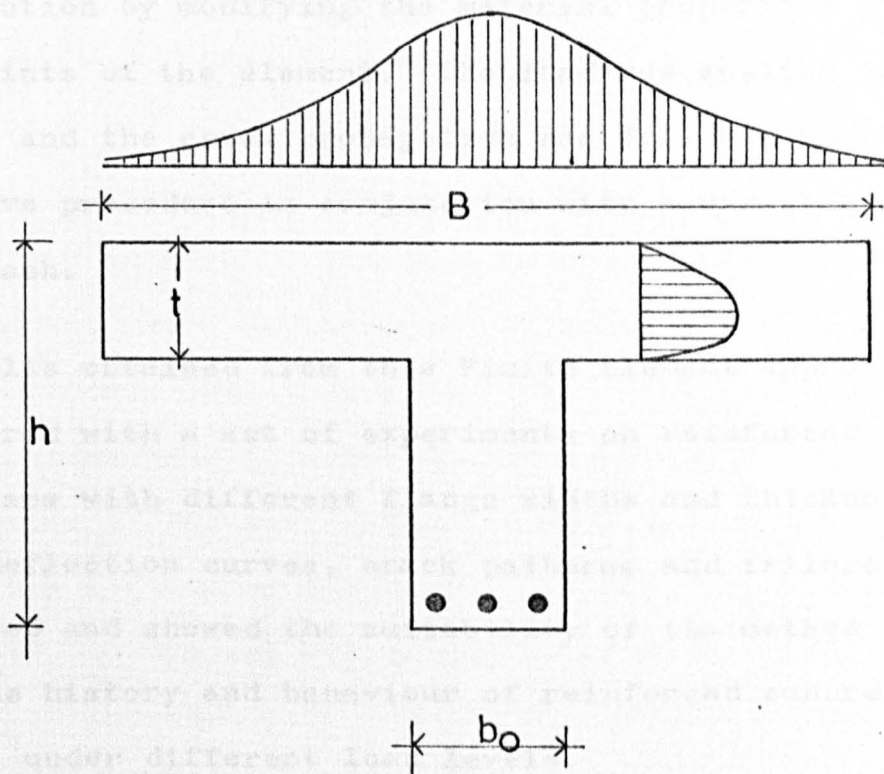


FIG. 8.1. SCHEMATIC SHEAR STRESS DISTRIBUTION IN THE FLANGE OF A T-BEAM

tension compression zones were studied. Multiaxial failure criteria based on experimental data obtained elsewhere (54) and (58), were discussed and used in predicting the cracking. Max_{imum} stress criteria were used to predict cracking in the tension zones, and failure criteria based on octahedral normal and shear stresses were used for tension compression zones. The cracking has been taken into account in the non-linear solution by modifying the material properties at the cracked points of the element. The load was applied in increments and the crack propagation was followed up through an iterative procedure in conjunction with a variable stiffness approach.

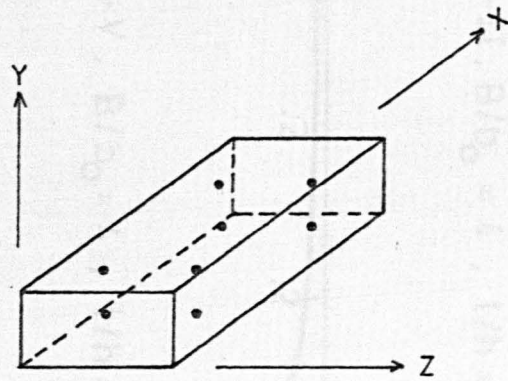
Results obtained from this Finite Element approach were compared with a set of experiments on reinforced concrete T-beams with different flange widths and thickness. The load deflection curves, crack patterns and failure loads were checked and showed the suitability of the method to predict the history and behaviour of reinforced concrete structures under different load levels.

The experimental tests carried out included reinforced concrete T-beams with B/b_o varied between 2 and 6, and t/h ranged from .167 to 0.3 as shown in Table 8.1. The aim of the tests was to study the shear strength of the flange. An inclined preformed crack was used in the web area to eliminate the shear forces resisted by aggregate interlock and dowel action. The tests were conducted on large scale beams of total length 3.4 metre and with shear span/depth ratio of 4.0.

From the non-linear 3-dimensional Finite Element Stress Analysis, six components of stresses were obtained at each of the eight sampling points in every element of the beam (three normal stresses and three shear stresses) as shown in Fig 8.2. The vertical shear stress component was taken at these individual points to form the shear stress distribution in the flange. The shear stress distribution obtained at ultimate load for the beams with different flange widths and thicknesses were used to evaluate 'effective widths'. The shear stresses in the flange were taken at the nearest sampling points to the head of the preformed crack, as this represents the maximum shear stresses in the flange. In the meantime these shear stresses are similar to the ones in actual beam when a diagonal crack forms in the rib width and extends into the flange underside. Moreover, the major part of the shear force is resisted by the flange alone in this section of the beam. The sampling points are located near the top and bottom surfaces of the flange, so the values of the shear stresses at the middle surface of the flange were obtained as the mean value between the shear stresses at these points. The shear stresses across the flange width for the different beams are plotted in Fig. 8.3.

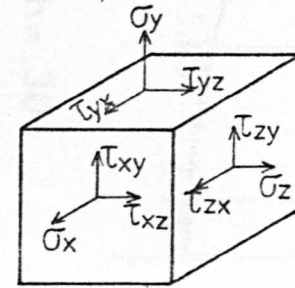
8.2.2 Definition of the 'Effective Width'

The 'effective width' is assumed to be that width of the flange which, when acting at a constant average shear stress, would sustain a shear force equal to that obtained by integrating the shear stresses across the middle surface of the flange,



(A)

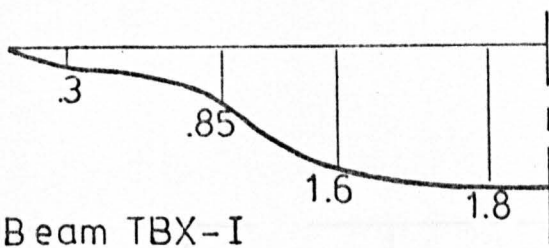
• Integration points



(B)

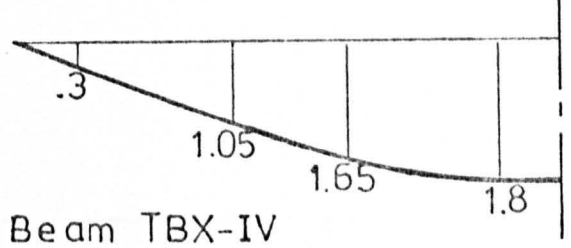
Stresses at each integration point

FIG.8.2. INTEGRATION POINTS AND STRESS COMPONENTS



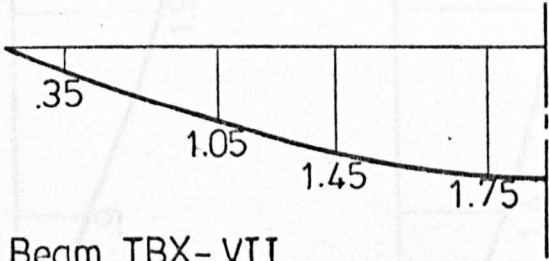
Beam TBX-I

$$B/b_0 = 2, \quad t/h = .167$$



Beam TBX-IV

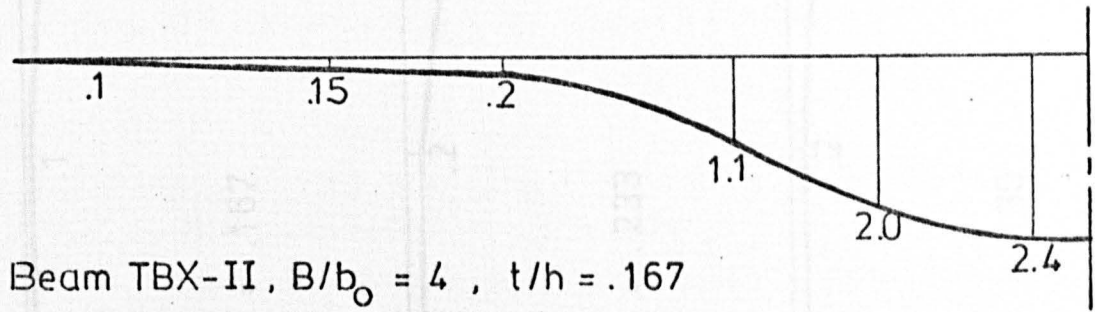
$$B/b_0 = 2, \quad t/h = .233$$



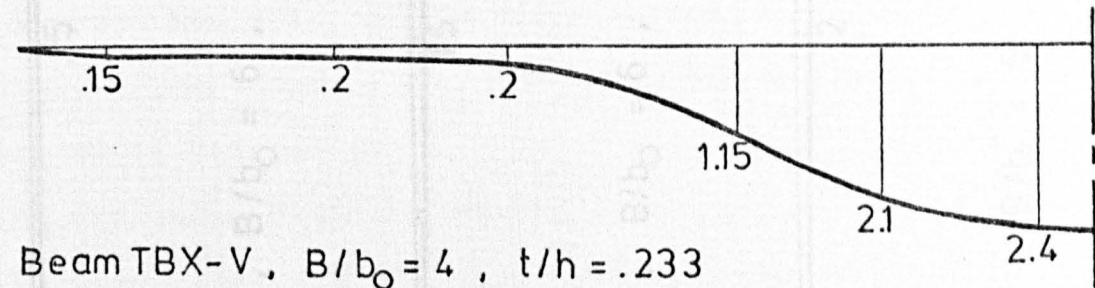
Beam TBX-VII

$$B/b_0 = 2, \quad t/h = .30$$

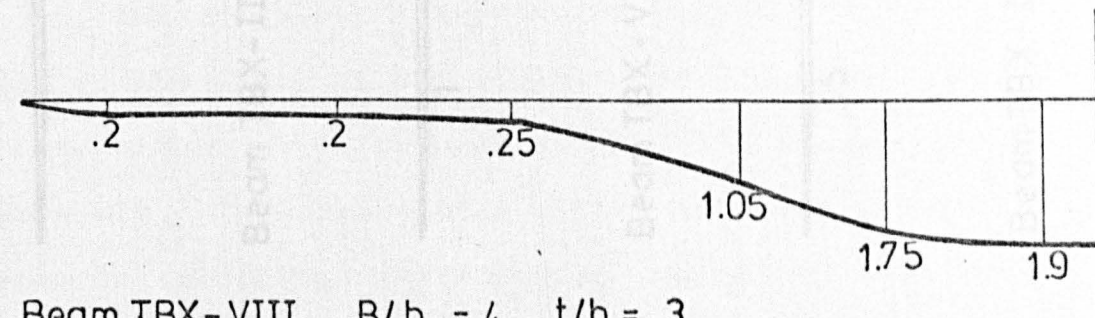
The values shown on the graphs are shear stresses in N/mm^2



Beam TBX-II, $B/b_0 = 4, \quad t/h = .167$



Beam TBX-V, $B/b_0 = 4, \quad t/h = .233$



Beam TBX-VIII, $B/b_0 = 4, \quad t/h = .3$

FIG. 8.3. SHEAR STRESS DISTRIBUTION AT THE MIDDLE SURFACE FOR DIFFERENT FLANGES

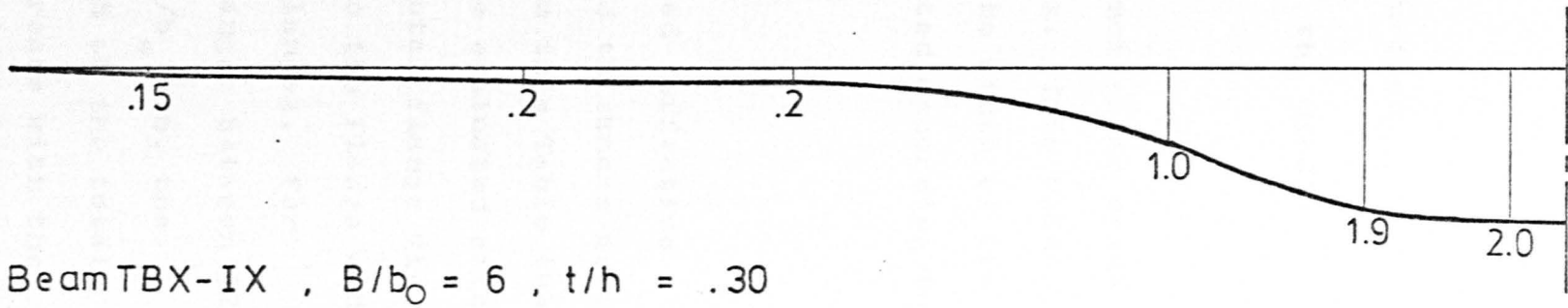
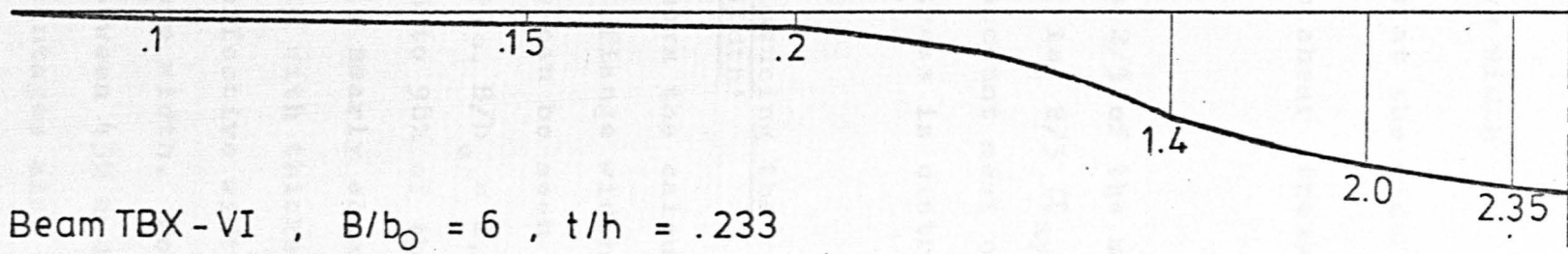
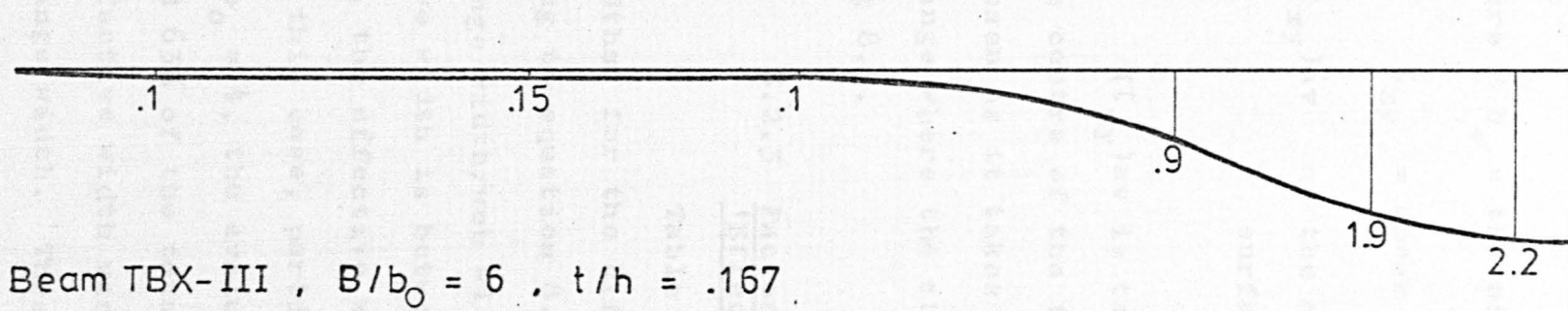


FIG. 8.3. - Continued

$$\text{ie } 2 b_e = \frac{2 \int_0^{B/2} \tau_{xy} dx}{(\tau_{xy})_{av}} \quad (8.1)$$

where $2 b_e$ = the effective width

τ_{xy} = shear stress at the middle surface

$(\tau_{xy})_{av}$ = the average shear stress at the middle surface

$(\tau_{xy})_{av}$ is taken as $2/3$ of the maximum shear value at the centre of the flange, ie $2/3 (\tau_{xy})_{max}$. This value is chosen as it takes into account most of the width of the flange where the shear stress is distributed according to Fig 8.3.

8.2.3 Factors Influencing the 'Effective Width'

Table 8.1 shows the calculated 'effective widths' for the different flange width and thickness according to equation 8.1. It can be seen from this Table that for flange width/web width ratio, $B/b_o = 2$, the evaluated effective width is between 94% to 98% of the total flange width ie, the effective width is nearly equal to the flange width in this case, particularly with thicker flanges. For $B/b_o = 4$, the evaluated effective width ranges between 52% and 63% of the total flange width. For $B/b_o = 6$, the effective width varies between 43% and 49% of the total flange width. These percentages also increase with the increase in the flange thickness and amount of main longitudinal reinforcement.

Table 8.1 Evaluated 'Effective Width', Equation (8.1)

Beam No	Flange		Ratio $\frac{B}{b_o}$	Ratio $\frac{t}{h}$	Ratio $\frac{100A_s}{b_o d}$	Evaluated Effective Width	<u>Evaluated E W</u> Flange width
	Width B mm	Thick t mm					
TBX-I	350	50	2	.167	1.16	328	.94
TBX-II	700	50	4	.167	1.78	367	.52
TBX-III	1050	50	6	.167	2.25	454	.43
TBX-IV	350	70	2	.233	1.32	342	.98
TBX-V	700	70	4	.233	1.92	393	.56
TBX-VI	1050	70	6	.233	2.90	459	.44
TBX-VII	350	90	2	.30	1.5	344	.98
TBX-VIII	700	90	4	.30	2.25	440	.63
TBX-IX	1050	90	6	.30	3.25	518	.49

Curves are plotted for the variation of the evaluated effective width at ultimate load, $2 b_e$, with change in the ratios of flange width to web width, B/b_o , flange thickness to beam depth, t/h , and area of main longitudinal reinforcement ρ , as shown in Fig 8.4. These curves indicate that there is an increase in the effective width with increasing flange width, flange thickness and percentage of main longitudinal reinforcement. Fig. 8.4b, shows also that when $B/b_o > 4$, there is a higher rate of increase in the 'effective width' with increasing flange thickness.

Also the ratios of the resulting calculated 'effective widths' to the flange widths, $2 b_e/B$, web width, $2 b_e/b_o$ and flange thickness, $2 b_e/t$, are plotted against the ratios B/b_o , t/h and ρ in Figs 8.5, 8.6 and 8.7. Fig 8.5a and c indicate that $2 b_e/B$ decreases non-linearly with increasing B/b_o or ρ . Fig 8.5b shows the increase in $2 b_e/B$ with increasing t/h . $2 b_e/b_o$ increased with the increase in B/b_o , t/h and ρ as shown in Fig 8.6 and the rate of increase was nearly constant particularly in Fig 8.6a. In Fig 8.7, $2 b_e/t$ increased with increasing B/b_o or ρ , while it decreased with increasing t/h .

8.2.4 Prediction of the 'Effective Width'

Examining the data plotted in Figs 8.4-8.7, a non-linear regression analysis was carried out to take into account the parameters influencing the effective flange width. This non-linear procedure gives the coefficients of a non-linear relationship between a set of independent variables and one dependent variable. Relationships were

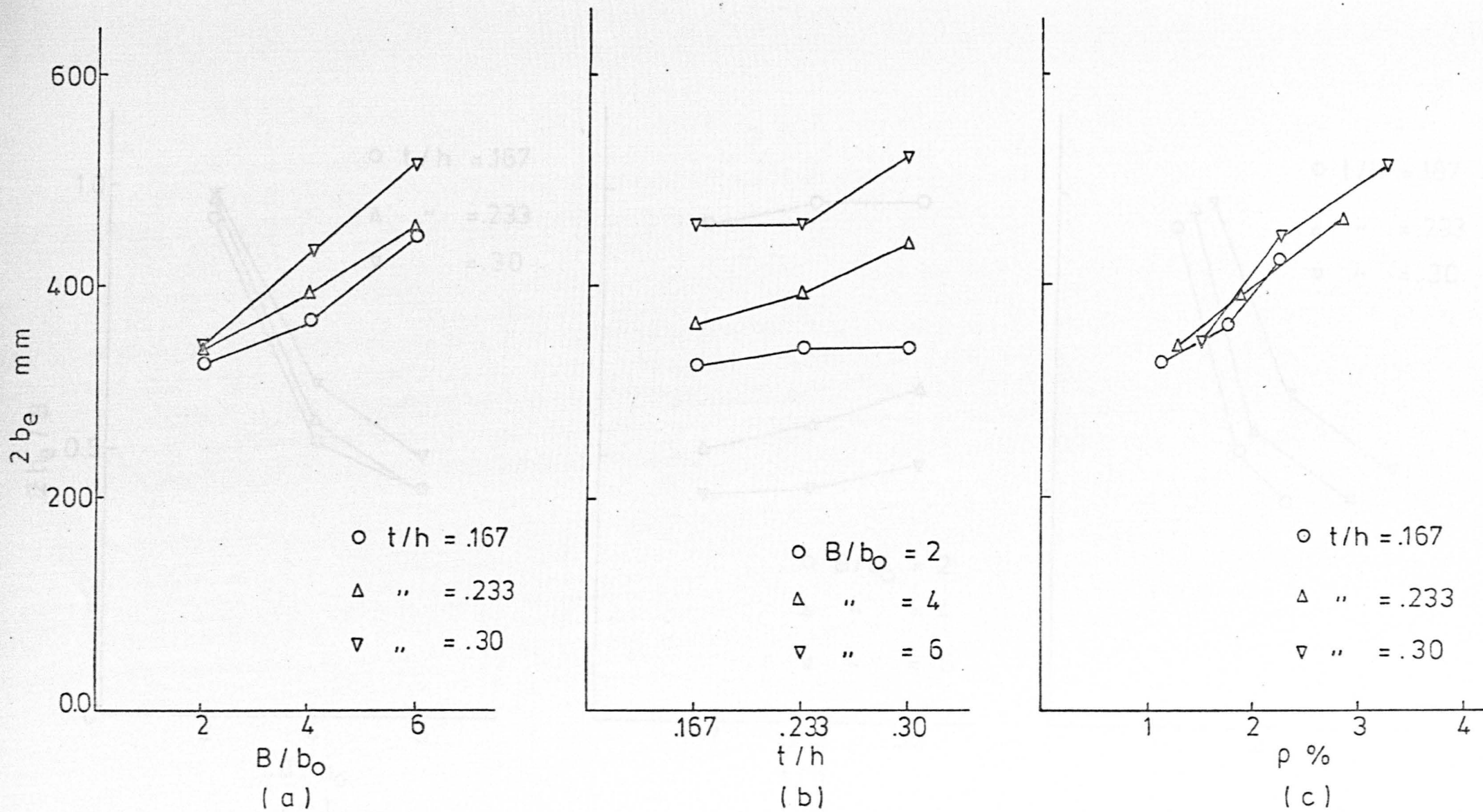


FIG. 8.4. EFFECTIVE WIDTH AT ULTIMATE LOAD

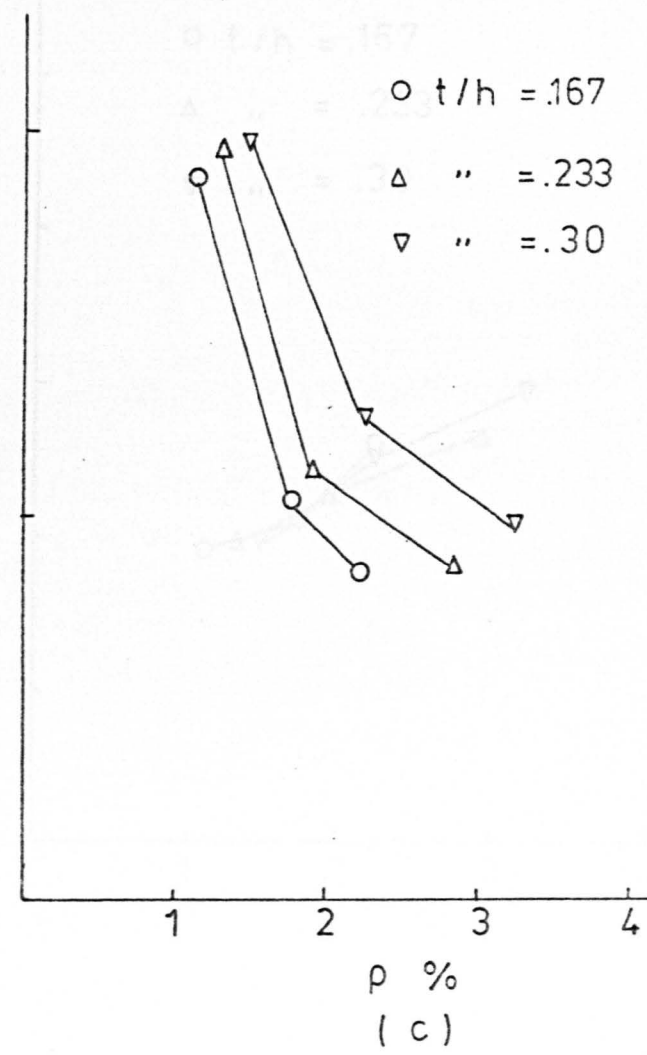
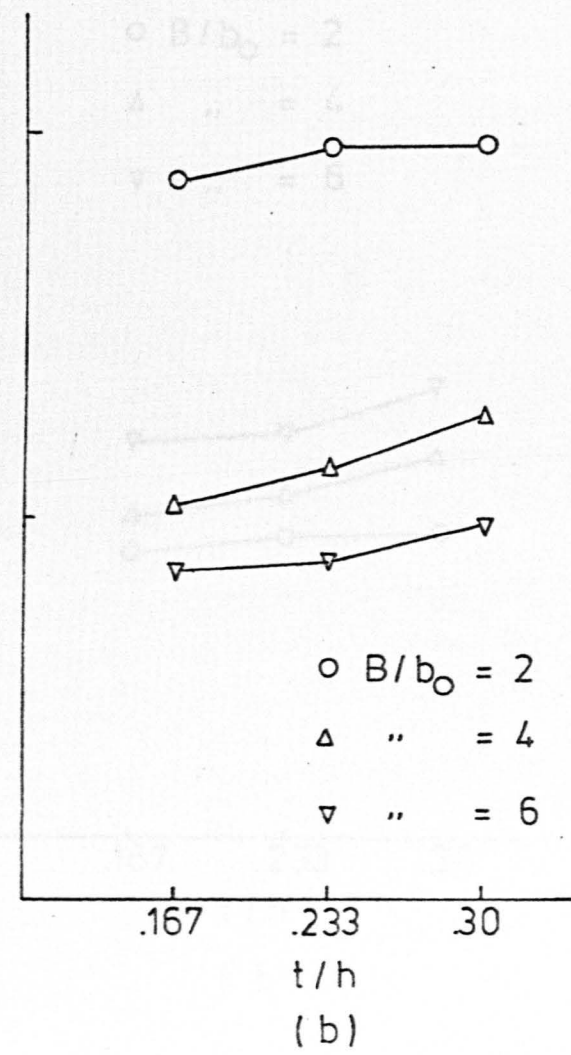
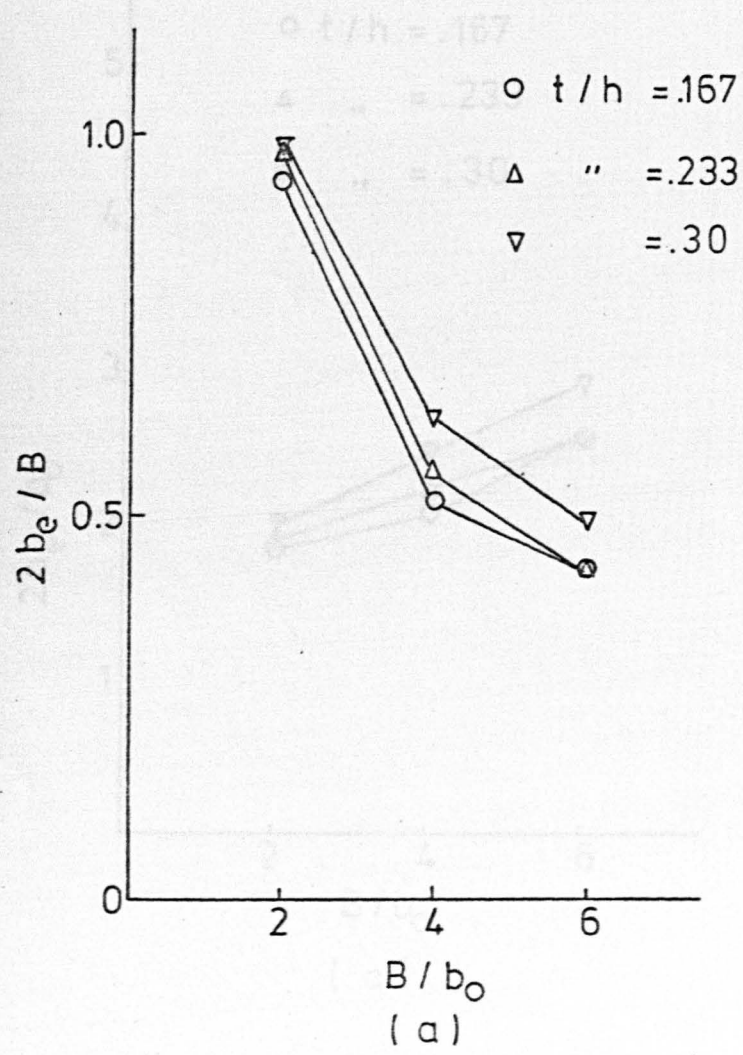


FIG. 8.5. EFFECTIVE WIDTH AT ULTIMATE LOAD

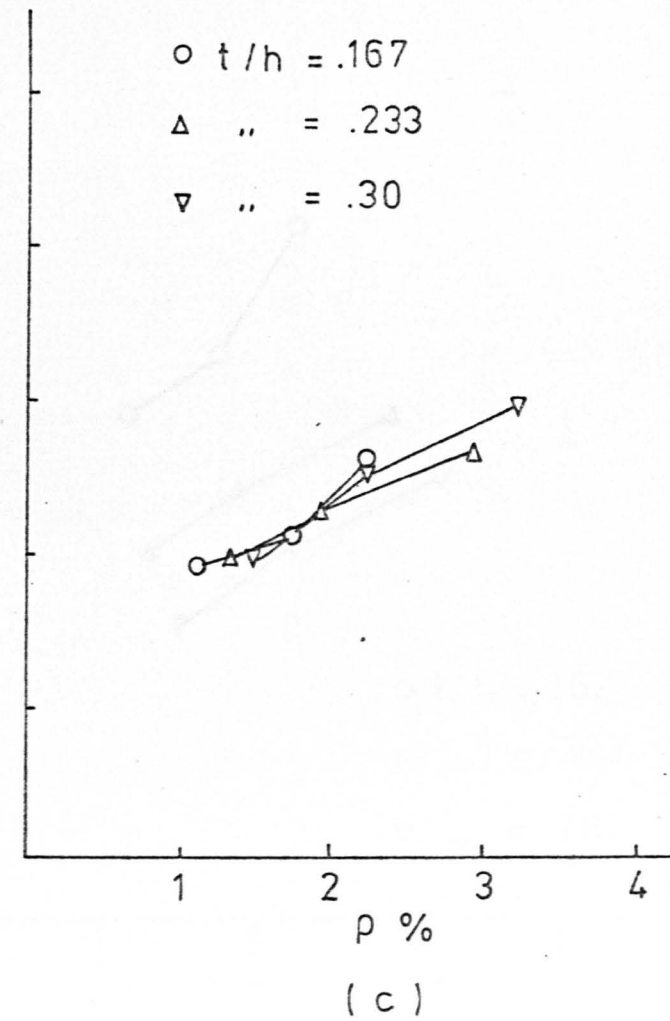
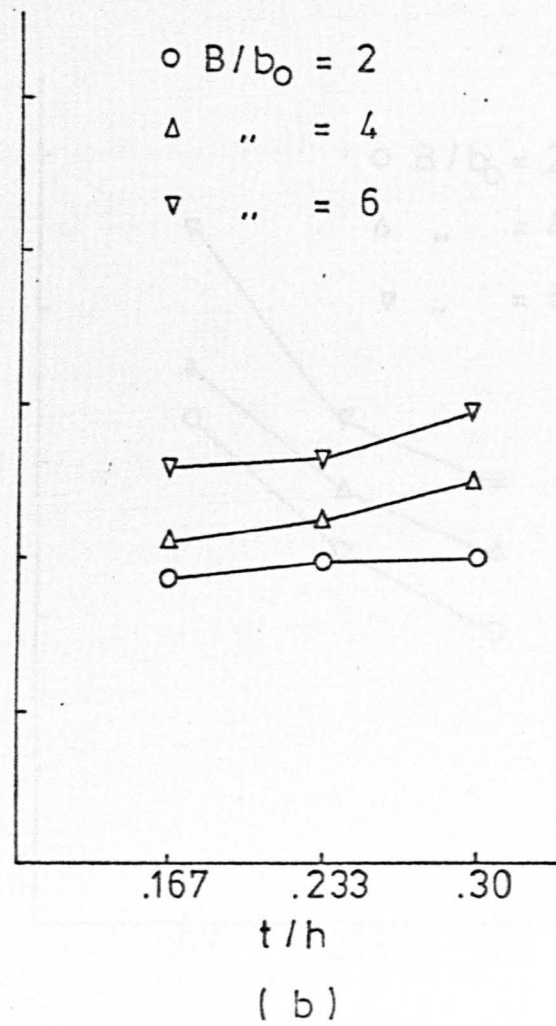
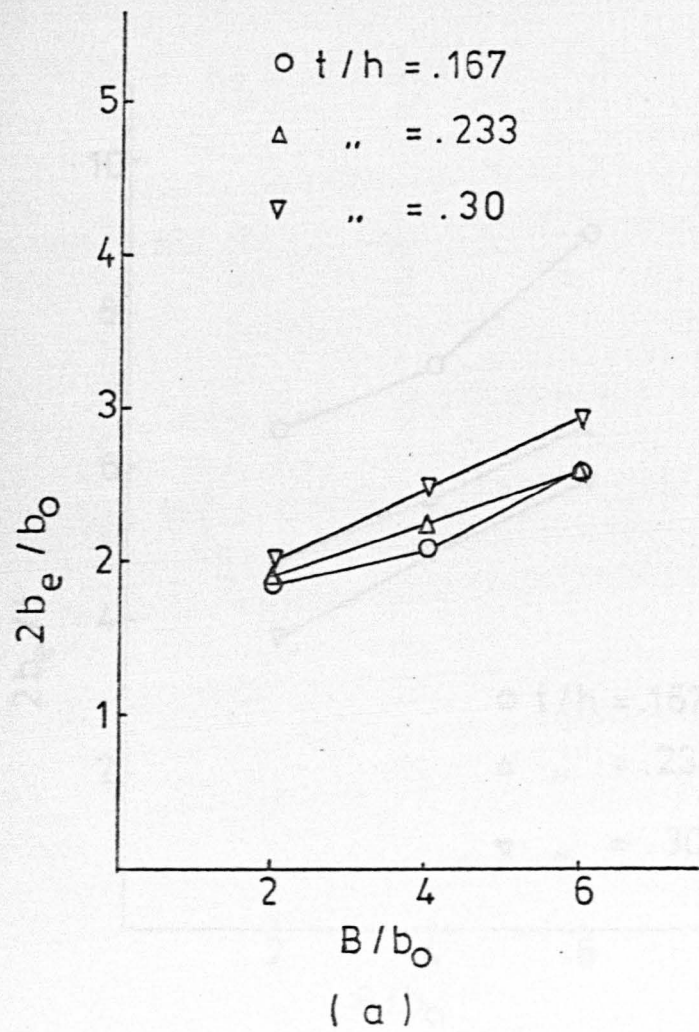


FIG. 8. 6. EFFECTIVE WIDTH AT ULTIMATE LOAD

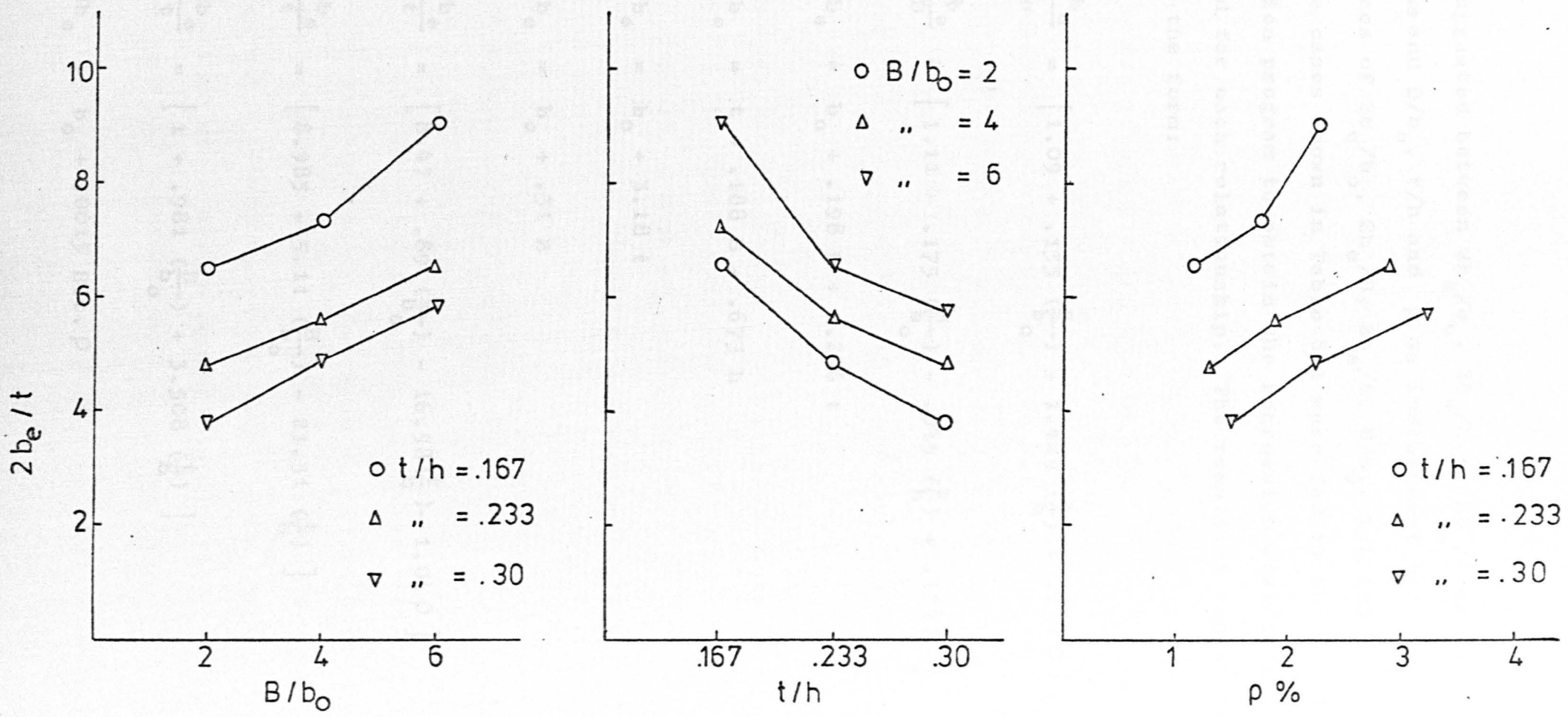


FIG.8.7. EFFECTIVE WIDTH AT ULTIMATE LOAD

first suggested between $2b_e/b_o$, $2b_e/B$ or $2b_e/t$ as dependent variables and B/b_o , t/h and ρ as independent variables. The values of $2b_e/b_o$, $2b_e/B$, $2b_e/t$, B/b_o , t/h and ρ for the nine cases shown in Table 8.1 were fed to the non-linear regression program to obtain the regression coefficients required for each relationship. The resulting equations were in the form:

$$\frac{2b_e}{b_o} = \left[1.09 + .135 \left(\frac{B}{b_o} \right) + 1.429 \left(\frac{t}{h} \right) + .172 \rho \right] \quad (8.2)$$

$$\frac{2b_e}{B} = \left[1.11 - .175 \left(\frac{B}{b_o} \right) - .045 \left(\frac{t}{h} \right) + .128 \rho \right] \quad (8.3)$$

$$2b_e = b_o + .198 B + 1.296 t \quad (8.4)$$

$$2b_e = t + .188 B + .673 h \quad (8.5)$$

$$2b_e = b_o + 3.18 t \quad (8.6)$$

$$2b_e = b_o + .31 B \quad (8.7)$$

$$\frac{2b_e}{t} = \left[8.47 + .89 \left(\frac{B}{b_o} \right) - 16.58 \left(\frac{t}{h} \right) - 1.04 \rho \right] \quad (8.8)$$

$$\frac{2b_e}{t} = \left[8.985 + 5.11 \left(\frac{B}{b_o} \right) - 21.31 \left(\frac{t}{h} \right) \right] \quad (8.9)$$

$$\frac{2b_e}{t} = \left[1 + .981 \left(\frac{B}{b_o} \right) + 3.508 \left(\frac{t}{h} \right) \right] \quad (8.10)$$

$$2b_e = b_o + .0015 B.t.\rho \quad (8.11)$$

$$2b_e = b_o + .0268 B.t^{.69} \rho^{-.57} \quad (8.12)$$

The calculated values from these equations are compared with the evaluated effective width from equation 8.1 in Table 8.2. The values obtained by equations 8.2, 8.4, 8.5 and 8.12 are more close to the ones obtained from equation 8.1. Equation 8.3 gave inconsistent values for cases II, III, V and VIII. Excluding the effect of flange width and amount of main steel reinforcement in equation 8.6, the obtained values are not in satisfactory agreement. Equation 8.7 gave conservative values in short flanges. Equation 8.10 gave lower values with thin flanges while with thick flanges the values were overestimated. Equation 8.11 also gave lower values except for wide and thick flanges.

In some cases of short flanges the 'effective width' predicted by the above equations was exceeding the actual flange width, so it must be emphasised that in this case the 'effective width' should be taken equal to the flange width.

8.3 Shear Resistance of the Flanges

8.3.1 Introduction

It was noticed during the tests that failure occurred by propagation of the diagonal cracks into the compression zone of the flange initiating tensile cracking in this area which precipitated the final break down of the beam. Failure was also accompanied by splitting along the main longitudinal reinforcement.

In this section the contribution of the compression

Table 8.2 'Effective Width' of the Flange

Beam No	Flange		Evaluated 'Effective Width' mm											
	Width B mm	Thickness t mm	Integ Eq 8.1	Eq 8.2	Eq 8.3	Eq 8.4	Eq 8.5	Eq 8.6	Eq 8.7	Eq 8.8	Eq 8.9	Eq 8.10	Eq 8.11	Eq 8.12
TBX-I	350	50	328	315	315	309	318	334	283	314	322	177	205	305
TBX-II	700	50	367	380	442	379	383	334	392	371	374	276	268	379
TBX-III	1050	50	454	442	360	448	449	334	499	436	425	374	352	443
TBX-IV	350	70	342	336	322	335	338	398	283	351	353	265	223	328
TBX-V	700	70	393	401	450	405	404	398	392	433	424	402	316	422
TBX-VI	1050	70	459	478	445	474	470	398	499	387	496	539	495	466
TBX-VII	350	90	344	358	330	361	357	461	283	355	325	361	246	344
TBX-VIII	700	90	440	428	480	431	423	461	392	426	417	537	387	444
TBX-IX	1050	90	518	505	490	500	489	461	499	493	509	715	635	501

zone of the flange in resisting shear forces is examined. Comparison is then made between the shear force carried by the flange and the total shear force supported by the beam at ultimate load.

8.3.2 Prediction of Shear Resistance of the Flange

In order to predict the shear force carried by the flange of a T-beam, one needs to know: the effective area of the flange involved in resisting shear forces, and the average shear stresses acting on it at failure. The effective area of flange is taken as the 'effective width' evaluated by the equations above, times the thickness of the flange.

Taylor (92) computed the shear stresses in the compression zone of rectangular beams from longitudinal strains measured on the side of the beams. The computational method used was derived from the differential equations defining stresses in the beam. Fig 8.8 shows the distribution of the shear stress in the compression zone. The maximum shear stress value obtained at ultimate load was about 1.7 N/mm^2 for concrete strength 60 N/mm^2 . Regan (93) took the average shear stress for the critical condition with respect to shear to be $0.2 (f'_c)^{2/3}$.

In this study, the average shear stress value is taken as $f'_c/20$. This value was chosen as an average value for the shear stresses computed by finite element analysis across the flange width at ultimate load. This value also agrees with the shear stresses given by CP 110, 1972, (1),

considering the shear stresses in the concrete is assumed to be a factor of safety of 1.5.

The shear strength of the flange can be expressed as:

$$V_{fs} = 2b_s \cdot l \cdot f_s / 20$$

Table 8.3 shows the shear forces calculated by using eqn (8.13) using effective width evaluated from eqns 8.2 to 8.12. The shear forces were then integrated from the stress distribution to compare the experimental values.

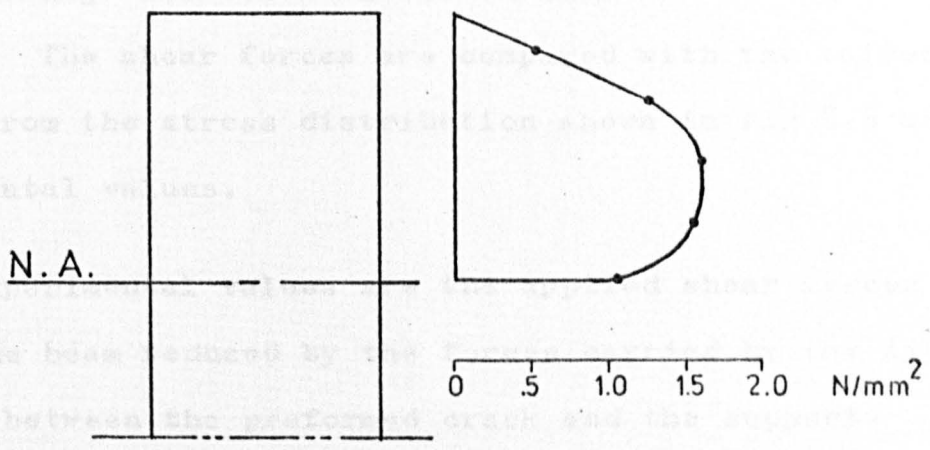


FIG. 8.8. SHEAR STRESS DISTRIBUTION IN THE COMPRESSION ZONE OF RECTANGULAR BEAM AT ULTIMATE LOAD (After Taylor)

where V_1 = shear force carried by the link
 f_y = yield strength of the steel = 250 N/mm²
 A_{sl} = cross sectional area of the link

(2) For a link that has not yielded

$$V_1 = 2 \cdot f_s \cdot l \cdot A_{sl} \tag{8.15}$$

considering the shear stresses in the code are divided by a factor of safety of 1.6.

The shear strength of the flange can therefore be expressed as:

$$V_c = 2b_e \cdot t \cdot f'_c / 20 \quad (3.13)$$

Table 8.3 shows the shear forces calculated by equation (8.13) using 'effective widths' evaluated from equations 8.2 to 8.12. The shear forces are compared with the values integrated from the stress distribution shown in Fig 8.3 and the experimental values.

The experimental values are the applied shear forces acting on the beam reduced by the forces carried by the links in the area between the preformed crack and the support. These forces are calculated as follows:

- (1) For a link that has yielded, the force carried is

$$V_l = 2 f_y \cdot A_{sl} \quad (8.14)$$

where V_l = shear force carried by the link
 f_y = yield strength of the steel = 250 N/mm²
 A_{sl} = cross sectional area of the link

- (2) For a link that has not yielded

$$V_l = 2 \cdot E_s \cdot \mu \cdot A_{sl} \quad (8.15)$$

Table 8.3 Shear Strength of the Flange

Beam No	Flange		V_{exp} kN	Integrated		E W Eq (8.2)		E W Eq (8.3)		E W Eq (8.4)		E W
	Width mm	Thickness mm		V_c kN	$\frac{V_c}{V_{exp}}$	V_c kN	$\frac{V_c}{V_{exp}}$	V_c kN	$\frac{V_c}{V_{exp}}$	V_c kN	$\frac{V_c}{V_{exp}}$	V_c kN
TBX-I	350	50	28.9	19.7	0.72	23.6	0.82	22.7	0.79	22.3	0.77	22.96
TBX-II	700	50	35.4	28.9	0.82	29.3	0.83	34.1	0.96	29.26	0.83	29.57
TBX-III	1050	50	38.2	33.3	0.87	34.4	0.90	27.8	0.73	34.85	0.92	34.9
TBX-IV	350	70	31.2	28.8	0.97	35.6	1.14	34.2	1.10	35.6	1.14	35.87
TBX-V	700	70	44.2	44.1	1.0	42.1	0.95	47.3	1.07	42.53	0.96	42.42
TBX-VI	1050	70	49.7	50.4	1.01	48.7	0.98	45.4	0.91	48.31	0.97	47.9
TBX-VII	350	90	38.1	36.2	0.95	43.8	1.15	41.3	1.08	43.85	1.15	43.95
TBX-VIII	700	90	50.2	50.2	1.0	55.6	1.10	62.4	1.24	56.	1.12	54.97
TBX-IX	1050	90	62.7	62.1	0.99	67.2	1.08	65.3	1.04	66.6	1.06	65.13

Table 8.3 (Continued)

Eq(8.5)	E W Eq (8.6)		E W Eq (8.7)		E W Eq (8.8)		E W Eq (8.9)		E W Eq (8.11)		E W Eq (8.12)	
$\frac{V_c}{V_{exp}}$	V_c kN	$\frac{V_c}{V_{exp}}$	V_c kN	$\frac{V_c}{V_{exp}}$	V_c kN	$\frac{V_c}{V_{exp}}$	V_c kN	$\frac{V_c}{V_{exp}}$	V_c kN	$\frac{V_c}{V_{exp}}$	V_c kN	$\frac{V_c}{V_{exp}}$
0.79	24.12	0.83	20.43	0.71	22.67	0.78	23.25	0.8	14.8	0.51	22.02	0.76
0.84	25.78	0.73	30.26	0.85	28.64	0.81	28.87	0.82	20.69	0.58	29.26	0.83
0.92	25.99	0.68	38.82	1.02	33.92	0.89	33.06	0.87	27.39	0.72	34.47	0.90
1.15	37.14	1.19	30.03	0.96	37.25	1.19	37.14	1.19	23.66	0.76	34.8	1.12
0.96	41.79	0.95	41.16	0.93	45.47	1.03	44.52	1.01	33.18	0.75	44.3	1.0
0.96	40.56	0.82	50.86	1.02	49.64	1.0	50.55	1.02	50.45	1.02	47.49	0.96
1.15	43.85	1.15	35.45	0.93	41.36	1.1	40.71	1.07	30.81	0.81	43.1	1.13
1.10	59.91	1.19	50.9	1.01	55.36	1.1	54.19	1.08	50.29	1.0	57.7	1.15
1.04	61.4	0.98	66.47	1.06	65.67	1.05	67.8	1.08	84.58	1.35	66.73	1.06

where E_s = Young's modulus of steel = $200 \times 10^3 \text{ N} \cdot \text{mm}^2$
 μ = recorded strain in the link

There were five links in this area, but the strains were only measured on the two nearest to the preformed crack. In some beams these two links had both yielded before the ultimate load was reached. In this case an additional value of 50% of the force carried by the second link was added to the force computed for the other two links. This approach was based on the observations of the measured strains in the links where it was noticed that the second link started to record strains after the first one had yielded.

For the range of flange widths and thicknesses considered in Table 8.3, the computed shear forces show satisfactory agreement with the experimental results except those calculated using the 'effective widths' from equations 8.3, 8.6, and 8.11. Using equation 8.3, the predicted shear strength of the flange was 0.73% of the experimental value in beam TBX III and 1.24% in TBX VIII. With equation 8.6, the correlation between the calculated and experimental values showed low values as in TBX II and TBX III (0.78% and 0.68%). Using equation 8.11, the comparison showed lower and higher values as TBX I (0.51%) and TBX IX (1.35%). Despite the exclusion of the effect of the amount of main steel and the flange thickness in calculating the 'effective width' by equation 8.7, the predicted shear forces are in good agreement with the experimental values except in beam TBX I (0.71%) which has short and thin flange.

It can be concluded now that equation (8.13) predicts the shear strength of the flange reasonably well. Among the predicted equations for the 'effective widths', equations (8.2), (8.4) and (8.7) are the simplest and reasonable equations for evaluating the 'effective width' of the compression zone.

8.3.3 Shear Strength of the Flange with Respect to Results of Full Beam Tests

Equation (8.13) has been applied to test results of other investigators (5), (6), (9), (10), (11), (13), (20) and (94). The 'effective widths' have been calculated using equations (8.2), (8.4) and (8.7). These tests had different B/b_o , t/h and area of longitudinal steel. The results are presented in Tables 8.4-8.8. It should be noticed that these tests represent the ultimate shear strength of the beam and hence include dowel and aggregate interlock forces, while the computed values obtained from equation (8.13) represent the shear strength of the compression zone alone.

The tests carried out by Placas (13) were on T-beams with shear reinforcement, so the value V_1 in Table 8.5 is calculated as the shear force resisted by the stirrups and this has been subtracted from the ultimate shear force to obtain V_u .

From Table 8.4, B/b_o was 4.33, t/h was 0.217 and ρ varied between 1.48% and 4.4%. The shear strength of the flange predicted by equation (8.13) and using equation (8.2) for the 'effective width' ranges between 52% and 71% of the

Table 8.4 Al Alusi Tests (6)

Beam No	B mm	t mm	$\frac{B}{b_o}$	$\frac{t}{h}$	$\rho \%$	rf_{yw}^2 N/mm ²	f'_c N/mm ²	$2b_e$ (1) mm	$\frac{2b_e}{b_o}$	V_c (1) kN	V_{ut} kN	$\frac{V_c(1)}{V_{ut}}$	$2b_e$ (2) mm	$\frac{2b_e}{b_o}$	V_c (2) kN	$\frac{V_c(2)}{V_{ut}}$	$2b_e$ (3)	$\frac{2b_e}{b_o}$	V_c (3)	$\frac{V_c(3)}{V_{ut}}$
11	330	32	4.33	.217	2.63	-	28.6	186	2.43	8.44	17.4	0.49	183	2.4	8.37	0.48	179	2.34	8.19	0.47
10	330	32	4.33	.217	2.7	-	28.6	187	2.45	8.45	14.75	0.58	183	2.4	8.37	0.57	179	2.34	8.19	0.56
4	330	32	4.33	.217	1.5	-	26.53	171	2.24	7.2	13.88	0.52	183	2.4	7.77	0.56	179	2.34	7.6	0.55
5	330	32	4.33	.217	1.48	-	27.32	171	2.24	7.39	14.2	0.52	183	2.4	7.97	0.56	179	2.34	7.8	0.55
1	330	32	4.33	.217	1.48	-	27.00	171	2.24	7.35	12.6	0.58	183	2.4	7.92	0.63	179	2.34	7.74	0.61
22	330	32	4.33	.217	1.49	-	28.6	171	2.24	7.76	13.02	0.60	183	2.4	8.37	0.64	179	2.34	8.19	0.63
7	330	32	4.33	.217	2.71	-	25.42	187	2.45	7.55	13.55	0.56	183	2.4	7.44	0.55	179	2.34	7.28	0.54
8	330	32	4.33	.217	2.71	-	26.25	187	2.45	7.8	13.4	0.58	183	2.4	7.67	0.57	179	2.34	7.52	0.56
19	330	32	4.33	.217	4.21	-	30.6	206	2.7	10.	14.02	0.71	183	2.4	8.96	0.64	179	2.34	8.76	0.63
9	330	32	4.33	.217	2.71	-	31.7	187	2.45	9.41	14.15	0.66	183	2.4	9.28	0.66	179	2.34	9.08	0.64
20	330	32	4.33	.217	4.21	-	27.25	206	2.7	9.	15.02	0.60	183	2.4	7.98	0.53	179	2.34	7.8	0.52
14	330	32	4.33	.217	2.7	-	27.0	187	2.45	8.02	12.68	0.63	183	2.4	7.92	0.62	179	2.34	7.73	0.61
23	330	32	4.33	.217	4.4	-	28.18	209	2.74	9.35	14.17	0.66	183	2.4	8.25	0.58	179	2.34	8.07	0.57

V_{ut} = Ultimate strength from tests

$2b_{e(1)}$ & $V_{c(1)}$, E W Calculated by Equation (8.2)

$2b_{e(2)}$ & $V_{c(2)}$, E W Calculated by Equation (8.4)

$2b_{e(3)}$ & $V_{c(3)}$, E W Calculated by Equation (8.7)

total shear forces carried by the beams. For beam No 11, a lower value was obtained about (49%). This beam had a lower a/d ratio (a/d was 3.32) than the others. When using equation (8.4) to calculate the 'effective width' the shear strength of the flange ranged between 53% and 66% of the ultimate shear strength, except for beam 11 (48%). The effect of neglecting the amount of main steel can be noticed in beams with high percentages of reinforcement, for example in beam 19 with $\rho = 4.21\%$, the shear strength of the flange decreased from 71% to 64%. The same occurred in beam 20 where the shear strength decreased from 60% to 53% and in beam 23 the decrease was from 66% to 58%. Using equation (8.7), the shear strength of the flange was between 52% and 64% and nearly the same decrease as occurred in beams with high percentages of longitudinal reinforcement.

For tests in Table 8.5, B/b_o was 4 (except 2 beams with B/b_o of 2 and 7), t/h was 0.25 (one beam t/h was 0.5) and ρ was between 1.25% and 4.16%. By using equation (8.2), the shear strength of the flange ranges between 52% and 67% of the experimental ultimate shear strength except for beams T 1 (48%) and T 35 (77%). When using equation (8.4) the shear strength of the flange was between 50% and 70% except T 2 (73%) and T 35 (75%). Again with beams of higher percentage of main reinforcement, the equation yields lower strength for the flange as in beams T 6, T 18 and T 34 ($\rho = 4.16\%$). The decrease in beam T 6 was from 62% to 56%, in beam T 18 was from 60% to 54% and in beam T 34 was from 63% to 52%. Using equation (8.7), the shear strength of

Table 8.5 Placas Tests (13)

Beam No	B mm	t mm	$\frac{B}{b_o}$	$\frac{t}{h}$	ρ %	rf_{yw_2} N/mm ²	f'_c N/mm ²	$2b_e$ (1) mm	$\frac{2b_e}{b_o}$	V_1 kN	V_{ut} kN	V_u kN	V_c (1) kN	$\frac{V_{c(1)}}{V_u}$	$V_{c(2)}$ kN	$\frac{V_{c(2)}}{V_u}$	$V_{c(3)}$ kN	$\frac{V_{c(3)}}{V_u}$
T1	610	76	4	0.25	1.25	.58	27.9	336	2.2	35.67	109.9	74.2	35.7	0.48	39.44	0.53	36.22	0.49
T2	610	76	4	0.25	1.46	-	28.04	341	2.24	-	54.74	54.7	36.4	0.67	39.75	0.73	36.4	0.67
T3	610	76	4	0.25	1.46	.58	27.5	341	2.24	35.67	104.58	68.91	35.7	0.52	38.98	0.56	35.7	0.52
T4	610	76	4	0.25	1.95	.58	32.45	354	2.32	35.67	109.47	73.8	43.77	0.59	46.0	0.62	42.12	0.57
T5	610	76	4	0.25	1.46	1.15	33.7	341	2.24	71.34	139.73	68.39	43.77	0.64	47.79	0.70	43.75	0.64
T6	610	76	4	0.25	4.16	2.25	25.77	412	2.70	139.17	204.7	65.43	40.44	0.62	36.53	0.56	33.45	0.51
T7	610	76	4	0.25	3.0	.58	27.35	382	2.51	35.67	109.47	73.8	39.81	0.54	38.77	0.53	35.5	0.48
T8	610	76	4	0.25	4.16	.58	31.2	412	2.70	35.67	124.6	88.93	48.99	0.55	44.22	0.50	40.5	0.45
T10	610	76	4	0.25	1.46	.38	28.18	341	2.24	23.8	86.78	62.98	36.61	0.58	39.94	0.63	36.58	0.58
T18	610	76	4	0.25	4.16	-	28.39	412	2.70	-	74.76	74.76	44.56	0.60	40.24	0.54	36.85	0.49
T34	305	76	2	0.25	4.16	.58	33.9	305	2.0	35.67	112.14	76.47	47.79	0.63	40.22	0.52	31.82	0.42
T35	1067	76	7	0.25	4.16	.58	33.62	473	3.1	35.67	114.8	79.14	60.59	0.77	59.20	0.75	61.74	0.78
T38	610	152	4	0.5	4.16	2.25	30.18	466	3.06	139.27	239.41	100.14	53.95	0.54	54.45	0.54	39.18	0.39

V_c (1), E.W. calculated by Equation (8.2)

V_c (2), E.W. calculated by Equation (8.4)

V_c (3), E. W. calculated by Equation (8.7)

the flange varied between 51% and 67%. But there are beams with higher and lower values than this. Neglecting the amount of main steel and thickness of the flange reduces the shear strength of the flange from 54% to 48% in beam T 7, from 55% to 45% in beam T 8 and from 60% to 49% in beam T 18. In beam T 34 with short flange width ($B/b_o = 2$), the decrease was from 63% to 42% and in beam T 38 with thick flange ($t/h = 0.5$) the decrease was from 54% to 39%. The greater decrease in the latter two cases show that in beams with thicker flanges the effect of flange thickness should be included when calculating the 'effective width'.

In Table 8.6, the tests by Erikitoala had B/b_o from 2 to 10, t/h of 0.3 and ρ of 2.54%, 6.52%, and 10.2%. The tests by Adepegba had B/b_o of 2.5, t/h of .33 and ρ of 2.54%. The shear strength of the flange was between 36% and 49% of the ultimate shear. The lower values obtained in this group of tests were probably due to the high percentage of longitudinal reinforcement used in these beams, which would increase the dowel effect. This was also noticed in the tests of Adepegba shown in the same table, where two rows of steel reinforcement were used. Two beams of these tests gave rather lower strength of the flange, beam 152 T-16 (28%) and beam T 6 (23%). The 'effective width' of these two beams was higher than the flange width and this may be due to the high percentage of the main steel with respect to a small flange ($B/b_o = 2$). The effective width was, therefore, taken equal to the flange width in these two beams, and this probably was the reason for the low strength of the flange. For the beam 152 T-10 with lower

Table 8.6 Erikitola Tests (20)

Beam No	B mm	t mm	$\frac{B}{b_o}$	$\frac{t}{h}$	ρ %	rf_{yw} N/mm ²	f'_c N/mm ²	$2b_e$ mm	$\frac{2b_e}{b_o}$	V_c (1) kN	V_{ut} kN	$\frac{V_c(1)}{V_{u\ test}}$	V_c (2)	$\frac{V_c(2)}{V_{ut}}$	V_c (3)	$\frac{V_c(3)}{V_{ut}}$
152T-10	152	38	2	.3	2.54	-	37.12	152	2.0	10.72	16.7	0.64	10.72	0.64	8.7	0.52
152T-16	152	38	2	.3	6.52	-	27.68	152	2.0	8.0	28.8	0.28	8.0	0.28	6.49	0.23
228T	228	38	3	.3	6.52	-	27.68	228	3.0	12.1	32.2	0.38	8.97	0.28	7.73	0.24
380T	380	38	5	.3	6.52	-	27.68	252	3.32	13.25	36.7	0.36	10.55	0.29	10.2	0.28
532T	532	38	7	.3	6.52	-	27.68	272	3.58	14.3	35.5	0.40	12.15	0.34	12.68	0.36
9T30	760	38	10	.3	6.52	-	28.16	303	3.98	16.2	39.9	0.41	14.76	0.37	16.68	0.42
T6	152	38	2	.3	10.2	-	27.6	152	2.0	7.97	35.0	0.23	7.97	0.23	6.49	0.19
T9	228	38	3	.3	10.2	-	27.6	228	3.0	11.96	32.3	0.37	8.97	0.28	7.73	0.24
T15	380	38	5	.3	10.2	-	27.6	300	3.94	15.78	32.3	0.49	10.55	0.33	10.2	0.32
T21	532	38	7	.3	10.2	-	27.6	321	4.22	16.88	36.1	0.47	12.15	0.34	12.68	0.35
6T30	760	38	10	.3	10.2	-	31.52	351	4.6	21.02	48.9	0.43	16.47	0.37	18.67	0.38
<u>Adepegba tests (94)</u>																
TD4	381	76	2.5	.33	2.54	-	33.07	357	2.34	44.94	91.67	0.49	41.12	0.45	33.99	0.37
TD5	381	76	2.5	.33	2.54	-	30.3	357	2.34	41.23	95.65	0.43	37.67	0.39	31.15	0.33
TD6	381	76	2.5	.33	2.54	-	30.8	357	2.34	41.98	91.63	0.46	38.29	0.42	31.66	0.35
TD7	381	76	2.5	.33	2.54	-	34.73	357	2.34	47.23	91.67	0.52	48.18	0.47	35.7	0.39

steel ratio (2.54%), the strength of the flange was 64% which was higher than that for any other beam of this group. When using equation (8.4), the shear strength of the flange ranged between 23% and 37% in Erikitoala tests. It can be noticed that the decrease in the strength of the flange is greater than that for beams in Tables 8.4 and 8.5. In Adepegba tests the range was between 39% and 47%. By using equation (8.7) the strength of the flange was between 19% and 38%. In beam 152 T-10, the percentage decreased from 64% to 52%. This shows the effect of flange thickness (t/h was 0.3). Also with Adepegba tests ($t/h = 0.33$) the decrease in the percentages was greater with equation (8.7).

In Table 8.7, the tests given by Ferguson had $B/b_o = 4.25$, $t/h = .162$ and $\rho = 4.79\%$. Tests of Quereshi had $B/b_o = 3$, $t/h = .22$ and $\rho = 3.49\%$. The tests by Guralnick had $B/b_o = 3.3$, $t/h = 0.26$ and ρ of 2.37% & 4.19%. Using equation (8.2), the strength of the flanges given by the tests of Ferguson were between 53% and 57% except beam A 5 (70%). Those by Quereshi were between 50% and 57% except beam S1-3 (38%), this beam had a/d ratio of 3.0. Those of Guralnick were between 52% and 78% except beam 1A-IM (41%, $a/d = 2.8$). The range of the flange strength of these beams coincides with that of Tables 8.4 and 8.5. When using equation (8.4), the strength of the flange of Ferguson tests ranged between 45% and 49% except beam A 5 (60%). Those of Quereshi were between 41% and 48% except beam S1-3 (32%). The greater decrease in these two groups of tests when using equation (8.4) is due to the higher percentage of longitudinal reinforcement used (4.29% and 3.49%). The tests by

Table 8.7 Ferguson Tests (5)

Beam No	B mm	t mm	$\frac{B}{b_o}$	$\frac{t}{h}$	$\rho\%$	rf_{yw} N/mm ²	f'_c N/mm ²	$2b_e$ (1) mm	$\frac{2b_e}{b_o}$	V_c (1) kN	V_{ut} kN	$\frac{V_c(1)}{V_{ut}}$	V_c (2) kN	$\frac{V_c(2)}{V_{ut}}$	V_c (3) kN	$\frac{V_c(3)}{V_{ut}}$
A1	432	38	4.25	.162	4.79	-	29.7	276	2.72	15.63	29.32	0.53	13.55	0.46	13.29	0.45
A2	432	38	4.25	.162	4.79	-	27.28	276	2.72	14.36	27.2	0.53	12.25	0.45	12.21	0.45
A3	432	38	4.25	.162	4.79	-	35.07	276	2.72	18.46	33.9	0.54	15.76	0.47	15.69	0.46
A4	432	38	4.25	.162	4.79	-	34.93	276	2.72	18.38	31.9	0.58	15.7	0.49	15.63	0.49
A5	432	38	4.25	.162	4.79	-	45.33	276	2.72	23.86	34.17	0.70	20.37	0.6	20.28	0.59
A6	432	38	4.25	.162	4.79	-	38.65	276	2.72	20.34	35.9	0.57	17.37	0.48	17.3	0.48
Quereshi Tests (10)																
S1-3	229	25.4	3	.22	3.49	-	30.87	184	2.41	7.21	19.24	0.38	6.06	0.32	5.77	0.3
S1-4	229	25.4	3	.22	3.49	-	30.87	184	2.41	7.21	13.8	0.52	6.06	0.44	5.77	0.42
S1-6	229	25.4	3	.22	3.49	-	30.87	184	2.41	7.21	14.46	0.50	6.06	0.42	5.77	0.4
SM-8	229	25.4	3	.22	3.49	-	27.84	184	2.41	6.5	11.79	0.55	5.46	0.46	5.2	0.44
S3-4	229	25.4	3	.22	3.49	-	31.97	184	2.41	7.47	15.56	0.48	6.27	0.41	5.98	0.38
S3-6	229	25.4	3	.22	3.49	-	30.04	184	2.41	7.02	12.37	0.57	5.89	0.48	5.62	0.45
S3-8	229	25.4	3	.22	3.49	-	31.47	184	2.41	7.36	13.91	0.53	6.17	0.44	5.88	0.42
Guralnik Tests (9)																
IA-IM	584	102	3.3	.26	2.37	-	26.86	411	2.31	56.07	139.73	0.41	58.3	0.42	49.05	0.35
IC-IM	584	102	3.3	.26	4.19	-	33.5	467	2.63	79.47	155.31	0.52	72.72	0.47	61.17	0.39
IIC-IM	584	102	3.3	.26	2.37	-	26.86	411	2.31	56.07	84.99	0.66	58.3	0.69	49.05	0.58
IIC-IM	584	102	3.3	.26	4.19	-	33.5	467	2.63	79.47	101.02	0.78	72.72	0.72	61.17	0.61

$V_{c(1)}$: E W Calculated by Equation (8.2)

$V_{c(2)}$: E W Calculated by Equation (8.4)

$V_{c(3)}$: E W Calculated by Equation (8.7)

Guralnick were between 42% and 72%. When using equation (8.7), there is a little difference in the strength of the flange of Ferguson and Quereshi's tests than those predicted using equation (8.4). This is due to the thin flanges used in these tests, while the difference is noticeable in Guralnick tests, where thicker flange was used ($t/h = 0.26$).

In Table 8.8, the tests had B/b_o between 2.57 and 3.54, t/h between .203 and .223 and ρ between 2.36% and 5.5%. By using equation (8.2), the shear strength of the flange varied between 48% and 72%. This range agrees with the percentages from Tables 8.4, 8.5 and 8.7. Using equation (8.4), the percentages ranged between 38% and 62%. The beams with higher percentages of main steel had higher decrease than the others. By using equation (8.7), the percentages were between 35% and 60%.

The discussions above show that equation (8.2) evaluates the 'effective width' of the compression zone in T-beams reasonably well. The effects of flange width, flange thickness and amount of main steel are all taken into consideration in this equation. When excluding the percentage of main reinforcement in equation (8.4), the 'effective width' decreases with higher percentages of steel and consequently, a decrease in the flange strength occurs. Thus equation (8.4) can be used within a limited percentage of main steel. From the tests shown in this discussion this limit can be suggested as 3%, ie equation (8.4) can be used for ρ not greater than 3%. When neglecting the amount of main steel and flange thickness in equation (8.7), higher

Table 8.8 Ramakrishnan Tests (11)

Beam No	Flange		$\frac{B}{b_o}$	$\frac{t}{h}$	ρ %	f'_c N/mm ²	$2b_e$ mm	$\frac{2b_e}{b_o}$	V_{ut} kN	V_c (1) kN	$\frac{V_c(1)}{V_{ut}}$	V_c (2)	$\frac{V_c(2)}{V_{ut}}$	V_c (3)	$\frac{V_c(3)}{V_{ut}}$
	B mm	t mm									$V_c(1)$ V_{ut}		$V_c(2)$ V_{ut}		$V_c(3)$ V_{ut}
S5	256	32	3.35	.208	5.5	33.9	213	2.79	24.2	11.46	.48	9.13	0.38	8.45	0.35
S3	256	33	3.35	.218	5.5	35.39	213	2.8	24.58	12.56	.51	10.03	0.41	9.1	0.37
S1	254	31	3.33	.203	5.5	36.38	211	2.78	24.92	11.87	.48	9.4	0.38	8.78	0.35
S2	256	33	3.35	.213	5.5	53.64	213	2.8	30.79	18.57	.60	14.42	0.47	13.79	0.45
1	391	40	3.62	.223	3.8	34.84	275	2.55	26.38	19.0	.72	16.38	0.62	15.97	0.61
2	391	40	3.62	.223	2.36	33.35	249	2.3	26.64	16.48	.62	15.68	0.59	15.28	0.57
3	394	40	3.54	.223	3.8	34.33	282	2.54	30.15	19.22	.64	16.14	0.54	16.03	0.53
4	394	40	3.54	.223	3.8	35.28	282	2.54	27.47	19.75	.72	16.59	0.6	16.47	0.6
S6	256	33	3.35	.218	5.5	29.99	213	2.8	16.97	10.64	.63	8.49	0.5	7.71	0.45
S7	256	33	3.35	.218	5.5	29.99	213	2.8	15.93	10.64	.67	8.49	0.53	7.71	0.48
S8	256	33	3.32	.213	5.5	30.87	215	2.8	17.7	10.69	.6	8.65	0.49	7.93	0.45
S9	256	32	3.39	.208	5.5	30.87	211	2.8	16.55	10.34	.62	8.39	0.51	7.69	0.46
12	256	32	3.35	.208	5.5	30.87	213	2.8	20.47	10.36	.51	8.39	0.41	7.69	0.38
M1A	251	32	2.59	.208	5.5	31.25	240	2.48	20.22	11.91	.59	9.4	0.47	8.74	0.43
M1B	251	32	2.59	.208	4.34	31.25	240	2.48	24.75	11.91	.48	9.4	0.38	8.74	0.33
M2B	251	32	2.59	.208	4.34	31.25	240	2.48	21.35	11.08	.52	9.4	0.44	8.74	0.41
M3A	251	32	2.57	.208	4.34	31.58	240	2.48	19.25	12.03	.63	9.5	0.49	8.85	0.46
M3B	251	32	2.57	.208	4.34	31.58	240	2.48	22.3	12.03	.54	9.5	0.43	8.83	0.40

decrease in the 'effective width' and shear strength of the flange was obtained in particular with beams of high percentage of main steel and thicker flanges.

Excluding the beams of Table 8.6 for the reasons discussed above, it can be estimated that the shear resistance of the flange represents between 50% and 70% of the total ultimate shear strength of T-beams. Bahia (83) predicted from his tests on fibre reinforced concrete T-beams that the contribution of the compression zone to shear resistance was between 55% and 60% of the total shear strength. It must be noted however, that Bahia's percentages were based on the assumptions that the three components contributing to the shear resistance are additive at the ultimate stage, and that the contributions of the dowel action and aggregate interlock are interdependent and constant throughout the full load range.

8.4 Conclusions

From the analytical results for shear resistance of the flange of T-beams presented in this chapter the following conclusions can be drawn:

- (1) The shear stress distribution at the middle surface of the flange takes the form shown in Fig 8.3 with higher values near the centre of the flange. The maximum shear stress values ranged between 1.75 N/mm^2 and 2.4 N/mm^2 .
- (2) With increasing flange width, the shear stresses are concentrated in a limited area of the flange adjacent to the web and reduced significantly towards the edges.

(3) The 'effective width' was found to be: for small flanges, $B/b_o = 2$, between 94% and 98% of the total flange width, for medium flanges, $B/b_o = 4$, between 52% and 63%, and for wide flanges, $B/b_o = 6$, between 43% and 49%.

(4) Different forms of equations were found to be satisfactory in evaluating the 'effective width' of the flange. These equations included the factors B/b_o , t/h and ρ . Equation of the form of (8.2) was used in this study. Equation (8.4) was also used which involved only flange dimensions cross section_λ as parameters. This equation was found to be used in beams with medium percentages of main reinforcement (ρ less than 3%). Equation (8.7)_λ^{which} expresses the 'effective width' in terms of B/b_o only was found to give rather conservative values for the 'effective width'.

(5) From the evaluated 'effective width' and the average value of the computed shear stresses ($f'_c/20$), an equation is predicted to estimate the shear strength of the flange. The calculated values from this equation compare satisfactorily with the corresponding ones obtained from the tests carried out.

(6) The comparison made between the shear force carried by the flange and the total shear force supported by the beam at ultimate load, showed that between 50% and 70% of the ultimate shear force was resisted by the compression zone in the flange.

CONCLUSIONS, LIMITATIONS AND
SUGGESTIONS FOR FUTURE WORK

9.1 Conclusions

The major purpose of this study was to investigate the contribution of the flange of a reinforced concrete T-beam in resisting shear forces at ultimate load. The study included theoretical analyses and experimental investigations. The theoretical study was carried out by using a 3-dimensional Finite Element Stress Analysis. The experimental work was conducted on T-beams provided with preformed cracks in the webs of the shear spans.

The major conclusions that can be drawn from this study are as follows:

I Theoretical Study:

(1) The behaviour and shear strength of reinforced concrete T-beams is well predicted by the non-linear finite element method used in this investigation. The computer program which was developed can be applied to predict the load-deflection curve, the failure load and the trend of the cracking pattern of reinforced concrete beams.

(2) Tensile cracking is the most important non-linear effect of reinforced concrete T-beams failing in shear. At failure the compressive concrete stresses did not exceed 40-50% of the 28 day cube crushing strength in any of the problems analysed. Therefore shear failures can be adequately predicted by the study of the crack propagation alone.

(3) The maximum tensile stress criterion and the multi-axial stress criterion in terms of octahedral normal and shear stresses predicted the behaviour of the beams satisfactorily. The former predicts the tensile cracking in the tension zones, while the latter predicts the cracking in the tension-compression zones.

(4) Normal, shear and principal stresses can be obtained in any part of the beam and at any load level. This made it possible to obtain the shear stress distributions across the flange width which were used in calculating the shear strength of the flange at ultimate load.

(5) Brick-type isoparametric elements with parabolic displacement functions proved to be efficient in non-linear applications. The cracked zones were spread smoothly in the beam. The numerical integration used with these elements made it possible to handle inelastic and elastic areas within the same element.

II Experimental Work:

(1) A workable structural concrete mix was achieved using PFA as a replacement for cement and sand. At 28 days, the concrete mix gave a cube strength of about 35 N/mm^2 and flexural tensile strength of about 4.2 N/mm^2 .

(2) The tests of beams with different locations of preformed cracks showed that the stiffness of the beams decreased as the location moved towards the load point.

(3) The location of the preformed crack used in the beams with different flange widths and thicknesses produced a shearing mode of failure in the flange.

(4) The distribution of the concrete strains across the top surface of the flange was uniform and compressive in the early stages of loading. These strains became non-uniform and changed to tensile when approaching the ultimate load particularly near the head of the preformed crack.

III 'Effective Width' and Shear Resistance of the Flange:

(1) The equations developed for the 'effective width' and shear resistance of the flange are based upon data obtained from theoretical analyses of beams with flange widths ranging between 350 mm and 1050 mm and flange thicknesses ranging from 50 mm to 90 mm.

(2) The shear stress distributions in the flanges are concentrated in the area above the web and are reduced significantly towards the outer edges.

(3) The 'effective width' and shear strength of the flange increase with the increase of flange width, flange thickness and area of main longitudinal reinforcement. Different equations were predicted to evaluate the 'effective width'. The equations included the parameters B/b_o , t/h and ρ . The best equation to evaluate the 'effective width' satisfactorily was found to be in the form:

$$2 b_e = b_o \left[1.09 + .135 (B/b_o) + 1.429 (t/h) + .172 \rho \right]$$

Simpler equations were predicted including only B/b_o or t/h , but they gave conservative values for the 'effective width'.

(4) The shear strength of the flange at ultimate load is expressed in an equation including the evaluated 'effective width' and an average value for the shear stress ($f'_c/20$) as follows:

$$V_c = 2 b_e \cdot t \cdot f'_c/20$$

The values obtained from this equation for the shear strength of the flange agree closely with the experimental values.

(5) The contribution of the flange in resisting shear forces at ultimate load calculated by the above equations is between 50% and 70% of the total shear force that the beam can support.

9.2 Limitations and Suggestions for Future Work

In the following, some phenomena noticed from the analysis are discussed and suggestions are made for further study:

(1) Due to the lack of experimental information and because of the fact that the compressive stresses were below 50% of the ultimate cube strength of concrete, the uniaxial stress-strain relationship was adopted in the Finite Element Analysis. In general, stress-strain relationships for concrete under different multiaxial stress states are needed. This depends on the available experimental information

and in particular the deformation characteristics of concrete under combined stresses. Work in this field will be fruitful.

(2) As discussed in Chapter 7, there were differences in ultimate strength between the predicted and the actual loads in some beams. An improvement in the failure laws is required to predict the failure and the crack patterns in the tension-compression zone. Moreover, experimental work must be directed to obtain a universal failure criterion for concrete under combined stresses.

(3) The variable stiffness technique used in conjunction with the incremental method proved to be an efficient technique in non-linear analysis despite it being expensive regarding computation time. More study is required to bring down the cost of computation. Other techniques could be incorporated in the program such as the residual forces method or modified Newton-Raphson techniques.

(4) The use of the 2 point integration rule with the parabolic brick-type element was found to be the cheapest in computation time and yielded reasonable load-deflection curves and cracking patterns. It was noticed however, from the shear stress distribution at different load increments, that some points were not consistent. This could be due to the reduced integration rules. More work is desirable on this point to verify the use of the reduced integration rules in non-linear analysis and the consistency of stress distribution within the elements.

- (5) Material properties laws can be extended to include other aspects of the behaviour of concrete such as:
- (a) Non-linear constitutive law in multiaxial compression stress states. An investigation could also be tried to predict the compressive failure of concrete in relation to internal microcracking.
 - (b) Aggregate interlock which is of fundamental importance in shear failures, needs thorough investigation. It might be worth trying to develop a relationship expressing aggregate interlock in terms of the crack width.
 - (c) Dowel action has an important rôle in shear failures, thus it should be involved in the analysis and a constitutive law has to be developed to tackle this phenomena.
 - (d) Non-linear bond-slip relationships defining the behaviour between concrete and steel has to be introduced into the analysis. This might need reformulation for the bar element used in this study. This could also be investigated through the use of linkage elements.
 - (e) Other phenomena such as repeated loading and temperature effects can also be incorporated in the finite element model.
- (6) The equations predicted for the 'effective width' and shear resistance of flange are based on a limited number of beams analysed by the Finite Element model. However,

these equations showed consistency when applied to other experimental data. It could be worth analysing different cases of beams where the shear span, flange geometry and main reinforcement are varied. Modifications in the constants of the equations could then be made.

REFERENCES

- (1) British Standards Institute, "The Structural use of Concrete" CP.110, Part 1, 1972
- (2) ACI-ASCE Committee 426 Report "The Shear Strength of Reinforced Concrete Members" Journal of the Structural Division, ASCE, V.99, No ST 6, June 1973, pp 1091-1187
- (3) Shear Study Group Report "The Shear Strength of Reinforced Concrete Beams" Institution of Structural Engineers, London, January 1969, 170 pp
- (4) Braune, G. M. and Myers, C. C. "Tests on Ten Reinforced Concrete T-Beams" V10, Concrete 1917, pp 163-165
- (5) Ferguson, P.M. & Thomson, F.N. "Diagonal Tension in T-Beams without Stirrups" ACI Journal, Proceedings V.49, March 1953, pp 665-676
- (6) Al-Alusi, A.F. "Diagonal Tension Strength of Reinforced Concrete T-beams with Varying Shear Span" ACI Journal, Proceedings, V.53, No.2, May 1957, pp 1067-1077
- (7) Neville, A.M. and Lord, E. "Some Factors in the Shear Strength of Reinforced Concrete Beams", The Structural Engineer, V.38, 1960, pp 213-223
- (8) Taub, J. and Neville, A.M. "Resistance to Shear of Reinforced Concrete Beams" Parts 1-5 ACI Journal, Proceedings, V.57, PTI, August, September, October, November, December, 1960
- (9) Guralnick, S. "High-Strength Deformed Steel Bars for Concrete Reinforcement" ACI Journal, Proceedings, V.57 No.3, September, 1960, pp 241-282
- (10) Swamy, R.N. and Quereshi, S.A., "Shear Behaviour of Reinforced Concrete T-beams with Web Reinforcement" Proc. Inst. Civ. Engrs. V.57, Pt. 2, March 1974, pp 35-49
- (11) Ramakrishnan, V. "Factors Affecting the Ultimate Shear Strength of Reinforced Concrete T-Beams" Ph.D. Thesis, London University, 1960
- (12) Leonhardt, T. "Reducing the Shear Reinforcement in Reinforced Concrete Beams and Slabs" Magazine of Concrete Research, V.17, No.53, December, 1965, pp 187-198
- (13) Placas, A. and P. Regan "Shear Failure of Reinforced Concrete Beams" ACI Journal, Proceedings, V.68, Pt.2, October, 1971, pp 763-773

- (14) Placas, A. "Shear Failure of Reinforced Concrete Beams" Ph. D. Thesis, University of London, 1969
- (15) Reeves, J. S. "The Strength of Concrete under Combined Direct and Shear Stresses" C & CA, Technical Report, TRA/365, November, 1962, pp 15
- (16) Khan, M. H. "Shear Strength of Concrete Beams Reinforced with Bent-up Bars" M. Phil. Thesis, University of London, 1969
- (17) Tang, M. "Shear Design of Large Concrete Box Girders" ACI Special Publications, sp 42-14, 1974, pp 305-313
- (18) Swamy, R.N., Andriopoulos, A. and Adepegba, D. "Arch Action and Bond in Concrete Shear Failure" Journal of the Structural Division, ASCE, V.96 No.ST6, June 1970, pp 1069-1091
- (19) Yunus, M. "Shear Strength of Reinforced Concrete T-Beams with Small Shear Spans" M. Eng. Thesis, University of Sheffield, 1971
- (20) Swamy, R. N., Bandyopadhyay, A.K., and Erikkitola, M.K. "Influence of Flange Width on the Shear Behaviour of Reinforced Concrete T-Beams" Proc. Inst. Civ. Engrs, V.55, Pt.2, March 1973, pp 167-190
- (21) Swamy, R.N. and Quereshi, S.A. "An Ultimate Shear Strength Theory for Reinforced Concrete T-Beams without Web Reinforcement" RILEM, Materials & Structures, V.7 No.39, May-June 1974, pp 181-188
- (22) Taylor, H.P.J. "Investigation of the Dowel Shear Forces Carried by the Tensile Steel in Reinforced Concrete Beams" C & C A Technical Report, TRA 431, November 1969 pp 24
- (23) Bresler, B. and Pister, K.S. "Strength of Concrete under Combined Stresses" ACI Journal, Proceedings V.55, Pt 1 September, 1958, pp 321-345
- (24) Newman, K. and Newman, J. B. "Failure Theories and Design Criteria for Plain Concrete" Int. Conf. on Structures, Solid Mechanics and Eng. Design in Civil Eng. Materials, Southampton University, April 1969, pp 963-995
- (25) Timoshenko, S. and Goodier, J. "Theory of Elasticity" McGraw-Hill Book Co. 1951
- (26) Zienkiewicz, O.C. "The Finite Element Method in Eng. Science" McGraw-Hill, London, 1971
- (27) Desai, C.S.R., Abel, J.F. "Introduction to the Finite Element Method" Van Nostrand Reinhold Co. 1972

- (28) Ergatoudis, I., Irons, B.M. and Zienkiewicz, O.C. "Curved Isoparametric, Quadrilateral Elements for Finite Element Analysis", Solids Structures Journal, V.4, 1968, pp 31-42
- (29) Ergatoudis, I. "Isoparametric Elements in Two and Three Dimensional Analysis" Ph.D. Thesis, University of Wales, 1968
- (30) Zienkiewicz, O.C., Owen, D.R., Phillips, D.V. and Nayak, C.G. "Finite Element Methods in the Analysis of Reactor Vessels" Nuclear Engineering and Design, V.20, No.2, 1972, pp 507-541
- (31) Argyris, J. H. "Three Dimensional Anisotropic and Inhomogeneous Elastic Media" Matrix Analysis of Small and Large Displacements, Proc. 11th International Congress Appl. Mech., Munich, 1964
- (32) Argyris, J.H. "Matrix Analysis of 3-Dimensional Media" Small and Large Displacements, AIAA Journal, V.3, No.1 1965, pp 45-51
- (33) Zienkiewicz, O.C., Irons, B.M., Scott, F.C., Campell, J.S. "Three Dimensional Stress Analysis" High Speed Computing of Elastic Structures; Tome I, Proc's. of the Symposium of Int. Union of Theoretical and Applied Mech., Universite de Liege, 1971, pp 413-431
- (34) Nayak, C.H. "Plasticity and Large Deformation Problems by Finite Element Method" Ph.D. Thesis, University of Wales, December 1971
- (35) Suidan, M., Schobrich, C. "Finite Element Analysis of Reinforced Concrete" Journal of the Structural Division, ASCE, V.99, No.ST 10, October 1973, pp 2109-2122
- (36) Clough, R.W., "Comparison of three-dimensional Finite Elements" Procs. Symposium on Application of FEM in Civil Eng., Vanderbilt University, ASCE, November 1969, pp 1-26
- (37) Irons, B.M. "Engineering Applications of Numerical Integration in Stiffness Methods" AIAA Journal, V.4, Pt 2, November 1966, pp 2053-2037
- (38) Kopal, Z. "Numerical Analysis" 2nd Ed., Chapman & Hall, 1961
- (39) Irons, B.M. "Quadrature Rules for Brick Based Finite Elements" Int. J. Num. Meth. in Eng., V.3, 1971, pp 293-294
- (40) Phillips, D.V. "Non-Linear Analysis of Structural Concrete by Finite Element Methods" Ph.D. Thesis, University of Wales, Swansea, 1973

- (41) Zienkiewicz, O.C., Taylor, R.L., and Too, J.J. "Reduced Integration Technique in General Analysis of Plates and Shells" Int. J. Num. Meth. in Eng., V.3, 1971, pp 275-290
- (42) Phillips, D.V. and Zienkiewicz, O.C. "Finite Element Non-Linear Analysis of Concrete Structures" Proc. Inst. of Civ. Engrs., V.61, Part 2, March 1976, pp 59-88
- (43) Too, J.J. "Two-Dimension, Plate, Shell and Finite Prism Isoparametric Elements and their Application" Ph.D. Thesis, University of Wales, 1971
- (44) Desayi, P. and Krishnan, S. "Equation for the Stress-Strain Curve of Concrete" ACI Journal, V.61, Pt. 1, March 1964, pp 345-349
- (45) Saenz, L.P. "Discussion of Reference (44)" ACI Journal, V.61, Pt 2, September 1964, pp 1229-1235
- (46) Hughes, B.P., and Chapman, G.P. "The Complete Stress-Strain Curve for Concrete in Direct Tension" Rilem Bulletin No.30, March 1966, pp 95-98
- (47) Hughes, B.P., and Ashe, J.E. "Short-Term Loading and Deformation of Concrete in Uniaxial Tension and Pure Torsion" Magazine of Concrete Research, V.20, No.64, September 1968, pp 145-154
- (48) Kupfer, H., Hilsdorf, H.K. and Rusch, H. "Behaviour of Concrete under Biaxial Stresses" ACI Journal, Proceedings, V.66, No.8, August 1969, pp 656-666
- (49) Wu, H.C., "Dual Failure Criterion for Plain Concrete" Journal of Eng. Mech, Vol.100, EM6, December 1974, pp 1167-1181
- (50) Chen, C. T. and Chen, W. "Constitutive Equations and Punch-Indentation of Concrete" Journal of the Mechanical Division, ASCE, V.101, EM6, December 1975, pp 889-906
- (51) Bresler, B. and Pister, K.S. "Failure of Plain Concrete under Combined Stresses" Transactions ASCE, V.122, 1957, pp 1049-1068
- (52) Good^e, C.D. and Helmy, M.A. "The Strength of Concrete under Combined Shear and Direct Stress" Magazine of Concrete Research, V.19, No.59, June 1967, pp 105-112
- (53) Johnson, R.P. and Lowe, P.G. "Behaviour of Concrete under Biaxial and Triaxial Stress" Int. Conf. Structures, Solid Mech., and Eng. Design, Southampton, Part 2, 1969, pp 1039-1051
- (54) Mahmood, N. and Hannant, D.J. "The Strength of Concrete Subjected to Compression-Compression-Tension Stress Systems" Journal of Testing and Evaluation, V.3, No.2, March 1975, pp 107-112

- (55) Launay, P. and Gachon, H. "Strain and Ultimate Strength of Concrete under Triaxial Stress" 1st Int. Conf. Structural Mechanics in Reactor Technology, Berlin, September 1971, pp 23-40
- (56) Launay, P. and Gachon, H. "Strain and Ultimate Strength of Concrete under Triaxial Stress" Concrete for Nuclear Reactors, ACI Special Publications, SP-34, October 1970
- (57) Hobbs, D.W., Pomeroy, C.D. and Newman, J.B. "Design Stresses for Concrete Structures Subject to Multi-axial Stresses" The Structural Engineer, V.55, No.4, April 1977, pp 151-164
- (58) Cedolin, L., Crutzen, R.D. and Poli, S.D. "Stress-Strain Relationship and Ultimate Strength of Concrete under Triaxial Loading Conditions" Construzione in Cemento Armato, Politecnico di Milana, Italcementi, 1976, pp 123-137
- (59) Ngo, D. and Scordelis, A.C. "Finite Element Analysis of Reinforced Concrete Beams" ACI Journal, Proceedings, V.64, No.3, March 1967, pp 152-162
- (60) Scordelis, A.C., Ngo, D. and Franklin, H.A. "Finite Element Study of Reinforced Concrete Beams with Diagonal Tension Cracks" ACI Special Publications Sp 42-4, V.1, 1974, pp 79-102
- (61) Nilson, A.H. "Non-linear Analysis of Reinforced Concrete by the Finite Element Method" ACI Journal, Proceedings, V.65, No.9, September 1968, pp 757-766
- (62) Loov, R.E. "The Determination of Stresses and Deformations of Reinforced Concrete after Cracking" Int. Conf. Structures, Solid Mech, and Eng. Design, Southampton, Part 2, 1969, pp 1257-1261
- (63) Loov, R.E. "Finite Element Analysis of Concrete Members considering the Effect of Cracking and the Inclusion of Reinforcement" Ph.D. Thesis, University of Cambridge, September 1972
- (64) Cervenka, V. "Inelastic Finite Element Analysis of Reinforced Concrete Panels under Inplane Loads" Ph.D. Thesis, University of Colorado, 1970
- (65) Cervenka, V. and Gerstle, K.H. "Inelastic Analysis of Reinforced Concrete Panels" Pub. of Int. Ass. for Bridge and Struct. Eng. V.31, II, 1971, pp 31-45
- (66) Cedolin, L. and Poli, S.D. "Finite Element Non-linear Plane Stress Analysis of Reinforced Concrete" Costruzioni in Cemento Armato, Politecnico Di Milano, Italcementi, 1976, pp 3-33

- (67) Cope, R.J. and Rao, P.V. "Non-linear Finite Element Analysis of Concrete Slab Structures" Proc. Inst. Civ. Eng., V.63, Part 2, March 1977, pp 159-179
- (68) Buyukozturk, O. "Non-linear Analysis of Reinforced Concrete Structures" Computers and Structures, V.7, 1977, pp 149-156
- (69) Robins, P.J. and Kong, F.K. "Modified Finite Element Methods Applied to Reinforced Concrete Deep Beams" Civil Eng. and Public Works Review, V. 68 , November 1973, pp 963-966
- (70) Mirza, M.S. and Mufti, A.A. "Non-linear Finite Element Analysis of Reinforced Concrete Structures" Conf. on F.E.M. in Eng., The University of New South Wales, 1974
- (71) Taylor, H.J. "Investigation of the Forces Carried Across Cracks in Reinforced Concrete Beams in Shear by Interlock of Aggregate" C & C A Technical Report, TRA 42. 447 November 1970, pp 22
- (72) Swamy, R.N. and Andriopoulos, A.D. "Contribution of Aggregate Interlock and Dowel Forces to Shear Resistance of Reinforced Concrete Beams with Web Reinforcement" ACI, Special Publications, SP42-6, 1974, pp 129-166
- (73) Smith, G.N. "An Introduction to Matrix and Finite Element Methods in Civil Engineering" Applied Science, London 1971
- (74) Smith, I.A. "The Design of Fly Ash Concretes" Proc. Inst. Civ. Engrs., V 36 , April, 1967, PP 769 - 790
- (75) Jackson, A.J., and Goodridge, W.F. "A New Approach to P.F. Ash Concrete" The Contract Journal, March 9, 1961, pp 1284-1287
- (76) British Standards Institute, "Specifications for Aggregates from Natural Sources for Concrete" BS.882/1201, 1965
- (77) Road Research Laboratory "Design of Concrete Mixes" Road Note No.4, London, 1950
- (78) British Standards Institute "Portland Cement, Ordinary and Rapid Hardening, BS.12:9, 1971
- (79) British Standards Institute, "P.F.A. for Use in Concrete", BS.3892, 1965
- (80) British Standards Institute "Method of Testing Concrete" BS.1881, Parts 4 & 5, 1970
- (81) Jones, L.L. "The Ultimate Flexural Strength of Reinforced and Prestressed Concrete Beams" C & CA Technical Report, November 1958

- (82) Hognestad, E., Hansen, N. and McHenry, D. "Concrete Stress Distribution in Ultimate Strength Design" ACI Journal, Proceedings, V.52, Part 1, 1955-56, pp
- (83) Bahia, H.M. "Shear Transfer in Fibre Reinforced Concrete T-beams" Ph.D. Thesis, Sheffield University, July 1976
- (84) Lee, J.N. "Effective Widths of T-beams" The Structural Engineer, V.40, No.1, January 1962, pp 21-27
- (85) Severn, R.T. "The Effective Width of T-beams" Magazine of Concrete Research, V.16, No.47, June 1964, pp 99-102
- (86) Brendel, G. "The Strength of the Compression Slab of T-beams Subject to Simple Bending" ACI Journal, Proceedings, V.61, Part 1, January 1964, pp 57-75
- (87) Jackson, N. and Lord, W.D. "Stresses in Wide-Flanged T-beams" Concrete and Constructional Eng., V.60, No.6, June 1965, pp 205-212
- (88) Adekola, A. "Effective Width of Composite Beams of Steel and Concrete" The Structural Engineer, V .46, No.9, 1968, pp 285-289
- (89) Fraser, D.J. and Hall, A. S. "The Effective Flange Width of Integral T- and L-beams" Civil Eng. Transactions, The Institution of Engineers, Australia, 1973, pp 74-76
- (90) Fan, H.M. "Effective Width of Composite Bridges at Ultimate Load" Ph.D. Thesis, University of Maryland, 1974
- (91) Morley, C.T. and Rajendran, S. "The Strength and Effective Width of Reinforced Concrete Flanges" Proc. Inst. Civ. Eng., V.59, Pt 2, March 1975, pp 103-122
- (92) Taylor, H.J. "Further Tests to Determine Shear Stresses in Reinforced Concrete Beams" C & CA Technical Report, RA.438, February 1970, pp 27
- (93) Regan, P.E. "Shear in Reinforced Concrete Beams" Magazine of Concrete Research, V.21, No.66, March 1969, pp 3-42
- (94) Swamy, N. and Adepegba, D. "A Criterion of Shear Failure for Reinforced Concrete Beams without Web Reinforcement", Särtryck ur Nordisk Betong nr.1, 1968, pp 1-24

I Determination of Principal Stresses

To determine the principal stresses σ_1 , σ_2 and σ_3 from the Cartesian stress components σ_x , σ_y , σ_z , τ_{xy} , τ_{yz} and τ_{zx} , the following cubic equation must be solved.

$$\begin{aligned} \sigma^3 - (\sigma_x + \sigma_y + \sigma_z) \sigma^2 + (\sigma_x \sigma_y + \sigma_y \sigma_z + \sigma_x \sigma_z - \tau_{yz}^2 \\ - \tau_{xz}^2 - \tau_{xy}^2) \sigma - (\sigma_x \sigma_y \sigma_z + 2 \tau_{yz} \tau_{xz} \tau_{xy} - \\ \sigma_x \tau_{yz}^2 - \sigma_y \tau_{xz}^2 - \sigma_z \tau_{xy}^2) = 0 \end{aligned} \quad (A.1)$$

The three roots of this equation give the values of the three principal stresses σ_1 , σ_2 and σ_3 , (25).

The above equation can be expressed in terms of the stress variants I_1 , I_2 and I_3 , (73) as:

$$\sigma^3 - I_1 \sigma^2 + I_2 \sigma - I_3 = 0 \quad (A.2)$$

where $I_1 = \sigma_x + \sigma_y + \sigma_z$

$$I_2 = \sigma_x \sigma_y + \sigma_y \sigma_z + \sigma_z \sigma_x - \tau_{yz}^2 - \tau_{xz}^2 - \tau_{xy}^2$$

$$\begin{aligned} I_3 = \sigma_x \sigma_y \sigma_z + 2\tau_{yz} \tau_{xz} \tau_{xy} - \sigma_x \tau_{yz}^2 - \sigma_y \tau_{xz}^2 \\ - \sigma_z \tau_{xy}^2 \end{aligned}$$

Defining $\sigma' = \sigma - \frac{I_1}{3}$ ie $\sigma = \sigma' + \frac{I_1}{3}$ (A.3)

Then equation (A.2) becomes:

$$\sigma'^3 - \left(\frac{I_1^2}{3} - I_2\right) \sigma' - \left(\frac{2 I_1^3}{27} - \frac{I_1 I_2}{3} + I_3\right) = 0 \quad (\text{A.4})$$

or

$$\sigma'^3 - I'_2 \sigma' - I'_3 = 0 \quad (\text{A.5})$$

where $I'_2 = \frac{I_1^2}{3} - I_2$ and $I'_3 = \frac{2 I_1^3}{27} - \frac{I_1 I_2}{3} + I_3$

If σ' is put equal to $r \cos \theta$, then equation (A.5) becomes

$$r^3 \cos^3 \theta - I'_2 r \cos \theta - I'_3 = 0 \quad (\text{A.6})$$

or

$$\cos^3 \theta - \frac{I'_2}{r^2} \cos \theta - \frac{I'_3}{r^3} = 0 \quad (\text{A.7})$$

which is identical to the standard trigonometrical expression

$$\cos^3 \theta - \frac{3}{4} \cos \theta - \frac{1}{4} \cos 3 \theta = 0 \quad (\text{A.8})$$

when

$$\frac{I'_2}{r^2} = \frac{3}{4} \quad \text{and} \quad \frac{I'_3}{r^3} = \frac{\cos 3 \theta}{4}$$

ie

$$r = \sqrt{\frac{4 I'_2}{3}} \quad \text{and} \quad \cos 3 \theta = \frac{4 I'_3}{r^3} \quad (\text{A.9})$$

from which three values for θ can be obtained and accordingly three values for σ' can be calculated. Then substituting in equation (A.3), three values for the principal stresses can be obtained.

II Calculation of the Principal Directions

To determine the rotation of the principal stress axes from the reference axes x, y, z the normalised modal matrix [A] must be obtained (73), where

$$[A] = \begin{bmatrix} a_{11} & a_{12} & a_{13} \\ a_{21} & a_{22} & a_{23} \\ a_{31} & a_{32} & a_{33} \end{bmatrix} \quad (\text{A.10})$$

Each eigenvector of this matrix will give the direction cosines of one of the principal stresses relative to the reference axis, ie:

a_{11} = direction cosine of angle between the major principal stress axis and ox

a_{21} = direction cosine of angle between the major principal stress axis and oy

a_{31} = direction cosine of angle between the major principal stress axis and oz

Knowing that the principal stresses are perpendicular to the planes on which they act, then the equilibrium equations for the stress components in the directions of the reference axes can be found and from these the direction cosines can be calculated. For example, the direction cosines for the major principal stress are $[a_{11} \ a_{21} \ a_{31}]$ and these can be calculated from:

$$(\sigma_x - \sigma_1) a_{11} + \tau_{xy} a_{21} + \tau_{xz} a_{31} = 0 \quad (\text{A.11})$$

$$\tau_{xy} a_{11} + (\sigma_y - \sigma_1) a_{21} + \tau_{yz} a_{31} = 0 \quad (\text{A.12})$$

$$\tau_{xz} a_{11} + \tau_{zy} a_{21} + (\sigma_z - \sigma_1) a_{31} = 0 \quad (\text{A.13})$$

These equations can be written in the form:

$$\begin{bmatrix} \sigma_x - \sigma_1 & \tau_{xy} & \tau_{xz} \\ \tau_{xy} & \sigma_y - \sigma_1 & \tau_{yz} \\ \tau_{xz} & \tau_{zy} & \sigma_z - \sigma_1 \end{bmatrix} \begin{bmatrix} a_{11} \\ a_{21} \\ a_{31} \end{bmatrix} = 0 \quad (\text{A.14})$$

From (A.11)

$$a_{11} = - \frac{\tau_{xy}}{\sigma_x - \sigma_1} a_{21} - \frac{\tau_{xz}}{\sigma_x - \sigma_1} a_{31} \quad (\text{A.15})$$

Substituting (A.15) into (A.12), then

$$a_{21} = \frac{[\tau_{xy} \tau_{xz} - \tau_{yz} (\sigma_x - \sigma_1)]}{[(\sigma_y - \sigma_1)(\sigma_x - \sigma_1) - \tau_{xy}^2]} a_{31} \quad (\text{A.16})$$

and

$$a_{11} = - \frac{\tau_{xy}}{\sigma_x - \sigma_1} \times \frac{[\tau_{xy} \tau_{xz} - \tau_{yz} (\sigma_x - \sigma_1)]}{[(\sigma_y - \sigma_1)(\sigma_x - \sigma_1) - \tau_{xy}^2]} a_{31} - \frac{\tau_{xz}}{\sigma_x - \sigma_1} a_{31} \quad (\text{A.17})$$

Putting $a_{31} = 1.0$, then the values a_{11} and a_{21} can be calculated and the eigenvector of equation (A.14) becomes:

$$\begin{bmatrix} a_{11} \\ a_{21} \\ 1.0 \end{bmatrix} \quad (A.18)$$

The length of this vector, A is given by:

$$A = \sqrt{a_{11}^2 + a_{21}^2 + 1.0^2} \quad (A.19)$$

The normalised vector is then given by:

$$\begin{bmatrix} a_{11}/A \\ a_{21}/A \\ 1.0/A \end{bmatrix} \quad (A.20)$$

which represents the direction cosines of the major principal stress or the 1st eigenvector of equation (A.14). The second and third eigenvectors of equation (A.14) can be obtained in the same way but using σ_2 and σ_3 respectively in equations (A.11) to (A.13).